

Nr. 322

# Carrier-phase Multipath in Satellite-based Positioning

Von der Fakultät für Bauingenieurwesen und Geodäsie  
der Gottfried Wilhelm Leibniz Universität Hannover  
zur Erlangung des Grades

**DOKTOR-INGENIEUR (Dr.-Ing.)**

genehmigte Dissertation  
von

M.Sc. Marios Smyrnaioi  
geboren am 15. August 1982 in Athen

HANNOVER 2016

---

Referent: Prof. Dr.-Ing. Steffen Schön  
Korreferenten: Prof. Dr.-Ing. habil. Christian Heipke  
Prof. Dr.-Ing. habil. Lambert Wanninger

Tag der mündlichen Prüfung: 04 February 2016

## Summary

In the presence of multipath, replicas of the direct signal reach the receiving antenna through paths other than the line of sight path. As a result, the receiver is tracking a compound signal and biases are introduced in the range and signal power observations measured by the receiver. Due to the continuously changing satellite-receiver geometry, these biases are not constant in time. They exhibit a sinusoidal like behaviour in the observation domain. This behaviour is immediately visible in the  $C/N_0$  observations generated by the receiver. On the contrary, in the range observations, such effects are not instantly visible. Differences should be formed or residuals should be analysed to isolate them. The resulting error magnitude, due to multipath propagation, depends on several factors. The most crucial are the signal characteristics, the environment in which the antenna is placed, the geometrical characteristics of the path of the reflected signals, the antenna characteristics, and the receiver design.

The major contribution of this thesis is the development of compact expressions for modelling the impact of multipath propagation on the GNSS observables. The equations for the computation of multipath effects in the phase and signal power GNSS observables are further developed by introducing compact expressions for the power computation of direct and indirect signal components. For the calculation of the power of the direct signal, the Friis transmission equation is evaluated. The gain information is introduced into the Jones vector that is utilized for modelling the transmitting/receiving antennas. In modelling the antenna gain patterns in such a way, the phase information is also present. For the indirect signal components, the reflection process is also taken into account. The expressions are used for characterizing the impact of multipath propagation in an extensive simulation analysis. The findings are validated via two measurement campaigns. The experimental configuration as well as the environment in which the antennas are placed are chosen and controlled in such a way that it would allow the isolation of multipath effects on the carrier phase domain and the comparison with the simulations.

Additionally to the significant contribution, two other not directly multipath related studies are presented in the framework of this thesis. In the first investigation, the capabilities of positioning with pseudolites are explored. Results show that pseudolite positioning in localized environments is more accurate compared to GNSS positioning, mainly due to the absence of ionospheric refraction.

In the second study, the impact of different estimation algorithms utilized for the estimation of the  $C/N_0$  observations are characterized. The motivation for this analysis emerged from the outcome of the major contribution of this work. There,  $C/N_0$  observables are simulated from a propagation point of view, and the impact of the receiver is not considered. The analysis shows that, indeed, the different algorithms used for the estimation of this GNSS observables are also impact-full. Different linear trends were identified in the resulted  $C/N_0$  time series estimated by different algorithms.

In this thesis, I demonstrate that when the geometrical characteristics of the reflected signals, the material properties of the reflector and the gain patterns of the transmitting and receiving antennas are known, then multipath effects on the carrier phase observations can be characterized in an epoch-wise sense and for complete satellite arcs.

**keywords:** GNSS, Multipath, Gain Pattern, Jones Vector, Signal Power



# Zusammenfassung

Sind Mehrwegeeffekte auf den GNSS-Signalen vorhanden, erreichen sowohl direkte Signale entlang der Sichtlinie zum Satelliten, als auch indirekte Signale (Replikas bzw. Umwegsignale des direkten Signals) die Empfangsantenne. Diese Mischsignale werden im Empfänger getrackt und führen zu Versätzen der gemessenen Trägerphasen- und Signalstärkebeobachtung. Aufgrund der sich stetig ändernden Satellitengeometrie relativ zum Empfänger sind diese Versätze zeitlich nicht konstant, sondern führen zu einem sinus-soidalen Verhalten im Beobachtungsraum. Dieses Verhalten ist direkt aus den Signalstärkewerten ( $C/N_0$  observations), die vom Empfänger erzeugt werden, ablesbar. Hingegen sind diese Effekte auf der Entfernungsmessung (range observations) nicht im gleichen Sinne direkt ablesbar. Um diese Effekte dennoch zu isolieren, sind Differenzen zu bilden, oder Residuen zu analysieren. Der durch den Mehrwegeeffekt resultierende Fehler ist von mehreren Faktoren abhängig. Die wichtigsten Effekte sind die Signaleigenschaften, die Umgebung, in der sich die Empfangsantenne befindet, die geometrischen Eigenschaften des Umwegsignals sowie die Antennencharakteristiken und das Empfängerdesign.

Der wesentliche Beitrag dieser Arbeit ist die Entwicklung von kompakten Ausdrücken zur Modellierung des Einflusses von Mehrwegeeffekten auf den GNSS-Beobachtungen. Die Formeln zur Berechnung des Mehrwegeefflusses für die Trägerphasen und die Signalstärke der GNSS-Beobachtungen wurden zusätzlich erweitert durch kompakte Ausdrücke der direkten und indirekten Signalanteile. Zur Berechnung der Signalstärke des direkten Signals wurde Friis Transmissionsgleichung verwendet. Die Information über den Antennengewinn wurde über den Jones Vektor eingeführt, der für die Modellierung der Sende- und Empfangsantenne verwendet wird. Durch die Beschreibung des Antennengewinndiagramms auf diese Weise, bleibt die Phaseninformation gut erhalten. Für den indirekten Signalanteil wird der Reflexionsvorgang ebenfalls berücksichtigt. Die so entwickelten Ausdrücke werden verwendet, um den Einfluss der Fortpflanzung des Mehrwegesignals in einer erweiterten Simulation zu charakterisieren. Die so gewonnenen Erkenntnisse werden durch zwei Experimente in kontrollierter Umgebung validiert. Die Konfiguration der Experimente wurde derart gewählt, dass die Trennung der Mehrwegeeffekte von der Trägerphasenbeobachtung erfolgreich durchgeführt und mit den Simulationen erfolgreich verglichen werden konnte.

Zusätzlich zum Hauptteil der Arbeit werden zwei weitere, nicht-Mehrwege bezogene Studien im Rahmen dieser Arbeit diskutiert. Im ersten Teil werden die Möglichkeiten zur Positionierung mittels Pseudo-Satelliten (pseudolites) näher analysiert. Die Ergebnisse zeigen, dass die Positionierung über Pseudolites in lokalisierten Umgebungen durch die nicht zu berücksichtigende Ionosphäre deutlich genauer ist, als die vergleichbare Positionierung mit GNSS.

In der zweiten Studie werden verschiedene Ausgleichsalgorithmen zur Bestimmung von GNSS  $C/N_0$ -Beobachtungen näher analysiert. Die Motivation zu dieser Untersuchung ergab sich aus den sich abzeichnenden Ergebnissen des Hauptteils dieser Arbeit. Dort werden  $C/N_0$ -Beobachtungen unabhängig vom Empfänger, allein auf Basis ihrer Ausbreitung simuliert. Der Einfluss unterschiedlicher Tracking-Algorithmen zeigt deutlich den Einfluss auf die GNSS-Signalstärkebeobachtung. Verschiedene lineare Trends konnten für die unterschiedlichen Algorithmen identifiziert werden.

Durch die in dieser Arbeit entwickelten Ausdrücke kann deutlich gezeigt werden, dass Mehrwegeeffekte auf der Trägerphasenbeobachtung in einem epochenweisen Ansatz beschrieben werden können, wenn die geometrischen Eigenschaften des reflektierten Signals, die Materialeigenschaften des Reflektors und der Antennengewinn der Sende- und Empfangsantennen bekannt sind.

**Schlüsselworte:** GNSS, Mehrwegeeffekte, Antennengewinndiagramm, Jones Vektor, Signalstärke

# Abbreviations

ACP	Average Carrier Power
ADC	Analog to Digital Converter
AoA	Angle of Arrival
AoD	Angle of Departure
AR	Axial Ratio
BPSK	Binary Phase Shift Keying
C/A	Coarse Acquisition Code
CDMA	Code Division Multiple Access
$C/N_0$	Carrier to Noise Density Ratio
CP	Circular Polarized
DD	Double Differences
DE	Differential Estimator
DGPS	Differential GPS
DLL	Delay Lock Loop
EGNOS	European Geostationary Navigation Overlay Service
EIRP	Effective Isotropic Radiated Power
EM	Electromagnetic
FDMA	Frequency-division multiple access
FNBW	First Null Beam Width
GATE	Galileo Test Environment
GBAS	Ground Based Augmentation Systems
GDOP	Geometrical Delusion of Precision
GDV	Group Delay Verification
GLONASS	Globalnaya navigatsionnaya sputnikovaya sistema
GNSS	Global Navigation Satellite Systems
GPS	Global Positioning System
HDOP	Horizontal Delusion of Precision
HPBW	Half-Power Beam Width
IEEE	Institute of Electrical and Electronics Engineers
IF	Intermediate Frequency
IGS	International GNSS Service
IOV	In-Orbit Validation
LC	Linear Combination
LFSR	Linear Feedback Shift Register
LHCP	Left Hand Circular Polarized
LHEP	Left Hand Elliptical Polarized
LNA	Low Noise Amplifier
LOS	Line Of Sight
LP	Linear Polarized
MPC	Multipath Component
NCO	Numerical Controlled Oscillator
NNSS	Navy Navigation Satellite System
NWPR	Narrow-Wide Power Ratio
OMC	Observed Minus Computed
PCO	Phase Center Offset

PCV	Phase Center Variations
PDF	Probability Density Function
PLL	Phase Lock Loop
PPP	Precise Point Positioning
PPS	Precise Positioning Service
PRN	Pseudorandom Noise
PSD	Power Spectral Density
PSL	Pseudolites
RF	Radio Frequency
RHCP	Right Hand Circular Polarized
RHEP	Right Hand Elliptical Polarized
RINEX	Receiver Independent Exchange Format
RMS	Root Mean Square Error
RS	Reference Station
RTCM	Radio Technical Commission for Marine Services
RTK	Real Time Kinematic
SBAS	Satellite Based Augmentation Systems
SE	Squaring Estimator
SPP	Single Point Positioning
UTD	Uniform Theory of Diffraction
VSE	Variance Summing Estimator
VSWR	Voltage Standing Wave Ratio



# Contents

<b>1. Introduction</b>	<b>1</b>
<b>2. GNSS Aspects, an Overview</b>	<b>3</b>
2.1. Satellite-Based Navigation Systems . . . . .	3
2.1.1. Absolute Positioning . . . . .	5
2.1.2. DGPS and Augmentation Systems . . . . .	5
2.1.3. Pseudolites . . . . .	6
2.1.4. Galileo Test-Beds . . . . .	6
2.2. Antenna Performance Parameters . . . . .	7
2.2.1. Radiation Pattern . . . . .	7
2.2.2. Field Regions . . . . .	10
2.2.3. Directivity and Gain . . . . .	11
2.2.4. Antenna Efficiency and Related Parameters . . . . .	14
2.3. Propagation Aspects . . . . .	17
2.3.1. Introduction to Polarization . . . . .	17
2.3.2. Polarization Representation . . . . .	21
2.3.3. Polarization Efficiency . . . . .	24
2.3.4. Friis Transmission Equation . . . . .	25
2.4. Signal Processing . . . . .	28
2.4.1. Signal Generation . . . . .	28
2.4.2. Receiver Front-End and Signal Conditioning . . . . .	30
2.4.3. Receiver Signal Processing Modules . . . . .	31
2.4.4. Acquisition . . . . .	32
2.4.5. Tracking . . . . .	33
2.5. GNSS Observables and Data Processing . . . . .	37
2.5.1. Observation Differencing . . . . .	38
2.5.2. Linear Combinations . . . . .	39
<b>3. Multipath Effects in GNSS</b>	<b>41</b>
3.1. Multipath Effects in GNSS Positioning . . . . .	41
3.1.1. Overview of Multipath Related Studies in GNSS . . . . .	42
3.2. GNSS Multipath Aspects . . . . .	46
3.2.1. Types of Multipath Interactions . . . . .	47
3.2.2. Diffraction Induced Multipath Effects . . . . .	47
3.2.3. Diffused Reflection . . . . .	48
3.2.4. Specular Reflection . . . . .	51
3.3. Multipath Characterization . . . . .	55
3.3.1. Signal Tracking in the Presence of Multipath . . . . .	56
3.3.2. Two Ray Analysis . . . . .	58
<b>4. Characterization of a Pseudo-satellite Multipath Scenario</b>	<b>63</b>
4.1. SEA GATE data processing . . . . .	63
4.2. Parameter Estimation and Least-squares theory . . . . .	64
4.3. PSL Observational Model . . . . .	65

4.4.	Data Analysis from RS1 and RS2 . . . . .	66
4.4.1.	SPP Pseudolites versus GPS . . . . .	68
4.4.2.	Residuals of the PSL Code-phases . . . . .	69
4.5.	Discussion . . . . .	72
<b>5.</b>	<b>On the Impact of Different <math>C/N_0</math> Estimation Algorithms</b>	<b>73</b>
5.1.	Introduction . . . . .	73
5.2.	Sidereal Repeatability of GNSS Ground Tracks . . . . .	74
5.3.	I and Q Data Analysis . . . . .	75
5.3.1.	Narrow-Wide Band Power Ratio Estimator . . . . .	76
5.3.2.	Variance Summing Estimator . . . . .	77
5.3.3.	Squaring and Differential Estimators . . . . .	78
5.4.	Comparison of Different Algorithms . . . . .	80
5.5.	Discussion . . . . .	84
<b>6.</b>	<b>Development of a Generalized Multipath Model</b>	<b>85</b>
6.1.	GNSS Signal Power Modelling . . . . .	85
6.2.	Simulation Analysis . . . . .	90
6.2.1.	Received signal power of direct and indirect signal components . . . . .	90
6.2.2.	Phase error w.r.t. antenna height and carrier frequency . . . . .	93
6.2.3.	Compound signal power and phase error w.r.t. different reflectors . . . . .	94
6.2.4.	Multipath Effects w.r.t. Different Receiving Antenna Gain Patterns . . . . .	95
6.2.5.	Discussion . . . . .	99
6.3.	Experimental Validation . . . . .	99
6.3.1.	First Experiment at PTB . . . . .	99
6.3.2.	Simulations versus Observations . . . . .	101
6.3.3.	Discussion . . . . .	108
6.3.4.	Second Experiment at PTB . . . . .	108
6.3.5.	Data Analysis . . . . .	110
6.3.6.	Simulation versus Observations . . . . .	113
6.3.7.	Discussion . . . . .	121
<b>7.</b>	<b>Summary and Conclusions</b>	<b>123</b>
<b>A.</b>	<b>Data Analysis from PTB Experiments</b>	<b>125</b>
A.1.	First experiment at PTB - $C/N_0$ Observed versus Simulated . . . . .	125
A.2.	Second experiment at PTB . . . . .	129
A.2.1.	$C/N_0$ Observed versus Simulated - Day 1 . . . . .	129
A.2.2.	$C/N_0$ Observed versus Simulated - Day 2 . . . . .	134

# List of Figures

2.1. GPS signals . . . . .	4
2.2. 3D pattern of an isotropic source . . . . .	8
2.3. 2D pattern of an isotropic source . . . . .	9
2.4. GNSS-like antenna pattern . . . . .	9
2.5. Field regions of an antenna . . . . .	10
2.6. Exemplary antenna partial gain patterns . . . . .	13
2.7. Exemplary GNSS antenna partial gain pattern in cartesian coordinates . . . . .	13
2.8. Smith chart . . . . .	15
2.9. Circular polarized electric field vector . . . . .	20
2.10. Polarization ellipse . . . . .	22
2.11. Polarization ellipse description with different quantities. . . . .	23
2.12. Polarization efficiency . . . . .	25
2.13. Off-nadir angle . . . . .	27
2.14. GNSS link budget . . . . .	27
2.15. C/A code generation scheme . . . . .	29
2.16. Auto- and Cross-Correlation of C/A code sequences . . . . .	29
2.17. GNSS front-end . . . . .	31
2.18. Acquisition block diagram . . . . .	33
2.19. Acquisition search space . . . . .	33
2.20. DLL architecture . . . . .	34
2.21. PLL architecture . . . . .	34
2.22. DLL Tracking . . . . .	36
2.23. PLL Tracking . . . . .	36
2.24. PLL thermal noise . . . . .	37
3.1. Multipath interactions . . . . .	47
3.2. Shadowing effects . . . . .	48
3.3. Diffused reflection . . . . .	48
3.4. Rayleigh criterion . . . . .	49
3.5. Rayleigh versus normal PDF . . . . .	50
3.6. Reflection coefficients for L1 . . . . .	52
3.7. Reflection coefficients for L5 . . . . .	53
3.8. Linear versus circular reflection coefficients . . . . .	54
3.9. First Fresnel ellipsoid and reflection zone . . . . .	54
3.10. Reflection Geometry . . . . .	55
3.11. Multipath phase rates . . . . .	56
3.12. The Correlation Function . . . . .	57
3.13. Phase Error Envelops . . . . .	58
3.14. Phase error of PLL due to one multipath component . . . . .	59
4.1. Rostock harbour area and Sea Gate infrastructure . . . . .	64
4.2. Observed PSL at RS1 . . . . .	66
4.3. Observed PSL at RS2 . . . . .	67
4.4. Observed GPS satellites at RS1 and RS2 . . . . .	67
4.5. SPP from pseudolite (C1) for RS1 and RS2 . . . . .	68

4.6. SPP from GPS (C1) for RS1 and RS2 . . . . .	68
4.7. SPP from GPS (C1) for for Warnemünde IGS RS station . . . . .	69
4.8. Residuals of the PSL code-phases at RS1 . . . . .	70
4.9. Boxplot of the residuals of the PSL code-phases at RS1 . . . . .	70
4.10. Residuals of the PSL code-phases at RS2 . . . . .	71
4.11. Boxplot of the residuals of the PSL code-phases at RS2 . . . . .	71
5.1. GIH rooftop environment . . . . .	73
5.2. GIH rooftop experimental set-up . . . . .	74
5.3. Sidereal repeatability of multipath signatures . . . . .	75
5.4. Estimated $C/N_0$ time series by the power ratio estimator . . . . .	77
5.5. Estimated $C/N_0$ time series by the variance summing estimator . . . . .	78
5.6. Estimated $C/N_0$ time series by the squaring estimator . . . . .	79
5.7. Estimated $C/N_0$ time series by the differential estimator . . . . .	80
5.8. Estimated $C/N_0$ time series by the different estimators . . . . .	81
5.9. Estimated $C/N_0$ time series with different integration intervals . . . . .	82
5.10. Estimated $C/N_0$ time series and regression lines . . . . .	83
6.1. Received signal power (LOS) . . . . .	86
6.2. Simulated compound signal power versus phase error . . . . .	88
6.3. Received signal power of LOS and MP signal components . . . . .	88
6.4. Reflection geometry of a ground reflection scenario . . . . .	89
6.5. Key factors for the resulting magnitude of the relative amplitude . . . . .	90
6.6. Partial gain patterns used for the simulations . . . . .	91
6.7. Received signal power for the LOS component . . . . .	91
6.8. Satellite antenna gain for both orthogonal polarizations . . . . .	92
6.9. Received signal power for the LOS component . . . . .	92
6.10. Received signal power of a MPC . . . . .	93
6.11. Phase error for different antenna heights (right side) and power spectral density of the simulated time series (left side) . . . . .	94
6.12. Phase error for different GNSS carrier frequencies . . . . .	94
6.13. Compound signal power and phase error for different reflectors . . . . .	95
6.14. Co- and Cross-polarized gain patterns used for the simulations . . . . .	96
6.15. Phase error versus different gain patterns . . . . .	96
6.16. Compound signal versus different gain patterns . . . . .	97
6.17. Exemplary gain pattern . . . . .	97
6.18. Phase error for a concrete reflector and different gain patterns . . . . .	98
6.19. Phase error for a metal reflector and different gain patterns . . . . .	98
6.20. Phase error for a wet soil reflector and different gain patterns . . . . .	98
6.21. Phase error for a sea water reflector and different gain patterns . . . . .	99
6.22. Experimental set-up of the first experiment at PTB . . . . .	100
6.23. Satellite visibility and skyplot at S1 station . . . . .	100
6.24. Reflection points at S1 and S2 stations . . . . .	101
6.25. Observed versus simulated $C/N_0$ . . . . .	102
6.26. Simulated phase error of the short baseline . . . . .	103
6.27. PSD of the simulated phase error time series present in the DDs and of the simulated DDs . . . . .	103
6.28. PSD for the simulated and observed phase DDs versus cross-PSD between the observations and the simulations . . . . .	104
6.29. Observed versus Simulated DD phase residuals . . . . .	105
6.30. Observed versus simulated DD phase residuals . . . . .	106

6.31. Left side: PSD for the simulated (in red) versus observed (in blue) phase DDs formed with PRN12 and PRN9. Right side: cross-PSD between the observations and the simulations . . . . .	107
6.32. Left side: PSD for the simulated (in red) versus observed (in blue) phase DDs formed with PRN12 and PRN27. Right side: cross-PSD between the observations and the simulations . . . . .	107
6.33. Left side: PSD for the simulated (in red) versus observed (in blue) phase DDs formed with PRN12 and PRN31. Right side: cross-PSD between the observations and the simulations . . . . .	108
6.34. Experimental set up at PTB Braunschweig . . . . .	109
6.35. Visibility plot on L1 and skyplot of the observed PRNs on 26.02.2013 . . . . .	109
6.36. Observed $C/N_0$ of PRN 9 . . . . .	110
6.37. Observed $C/N_0$ of PRN 26 . . . . .	111
6.38. MP1 LC of PRN 9 on day 1 and day 2 . . . . .	111
6.39. MP1 LC of PRN 26 on day 1 and day 2 . . . . .	112
6.40. Computed carrier-phase DDs on day 1 and day 2 for the exempalry PRNs . . . . .	112
6.41. Observed versus Simulated DD phase residuals of the second experiment (1) . . . . .	114
6.42. Observed versus Simulated DD phase residuals of the second experiment (2) . . . . .	115
6.43. Observed versus Simulated DD phase residuals of the second experiment (3) . . . . .	116
6.44. Observed versus Simulated DD phase residuals of the second experiment (4) . . . . .	117
6.45. PSD for the simulated (in red) versus observed (in blue) and cross-PSD between the observations and the simulations. of the DD residuals formed by PRN9 and PRN1 for both observational days . . . . .	118
6.46. PSD for the simulated (in red) versus observed (in blue) and cross-PSD between the observations and the simulations. of the DD residuals formed by PRN9 and PRN17 for both observational days . . . . .	119
6.47. PSD for the simulated (in red) versus observed (in blue) and cross-PSD between the observations and the simulations. of the DD residuals formed by PRN9 and PRN26 for both observational days . . . . .	120
A.1. Observed versus simulated $C/N_0$ - First experiment at PTB . . . . .	125
A.2. Observed versus simulated $C/N_0$ - First experiment at PTB . . . . .	126
A.3. Observed versus simulated $C/N_0$ - First experiment at PTB . . . . .	127
A.4. Observed versus simulated $C/N_0$ - First experiment at PTB . . . . .	128
A.5. Observed versus simulated $C/N_0$ - First experiment at PTB . . . . .	129
A.6. Observed versus simulated $C/N_0$ - Second experiment at PTB . . . . .	129
A.7. Observed versus simulated $C/N_0$ - Second experiment at PTB . . . . .	130
A.8. Observed versus simulated $C/N_0$ - Second experiment at PTB . . . . .	131
A.9. Observed versus simulated $C/N_0$ - Second experiment at PTB . . . . .	132
A.10. Observed versus simulated $C/N_0$ - Second experiment at PTB . . . . .	133
A.11. Observed versus simulated $C/N_0$ - Second experiment at PTB . . . . .	134
A.12. Observed versus simulated $C/N_0$ - Second experiment at PTB . . . . .	134
A.13. Observed versus simulated $C/N_0$ - Second experiment at PTB . . . . .	135
A.14. Observed versus simulated $C/N_0$ - Second experiment at PTB . . . . .	136
A.15. Observed versus simulated $C/N_0$ - Second experiment at PTB . . . . .	137
A.16. Observed versus simulated $C/N_0$ - Second experiment at PTB . . . . .	138



# List of Tables

2.1.	Complex vector representation of particular polarization states . . . . .	20
2.2.	Polarization efficiency of characteristic cases . . . . .	24
2.3.	Code discriminators . . . . .	35
2.4.	Phase discriminators . . . . .	35
3.1.	Exemplary material properties . . . . .	51
4.1.	Elevation, azimuth and distance of the PSL relative to RS1 . . . . .	66
4.2.	Elevation, azimuth and distance of the PSLs relative to RS2 . . . . .	67
5.1.	Sidereal repeatability of the observed PRNs . . . . .	76
5.2.	NWPR and VS estimators overview . . . . .	81
5.3.	Differential and Squaring estimators overview . . . . .	82
5.4.	$C/N_0$ time series versus integration time . . . . .	82
6.1.	Magnitude squared coherence between the observations and the simulations - First experiment at PTB . . . . .	104
6.2.	RMS of the multipath free linear combination (MP1) for PRN9 and PRN26 . . . . .	112
6.3.	RMS of the double differenced phase observations . . . . .	113
6.4.	Magnitude squared coherence between the observations and the simulations - Second experiment at PTB, day 1 . . . . .	121
6.5.	Magnitude squared coherence between the observations and the simulations - Second experiment at PTB, day 2 . . . . .	121





# 1. Introduction

GNSS technology was originally designed for precise 3D positioning, navigation and timing purposes. In the last decades, many advances have been made in modelling the different error sources that are biasing GNSS signals and reduce the positioning accuracy. In our days, positioning with GNSS can reach accuracies of up to mm level. One of the last remaining un-modelled error source in GNSS is multipath propagation.

Multipath related biases occur when apart from the direct signal, delayed replicas of it arrive also at the receiving antenna. These signal components arrive delayed, phase shifted, attenuated and depolarized relative to the direct signal and result in compound signal tracking by the receiver. In this way, the range observations generated by the receiver are biased by multipath propagation. These biases propagate to the estimated positioning solution and reduce the resulting accuracy and precision. The unknown number of indirect signal components, the geometrical characteristics of their path and the different types of multipath interactions that may occur together with a complex receiver and antenna design make multipath mitigation very challenging. Furthermore, such station dependent error sources decorrelate at different antenna locations and in contrast to other GNSS error sources, multipath effects can not be mitigated or reduced by differential techniques.

Different strategies have been developed during the last decades for the mitigation and/or characterization of this propagation phenomenon. The developed strategies are very diverse. They can be, roughly, categorized into signal processing, observation domain, antenna design related, and analytical modelling approaches.

The development of compact expressions for modelling the impact of multipath propagation on the GNSS observables are the core of the thesis. The used, within the GNSS community, expressions for the computation of the phase error and the compound signal amplitude/power due to multipath propagation are further generalized by integrating analytical expressions for the computation of the received signal power of direct and indirect signal components. Thus, it becomes possible to simulate multipath effects in the phase and  $C/N_0$  observations, in an epoch-wise sense, with a low implementation complexity method via the evaluation of one expression for each GNSS observation type. For the evaluation of the expressions, a dedicated algorithm was developed and two different controlled experiments were performed. It is demonstrated in this thesis that multipath effects can be characterized in an epoch-wise sense and for complete satellite arcs when the path of the indirect signals as well as the gain information of the transmitting/receiving antennas and the material properties of the reflector are known.

This thesis is structured as follows. In chapter 2, different aspects of the GNSS technology are presented. In a first step, antenna performance parameters associated with the antenna radiation patterns are introduced. Despite the fact that antennas are a crucial element of the GNSS satellite-receiver radio link they are, most of the time, considered as black boxes and their impact is neglected. In this part, the antenna gain is formally introduced since it is a crucial element for the power link computations of the GNSS signals. In a second step, polarization aspects are introduced. Different mathematical representations are introduced together with the Jones vector notation that is used, in this thesis, for the antenna gain pattern modelling. The Friis transmission equation is presented after. The reason for writing these sections is that such antenna measurement/calibration aspects and background information on antenna diagrams are not so frequently present in the GNSS literature. Nevertheless, such aspects can be found in remote sensing courses typically given in under- and/or post-graduate programs of Geodetic sciences. In the following section, the different signal processing stages that are utilized by a receiver for navigation purposes are presented. In the last part

of chapter 2, GPS observation equations are explained together with observation differences and linear combination concepts.

In chapter 3, multipath related aspects are presented. After an introductory section and a literature survey on multipath related studies in GNSS, different types of multipath interactions are introduced. Aspects of diffraction induced multipath as well as of the diffused reflection process are explained in this section. Specular reflection and Fresnel coefficient are explained after that. For the main contribution of this thesis, only specular reflections are considered. The derivation of the equations that describe the impact of multipath propagation on the phase and  $C/N_0$  observations is presented in detail in the last section.

Chapter 4 of the thesis contains work related to pseudolite positioning. A critical analysis of pseudolite data from the SEA GATE environment is performed via dedicated navigation algorithms that were developed for this purpose. A characterization of multipath effects for this pseudolite scenario is taking place in this chapter.

In the fifth chapter, the impact of different  $C/N_0$  estimation algorithms is characterized via a dedicated experimental measurement campaign. RINEX data and IF raw GNSS signal are captured and analysed for this purpose. The analysis showed that signal strength observables generated by different receivers may slightly vary. In the analysis of the estimated time series from the different  $C/N_0$  estimation algorithms which were implemented in software, different linear trends were identified.

In chapter 6, the development of expressions for the computation of the received GNSS signal power of both direct and indirect signal components is presented in detail in a first step. The expressions are then used in simulation analysis for the characterization of the impact of multipath propagation on the GNSS observables. Simulations w.r.t. key factors that are involved in the processes are performed. The characterization of the impact that different antennas and reflectors have on the resulting multipath effects is performed in the second section of this chapter. The different antennas are simulated w.r.t. their gain pattern characteristics, orientation, and polarization. In the third part, the validation of the theoretical part as well as of the findings of the simulation analysis takes place. For the validation, two controlled experiment were planned and carried out. The first one lasted about 7 hours and from the second one, data from two consequent observational days were analysed. In both cases, a short baseline with a high-low antenna set-up was measured. The specific environment in which the antennas were placed in was chosen due to the flat terrain characteristics of it. In this way, it was ensured that reflections could only occur from the ground and, therefore, their geometrical path characteristic were considered known. Furthermore, the short baseline set-up with the high-low antenna configuration allowed the isolation multipath propagation effects in the double differenced phase residuals. Thus, the comparison of the simulated double differenced phase error with the observed double differenced phase residuals was possible and was made in the last section.

Finally, the seventh chapter summarizes and concludes this thesis and in appendix A, simulation versus observations of the  $C/N_0$  data from all observed PRNs of the two experiments at PTB are illustrated for the sake of completeness.

## 2. GNSS Aspects, an Overview

This chapter serves as an introductory chapter of different aspects of the satellite navigation systems that will be further used in the following chapters of this thesis. In the first section, satellite navigation systems are introduced together with the concepts of absolute and relative positioning. Furthermore, pseudo-satellites and their applicability in test environments for the future Galileo signals and applications are also presented. After that, basic antenna performance parameters that are associated with the antenna radiation patterns are introduced. Gain is formally introduced in this section. Subsequently, polarization aspect and Friis transmission equation are explained. GNSS signal processing aspects follow after. In the last section, the GPS observation equations are described together with the observation differencing schemes and various linear combinations.

### 2.1. Satellite-Based Navigation Systems

The history of satellite-based navigation systems or Global Navigation Satellite Systems (GNSS) started in the late 50's with the development of the US TRANSIT. TRANSIT or Navy Navigation Satellite System (NNSS) was the predecessor of Global Positioning System (GPS) and the first satellite navigation system in operational use. Signals were transmitted at 400 and 150 MHz frequencies and Doppler shift measurements were performed by the user for positioning purposes. The system was in operational use from mid 60's to mid 90's. More information about TRANSIT system can be found in Seeber (2003).

In the early 70's, GPS was first proposed. The satellite-user ranges are to be determined with the use of pseudorandom noise (PRN) signals. The system was originally designed as a military only navigation system for precise 3D positioning, navigation and timing purposes. Further design criteria are global coverage and continuous/all-weather operation. In July 1995, the full operational capability of GPS was officially declared. Nevertheless, the system was already available for civilian use since the 80's.

The GPS space segment consists of about 31 active satellites orbiting in nearly circular orbits. They are placed in six orbital planes with  $55^\circ$  inclination on the equatorial plane. The revolution period is about 11h 58 min, and the satellite vehicles are repeating their ground tracks after roughly one sidereal day (23h 56min). The GPS control segment is continuously monitoring the system. The user segment consists of all the receivers on the surface of the Earth, in the air and in low Earth orbits, that are using GPS for different applications.

GPS signals are generated by atomic clocks on board the satellites. The fundamental frequency is 10.23 MHz and the transmitted L-Band carrier signals are  $L1 = 154 \times 10.23 = 1575.35$  MHz and  $L2 = 120 \times 10.23 = 1227.60$  MHz. The Code division multiple access (CDMA) navigation codes are modulated on the carrier by binary phase shift keying (BPSK). GPS provides two navigation services; the standard positioning service (SPS) which is publicly available and utilized by the coarse/acquisition (C/A) code and the precise positioning service (PPS), which is available only to authorized users and it is provided by the encrypted, precise P(Y) code. Currently, GPS is in a modernization phase. New generations of navigation satellites are providing new signals (see fig. 2.1). L2C is a second civil signal transmitted by Block IIR-M. Block IIF satellites are also transmitting a third carrier-frequency (L5) on which I5 and Q5 codes are modulated. A new military signal (M-code) is transmitted in L1 and L2 carrier-frequencies by the previously mentioned Blocks of GPS satellites. Finally, the upcoming block III GPS satellites will transmit a new civil signal (L1C) in L1 frequency.

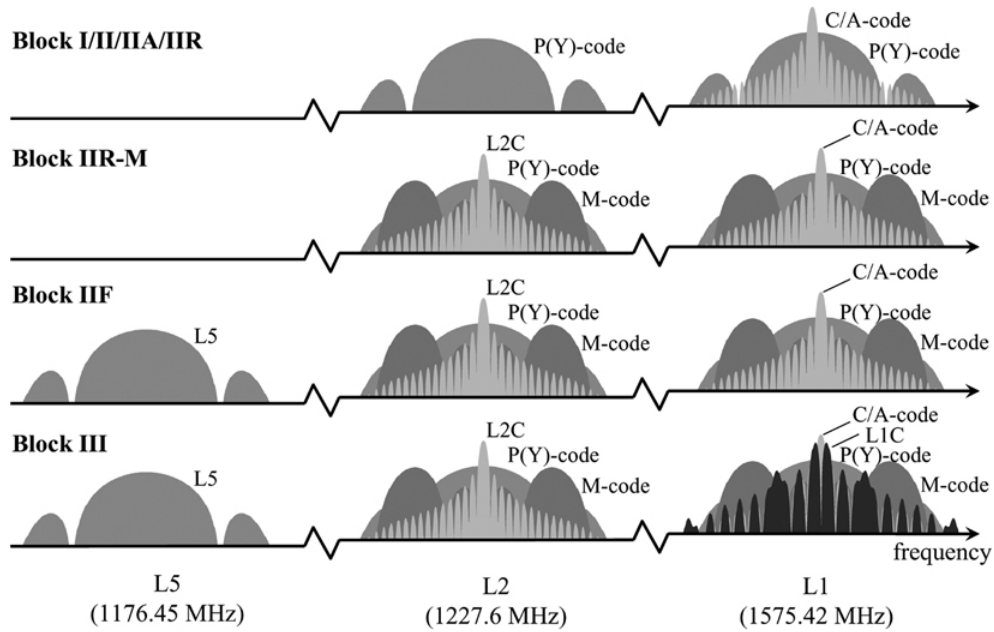


Figure 2.1.: Spectra of current and future GPS signals (Hegarty and Chatre, 2008).

The second operational satellite-based navigation system is the Russian Globalnaya navigatsionnaya sputnikovaya sistema (GLONASS). The development of the system started in the mid 70's and it was primarily developed for military use. The system was completed in the mid 90's and a decline of the capacity occurred the years after. Currently, GLONASS is in a modernization phase also. About 24 satellites are in orbit, and most of them are transmitting Frequency-division multiple access (FDMA) civil signals at L1 (1.6 GHz) and L2 (1.25 GHz) frequencies. The satellite orbits are circular, and the vehicles are distributed in three orbital planes which are  $64.8^\circ$  inclined on the equatorial plane. Since 2011, GLONASS-K new generation satellites are transmitting the first CDMA navigation signal in the L3 band coherently with the existing L1 and L2 signals (Urlichich *et al.*, 2011).

The European satellite-based navigation system, Galileo, is currently under development. In October 2011, the first two Galileo satellites were launched and one year after two more followed. The system is currently in the In-Orbit Validation (IOV) phase, and more satellites are currently being launched. In its fully operational mode, the space segment will consist of about 30 satellites placed in medium earth orbits. The satellite orbits are almost circular and are inclined w.r.t. the equatorial plane by about  $56^\circ$ . The ground mission segment is generating the required data that are broadcast by the satellites. According to Kaplan and Hegarty (2006), Galileo will provide the following services: an open and free of charges service, a commercial service with additional data for high-accuracy positioning, a Safety-of-life service for the safety of critical users, a service for authorized users and a support service for search and rescue applications.

Galileo signals are generated by new generation atomic clocks and are being transmitted by five different carrier frequencies in L-band. Namely, on E5a (1176.450 MHz), E5b (1207.140 MHz), E5 (1191.795 MHz), E6 (1278.750 MHz) and E1 (1575.420 MHz) with E5a and E5b signals being part of the E5 signal in its full bandwidth (ESA, 2015).

Finally, the Chinese satellite navigation system BeiDou is under development also. In this case, the regional system, BeiDou-1, is expanded into a global one. When fully developed, it will consist of about 35 satellites with 5 orbiting in geostationary orbits, 27 in medium earth orbits and 3 in inclined geosynchronous orbits. Navigation signals will be transmitted by four different frequencies in the L-band.

### 2.1.1. Absolute Positioning

Satellite navigation systems are developed, primarily, for positioning purposes. The fundamental principle of positioning with GNSS consists of observing receiver-satellite distances which are obtained by measuring the travel time of the GNSS radio signal. Since the satellite positions are known (broadcast to the user) and the distances to the satellites are observed, the user position can be determined by the mathematical technique of trilateration. Observations of at least four satellites are needed for a 3D solution because the receiver clock offset should also be determined since, usually, the receiver clock is not accurate enough and not synchronized with the atomic clocks on board of the satellites. The observed ranges are called pseudoranges because they are biased by the receiver clock error and other error sources. The positioning solution is known as single point positioning (SPP) or absolute, pseudorange positioning and its accuracy lie in the order of 5 to 10 meters.

Precise point positioning (PPP) is a standalone precise positioning approach that uses dual-frequency carrier phase or pseudorange observation together with precise orbits and clock products and can reach accuracy levels of the order of decimetre to centimetre (Weinbach, 2013). This positioning technique has received attention from the positioning community because such accuracies can be obtained world-wide with a single receiver in static or kinematic mode. The ionosphere-free linear combination is traditionally used in PPP approach in order to eliminate the ionospheric refraction biases though single frequency approaches with decimetre accuracy have been developed (e.g. Le and Tiberius (2006)). A major limitation of the PPP algorithms is the requirement of long observational periods for the determination of the unknown carrier phase ambiguities (Weinbach, 2013).

#### The International GNSS Service

The International GNSS Service (IGS) is a voluntary union of many agencies and institutes, worldwide, that process and analyse permanent GNSS station data to generate precise GNSS products in support of Earth science research, multidisciplinary applications, and education (IGS, 2014). Currently, the IGS includes two GNSS, the American GPS and the Russian GLONASS, and intends to incorporate future GNSS (IGS, 2014). IGS coordinates a worldwide reference station network, of more than 300 stations, from which data are analysed by the different IGS analysis centres so as to generate different products, like e.g., precise orbits and satellite clocks (IGS, 2014).

As stated in IGS (2014) the long-term goals and objectives of IGS are to provide the highest quality GNSS data and products to the users, promote universal acceptance of the computed products, continuously innovate and maintain the voluntary character of the organization.

### 2.1.2. DGPS and Augmentation Systems

Absolute point positioning accuracy may not be sufficient for several applications, like e.g., for the landing approach of an aircraft or for ship navigation and docking inside a harbour area. Differential-GPS (DGPS) concepts can be used for the improvement of the accuracy as well as for integrity and reliability purposes in local/wide areas (e.g. airport area/Europe). DGPS schemes are utilized by monitoring stations at known locations which are computing error corrections and then broadcast them to the users. Error corrections may be broadcast by ground-based wireless communication links (i.e. local area) or by satellite links (i.e. wide area). The communication between a reference station and a rover user is utilized with defined communication protocols, like e.g., the Radio Technical Commission for Marine Services (RTCM) standards.

Satellite based augmentation systems (SBAS), like the European Geostationary Navigation Overlay Service (EGNOS), are designed to augment GNSS with the following three services: a ranging function for improving the availability and reliability; differential GPS corrections for improving the accuracy; and integrity monitoring for improving the safety (Parkinson and Spilker, 1996b). SBAS are consisting of two core components: A network of monitoring station which is distributed across the service area (e.g. Europe for EGNOS) and satellites placed in geostationary orbits illuminating the serve area.

The ground network is transferring the collected data to the processing facilities. Data are then processed, and integrity, differential corrections, residual errors and ionospheric delay information for the monitored satellites are determined (Parkinson and Spilker, 1996b). This information together with the ephemeris and the clock parameters of the geostationary satellites are uplinked to the satellites via dedicated uplink stations. The geostationary satellites broadcast the data via GPS-like signals which can be received and processed by the users with receivers that can track and demodulate SBAS signals.

Ground based augmentation systems (GBAS) operate in a similar sense, as the SBAS, but in this case the service area is much smaller (e.g. airport area), and the correction messages are broadcast to the users by ground based wireless data links. GBAS consist of a network of reference stations for data collection, a processing facility or master station for the generation of the correction message and a wireless communication link for broadcasting the data to the users.

### 2.1.3. Pseudolites

Pseudo-satellites or pseudolites (PSLs) are ground based transmitters of GNSS like signals. PSLs are in use, for navigation purposes, since the early development phase of GPS when they were used as direct replacements of satellites which had not yet been launched (Cobb, 1997). In this way, tests of the future navigation signals had been performed. In our days, PSLs are used for testing the upcoming Galileo signals as well as for many other positioning applications, e.g. to augment satellite signals and to increase the integrity, availability and accuracy of the positioning solution for critical applications (e.g. Barltrop *et al.* (1996)) or to augment positioning in indoor environments (e.g. Kuusniemi *et al.* (2012)). Moreover, PSL-only positioning can be utilized in environments where satellite signals are not available.

The near/far problem is a critical issue when PSL applications are developed. PSLs are much closer to the receiving antenna, in contrast to the satellites, and their signal levels can be significantly higher. As a result, satellites signals are jammed and also interference problems between the different PSL signals may occur. CDMA receivers are, in general, vulnerable to near/far interference problems. To counter attach this problem, several approaches have been developed. The use of pulsed (in contrast to continues) signals is a widely used approach. According to Parkinson and Spilker (1996b) other solutions to the near/far problem can be, for example, to transmit signals with a certain frequency offset but within the certain GNSS frequency band of interest or to use codes with longer sequences than the existing GNSS codes. Other crucial issues that may arise, when PSL applications are considered, are synchronization issues between the transmitting signals, transmitting antenna characteristics (e.g. hemispherical pattern or a more directive pattern) or even regulation and authorization issues under which these devices can operate.

In general, and as mentioned in Martin *et al.* (2007), the parameters of a PSL system are scenario dependent but the most crucial ones are: carrier frequency, effective isotropic radiated power (EIRP), antenna characteristics, pulse shaping, applied duty cycle, number of PSLs and location of them.

### 2.1.4. Galileo Test-Beds

As mentioned previously, PSLs are used for testing new navigation signals and critical applications of upcoming navigation systems (e.g. harbour/airport navigation). Gate environments are test-bed environments which allow the development and testing of the future Galileo-based navigation signals, algorithms and applications. Currently, different GATE environments exist in Germany. The GATE test area in Berchtesgaden (IFEN, 2014) consist of eight ground transmitters emitting Galileo-like signals. Transmitters are located in the mountains around Berchtesgaden. This GATE environment mainly aims at the development of Galileo signals and signal processing, as well as on the development of Galileo receivers. The railGATE and automotiveGATE test beds are two other GATE environments dedicated to rail traffic and road-based traffic (RWTH, 2014) applications. Moreover, GATE environments have been developed for air traffic, aviationGATE (DLR, 2014) and ship traffic, SeaGATE (RST, 2014), applications.

## 2.2. Antenna Performance Parameters

According to IEEE (2004), an antenna is a part of a transmitting or receiving system that is designed to radiate or to receive EM waves. Different GNSS antenna types have been developed due to suitability issues of specific applications. As mentioned in Rao *et al.* (2013), some of the most popular types of fixed radiation pattern antennas are the microstrip, quadrifilar, spiral, crossed bow tie, helical reflector antennas and cavity-backed antennas. Beam forming antenna arrays are also in use.

Antennas are a crucial element of the GNSS satellite-receiver link and their characteristics and behaviour directly affects the overall performance of the link. Depending on the specific characteristics and challenges of certain applications, antenna impact and related effects can be considered as nuisance and ignored or can be considered as a crucial and a limiting factor. For example, the necessity of antenna phase center correction terms for precise GNSS applications is recognized by the GNSS community. Thus, such correction terms are, nowadays, a standard IGS product which can be applied during GNSS data processing and improve the achievable positioning accuracy. Furthermore and as shown in Smyrnaiois and Schön (2015), in the case of site-dependent error sources, like multipath, the receiving antenna radiation characteristics are having a direct impact on the resulting error magnitude. Thus, in this section basic antenna parameters and terminology associated with antenna patterns are going to be introduced since they will be used in the following chapters of this thesis. It should be stated that the reciprocity principle of antennas is always assumed valid. Thus, the receive and transmit properties of an antenna are considered identical as well as the transmit and receive radiation characteristics. Basic antenna terminology which is used for the characterization of the performance of an antenna, is the radiation pattern, the directivity and gain, the different antenna efficiency factors, the impedance and the bandwidth. The discussion on antenna pattern aspects that is taking place in this part of the thesis is realized following Kraus (1998), Balanis (2005), Stutzman and Thiele (2013), Vaughan and Andersen (2003), Rao *et al.* (2013) and (IEEE, 2004).

### 2.2.1. Radiation Pattern

The radiation pattern (antenna pattern) is the spatial distribution of a quantity that characterizes the electromagnetic field generated by an antenna (IEEE, 2004). Thus, a radiation pattern describes how an antenna radiates (or receives) energy. An antenna radiates in all directions, and when the radiated energy in all directions is equal, the antenna is called isotropic. Its radiation pattern has the shape of a sphere (see fig. 2.2a). The 3D pattern can also be described with 2D patterns cuts. They are obtained by making cuts of the 3D pattern at different azimuth ( $\phi$ ) and/or elevation ( $\vartheta$ ) angles. It should also be noticed at this point, that for the discussion on antenna patterns that will take place in this part of the thesis, only far-field patterns are considered.

According to Kraus (1998), to completely specify the radiation pattern with respect to field intensity (i.e. power per solid angle) and polarization requires three patterns:

- The  $\vartheta$  component of the electric field as a function of the angles  $\vartheta$  and  $\phi$   $E_{\vartheta}(\vartheta, \phi)[V/m]$ .
- The  $\phi$  component of the electric field as a function of the angles  $\vartheta$  and  $\phi$   $E_{\phi}(\vartheta, \phi)[V/m]$ .
- The phases of these fields as a function of the angles  $\vartheta$  and  $\phi$   $\delta_{\vartheta}(\vartheta, \phi)$  and  $\delta_{\phi}(\vartheta, \phi)$  [rad or deg].

Dividing a field component by its maximum value, one can obtain a normalized (dimensionless) pattern (Kraus, 1998):

$$E_{\vartheta}^{norm}(\vartheta, \phi) = \frac{E_{\vartheta}(\vartheta, \phi)}{E_{\vartheta}^{max}(\vartheta, \phi)}. \quad (2.1)$$

Patterns may also be expressed in terms of power per unit area (radiation density) or Poynting vector [ $W/m^2$ ] ( $\mathbf{W}$ ) or in terms of power per unit solid angle, sr ( $1sr = (180/\pi)^2$ ), or radiation intensity [ $W/sr$ ]

( $\mathbf{U}$ ) (Balanis, 2005). They can also be normalized on the maximum value and yield a normalized power pattern with a maximum value of unity.

The Poynting vector ( $\mathbf{S}$ ) represents the rate of energy transfer per unit area, in units of Watts per square meter [ $W/m^2$ ] of an electromagnetic field and it is related to the distance from the antenna (Balanis, 2005). The radiation intensity is also used to characterize the transmission/reception of radiation by an antenna since it refers to the far-field properties of the antenna and is not a function of the distance from the antenna (Balanis, 2005). Given an antenna's power density  $\mathbf{S}$  that is measured at some distance  $r$  from the antenna, radiation intensity is calculated by multiplying by the square of the distance as  $\mathbf{U} = \mathbf{S}r^2$  (Balanis, 2005). Thus, the radiation intensity in a given direction can be defined as the power radiated from an antenna per unit of solid angle and it has the units of [ $W/\text{unit solid angle}$ ]. Since it is defined as the power divided by solid angle, the decreasing power density over distance due to the inverse-square law is offset by the increase in area with distance (Balanis, 2005). The radiation intensity as a function of the far-field electric field components ( $E_\vartheta$  and  $E_\phi$ ) of the antenna and impedance of free space  $Z_0$  (physical constant equal to  $376.7\Omega$ ) can be written as (Balanis, 2005):

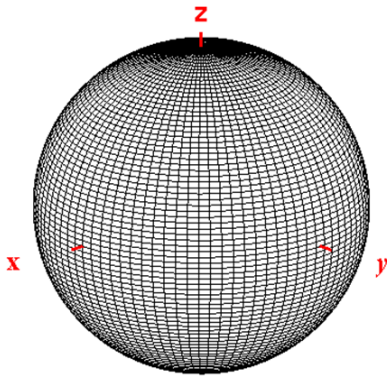
$$U(\vartheta, \phi) = \frac{1}{2Z_0} [|E_\vartheta(\vartheta, \phi)|^2 + |E_\phi(\vartheta, \phi)|^2]. \quad (2.2)$$

And the normalized power pattern is defined as:

$$P_{norm}(\vartheta, \phi) = \frac{U(\vartheta, \phi)}{U_{max}(\vartheta, \phi)}, \quad (2.3)$$

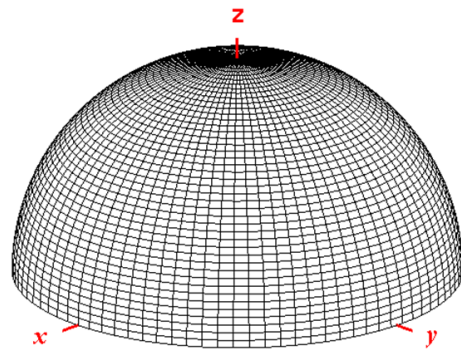
with  $U_{max}(\vartheta, \phi)$  the maximum radiation intensity.

**3D Isotropic Radiation Pattern**



(a) 3D Radiation pattern of an isotropic radiating source.

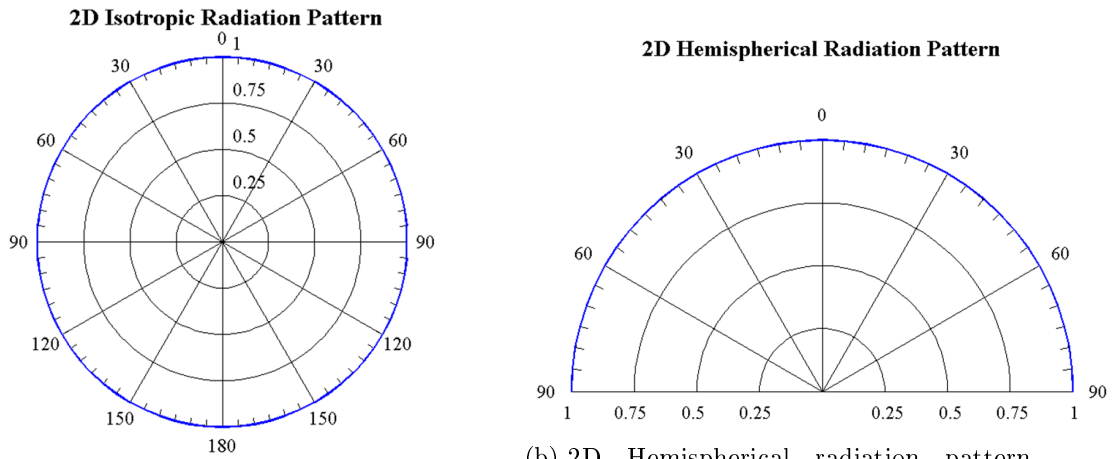
**3D Hemispherical Radiation Pattern**



(b) 3D Hemispherical radiation pattern.

Figure 2.2.: The radiation characteristics of an isotropic radiator (a) and the radiation characteristics of an ideal GNSS antenna which receives radiation from the upper hemisphere and does not receive any radiation for negative elevation angles (b).



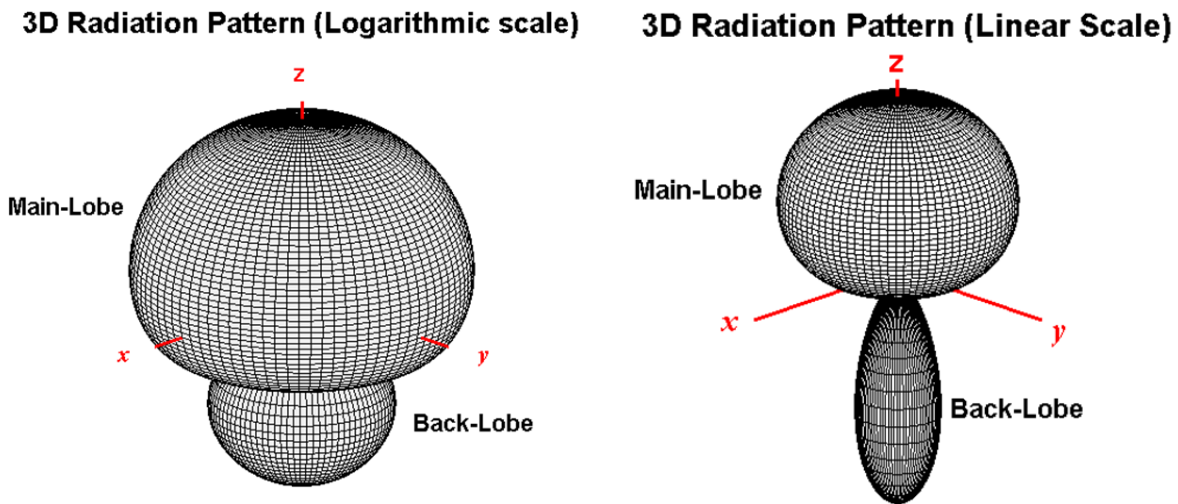


(a) 2D Radiation pattern of an isotropic radiating source, elevation ( $\vartheta$ ) cut (normalized and in linear scale).

(b) 2D Hemispherical radiation pattern, elevation ( $\vartheta$ ) cut (normalized and in linear scale).

Figure 2.3.: The radiation characteristics of an isotropic radiator plotted in a 2D polar plot (a) and the radiation characteristics of an ideal GNSS antenna which radiates (or receives radiation) isotropically from the upper hemisphere and does not receive any energy for negative elevation angles plotted in a 2D polar plot(b).

In fig. 2.2a the 3D pattern of an ideal isotropic antenna is plotted and in fig. 2.2b the radiation characteristics of an ideal GNSS antenna are plotted. Such an ideal antenna is isotropic on the upper hemisphere while it does not receive any radiation from below the horizon. In fig. 2.3 2D cuts (elevation cuts) of the 3D patterns of fig. 2.2 are plotted. The 2D and 3D plots are in linear scale.



(a) Omnidirectional 3D pattern with its main beam having a hemispherical coverage (logarithmic scale).

(b) Omnidirectional 3D pattern with its main beam having a hemispherical coverage (linear scale).

Figure 2.4.: GNSS-like omnidirectional antenna pattern with its main beam having a hemispherical coverage in logarithmic scale (a) and in linear (b).

Different parts of the radiation pattern are referred as radiation lobes. The main lobe, the main beam of the antenna, is the part of the pattern that contains the maximum radiation or, in other words, the region of the radiation pattern that is bounded by regions of relatively weak radiation intensity (Balanis, 2005). The back lobe is the lobe of the pattern that radiates energy in the opposite direction

of the main beam. Furthermore, all other lobes are called minor lobes of the pattern. In general, a lobe is a part of the pattern which is enclosed by regions of weak radiation. The half-power beam width (HPBW) is the angle that encloses the half power points of the main lobe or, in other words, the angle between the points of the main lobe that are down from the maximum gain by 3 dB (Balanis, 2005). The first null beam width (FNBW) is the angle that subtends the main beam of the pattern (Balanis, 2005). For GNSS antennas that are designed to have a hemispherical coverage, the main lobe of the pattern is extended over the upper half hemisphere (see fig. 2.4) while the back/side lobes and their magnitude play a crucial role for the resulting error magnitude in the case of multipath (e.g. Smyrnaiois *et al.* (2013), Smyrnaiois and Schön (2015)).

Another metric that is used for the characterization of the antenna pattern is the front-to-back ratio, which is the ratio of the gain in maximum direction and the gain  $180^\circ$  behind the peak. In dB scale, it is simply the difference between the gain values of this two point of the pattern (Balanis, 2005). Finally, the axial ratio (AR) of an antenna in a certain direction is the ratio of the orthogonal components of the electric field  $E_\vartheta(\vartheta, \phi)$  and  $E_\phi(\vartheta, \phi)$  in this direction. The AR for linear polarization is infinite, for elliptical is  $> 1$  and for circular polarization is 1 or 0 dB. The AR of geodetic GNSS antennas is very close to 0 [dB] for all positive elevation angles-of-arrival (AoA).

### 2.2.2. Field Regions

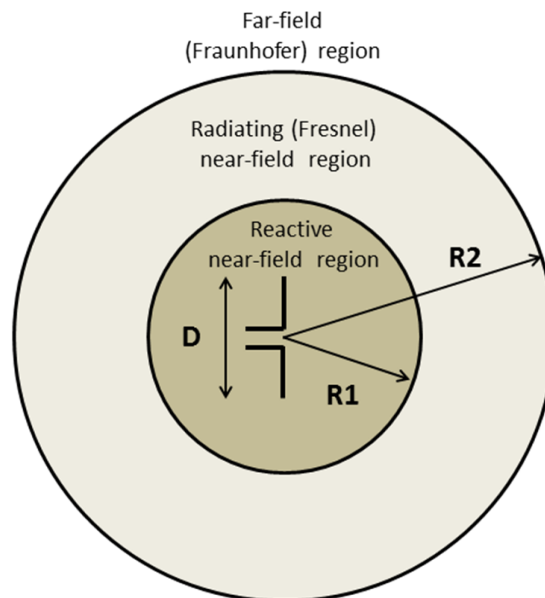


Figure 2.5.: Field regions of an antenna. Adopted from (Balanis, 2005)

The area surrounding an antenna can be divided into the three regions presented in fig. 2.5 and they represent the field distribution of the antenna. The reactive near-field region is defined as that portion of the near-field region immediately surrounding the antenna wherein the reactive field predominates (Balanis, 2005). This region covers a sphere around the antenna with radius (Balanis, 2005):

$$R_1 = 0.62\sqrt{D^3/\lambda}, \quad (2.4)$$

with  $D$  the maximum dimension of the antenna element. The radiation near-field (Fresnel) region is an intermediate region between the reactive near-field and the far field regions. Wherein the radiation field predominates and the angular field distribution (the radiation pattern) is dependent on the distance from the source (a dipole in fig. 2.5) (Balanis, 2005). According to Balanis (2005) if the antenna dimensions are much smaller relative to the wavelength, this region may not exist. The inner boundary

of this region is given by eq. 2.4 and the outer by (Balanis, 2005):

$$R_2 = \frac{2D^2}{\lambda}. \quad (2.5)$$

In the far-field (Fraunhofer) region the antenna radiation characteristics are independent of the distance to the source (Balanis, 2005). For most antennas, this region starts with distances greater than  $R_2$  (see eq. 2.5) and the fields are perpendicular to each other (transverse EM) (Balanis, 2005). As mentioned in Balanis (2005), the antenna pattern in the reactive region is smooth, near uniform with small variations, in the Fresnel region the pattern begins to form lobes and in the far-field region the pattern is well formed and consist of the major and minor lobes.

Objects placed in the near-field region of a receiving antenna may have a smaller or bigger impact on the radiation characteristics of the antenna and alter its radiation patterns (phase and/or amplitude). Thus, the same GNSS antenna mounted on a metallic, or wooden base may have slightly different radiation characteristics which perhaps for a code based navigation application can be insignificant but for a high precision application there can have a significant impact on the resulting solution accuracy (e.g. Dilssner *et al.* (2008)).

### 2.2.3. Directivity and Gain

The directivity of an antenna in a given direction is defined in IEEE (2004) as the ratio of the radiation intensity in a given direction from the antenna to the radiation intensity averaged over all directions or as mentioned in Balanis (2005), the directivity of a non-isotropic source is equal to the ratio of its radiation intensity in a given direction over that of an isotropic source and can be written as:

$$D = \frac{U}{U_0} = \frac{4\pi U}{P_{rad}}, \quad (2.6)$$

with  $U$  the radiation intensity (in a given direction) in  $[W/sr]$ ,  $U_0$  the radiation intensity of an isotropic radiator in  $[W/sr]$  and  $P_{rad}$  the total radiated power in  $[W]$ . The directivity pattern, which is dimensionless, is therefore describing the spatial directivity of the antenna, which for an isotropic source is equal to 1 for all direction (i.e. has the shape of a sphere). When the different polarization components, which are going to be introduced in the next section, are to be considered one may talk for partial directivity patterns or directivity patterns of the co-polar and cross-polar components. Partial directivity in a given direction is defined in IEEE (2004) as that part of the radiation intensity corresponding to a given polarization divided by the total radiation intensity averaged over all directions. Thus, the directivity,  $D$ , in a certain direction can be defined as a function of the partial directivity of the orthogonal components in a certain direction as (Balanis, 2005):

$$D = D_{co} + D_{cross}, \quad (2.7)$$

with the partial directivity  $D_{co}$  and  $D_{cross}$ :

$$D_{co}(\vartheta, \phi) = \frac{4\pi U_{co}(\vartheta, \phi)}{P_{rad}}, \quad (2.8)$$

$$D_{cross}(\vartheta, \phi) = \frac{4\pi U_{cross}(\vartheta, \phi)}{P_{rad}}, \quad (2.9)$$

with  $U_{co}$  and  $U_{cross}$  the radiation intensity of the co- and cross-polar field components in a certain direction and  $P_{rad}$  the radiated power in all directions. As can be seen from the presented equations, the directivity is directly derived from the shape of the radiation pattern.

The antenna gain, on the other hand, does involve the different antenna efficiency factors, which will be presented in the next part of this section. The gain is therefore closely related with the directivity but it is not only a function of the radiation pattern but also of the antenna efficiency and therefore can be related to other antenna properties (Balanis, 2005). It is defined as the ratio of the radiation intensity, in a given direction, to the radiation intensity that would be obtained if the power accepted by the antenna were radiated isotropically (IEEE, 2004). In this case, the radiating isotropic source is lossless. The gain is dimensionless and can be expressed as:

$$G = \frac{4\pi U(\vartheta, \phi)}{P_{rad}^{lossless}}, \quad (2.10)$$

with

$$P_{rad} = \eta P_{rad}^{lossless}, \quad (2.11)$$

where  $\eta$  is the efficiency factor of the antenna. It is composed of the reflection efficiency ( $\eta_r$ ), the conduction efficiency ( $\eta_c$ ) and the dielectric efficiency ( $\eta_d$ ) (Balanis, 2005). Thus, the gain, in a certain direction, as a function of the directivity and the overall efficiency (polarization efficiency is not considered) can be written as:

$$G(\vartheta, \phi) = \eta \left[ \frac{4\pi U(\vartheta, \phi)}{P_{rad}} \right] = \eta D(\vartheta, \phi). \quad (2.12)$$

As already done with the directivity, the partial antenna gain in a given direction for a given polarization is defined as that part of the radiation intensity corresponding to a given polarization divided by the radiation intensity that would be obtained if the power accepted by the antenna were radiated isotropically (IEEE, 2004). The (total) gain of an antenna, in a specified direction, is the sum of the partial gains for any two orthogonal polarizations (IEEE, 2004):

$$G = G_{co} + G_{cross}, \quad (2.13)$$

with the partial gain  $G_{co}$  and  $G_{cross}$ :

$$G_{co} = \frac{4\pi U_{co}(\vartheta, \phi)}{P_{rad}^{lossless}}, \quad (2.14)$$

$$G_{cross} = \frac{4\pi U_{cross}(\vartheta, \phi)}{P_{rad}^{lossless}}, \quad (2.15)$$

with  $U_{co}$  and  $U_{cross}$  the radiation intensity of the co- and cross-polar field components in a certain direction and  $P_{rad}^{lossless}$  the radiated power of a lossless antenna in all direction. Exemplary 2D partial gain patterns of the co-polar, right-hand circular polarized (RHCP), component and the cross-polar, left-hand circular polarized (LHCP), component of GNSS antennas similar to existing ones can be seen in fig. 2.6.

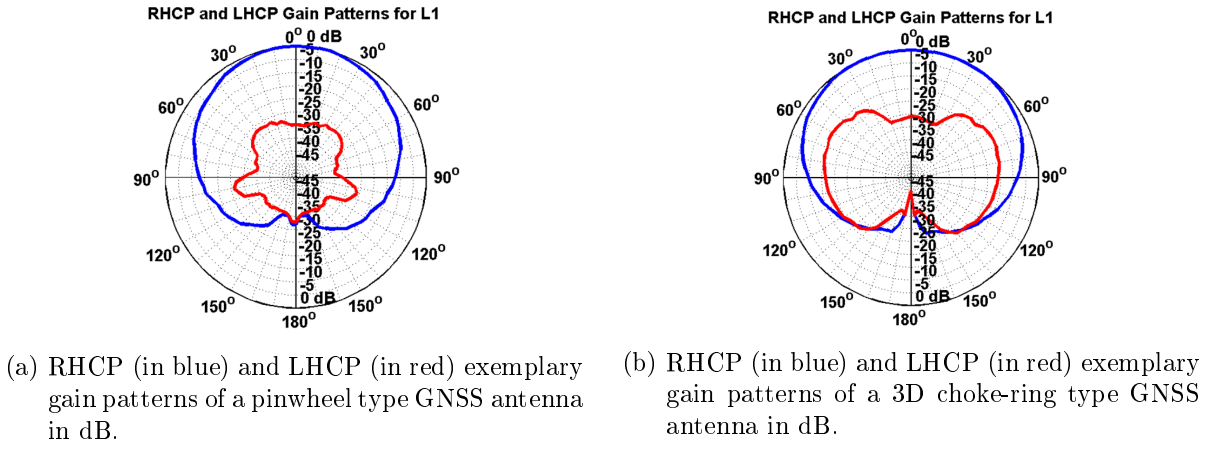


Figure 2.6.: Exempaly gain patterns for both orthogonal polarizations (RH in blue and LH in red) for two different GNSS antennas types.

The normalized partial gain patterns plotted in fig. 2.6 show hemispherical coverage for positive elevation angles with the main lobe of the pattern extending below the horizon. The gain role-off from the zenith down to the horizon for the co-polar (RHCP) component is about 12 dB for the antenna in fig. 2.6a and about 10 dB for the antenna in fig. 2.6b. For an ideal antenna, with hemispherical characteristics, it would have been 0 dB. Furthermore, the cross-polar (LHCP) gain pattern is much weaker so that the antenna will be less sensitive to multipath signal that are not RHCP as the line-of-sight (LOS) signal and they contain both orthogonal polarizations.

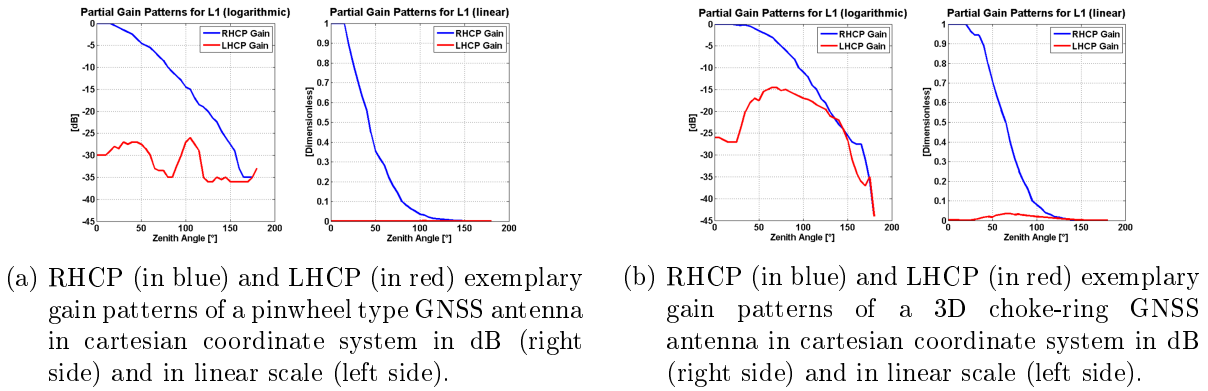


Figure 2.7.: Exemplary GNSS antenna partial gain patterns of Fig. 2.6 in cartesian coordinate system and in logarithmic and linear scales.

In fig. 2.7 the gain patterns for both orthogonal polarizations of fig. 2.6 are plotted in Cartesian coordinates both in logarithmic and in linear scale against the zenith angle that goes from the zenith  $0^\circ$  down to  $180^\circ$  (nadir direction).

Balanis (2005) introduces the term absolute gain ( $G_{abs}$ ) that takes into account the reflection/mismatch losses/efficiency ( $\eta_r$ ) which is going to be introduced in the next part of this chapter. Thus, we have:

$$\eta_r = (1 - |\Gamma|^2), \quad (2.16)$$

where  $\Gamma$  is the voltage reflection coefficient at the input terminal of the antenna, or the  $S_{11}$  antenna parameter, which can be measured with a vector network analyser. Thus  $G_{abs}$  in a certain direction reads:

$$G_{abs}(\vartheta, \phi) = \eta_r G(\vartheta, \phi) = \eta_r \eta_c \eta_d D(\vartheta, \phi), \quad (2.17)$$

The above concept is used in Chen *et al.* (2012) where the  $G_{abs}$  is mentioned as realized-Gain. The concept is used for the investigation of human body effects and how they deform the GNSS antenna gain pattern and affect the antenna performance. To the understanding of the author, this concept can be generalized for the investigation of the so-called near field effects. Thus, investigating distortions of the "free space" antenna patterns (phase and amplitude/power) of the antenna due to objects that are placed very close to the antenna e.g. due to the use of different antenna mounting. Such antenna effects may have an impact on the phase and power observations measured by the receiver that perhaps for certain precise applications are significant.

#### 2.2.4. Antenna Efficiency and Related Parameters

In this section the antenna efficiency factors ( $\eta$ ) will be introduced together with other antenna parameters that are involved and directly related to them and thus, have an impact on the antenna gain pattern. Mainly, we will focus on the reflection mismatch efficiency (see eq. 2.16). The conduction efficiency ( $\eta_c$ ) and the dielectric efficiency ( $\eta_d$ ) are very difficult to compute and most of the time they are measured (Balanis, 2005). Together they form the antenna radiation efficiency which is related to the gain. It describes circuit losses that affect the portion of power radiated to the total power that was delivered in the antenna (Balanis, 2005):

$$\eta = \frac{P_{rad}}{P_{input}}. \quad (2.18)$$

It is a ratio with maximum 1 (i.e. input power and radiated power are equal) and minimum 0 (i.e. no power is radiated or captured). Thus, for example, an overall low efficiency ( $\eta$ ) shows that most of the delivered power is lost inside the antenna ( $\eta_c, \eta_d$ ) or reflected away ( $\eta_r$ ). If we rearrange eq. 2.17, the losses inside the antenna can be expressed as a function of the gain and the directivity of the antenna as (Balanis, 2005):

$$\eta_{\eta_c \eta_d} = \frac{G_{abs}}{D}. \quad (2.19)$$

The reflection efficiency or impedance mismatch,  $\eta_r$ , shows how much of the delivered power is reflected away. For the receiving antenna, it shows how much of the incoming power is reflected away and therefore not captured. It is given by eq. 2.16 and, therefore, is only a function of the reflection coefficient  $\Gamma$ . It is a number between 0 and 1 and it can also be expressed in dB scale. In other words, when  $\Gamma$  is zero, the reflection efficiency is 1 (no loss) while, when  $\Gamma$  is equal to 1,  $\eta_r = 0$ , i.e. all incoming power is reflected away from the antenna due to impedance mismatch. The voltage reflection coefficient ( $\Gamma$ ) of the transmission line to the receiver/transmitter is given by the the impedance of the transmission line,  $Z_0$  [ $\Omega$ ], and the impedance of the antenna,  $Z_L$  [ $\Omega$ ], as (Vaughan and Andersen, 2003):

$$\Gamma = \frac{Z_L - Z_0}{Z_L + Z_0}. \quad (2.20)$$

When the impedance of the transmission line and of the antenna match (i.e.  $Z_L=Z_0$ ) then  $\Gamma=0$  and  $\eta_r=1$ .

The impedance is the ratio of voltage (V) to current (I) (AntennaTheory, 2014). It determines the current at the antenna input if a certain voltage is applied to the antenna. Typical impedance values for geodetic GNSS antennas lie at 50 [ $\Omega$ ], e.g. Novatel (2012), for the GNSS frequencies. Thus, if a voltage is applied to this antenna with amplitude 1 Volt, the current at the input will have an amplitude of  $1/50=0.02$  Amperes. The impedance can also be a complex number and affect both the phase and the amplitude of the resulting current. For example if  $Z = 50 + j35$  [ $\Omega$ ], then it will have a magnitude of  $\sqrt{50^2 + 35^2} = 61.03$  [ $\Omega$ ] and the phase will be  $\tan^{-1}\left(\frac{50}{35}\right) = 55^\circ$ . Thus, the amplitude

of the current if a voltage with amplitude 1 Volt is applied to the antenna is 0.016 Amperes and the current will lag the voltage by  $55^\circ$ . Similar examples can be found in AntennaTheory (2014).

The before mentioned related quantities can be graphically visualized with the Smith chart. Thus, with the Smith chart we can plot the impedance and calculate the reflection coefficient,  $\Gamma$ , or related parameters like the voltage standing wave ratio (VSWR) or plot the changes of these parameters for different frequencies. In fig. 2.8, an exemplary Smith chart polar plot is visualized using the corresponding Matlab function. The green lines represent the constant load reactance and thus describe the imaginary part of the impedance and the blue lines are the constant load resistance lines that are related to the real part of the impedance.

If for example the antenna impedance is  $Z_L = R + jX = 50 + j50$  [ $\Omega$ ] and the impedance of the transmission (radio) line  $Z_0$  is 50 [ $\Omega$ ], the normalized load impedance is  $Z_L^{norm} = 1 + j1$ . Thus the real part (R) can be visualized in the Smith chart of fig. 2.8 as the blue curve with constant values of 1. The imaginary part of  $Z_L^{norm}$  is also 1 and can be visualized in fig. 2.8 with the green curve of constant values of 1 for the imaginary part. The point where these two curves cross (is marked with a red dot in fig. 2.8) is the visualization of the exemplary antenna impedance of our example. In fig. 2.8, two more examples are plotted, the one for  $Z_L^{norm} = 1$  and the other one for  $Z_L^{norm} = 0.3$ .

Finally, a close related parameter with the reflection coefficient  $\Gamma$  is the VSWR, which is very often provided by the GNSS antenna manufactures. It can be expressed as (AntennaTheory, 2014):

$$VSWR = \frac{1 + |\Gamma|}{1 - |\Gamma|}, \quad (2.21)$$

thus  $\Gamma$  as a function of VSWR can be expressed as (AntennaTheory, 2014):

$$\Gamma = \frac{VSWR - 1}{VSWR + 1}. \quad (2.22)$$

VSWR describes how well the antenna is matched to the radio, in the case of GNSS, line it is connected to. The smaller the VSWR is, the minimum the match losses are. In the ideal case VSWR is 1.0, which means that no power is reflected from the antenna. Typical VSWR values for Geodetic antennas are usually less than 2. A VSWR value of 2 means that about 11% of the power reaching the antenna is reflected away.

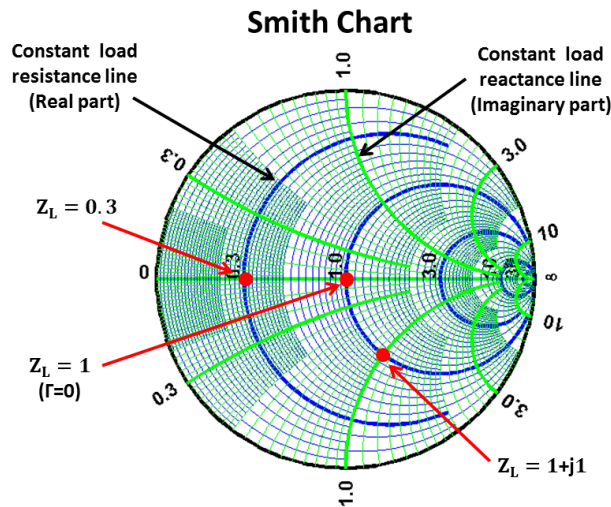


Figure 2.8.: Smith Chart.

All introduced parameters, in this section, are assumed constant across the antenna bandwidth. This is not the case in reality. Antenna patterns and other related parameters will be slightly different for the different GNSS carrier frequencies. On the other hand, at least for the case of geodetic antennas, the shape of the radiation pattern and related parameters will not change radically.

### Ground plane

Different types of ground planes are used by different GNSS antenna types (e.g. choke-ring, planar, rolled edged and others) for different reasons (e.g. antenna type, multipath mitigation, phase center stability, etc.). A ground plane will have a large impact on the shape of the antenna radiation (reception) pattern. In general, the goal is to increase directivity for positive elevation angles while simultaneously cut-off the pattern for negative elevation angles (Rao *et al.*, 2013). In the ideal case, of an infinite ground plane, the radiation pattern will be hemispherical with its directivity to be double relative to its full sphere shape without the ground plane for the same antenna bandwidth (Vaughan and Andersen, 2003). According to Rao *et al.* (2013), for many antenna types (e.g. microstrip patch, crossed slot) the ground plane is an integral part of the antenna structure while for others (e.g. quadrafililar helix, log spiral) it is an auxiliary part (for shaping the radiation pattern).

Diffraction on the edges of the ground plane is very carefully examined because it can create problems for the performance of the antenna. On the one hand, for negative elevation angles, it can cause significant back lobes and make the antenna prone to multipath contamination from ground reflections. On the other hand, for positive elevation angles, it can deform the amplitude and phase patterns of the antenna and introduce, for example, phase errors due to the not so stable phase center.

In the content of this thesis, it is assumed that the used antenna gain patterns include the ground plane effects. In other words, it is assumed that the used antenna diagrams were measured or simulated with the ground plane considered as part of the antenna and thus, its impact is included in the resulting shape of the pattern.

### Antenna Measurements

The antenna patterns and all the relevant antenna parameters that were introduced in the previous sections can be measured and thus the performance of an antenna can be characterized. In a general sense, the antenna pattern measurements refer to the measurement of the amplitude and phase of a received signal from the antenna under test from different directions and they can be obtained by using the antenna either in transmitting or receiving modes.

A representation of any of the radiation properties (e.g. amplitude, phase, polarization and/or power gain) as a function of space coordinates is defined as a radiation pattern (IEEE, 2003). Such measurement can take place in anechoic chambers or in situ. They can be relative or absolute measurements which can be performed with different antenna/range configurations that have been developed and are in use for different antenna measured parameters (e.g. phase center, gain, polarization, impedance).

In Rao *et al.* (2013) different measurement configurations for measuring and characterizing the performance of GNSS antennas are presented. The focus in this textbook is on the following performance parameters (Rao *et al.*, 2013):

- The measurements of far-field radiation patterns and the amplitude and phase of the orthogonal polarization components for different indoor antenna test ranges.
- Gain and AR measurements for the RHCP GNSS antennas.
- Bandwidth measurements of the antennas under test to characterize the stability of the antenna properties for different frequencies.



- Phase center offset (PCO) and phase center variations (PCV) measurement as a function of the frequency for different AoA.
- Group delay verification (GDV) measurements as a function of frequency and AoA.

Currently two different types of GNSS antenna calibration methods are used; dedicated anechoic chambers like the one developed in Bonn University (Zeimetz and Kuhlmann, 2008) or others and in situ calibration approaches with actual GNSS signals via the use of dedicated robots as, for example, the Hannover concept of absolute antenna calibration (Wübbena *et al.* (1996), Böder (2002)). A detailed literature survey for GNSS antenna calibration developments with a primary focus on the GNSS antenna phase patterns can be found in Kersten (2014).

Antenna performance and related parameters can be simulated via dedicated algorithms/software. In Maqsood *et al.* (2013), the impact of the ground plane of different GNSS antennas (commercial and self-built) is investigated with respect to the resulting multipath mitigation capabilities of the antenna. Different parameters of the antennas under investigation are measured and simulated (e.g. gain patterns, reflection coefficient). It can be noticed in this paper that the simulated and the measured parameters in some cases may, slightly, deviate.

## 2.3. Propagation Aspects

The polarization state of an antenna is the polarization of the transmitted, by the antenna, wave in a certain direction in the far-field. Usually, in literature, when the polarization of an antenna is mentioned, it is referred to as the polarization of the transmitted wave from the main lobe of the radiation pattern.

GNSS signals are electromagnetic (EM) waves that are composed of electric and magnetic fields that are related to each other via Maxwell's equations. They are transverse-waves, since the field vectors are perpendicular to each other and to the direction of propagation. At long distances from the source (i.e. the satellite antenna) the surface of constant phase, the phase front, of GNSS signals is so large that over small regions it can be considered planar. Electromagnetic waves can be described by four parameters; the amplitude, the frequency, the phase and the polarization. Polarization describes the direction and magnitude of the field vectors in space and time. For satellite communication and navigation purposes circularly polarized (CP) signals are very often used. In using CP signals, changes of the relative orientation between the transmitting-receiving antennas as well as orientation changes of the propagating field vector caused by atmospheric or other effects result in minimum polarization mismatch losses.

### 2.3.1. Introduction to Polarization

The polarization state of a (completely polarized) signal can be either linear, circular or elliptical. Linear and circular polarization states can be seen as special cases of elliptical polarization state. In the general case of an elliptical polarized wave, propagating in z direction, the electric field vector can be decomposed into the orthogonal components and written as:

$$\mathbf{E}(t) = E_{X0}\cos(\omega t)\vec{x} + E_{Y0}\cos(\omega t + \zeta)\vec{y}, \quad (2.23)$$

where  $E_{X0}$  and  $E_{Y0}$  are the maximum amplitudes of the instantaneous electric field components in x and y directions [V/m], respectively,  $\omega$  is the angular frequency in [rad/sec] and  $\zeta$  is the relative phase shift [rad] by which the y component leads the x component. The phase of the component in the x is set to  $0^\circ$  for simplification.

A time-harmonic wave is **linearly polarized** at a given point in space if the electric field vector is always oriented along a straight line at every instant in time (Balanis, 2005). The time-phase difference,

$\zeta$ , between the orthogonal components must be (Balanis, 2005):

$$\zeta = \phi_y - \phi_x = n\pi, n = 0, 1, 2, 3... \quad (2.24)$$

Thus, a wave is linearly polarized if (Balanis, 2005):

- Only one linear component exists.
- The two orthogonal linear components are  $180^\circ$  (or multiples of  $180^\circ$ ) out of phase.

A time-harmonic wave is **circular polarized** at a given point in space if the electric field vector traces a circle on a fixed plane normal to the direction of propagation. Thus, it should fulfil the following conditions (Balanis, 2005):

- Two orthogonal linear components exist.
- Time quadrature, i.e.  $\zeta = 90^\circ$  (or odd multiples of  $90^\circ$ ) for LH or  $\zeta = -90^\circ$  (or odd multiples of  $-90^\circ$ ) for RH polarization.
- Equal amplitude, i.e.  $E_{X0} = E_{Y0}$ .

Thus,

$$E_{X0} = E_{Y0}, \quad (2.25)$$

and

$$\zeta = \phi_y - \phi_x = \begin{cases} +(\frac{1}{2} + n)\pi, n=0,1,2,3... \text{ for LHCP.} \\ -(\frac{1}{2} + n)\pi, n=0,1,2,3... \text{ for RHCP.} \end{cases} \quad (2.26)$$

A time-harmonic wave is **elliptical polarized** at a given point in space if the electric field vector traces an ellipse on a fixed plane normal to the direction of propagation. Thus, it should fulfil the following conditions (Balanis, 2005):

- Two orthogonal linear components exist.
- The orthogonal components may or may not have the same magnitude.
- When the two linear orthogonal components do not have the same magnitude, the phase different ( $\zeta$ ) should not be  $0^\circ$  or  $180^\circ$  (linear polarization).
- When the two linear orthogonal components have the same magnitude, the phase different ( $\zeta$ ) should not be  $90^\circ$  (circular polarization).

Thus,

$$E_{X0} \neq E_{Y0} \quad \text{and} \quad \zeta = \phi_y - \phi_x \neq 0^\circ, 180^\circ. \quad (2.27)$$

Or

$$E_{X0} = E_{Y0} \quad \text{and} \quad \zeta = \phi_y - \phi_x \neq |90^\circ|. \quad (2.28)$$

Another decomposition of the electric field vector yields orthogonal circular polarization states (LHCP and RHCP). The electric field phasor expressed in terms of CP phasors can be written as Stutzman (1993):

$$\mathbf{E}(t) = E_R(t) + E_L(t), \quad (2.29)$$

with the two circular orthogonal components  $E_R$  and  $E_L$ :

$$E_R(t) = \frac{E_{R0}}{\sqrt{2}} (\vec{x} \cos(\omega t + \phi_{shift}) + \vec{y} \cos(\omega t - 90 + \phi_{shift})) = \quad (2.30)$$

$$\frac{E_{R0}}{\sqrt{2}} (\vec{x} \cos(\omega t + \phi_{shift}) + \vec{y} \sin(\omega t + \phi_{shift})), \quad (2.31)$$

and

$$E_L(t) = \frac{E_{L0}}{\sqrt{2}} (\vec{x} \cos(\omega t) + \vec{y} \cos(\omega t + 90)) = \frac{E_{L0}}{\sqrt{2}} (\vec{x} \cos(\omega t) - \vec{y} \sin(\omega t)), \quad (2.32)$$

with  $\phi_{shift}$  to be introduced so as to allow the possibility of different phase shifts between the circular orthogonal components (Stutzman, 1993).

By combining the circular components, different polarization states can be obtained as a function of the linear components as:

$$E_x(t) = \frac{[E_{R0} \cos(\omega t + \phi_{shift}) + E_{L0} \cos(\omega t)]}{\sqrt{2}}, \quad (2.33)$$

and

$$E_y(t) = \frac{[E_{R0} \cos(\omega t + \phi_{shift}) - E_{L0} \cos(\omega t)]}{\sqrt{2}}. \quad (2.34)$$

Finally, the equations introduced before can be rewritten in complex vector notation as:

$$E_L(t) = \frac{[\vec{x} E_{L0} + j \vec{y} E_{L0}]}{\sqrt{2}} = \frac{E_{L0}(\vec{x} + j \vec{y})}{\sqrt{2}}, \quad (2.35)$$

and

$$E_R(t) = \frac{[\vec{x} E_{R0} e^{j\phi_{shift}} - j \vec{y} E_{R0} e^{j\phi_{shift}}]}{\sqrt{2}} = \frac{E_{R0} e^{j\phi_{shift}} (\vec{x} - j \vec{y})}{\sqrt{2}}. \quad (2.36)$$

For the linear components, the expression in complex notation yields:

$$\mathbf{E}(t) = E_{X0} \vec{x} + E_{Y0} e^{j\zeta} \vec{y}. \quad (2.37)$$

Eq. 2.37 can be written in complex vector notation (Jones vector) as:

$$\mathbf{E}(t) = \begin{pmatrix} E_{X0} \\ E_{Y0} e^{j\zeta} \end{pmatrix}. \quad (2.38)$$

Eq. 2.38 completely describes the polarization state of a wave since information of the amplitude of both electric field components, as well as their relative phase, can be extracted. Complex vector notation of characteristic polarization states can be seen in table 2.1:

---

**Polarization State**


---

Linearly polarized in x direction	$(1 \ 0)$
Linearly polarized in y direction	$(0 \ 1)$
Right-hand circularly polarized (RHCP)	$\frac{1}{\sqrt{2}}(1 -j)$
Left-hand circularly polarized (LHCP)	$\frac{1}{\sqrt{2}}(1 \ j)$

---

Table 2.1.: Complex vector representation of particular polarization states.

Transmitted GNSS signals are right hand circularly polarized (RHCP), though reflected GNSS signals have a different polarization state due to the reflection process. Thus, the electric field vector is propagating in a helical way (see fig. 2.9), where the projection of the tip of this vector forms a circle in a fixed plane normal to the direction of propagation (i.e. the polarization plane). The clockwise or counter clockwise sense of rotation of the electric field vector looking towards the direction of propagation defines whether the signal is left or right-hand circularly polarized, respectively. At each instant in time, the electric field vector is a combination of linear components (see fig. 2.9):

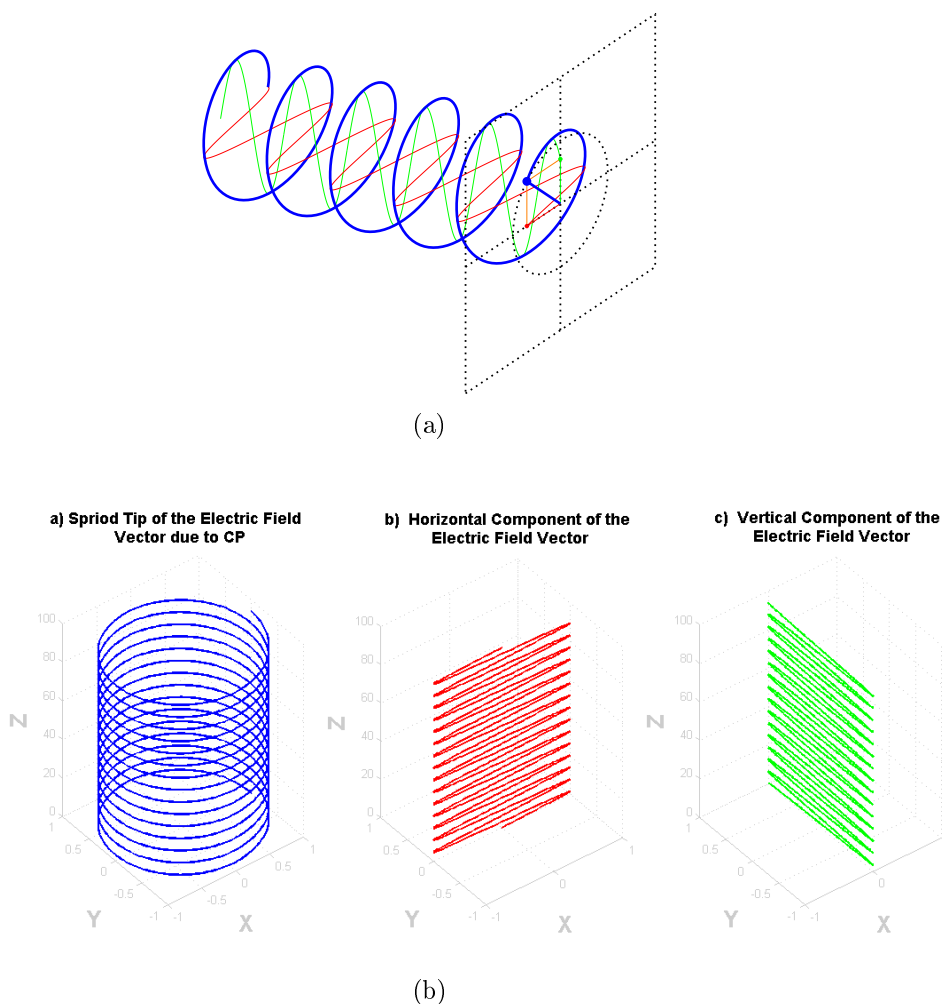


Figure 2.9.: The combination of the two electric field vector components with equal amplitudes and with  $90^\circ$  relative phase shift, in horizontal (red) and vertical direction (green), result in circular polarization. The electric field vector propagates in a spiroidal way and forms a circle in the plane normal to the direction of propagation.

Each of the two components (in green and in red) represents a linearly polarized (LP) wave. For circular polarization, as already mentioned, there are two requirements on the linear components: i) time quadrature, i.e.  $\zeta = 90^\circ$  for LH or  $\zeta = -90^\circ$  for RH polarization, and ii) equal amplitude, i.e.  $E_{X0} = E_{Y0}$ .

Finally, a relationship between the circular and linear polarizations, for antenna patterns as a function of the Jones vector reads (Vaughan and Andersen, 2003):

$$E_X = \frac{1}{\sqrt{2}}(E_R + E_L), E_Y = \frac{-j}{\sqrt{2}}(E_R - E_L). \quad (2.39)$$

With  $E_X = -jE_Y$  the condition for RHCP in a certain direction.

### 2.3.2. Polarization Representation

There are different ways to represent the polarization state of a signal or of an antenna (Stutzman, 1993). The different mathematical representation of polarization are used by different disciplines, like e.g., optics, communication engineering, radar or radiometry, remote sensing for different type of investigations, like e.g., material properties or roughness investigations, link budget calculations, measurements of different antenna parameters and/or for extracting geophysical parameters.

Different representations may suit better in different investigation. For example, the Jones vector is an easy to implement approach but is only applicable to completely polarizes signals (Stutzman, 1993). On the contrary, random or partially polarized waves can be represented by the Stokes parameters. The Poincaré sphere is a convenient to visualize approach (Stutzman, 1993). The complex polarization factor is a compact way for the representation of the polarization state, details of this approach can be found in (Beckmann, 1968). The different representations of polarization are directly related to each other via different transformations. In this thesis, the Jones vector (complex vector) notation is utilized for modelling the transmitting and the receiving antenna gain patterns.

Since there is no universal conversion for the definition of the sense of rotation of the field vector, as a reminder to the reader, it should be mentioned that in this thesis the RH rotation is defined as counter-clock wise with the z axis of fig. 2.10 pointing towards the reader and with the relative phase  $\zeta$  by which the y component leads the x component equal to  $-90^\circ$ .

### Ellipse Equation

In the general case of an elliptical polarization state, the electric field vector traces an ellipse in a plane normal to the direction of propagation. The electric field vector traces one ellipse every  $t_{L1} = \frac{1}{f_{L1}}$ , for the L1 frequency. Assuming a relative phase shift  $\zeta$  between the linear components, the linear components in x and y direction read:

$$E_x = E_{X0} \cos(\omega t), \quad (2.40)$$

$$E_y = E_{Y0} \cos(\omega t + \zeta). \quad (2.41)$$

With  $E_{X0}$  and  $E_{Y0}$  the amplitudes of the linear components,  $\omega t$  the carrier frequency and  $\zeta$  the relative phase. Rearranging the previous equations and multiplying the component in x direction with  $\cos(\zeta)$  we have:

$$\frac{E_x}{E_{X0}} \cos(\zeta) = \cos(\omega t) \cos(\zeta), \quad (2.42)$$

$$\frac{E_y}{E_{Y0}} = \cos(\omega t) \cos(\zeta) - \sin(\omega t) \sin(\zeta). \quad (2.43)$$

Subtracting the previous equations we have:

$$\frac{E_y}{E_{Y0}} - \frac{E_x}{E_{X0}} \cos(\zeta) = -\sin(\omega t) \sin(\zeta). \quad (2.44)$$

Replacing  $\sin(\omega t)$  with  $\sqrt{1 - \cos^2(\omega t)} = \sqrt{1 - \left(\frac{E_x}{E_{X0}}\right)^2}$  and squaring eq. 2.44 we have:

$$\frac{E_y^2}{E_{Y0}^2} - 2 \frac{E_y E_x}{E_{Y0} E_{X0}} \cos(\zeta) + \frac{E_x^2}{E_{X0}^2} \cos^2(\zeta) = \sin^2(\zeta) - \frac{E_x^2}{E_{X0}^2} \sin^2(\zeta). \quad (2.45)$$

Rearranging the previous equation:

$$\frac{E_y^2}{E_{Y0}^2} - 2 \frac{E_y E_x}{E_{Y0} E_{X0}} \cos(\zeta) + \frac{E_x^2}{E_{X0}^2} \cos^2(\zeta) + \frac{E_x^2}{E_{X0}^2} \sin^2(\zeta) = \sin^2(\zeta). \quad (2.46)$$

Since  $\cos^2(\zeta) + \sin^2(\zeta) = 1$ , the previous can be further simplified:

$$\frac{E_y^2}{E_{Y0}^2} - 2 \frac{E_y E_x}{E_{Y0} E_{X0}} \cos(\zeta) + \frac{E_x^2}{E_{X0}^2} = \sin^2(\zeta). \quad (2.47)$$

The previous equation is associated with the ellipse geometry. The before described derivation of the ellipse equation can be (partially) found in Stutzman (1993). By considering  $\zeta = \frac{\pi}{2}$  the previous equation is reduced to a well known ellipse equation:

$$\frac{E_y^2}{E_{Y0}^2} + \frac{E_x^2}{E_{X0}^2} = 1. \quad (2.48)$$

From the previous it can be shown, as a special case, that when  $E_{Y0} = E_{X0}$ , the field vector traces a circle.

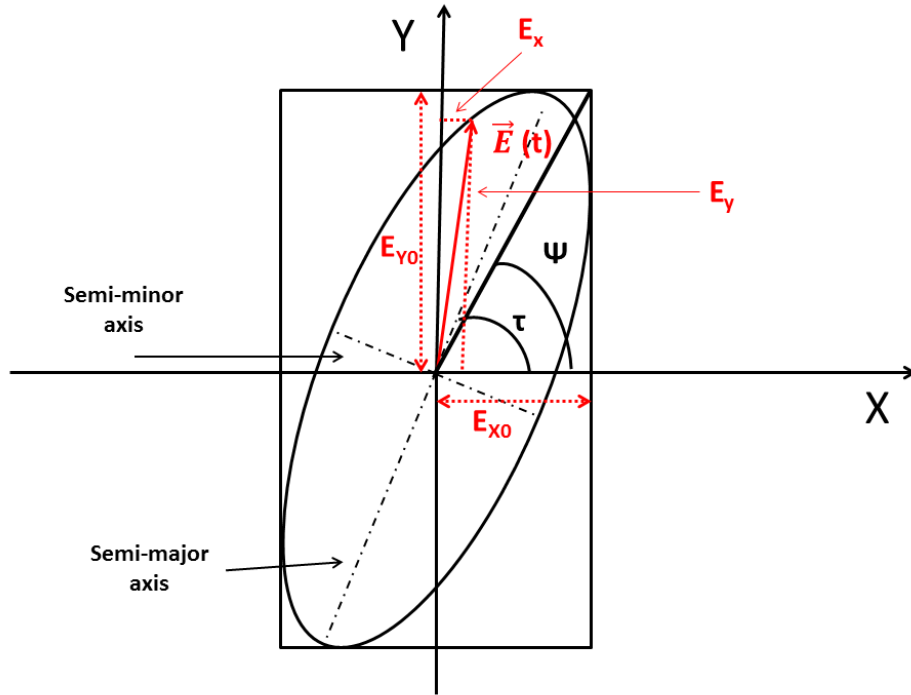


Figure 2.10.: Polarization Ellipse.

In fig. 2.10, the polarization ellipse is visualized with  $\tau$  the tilting angle which describes the orientation of the ellipse and  $\Psi$  gives the ratio of amplitudes of the linear components as (Stutzman, 1993):

$$\tan(\Psi) = \frac{E_{Y0}}{E_{X0}}. \quad (2.49)$$

The angle  $\Psi$  together with the relative phase  $\zeta$ , are sufficient information for the characterizations of the polarization state of a wave. These quantities are the fundamental observables in ellipsometry (Azzam and Bashara, 1987). Another set of quantities for the description of the polarization state can be directly calculated from the before mentioned parameters as (Stutzman, 1993):

$$\sin(2\epsilon) = \sin(2\psi)\sin(\zeta), \quad (2.50)$$

$$\tan(2\tau) = \tan(2\psi)\cos(\zeta). \quad (2.51)$$

Rearranging the above, leads to the quantities  $\epsilon$  and  $\tau$  (Stutzman, 1993):

$$\epsilon = \frac{1}{2}\sin^{-1}(\sin(2\psi)\sin(\zeta)), \quad (2.52)$$

$$\tau = \frac{1}{2}\tan^{-1}\left[\frac{\sin(2\psi)\cos(\zeta)}{\cos 2\psi}\right]. \quad (2.53)$$

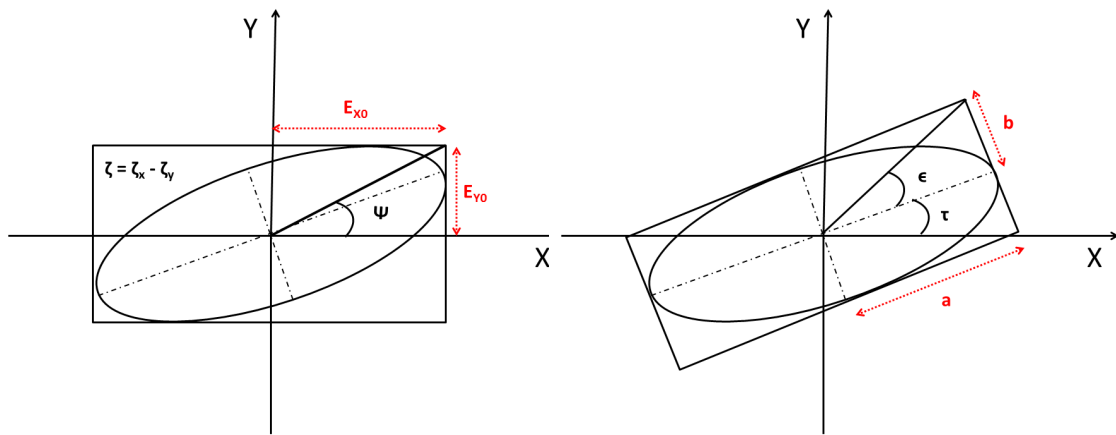
Where  $\tau$  describe the orientation of the polarization ellipse (see fig. 2.10) and  $\epsilon$  is related to the AR of the ellipse, and therefore the shape of the ellipse, as (Stutzman, 1993):

$$\epsilon = \cot^{-1}(-AR), \quad (2.54)$$

with the sign indicating the sense of rotation (i.e. - for RH and + for LH). From the  $\epsilon$  and  $\tau$  ellipse quantities, one can calculate the ellipsometric parameters  $\psi$  and  $\zeta$  as (Stutzman, 1993):

$$\psi = \frac{1}{2}\cos^{-1}(\cos(2\epsilon)\cos(2\tau)), \quad (2.55)$$

$$\zeta = \tan^{-1}\left[\frac{\tan(2\epsilon)}{\sin(2\tau)}\right]. \quad (2.56)$$



(a) Polarization ellipse and  $\psi$ ,  $\zeta$  parameters. (b) Polarization ellipse and  $\epsilon$ ,  $\tau$  parameters.

Figure 2.11.: Polarization ellipse description with (a)  $\psi$ ,  $\zeta$  quantities and with (b)  $\epsilon$ ,  $\tau$  quantities.

The different representations of polarization describe the shape of the ellipse, its orientation w.r.t. the defined coordinate system and the sense of rotation. As mentioned previously, all the different representations are related to each other. Thus, for example, the quantities for the description of the polarization ellipse (e.g.  $\psi$  and  $\zeta$ ) are related to the Jones vector (see eq. 2.38) since the relative phase  $\zeta$  is known and the angle  $\psi$  can be computed as (Stutzman, 1993):

$$\psi = \tan^{-1} \left( \frac{E_{Y0}}{E_{X0}} \right). \quad (2.57)$$

### 2.3.3. Polarization Efficiency

The antenna efficiency and the related losses that were presented in previous parts of this chapter are associated with power loss caused by the antenna. Polarization mismatch losses, on the other hand, are losses associated with the interaction of electromagnetic waves with the antenna and they are not included in the gain (Stutzman, 1993). Such losses occur when the polarization of the receiving antenna is not the same as the polarization of the incident wave. Thus, the polarization loss factor or polarization efficiency ( $\eta_p$ ) characterizes the loss of EM power due to the polarization mismatch (Stutzman, 1993). In table 2.2 characteristic cases of polarization efficiency between different incident waves and receiving antennas (in terms of polarization state) are presented.

Wave Polarization	Antenna Polarization	$\eta_p$
Any complete polarization state	Identical to wave	1
Any complete polarization state	Orthogonal to wave	0
Unpolarized (random polarization)	Any	0.5
Circular	Linear	0.5
Vertical linear	Linear 45°	0.5

Table 2.2.: Polarization efficiency of characteristic cases (Stutzman, 1993).

GNSS signals, as well as the receiving GNSS antennas for positive elevation angles, are RHCP. Most of the high-end geodetic GNSS antennas have ARs for all possible AoA very near to one (or 0 dB). Thus, polarization losses are kept very low and mainly depend on the ellipticity of the transmitted signal which is not worst that 1.2 dB for L1 and 3.2 dB for L2 (NavstarGPS, 2011). On the other hand, non-geodetic GNSS navigation antennas have higher ARs (e.g. 2 dB) and, in this case, polarization efficiency losses can be higher. In general, antennas with AR smaller than 3dB are considered CP.

In the case of reflected GNSS signals, were the initial polarization is alerted, polarization mismatch losses become bigger and, moreover, are not constant since the reflection process and the resulting depolarization effects are continuously changing due to the motion of the satellite. When these signal components arrive under the horizon of the receiving antenna; the situation is even more complex because neither the receiving antenna nor the reflected signal are CP.

In the following an example is presented for the quantification of  $\eta_p$  between an RHCP and an LHCP antenna and an incoming, RHEP, signal with varying AR and, thus, varying polarization state. The polarization state of the approaching signal as well as of the receiving antenna are represented by the appropriate complex vector. As a reminder to the reader, it should be stated that the normalized complex vectors contain only the polarimetric information since signal intensity is not considered (i.e.



equal to 1). Let the polarization state of the receiving antenna be equal to:

$$\mathbf{E}_{A_{rhcp}} = \frac{1}{\sqrt{2}} \begin{pmatrix} 1 \\ -j \end{pmatrix} \quad \text{or} \quad \mathbf{E}_{A_{lhcp}} = \frac{1}{\sqrt{2}} \begin{pmatrix} 1 \\ j \end{pmatrix}, \quad (2.58)$$

with  $\mathbf{E}_{A_{rhcp}}^H * \mathbf{E}_{A_{rhcp}} = 1$  and  $\mathbf{E}_{A_{lhcp}}^H * \mathbf{E}_{A_{lhcp}} = 1$ . With  $H$  denoting the Hermitian conjugate. Let the approaching wave have a constantly varying polarization with AR starting from -1 (i.e. RHCP) down to inf (i.e. LP):

$$\mathbf{E}_{W_{rhep}}(AR; t) = \frac{1}{\sqrt{2}} \begin{pmatrix} x(t) \\ -jy(t) \end{pmatrix}, \quad (2.59)$$

with  $\mathbf{E}_{W_{rhep}}(AR; t)^H * \mathbf{E}_{W_{rhep}}(AR; t) = 1$ . The polarization efficiency between the RHEP approaching wave and the RHCP or LHCP receiving antenna is equal to:

$$\eta_p = | \mathbf{E}_{A_{rhcp/lhcp}}^H * \mathbf{E}_{W_{rhep}}(AR; t) |^2 \quad (2.60)$$

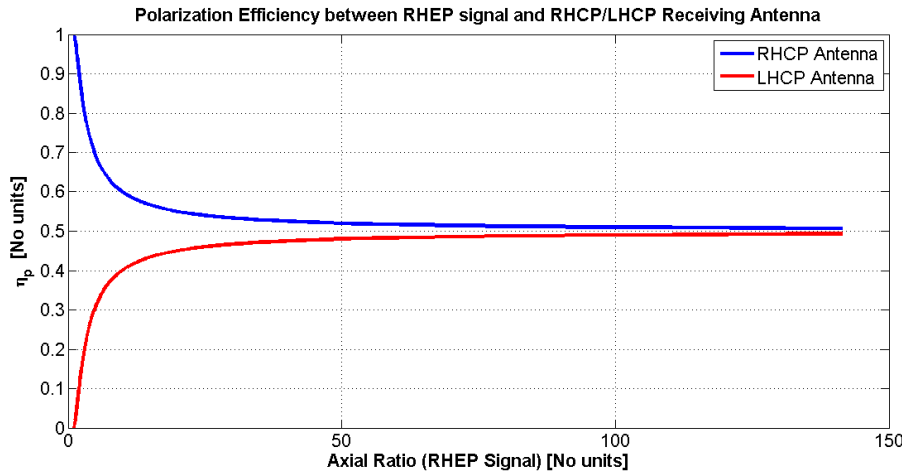


Figure 2.12.: Polarization Efficiency between RHCP/LHCP receiving antenna and RHEP incoming wave with varying AR from -1 (i.e. *RHCP*) up to  $\infty$  (i.e. *LP*).

In fig. 2.12 the simulated  $\eta_p$  is plotted for an RHCP (in blue) and an LHCP (in red) antennas and a wave with changing polarization state. In the case of RHCP antenna,  $\eta_p$  is 1 (no loss) in the beginning because the polarization state of the approaching wave is also RHCP (AR near to -1). As the wave is becoming more and more elliptical (AR is increasing)  $\eta_p$  increases also. When the AR is near to infinity and the approaching wave is LP,  $\eta_p$  is approaching 0.5 (or 3 dB loss). The reverse situation can be seen in the same figure for an LHCP receiving antenna (in red). The  $\eta_p$  is, in this case, 0 (i.e. the antenna and the wave have orthogonal polarization states) and is approaching 0.5 as the AR of the RHEP wave is approaching infinity.

### 2.3.4. Friis Transmission Equation

Several factors should be considered when calculating the received power link of GNSS signals. The most crucial are: Transmit power ( $P_t$ ), transmitting antenna gain towards the direction of the receiving antenna ( $G_t$ ), free space propagation loss at a given nadir angle (i.e. function of the transmitter-receiver geometry ( $R_{txrx}$ )), receiver losses, atmospheric losses and the gain of the receiving antenna ( $G_r$ ). Given two antennas, the power available at the output of the receiving antenna, ( $P_r$ ), without accounting

for atmospheric losses and assuming a polarization match between the antennas, is given by Friis transmission equation.

At a certain distance  $R_{txrx}$  between the phase centres of the antennas, the power density  $S$  [ $W/m^2$ ] is:

$$S = \frac{P_t G_t}{4\pi R_{txrx}^2}. \quad (2.61)$$

At the receiving antenna the power density is multiplied by the antenna effective area or effective aperture [ $m^2$ ] which is related to the gain as (Stutzman, 1993):

$$A_r = \frac{\lambda^2}{4\pi} G_r(\vartheta, \phi), \quad (2.62)$$

with  $\lambda$  the wavelength. The received power expressed as a function of eq. 2.61 and 2.62 in [W] is given by:

$$P_r = S A_r. \quad (2.63)$$

Eq. 2.63 expresses the power density to power conversion process that a receiving antenna performs (Stutzman, 1993). The Friis transmission equation in its simplest form is expressed as:

$$P_r = P_t G_t G_r \left( \frac{\lambda}{4\pi R_{txrx}} \right)^2. \quad (2.64)$$

The previous expression gives the power of the received signal as a function of the gains of both transmitting and receiving antennas, the input power of the transmitter, the wavelength and the geometrical distance between the antennas. The last part in the brackets is referred to as free space loss/attenuation. According to Stutzman and Thiele (2013) this term maybe misleading since it contains the wavelength (coming from the antenna effective area).

The RF transmitted power must be set to a certain value so that the received signal power, within the area of service is equal or higher than the minimum received power specifications of the system. According to NavstarGPS (2011) the power at the satellite antenna input is 27 watt (or 14.3 dBW) and it is independent of the off-nadir angle. On the other hand, the satellite antenna gain as well as the distance between transmitting and receiving antennas vary as a function of the off-nadir angle. The satellite to user range can also be computed as a function of the satellite elevation as (Misra and Enge, 2006):

$$R_{txrx} = -R_{earth} \sin(el) + \sqrt{R_{earth}^2 (\sin^2(el - 1)) + R_{SV}^2}, \quad (2.65)$$

with  $R_{earth}$  the radius of the earth (6371 km),  $R_{SV}$  the distance of the satellite from the center of the earth ( $\approx 26.560km$ ) and  $el$  the satellite elevation relative to the receiving antenna position. The off-nadir angle is computed by:

$$\alpha = \sin^{-1} \left[ \frac{R_{earth} \sin(el + 90^\circ)}{R_{SV}} \right], \quad (2.66)$$

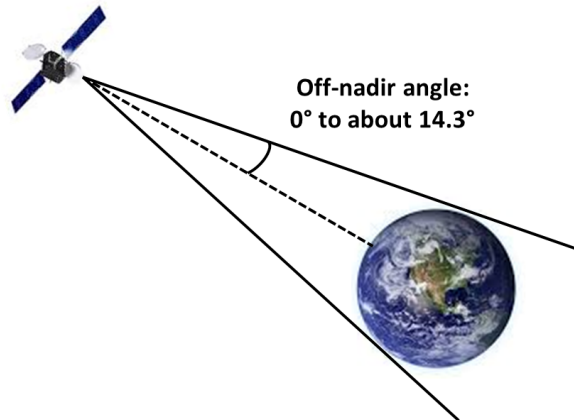


Figure 2.13.: Off-nadir angle geometry.

In fig. 2.13 the off-nadir angle, the satellite-receiver distance, the received signal power and the satellite antenna gain pattern versus satellite elevation are plotted for an exemplary observed PRN arc.

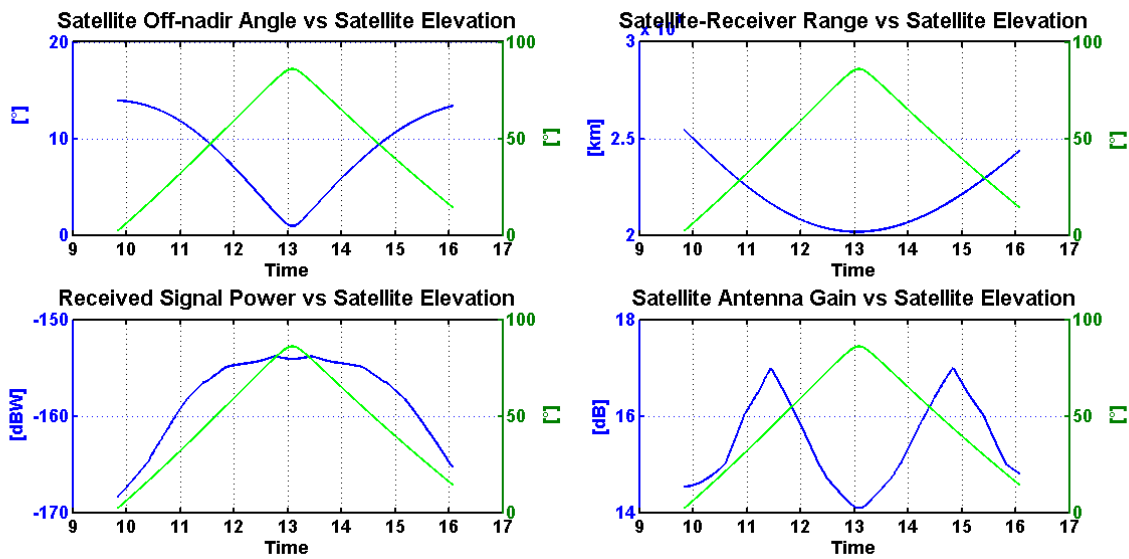


Figure 2.14.: Off-nadir angle, satellite-receiver distance, received signal power and satellite antenna gain pattern versus satellite elevation for an exemplary observed PRN arc. The plotted gain pattern of satellite block IIA was adapted from Kronman (2000).

The received signal power of fig. 2.14 is calculated by eq. 2.64 expressed in logarithmic scale as:

$$P_r = 10\log_{10}(P_t) + 10\log_{10}(G_t) + 10\log_{10}(G_r) - 20\log_{10}\left(\frac{\lambda_{L1}}{4\pi R_{txrx}}\right). \quad (2.67)$$

For the calculation of the received signal power the satellite gain of fig. 2.14 was used together with the receiving antenna gain diagram of fig. 2.6a. The transmitted signal power was set, according to the specification of the system. Receiver and atmospheric/cable losses were neglected.

## 2.4. Signal Processing

Spread-spectrum modulation techniques are in use, for communication purposes, before the development of satellite navigation systems. These modulation techniques can yield significant advantages. For example, the use of the same frequency band from different transmitters and the high processing gain that can be acquired when the signals are despread. This is a major advantage when the power consumption of the transmitter should be kept as low as possible (e.g. satellite transmitters). According to (Viterbi, 1979), the purpose and applicability of spread-spectrum techniques are interference suppression, energy density reduction and ranging or time delay measurements. In the most general form, spread-spectrum communication systems take a binary data sequence and multiply it by a higher rate PRN binary sequence (Simon *et al.*, 1994). This causes the modulated signal spectrum to spread by a factor of  $N$ , the ratio of the PRN sequence bit rate to the data bit rate (Simon *et al.*, 1994).

GPS signals are BPSK modulated and are composed of the PRN codes that have a chipping rate of 1.023 MHz for the C/A code and of 10.23 MHz for the encrypted P(Y) code, and the navigation data. The chip rate determines the amount of signal spreading that occurs and creates a transmitted power spectral density, which can be modelled with the  $\text{sinc}^2$  function with the maximum of the main lobe of the spectrum located at the carrier frequency and the null-to-null bandwidth equal to twice the chipping rate (Godsoe, 2010).

This section serves as an introductory section of the GPS signal generation and of the GPS signal processing modules that are utilized in a typical GNSS receiver architecture to process the recorded raw GPS signal. The output of the processed signal are the decoded navigation data, the time delay and carrier phase measurements of the ranging codes as well as signal power measurements and Doppler observations.

### 2.4.1. Signal Generation

GPS signals are composed of the carrier wave, the navigation data, and the spreading sequence. Each satellite has a unique code sequence, also called pseudo-random code. The coarse acquisition or C/A code is publicly available, and SPS is based on it. On the other hand, the PPS is based on the encrypted P(Y) code. C/A code is a sequence of 1023 chips that is repeated after 1 ms (1.023 MHz chipping rate). Those codes are deterministically generated sequences with noise like properties. Such codes have maximum auto-correlation value when their relative shift is zero and near zero auto-correlation value for all other relative shifts. Furthermore, the cross-correlation between two different codes is near zero. They belong to the Gold codes family (Gold, 1967) and they are generated by combining the outputs from two linear feedback shift registers (LFSRs), namely  $G1$  and  $G2_i$  (fig. 2.15), each consisting of ten unit cells or delay units and are initialized with a value of 1 (phase indication). LFSR generates a maximal length sequence of  $N = 2^n - 1$  elements, where  $n=10$ .

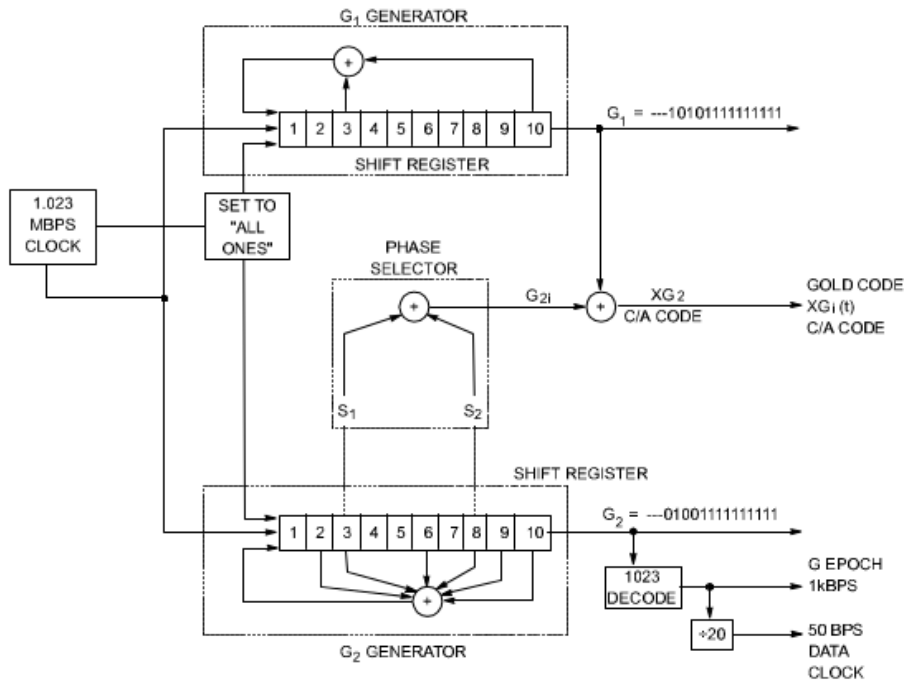


Figure 2.15.: C/A code generation from two shift registers,  $G_1$  and  $G_{2i}$  (NavstarGPS, 1995).

$G_1$  and  $G_2$  sequences are generated by 10-stage shift registers having the following polynomial forms:

$$G_1 = X^{10} + X^3 + 1, \quad (2.68)$$

and

$$G_2 = X^{10} + X^9 + X^8 + X^6 + X^3 + X^2 + 1. \quad (2.69)$$

The powers of the above polynomials indicate the tapping at each particular unit cell in the LFSRs (NavstarGPS, 2011). The tapping in each LFSR are XORed and the output is given as feedback to the first unit cell (NavstarGPS, 2011). Different phase selectors are used for the generation of the different PRN sequences. The different phase selectors for all the GPS satellites can be found in NavstarGPS (2011).

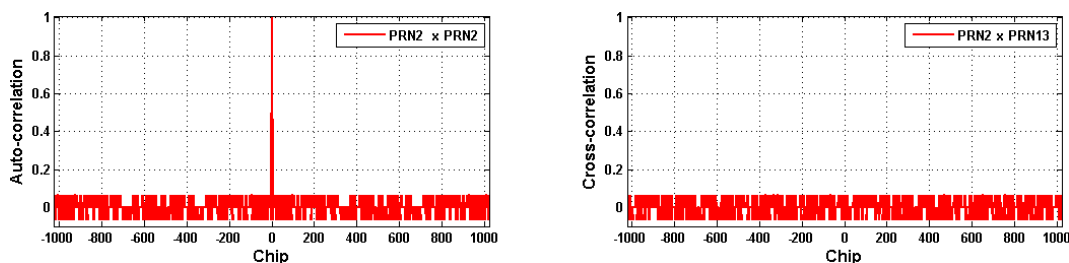


Figure 2.16.: The auto-correlation is maximum when the relative shift between the correlated codes is zero and the cross-correlation between two different C/A code sequences is always near zero.

The auto-correlation function, which measures the similarity between any PRN sequence and the time shifts of it, for a PRN C/A code can be expressed as (Misra and Enge, 2006):

$$R_{s_1 s_1} = \frac{1}{T_{code}} \int_0^{T_{code}} x_{s_1}(t)x_{s_1}(t - \tau)dt = \begin{cases} 1, & \text{for } \tau = 0 \\ \approx 0, & \text{for } \tau \neq 0 \end{cases} \quad (2.70)$$

The auto-correlation (see equation: 2.70) multiplies the one sequence by time shifted versions of itself and integrates the product, with  $T_{code} = 1ms$  for the C/A code (see left side of figure: 2.16). While the cross-correlation of two different code sequences:

$$R_{s_1 s_2} = \frac{1}{T_{code}} \int_0^{T_{code}} x_{s_1}(t)x_{s_2}(t - \tau)dt \approx 0, \quad (2.71)$$

is near zero for all the different relative shifts between the correlated codes (see right side of figure: 2.16).

The navigation signals are modulated with a 50-bps navigation data message which is transmitted in five 300-bit subframes. Each subframe consist of ten 30-bit words and it contains information about GPS time, health flags, clock correction terms, ephemeris parameters and almanac data. The beginning of each subframe is marked with an 8-bit sequence (preamble) which due to the 180 deg phase shift can be either 10001011 or 01110100. After the identification of the beginning of the sub-frame, the receiver can lock to GPS time. The broadcasting signals are a product of navigation data  $D(t)$ , spread spectrum codes,  $x_{C/A,P(Y)}$ , and radio frequency (RF), e.g.  $L1$ , and they have a certain amplitude. The transmitted signal on  $L1$  carrier, without accounting for the noise, can be expressed as:

$$s_{L1}(t) = \sqrt{2P_{C/A}}D(t)x_{C/A}(t)\cos(2\pi f_{L1}t + \vartheta_{L1}) + \sqrt{2P_{P(Y)}}D(t)x_{P(Y)}(t)\sin(2\pi f_{L1}t + \vartheta_{L1}). \quad (2.72)$$

### 2.4.2. Receiver Front-End and Signal Conditioning

The receiver front-end is the first part in the receiver cascade that conditions the received signal, down-converts it to an indeterminate frequency (IF) and digitalises it so that it can be further processed by the receiver. Though antennas are not considered as a part of the front-end, in many cases commercial antennas are constructed together with it. Key components of a front-end are amplifiers, oscillator, mixers, filters and analog-to-digital converters.

GNSS antennas can be either active or passive. Active antennas are coupling the radiating element with a low noise amplifier (LNA) and by doing so they reduce signal losses from the cables and decrease the noise level. On the other hand, such antennas should be powered by the receiver and they are increasing the power consumption of the receiver. When passive antennas are used, the cable length and its properties should be carefully considered since the noise figure of the cascade will increase.

Received GNSS signals are very weak, and they are buried under the noise floor. Thus, amplification will improve the processing efficiency of the receiver as well as the analog-to-digital conversion. LNA is the first components after the antenna and should have high gain and low noise figure since the first element of the RF cascade has the largest impact on the resulted noise level entering the receiver according to Friis formula for the noise of the cascade (Stutzman and Thiele, 2013).

The receiver oscillator is a key component of the receiver for the different processing stages of the incoming signal. The measurements performed by the receiver are actual estimates of the signal time of arrival, carrier phase and frequency which the receiver would not be able to perform without the use of a local reference oscillator. The requirements for the local oscillator may vary depending on the

need of certain applications. Major requirements are size, power consumption, short- and long-term stability and phase-noise.

Mixers combined with the reference oscillator are utilized for the down-conversion of the receiver signal to an intermediate lower frequency without alerting the modulation of the signal. They are followed by a bandpass filter to remove unwanted signals.

The final operation of the front-end is the analog to digital conversion where the analog signal is converted to digital samples. Baseband signal processing will follow after with the acquisition and tracking modules of the receiver. In a typical commercial GNSS receiver front-end the down conversion of the signal or other signal conditioning stages of the cascade are performed with intermediate steps.

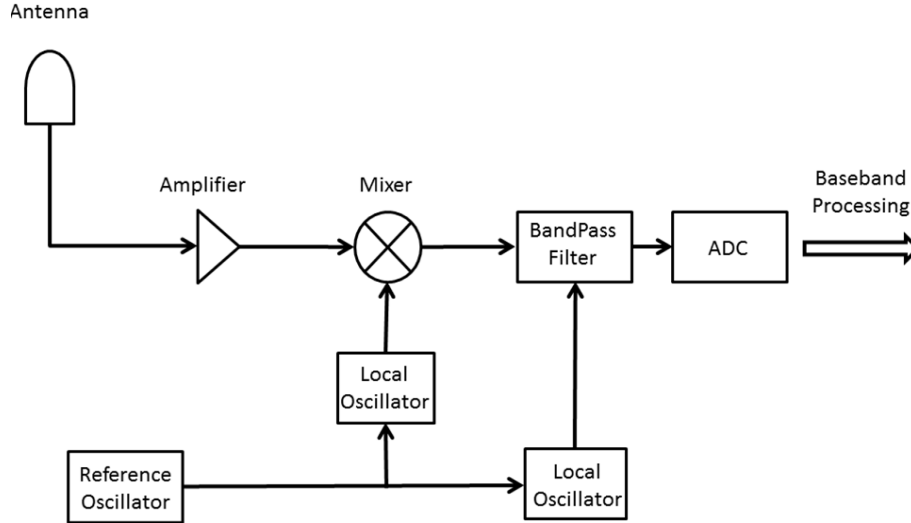


Figure 2.17.: GNSS front-end components.

### 2.4.3. Receiver Signal Processing Modules

A digitalized raw GNSS signal at a certain IF is the output of the front-end. The raw signal can be modelled as:

$$s(t) = r(t) + n(t). \quad (2.73)$$

The deterministic ( $r(t)$ ) part represents the received sum of all GNSS signals from the satellites in view and the stochastic ( $n(t)$ ) part represent the noise which is assumed to be uncorrelated, zero-mean white noise. This signal is further processed by the different modules of the receiver in order to acquire the satellites in view, track them and finally demodulate the data that they broadcast. These three core functions of the GNSS signal processing chain are based on the correlator outputs between the received signal and the locally generated replicas of it.

The received signal of eq. 2.73 is buried under the noise floor and it will rise when despread. The receiver can identify and track the PRNs in view by correlating short periods of the recorded signal with locally generated replicas of it:

$$S(\tau) = \int_0^{T_i} c(t)s(t - \tau)dt = \int_0^{T_i} c(t)r(t - \tau)dt + \int_0^{T_i} c(t)n(t - \tau)dt = S_r(\tau) + S_n(\tau). \quad (2.74)$$

Thus, the power of a certain received PRN signal in the presence of noise is:

$$\langle S_{PRN}(\tau) \rangle^2 = \langle S_{signal}(\tau) \rangle^2 + \langle S_n(\tau) \rangle^2. \quad (2.75)$$

In a typical receiver architecture the receiver generates in-phase (I) and quadrature (Q) local replicas of the signal that are multiplied with the recorded signal and then are further processed by an integrate and dump filter. The correlator output for I and Q components, assuming no Doppler shift during the integration interval (T), for the C/A code it can be approximated by:

$$I = \sqrt{2C1}R(\delta\tau)\cos(\phi_\epsilon) + n_I, \quad (2.76)$$

$$Q = \sqrt{2C1}R(\delta\tau)\sin(\phi_\epsilon) + n_Q, \quad (2.77)$$

with R the correlation function,  $\delta\tau$  the code tracking error,  $\phi_\epsilon$  the phase tracking error and n the zero mean, Gaussian distribute noise.

Three factors have significant impact on the correlation process. External disturbances (e.g. thermal noise, multipath, interference etc.), the presence of the carrier and the front-end filter band limiting effects that prevent the receiver from receiving the full signal spectrum (Julien, 2005) and this results in rounding of the correlation peak and a reduction of the tracking accuracy.

#### 2.4.4. Acquisition

Signal acquisition is a search process that is utilized by the correlation of received signal snapshots with local replicas of it generated by the receiver. In order to acquire a certain PRN the recorded signal should match the local replicas in two dimensions. The range dimension is associated with the replica code and the Doppler dimension is associated with the replica carrier (Kaplan and Hegarty, 2006). The goal of the acquisition process is to detect the presence of a useful signal and give a rough estimation of the code delay and Doppler shift in order to initialize the tracking process. Each signal is processed separately in a receiver channel since it requires correlation with its locally generated code. As stated in Julien (2005), the power of the useful signal is fluctuating between the I and Q channels due to the rough estimation of the phase error and the only way to detect the presence of a signal is to detect its power.

Cold-start acquisition is performed by the receiver when no apriori information of the satellites in view and their directions is known. Thus, the receiver has to compute correlation values for all PRN codes and for all possible code-phases and Doppler shift of them. This process may last several minutes. On the other hand, warm-start acquisition is faster since the satellites in view and their rough position are known. Different implementations of the acquisition process can be found in the literature that fit better to the needs of specific applications. For example, the search space dimensions (Doppler-delay map) and the bin size may vary depending on the dynamics of the scenario or the correlation process, can be performed with more than one steps. For applications where the signal quality is low (e.g. indoor scenarios) longer integration periods are often utilized.

The detection performance of the process is based on the comparison of the signal detector with a predefined threshold value. The theoretical performance is based on a hypothesis test with hypothesis  $H_0$ : No useful signal present and hypothesis  $H_1$ : Useful signal is present (Julien, 2005).



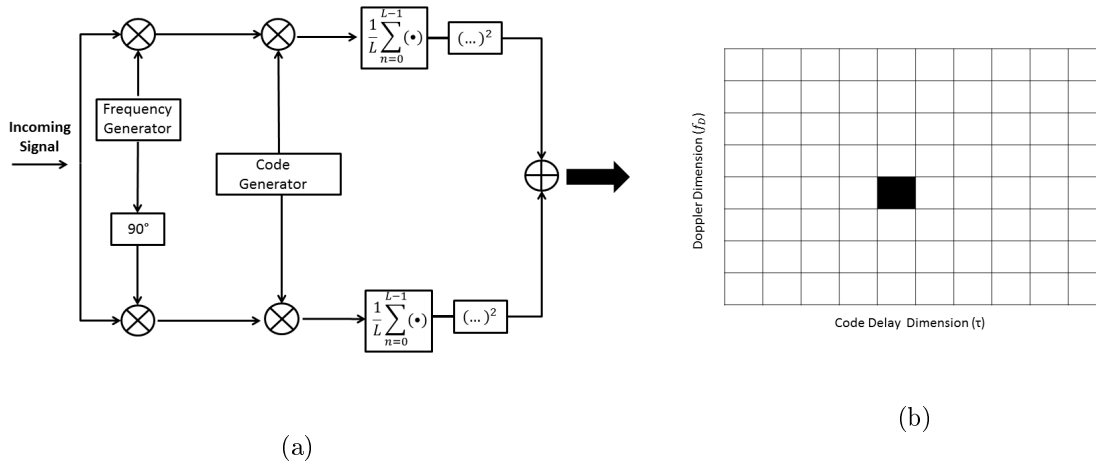


Figure 2.18.: Acquisition block diagram (a) for each bin in the search space (b).

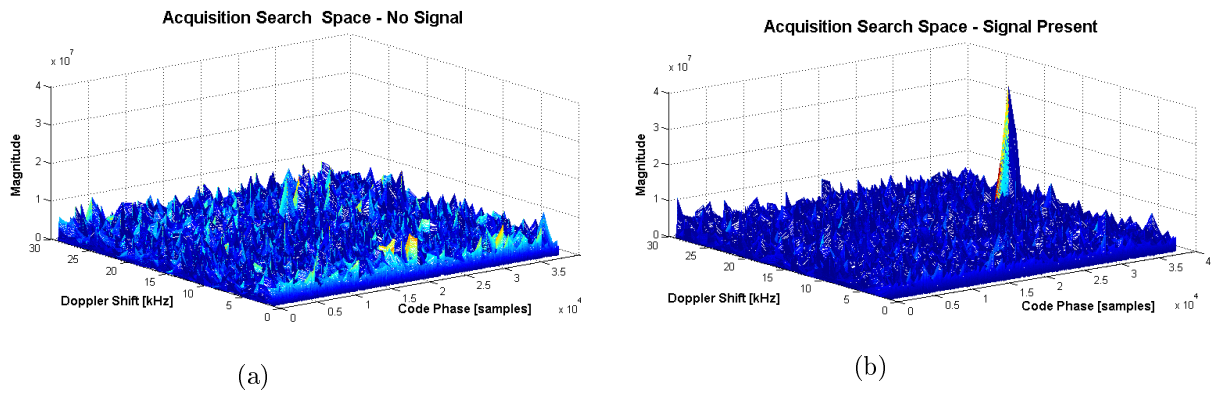


Figure 2.19.: The doppler-delay map with (b) and without (a) the presence of useful signal.

### 2.4.5. Tracking

The results of the acquisition process are, as mentioned in the previous section, the identification of the PRNs in view and a rough determination of their code delay and Doppler shift. These parameters are used for initiating the tracking process of the observed signals. In a typical GNSS receiver architecture, the signal is tracked in closed loops and the output of them is used for the correction of a numerical controlled oscillator (NCO) so that the delay and the Doppler shift change of the incoming signal are continuously followed by the receiver and the locally generated replicas. The results of signal tracking are the extraction of the navigation message transmitted by the satellite and the determination of the ranging observations.

Key components of the tracking loops in a typical GNSS receiver architecture are pre-detection integrators, loop discriminators and loop filters (see fig. 2.20 and 2.21) (Kaplan and Hegarty, 2006). These three functions determine the two most important performance characteristics of the receiver tracking loop design: the code/phase loop thermal noise error and the maximum LOS dynamic stress threshold (Kaplan and Hegarty, 2006).

The fundamental task of the code tracking loop or delay lock loop (DLL) is to generate PRN signal replicas that are perfectly synchronized with the captured signal. To achieve this synchronization, it determines the synchronization error which is filtered and used to control the NCO which commands the shift register for the generation of the signal replica for the next iteration of the loop. In a similar sense, the task of the carrier phase tracking loop (PLL) is the synchronization of the local carrier with

the received one and this is achieved by determining the phase error which is then filtered and used to control the NCO. Thus, the NCO is constantly adjusted to maintain the code and phase (frequency) lock.

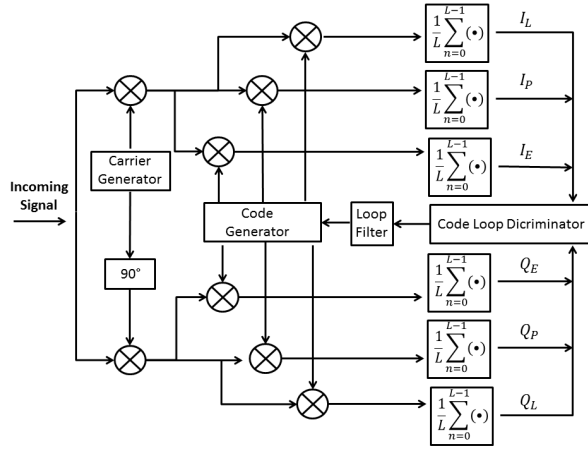


Figure 2.20.: DLL architecture.

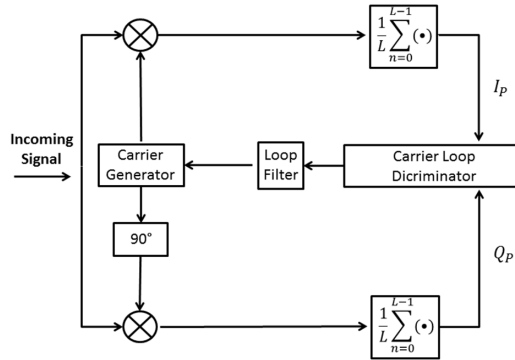


Figure 2.21.: PLL architecture.

Given a spacing,  $d$ , between the early and late correlators, the correlator outputs for the early, late and prompt replicas in the I and Q channels can be expressed as Van-Dierendonck *et al.* (1992):

$$I_E = AR(\delta\tau - \frac{d}{2})\cos(\phi_\epsilon) + n_{I_E}, \quad (2.78)$$

$$I_L = AR(\delta\tau + \frac{d}{2})\cos(\phi_\epsilon) + n_{I_L}, \quad (2.79)$$

$$I_P = AR(\delta\tau)\cos(\phi_\epsilon) + n_{I_P}, \quad (2.80)$$

$$Q_E = AR(\delta\tau - \frac{d}{2})\sin(\phi_\epsilon) + n_{Q_E}, \quad (2.81)$$

$$Q_L = AR(\delta\tau + \frac{d}{2})\sin(\phi_\epsilon) + n_{Q_L}, \quad (2.82)$$

$$Q_P = AR(\delta\tau)\sin(\phi_\epsilon) + n_{Q_P}. \quad (2.83)$$

In the previous equations the navigation data is omitted, the  $\delta\tau/\phi_\epsilon$  account for the code/phase error and  $A$  accounts for the signal amplitude. The correlator outputs are used for the formation of the code

and phase discriminators (see fig. 2.20 and 2.21) for the estimation of the synchronization error. The carrier phase discriminators in a typical receiver architecture must be chosen so as to be insensitive to the phase shifts due to the change of polarity of the navigation message (Kaplan and Hegarty, 2006). Commonly used discriminators for the code and phase tracking loops of GNSS receivers can be found in Kaplan and Hegarty (2006), Irsigler (2008) and in many other textbooks on navigation and GNSS.

Code Discriminators	
Early minus Late Power	$D_{code} = (I_E^2 + Q_E^2) - (I_L^2 + Q_L^2)$
Dot product	$D_{code} = (I_E - I_L)I_P + (Q_E - Q_L)Q_P$
Normalized Early minus Late	$D_{code} = \frac{\sqrt{I_E^2 + Q_E^2} - \sqrt{I_L^2 + Q_L^2}}{\sqrt{I_E^2 + Q_E^2} + \sqrt{I_L^2 + Q_L^2}}$

Table 2.3.: Commonly used code discriminators.

Phase Discriminators	
Costas	$D_{phase} = I_P Q_P$
Decision directed Costas	$D_{phase} = Q_P \text{sign}(I_P)$
Arctangent	$D_{phase} = \arctan\left(\frac{Q_P}{I_P}\right)$

Table 2.4.: Commonly used phase discriminators.

The loop filters transform the estimated error (from the discriminator) into an estimated frequency error that controls the NCO frequency. The loop filter bandwidth ( $B_L$ ) is a crucial parameter of the filter design since it is related to the level of noise that affects the tracking. On the one hand, a small  $B_L$  will reduce the noise and, on the other hand, it will limit the capability of the loop to track signal in scenarios with high dynamics. The loop bandwidth of a PLL for a typical GNSS receiver may vary from 5 to 20 Hz. In fig. 2.22 the amplitude of the early and late correlators as well as the DLL discriminator error are plotted for different integration intervals and a 0.5 sec IF raw GNSS signal record. The amplitude of the prompt correlator and the PLL discriminator error is plotted for different integration intervals in fig. 2.23. A 0.5 sec IF raw GNSS signal was used for the generation of this plot also.

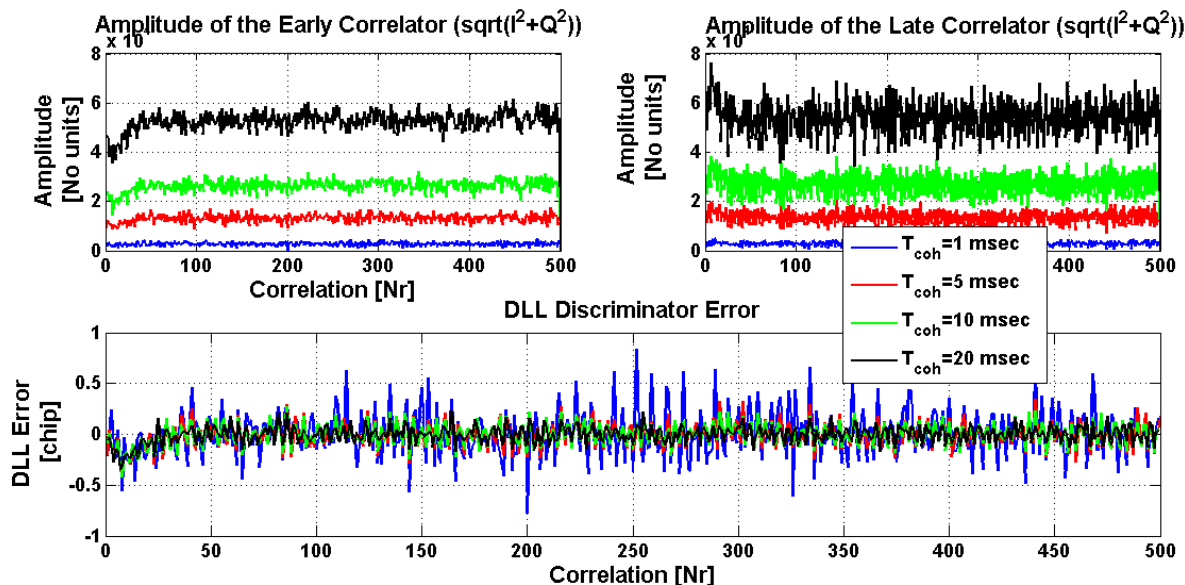


Figure 2.22.: PRN3 early, late correlator amplitudes and DLL discriminator (normalized early-late) for different coherent integration time ( $T_{coh}$ ) and with a 0.5 chip spacing.

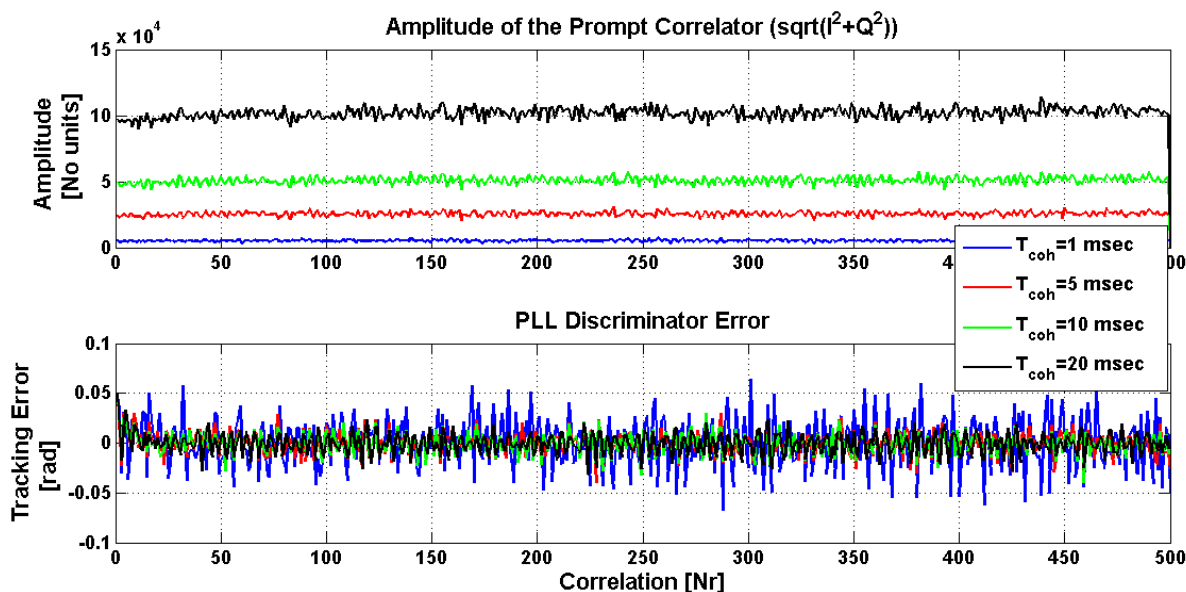


Figure 2.23.: PRN3 prompt correlator amplitude and PLL discriminator (arctangent) for different coherent integration time ( $T_{coh}$ ).

### Tracking Accuracy

The main receiver related error sources affecting the carrier phase tracking are thermal noise, vibration induced oscillator noise, stability behaviour of the reference oscillator, dynamic stress error (Kaplan and Hegarty, 2006) and other external disturbances as multipath or interference. On the other hand, the code tracking behaviour is also affected by effects as multipath or interference as well as thermal noise but oscillator induced errors are minimal (Kaplan and Hegarty, 2006). Thus, the dominant error

sources in a GPS receiver code tracking loop are the thermal noise and the dynamic stress error. More information on the PLL and DLL error sources can be found in Kaplan and Hegarty (2006). The thermal noise jitter (in meters) for an arctangent PLL can be computed as (Kaplan and Hegarty, 2006):

$$\sigma_{PLL} = \frac{\lambda}{2\pi} \sqrt{\frac{B_L}{C/N_0} \left(1 + \frac{1}{2TC/N_0}\right)}, \quad (2.84)$$

where  $B_L$  is the carrier loop bandwidth (Hz),  $C/N_0$  is in linear scale,  $T$  is the integration time (sec) and  $\lambda$  is the wavelength.

By looking eq. 2.84, one can notice that the parameters that affect the carrier thermal noise error are loop filter bandwidth  $B_L$ , the integration time  $T$  and the  $C/N_0$ . The last part of the expression in brackets account for the squaring loss (Kaplan and Hegarty, 2006). In fig. 2.24, PLL thermal noise jitter in [m] is plotted versus different  $C/N_0$  values for different PLL bandwidth and integration intervals.

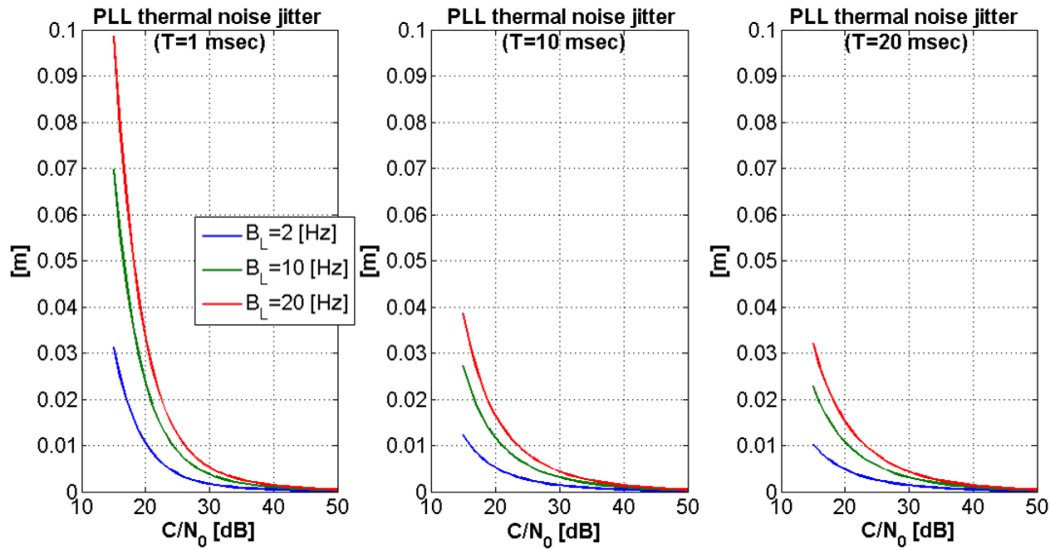


Figure 2.24.: PLL thermal noise error [m] for different  $C/N_0$ , integration time and loop filter bandwidth.

## 2.5. GNSS Observables and Data Processing

The output of the navigation signal processing of a GNSS receiver are data files that contain code and phase range observations together with Doppler and signal quality measurements and the decoded ephemeris data together with other broadcast correction terms. These data are further post-processed by dedicated algorithms to estimate users position and velocity or for timing purposes.

Two observations are the fundamental ranging observations for positioning and navigation purposes: The code phase and the carrier phase observables that are broadcast on the different GNSS frequencies. The code observable or pseudorange is the actual difference between the time of emission and the time of reception of the signal. When multiplied by the speed of light ( $c$ ) it gives the range information between the transmitted and receiving antennas that is biased by different error sources. The most dominant error sources are the satellite and the receiver clock errors. Thus, the pseudorange measurement can be written as:

$$P_s = c(T_r - T^s), \quad (2.85)$$

where  $T_r$  is the time of reception of the signal and contains the receiver clock error and  $T_s$  is the time of transmission which is biased by the satellite clock error. Thus, eq. 2.85 can be rewritten as:

$$P^s = c(t_r - t^s) + c\delta t_r - c\delta t^s. \quad (2.86)$$

Thus, by including the geometrical distance between the satellite and the receiver  $\rho_r^s = \|X^s - X_r\|$  and the error sources that are affecting the pseudorange observable, the code-phase observation equation for a certain satellite (s) can be modelled as:

$$P^s = \rho_r^s + c\delta t_r - c\delta t^s + T + I + \delta t_{rel} + M + \epsilon_{P_{prn}}, \quad (2.87)$$

with

$P^s$	Pseudorange observation from a certain PRN at a certain frequency
$\rho_r^s$	Geometrical distance between the transmitting and receiving antennas
$\delta t_r$	Receiver clock error
$\delta t^s$	Satellite clock error
T	Refraction caused by neutral atmosphere
I	Refraction caused by ionosphere (frequency dependant)
$\delta t_{rel}$	Relativistic effects
M	Multipath effects
$\epsilon_{P_{prn}}$	Code observation noise and remaining errors

The observation equation for the carrier phase observations is different from the code observable in two ways. The ionospheric refraction has an opposite sign and there is an ambiguity term  $\lambda N_r^s$  that accounts for the unknown initial carrier phase integer cycles. Thus, the observation equation for the carrier phase of a certain satellite (s) can be written as:

$$L^s = \rho_r^s + c\delta t_r - c\delta t^s + T - I + \delta t_{rel} + M + \lambda N_r^s + \epsilon_{L_{prn}}. \quad (2.88)$$

### 2.5.1. Observation Differencing

Observation differencing between the observables of two receivers is often utilized during GNSS data analysis for the investigation of certain error sources or for relative positioning purposes. The basic idea is that by forming differences, different error sources cancelled and relative positioning (i.e. estimation of the vector between two stations) is more accurate or certain error sources can be isolated and further studied.

Single differences (SD) between two different stations (A and B) can be formed by differencing synchronized observations of a commonly observed satellite (s). By doing so, satellite related error sources (e.g. satellite clock error) are cancelled and remaining error sources, with the exception of station related error sources (e.g. multipath), are reduced. The observation equation for carrier phase single/station differences reads:

$$\Delta L_{AB}^s = \Delta \rho_{AB}^s + \Delta c\delta t_{AB}^s + \Delta T_{AB}^s - \Delta I_{AB}^s + \Delta \delta t_{ABrel}^s + \Delta M_{AB}^s + \Delta \lambda N_{AB}^s + \Delta \epsilon_{L_{AB}}^s. \quad (2.89)$$

A zero baseline (ZB) configuration set-up is an antenna-receiver configuration that can be used to access receivers or a data processing algorithm performance. This set-up is carried out by connecting two receivers to the same antenna and forming differences between the same observed PRNs from both receivers. In this case, the resulting satellite SD residuals should contain only noise or when different receivers are used, residuals may contain biases due to the different signal processing properties of the two receivers. Thus, zero baseline tests can be conducted to examine, for example, the receiver performance where all common errors due to multipath, LNA noise, and propagation effects cancel in the GPS processing (e.g. Jackson *et al.* (2000)).

Double differences (DD) are formed by creating between satellites (s1 and s2) differences of two single differences. By doing so, receiver related error sources are cancelled and further atmospheric effects are reduced. The double differenced carrier phase observation has the following form:

$$\begin{aligned} \nabla \Delta L_{AB}^{s1s2} = & \nabla \Delta \rho_{AB}^{s1s2} + \nabla \Delta c\delta t_{AB}^{s1s2} + \nabla \Delta T_{AB}^{s1s2} - \nabla \Delta I_{AB}^{s1s2} + \nabla \Delta \delta t_{ABrel}^{s1s2} \\ & + \nabla \Delta M_{AB}^{s1s2} + \nabla \Delta \lambda N_{AB}^{s1s2} + \nabla \Delta \epsilon_{L_{AB}^{s1s2}}. \end{aligned} \quad (2.90)$$

Multipath effects, which will be introduced in the next chapter, in a DD configuration are not cancelled or mitigated due to the site-dependent properties that they have. On the other hand, atmospheric effects and resulting biases will be cancelled or reduced to a great extent when the baseline length is small (a few meters). Such a short-baseline set-up can be used for the isolation of multipath effects (Georgiadou and Kleusberg, 1988) and their study since the remain DD residuals of the short baseline will be dominated by the combined impact of multipath components from the same two satellites at two different antenna locations.

### 2.5.2. Linear Combinations

Linear combinations (LS) of different type of observations or observations of the same type but of different frequencies, from the same receiver and station, can be formed during data processing in order to eliminate or reduce certain error sources or for other tasks such as data screening and cycle slip fixing. Among the unlimited number of linear combinations, only those that fulfil some important criteria for the combined signals are of interest (Seeber, 2003) as: integer coefficients to produce integer ambiguities, reasonably large wavelengths to help ambiguity fixing, reduction of ionospheric refraction or multipath contamination and reduction of the observed noise.

In a general form, code/phase observable combination of different frequencies is formed from the original observations and particular coefficients ( $n_x$ ) as:

$$P_x = n_1 P_1 + n_2 P_2 + n_3 P_5, \quad (2.91)$$

$$L_x = n_1 L_1 + n_2 L_2 + n_3 L_5. \quad (2.92)$$

The wide and narrow lane LC are very often used in GNSS data analysis. The wide lane reads:

$$L_{\Delta} = L_1 - L_2, \quad (2.93)$$

and the narrow lane is computed as:

$$L_{\Sigma} = L_1 + L_2. \quad (2.94)$$

The wavelength of the wide lane LC is  $\lambda_{\Delta} = 0.862$  m, and that of the narrow lane is  $\lambda_{\Sigma} = 0.107$  m. The advantage of the wide lane observable is that the wavelength is four times larger as the one of the original observations and this will assist ambiguity resolution but, on the other hand, the noise is six times larger (Seeber, 2003). Narrow lane has the smallest wavelength has the lowest noise level of all LC and hence yields the best results (Seeber, 2003).

The ionospheric free linear combination of the code or phase observables is commonly used when dual frequency data are processed to eliminate ionospheric refraction.

$$P_3 = \frac{f_1^2 P_1 - f_2^2 P_2}{f_1^2 - f_2^2}, \quad (2.95)$$

$$L_3 = \frac{f_1^2 L_1 - f_2^2 L_2}{f_1^2 - f_2^2}. \quad (2.96)$$

$L_3$  LC eliminates ionospheric effects. However the ambiguity term is not integer any more due to the non integer coefficients. Furthermore,  $L_3$  LC has a higher standard deviation which can be computed as (Weinbach, 2013):

$$\sigma_{L3} = \sqrt{(2.546)^2 \sigma_{L1}^2 + (-1.546)^2 \sigma_{L2}^2}. \quad (2.97)$$

Finally, the multipath free LC are frequently used during GNSS data analysis to characterize and quantify multipath effects of the code observables (Rocken *et al.*, 1996). The original code and carrier-phase observations from dual frequency receivers are combined in such a way, that the code multipath can be isolated (Rocken *et al.*, 1996):

$$MP_1 = P_1 - L_1 - \frac{2}{a-1}(L_1 - L_2), \quad (2.98)$$

$$(2.99)$$

with the coefficient  $a = \left(\frac{f_1}{f_2}\right)^2$ .



### 3. Multipath Effects in GNSS

GNSS signals may arrive at the receiving antenna not only through the direct path, i.e. the line-of-sight (LOS) path, but also on multiple indirect paths, due to different electromagnetic effects as signal reflection or diffraction (Smyrnaioi *et al.*, 2013). These signal components arrive delayed, phase-shifted, depolarized and attenuated relative to the LOS component. We will call these signal components multipath components (MPCs) and the phenomena multipath propagation (Smyrnaioi *et al.*, 2013).

Multipath effects can be considered as an interference problem between the GNSS signal and delayed replicas of it. In the code observation domain, which is not treated in this thesis, they add additional biases of the order of dm to m in typical reference station scenarios. In urban environments, such biases will, most probably, be much larger and may reach up to 100 m in the extreme case. In the carrier-phase observation domain, the resulting biases due to multipath are, usually, smaller than a quarter of the wavelength (up to 4.5 cm for L1). Mitigation is only possible, at the time of writing, for indirect signals with extra path delays larger than, about, 30 m.

This chapter is structured as follows. After an introductory section, an overview of different approaches for multipath mitigation or characterization will be presented. Then, the different types of multipath interaction are introduced. Finally, multipath effects and their impact on the correlation and observation level is characterized.

#### 3.1. Multipath Effects in GNSS Positioning

Multipath propagation degrades the positioning accuracy. Moreover, in applications with high accuracy requirements, multipath errors dominate the total error budget. Despite the different approaches developed, several aspects of multipath propagation are still not fully understood (Smyrnaioi *et al.*, 2013). The unknown number of MPCs and their path geometry, the signal characteristics, the diffraction and reflection effects as well as their changing nature together with a complex antenna and receiver design make multipath mitigation very challenging (Smyrnaioi *et al.*, 2013). Furthermore, the site-dependent characteristics of multipath decorrelate the errors caused by multipath propagation at different antenna locations and thus, differential techniques, like e.g. DDs cannot mitigate it (Smyrnaioi *et al.*, 2013).

The superposition of the MPCs and the LOS signals yields a compound signal at the receiving antenna (Smyrnaioi *et al.*, 2013). Depending on the relative phase between the direct and indirect signal components, constructive or destructive interference appears (Smyrnaioi *et al.*, 2013). As a result, during signal tracking the correlation output between the received signal and the local PRN code replica generated by the receiver is deformed (Smyrnaioi *et al.*, 2013). Since MPCs generally arrive at the receiving antenna with small extra paths (i.e.  $\leq 30$  m, relative to the LOS signal, the correlation output is biased/deformed, and the receiver is not able to discriminate between MPC and the LOS signals (Smyrnaioi *et al.*, 2013). This correlation output is the fundamental input for the next iteration of the code and phase tracking loops of the receiver as well as for  $C/N_0$  estimation algorithms (Smyrnaioi *et al.*, 2013). As a result, the code-phase, carrier-phase, and  $C/N_0$  observables are biased by multipath propagation. In the framework of this thesis, errors in code- and carrier-phase observations caused by multipath propagation are referred to as code multipath and carrier-phase multipath, respectively, and in general as multipath errors (Smyrnaioi *et al.*, 2013).

In the observation domain, multipath errors are not constant in time (Smyrnaioi *et al.*, 2013). They show a sinusoidal behaviour which can be noticed in carrier-phase residuals from Precise Point

Positioning (PPP), double differences (DD) or  $C/N_0$  time series (Smyrnaioi *et al.*, 2013). This behaviour results from the change of the relative phase between direct and indirect signals as the satellite vehicle moves above the local horizon of the antenna (Smyrnaioi *et al.*, 2013). The amplitude of these oscillations depends on the amplitude/power of both, MPC and LOS signal components, which are also varying as geometry changes (Smyrnaioi *et al.*, 2013). The  $C/N_0$  observable is the only GNSS observation type in which multipath propagation effects are directly visible without any sophisticated data pre-processing (Smyrnaioi *et al.*, 2013). In contrast, in the phase or code domain residuals should be analysed or differences should be formed to eliminate all other errors sources and isolate them.

Multipath biases propagate to estimated coordinate time series as non-modelled error sources present in the observed minus computed (OMC) vector of the least square adjustment. Carrier phase multipath effects result in fluctuations of the estimated coordinates (or coordinate differences) of the order of sub mm to several mm with the deviations of the up component to be larger than the deviations of the horizontal component (e.g. King and Watson (2010), Goebell and King (2011)). These height biases due to multipath will likely result in biased estimates of tropospheric zenith delay and hence precipitable water vapour (King and Watson, 2010).

### 3.1.1. Overview of Multipath Related Studies in GNSS

The literature discussion on multipath related studies for GNSS that takes place in this section, is similar to the one presented in Smyrnaioi *et al.* (2013). Additions of recent multipath approaches are incorporated in this version.

In the beginning of the 1970s multipath effects on L1 frequency were first studied by Hagerman (1973) and the fundamental relationships between code error due to multipath and the driving parameters were derived. In Georgiadou and Kleusberg (1988), it was shown that the presence of multipath can be identified by using double differenced phase observations of a short baseline. Since then and during the last 4 decades many researchers have been involved in the characterization and modelling of this propagation phenomenon. A large number of scientific papers have been published on this topic, where different approaches and aspects of the problem have been investigated under certain predefined assumptions. Consequently, the scientific literature on multipath propagation for GNSS positioning can appear very rich for scientists. Despite the large number of different approaches developed, a universal solution of this problem is not achieved until the time of writing. Nevertheless, different promising approaches are under consideration and development.

In almost all textbooks on geodesy or navigation, with very few exceptions (e.g. Braasch (1996)), multipath propagation is presented in short texts of a couple of pages (e.g. Seeber (2003), Leick (2004), Hofmann-Wellenhof *et al.* (2008)). Most of the time, the phenomenon is explained geometrically, while other physical or electromagnetic properties of the reflected signals are not discussed. The progress in multipath-related studies is documented in various PhD thesis, we cite here exemplary: Hannah (2001), Lau (2005), Irsigler (2008), Rost (2011), Van-Nee (1991), Ray (2000), Bilich (2006), Weiss (2007), Böder (2002), Dilssner *et al.* (2008).

A prominent example for the successful reduction of code multipath is the smoothing of the code observations by the about two orders of magnitude more precise carrier-phase observations (Misra and Enge, 2006). Some manufacturers apply code smoothing as a default setting in the receiver. Longer smoothing periods give better performance in general (Hatch (1986), Irsigler (2008)). According to Irsigler (2008), the benefits of such an approach can yield a significant reduction of multipath impact given a sufficiently large smoothing time constant, e.g. in aviation typically 100 sec are used. However, the variability of the ionospheric conditions may create additional range biases when smoothing. Van Nee in Van-Nee (1991) showed that due to the non-zero mean of code-phase multipath, multipath effects cannot be eliminated by simply averaging over longer periods.

One of the most popular methods to characterize and quantify code multipath are the so-called

multipath linear combinations (Rocken *et al.*, 1996). The original code and carrier-phase observations from dual frequency receivers are combined in such a way, that the code multipath can be isolated. Due to its computational simplicity, this approach is often used to assess the overall multipath contamination at continuously operating reference stations (CORS), for example, the IGS network, or to characterize the performance of new receivers or new satellite signals, like e.g., the upcoming Galileo or GPS L5. However, it should be noted that the characterization is only valid if no code smoothing was applied.

In the observation domain, Iwase *et al.* (2010) detect the multipath errors in the satellite signals and exclude these signals to improve the positioning accuracy. An autoregressive moving average multipath estimator is developed in Miceli *et al.* (2011) using dual frequency observations. Consistency checking of signals is utilized in Jiang *et al.* (2011), whereby measurements from different satellites are compared with each other to identify the NLOS and most multipath-contaminated signals. Rost and Wanninger (2010) developed an algorithm which directly estimates carrier phase multipath corrections from signal quality measurements. Goebell and King (2011) investigate the effect of simulated carrier phase multipath on time series of several sites covering a period of about 6 years. In Moradi *et al.* (2014) a new carrier-phase multipath error observable is developed that isolates the inter-frequency carrier-phase multipath error for linear combinations of observables. A data-driven method called Hilbert Huang Transform is used in Hirle and Engler (2010). Finally, the use of an empirical site model derived from post-fit phase residuals to mitigate unmodelled site-specific errors is published in Moore *et al.* (2014).

Contrary to the code observations, the multipath error on the carrier phase observations is restricted in magnitude, since it is smaller than a quarter of the respective wavelength, i.e. about 5 cm maximum for the GPS L1 frequency. However, this is still large compared to the precision that carrier-phase observation could reach. Wanninger *et al.* (2000) proposed a method for carrier-phase multipath characterization of GPS reference stations. They analyse the double difference residuals in GPS networks. Consequently, it may sometimes be challenging to assign exactly the multipath signature to a specific site or satellite.

In post-processing, sidereal filtering or sidereal differencing is often applied. Taking advantage of the sidereal repetition of the GPS orbits, observations or coordinate time series of subsequent days can be subtracted in order to reduce the impact of multipath. Genrich and Bock (1992) showed that a reduction of about 80% can be obtained in this way. However, strictly speaking, each GPS satellite has its own, time-varying orbital period differing up to 10 sec with respect to the nominal sidereal period. Different approaches have been proposed to find the correct individual repeat times (e.g. Agnew and Larson (2007), Dilssner *et al.* (2008)). Finally, changing weather conditions like rain or snow will influence the reflection properties of the antenna vicinity, so that the similarity of multipath errors is reduced. The effects mentioned before restrict the power of multipath mitigation by sidereal differencing, especially over longer time intervals.

Finally, the analysis of un-differenced carrier-phase residuals from PPP is a useful tool for accessing the impact of multipath effects (Granström, 2006). For this purpose, the residuals are color-coded and depicted in a sky-plot. The variations of the residuals translate into a sequence of concentric rings in the sky-plot. But, since PPP residuals contain further remaining systematic effects, like e.g., varying tropospheric refraction, averaging strategies may be necessary (Iwabuchi *et al.*, 2004).

Observations of the signal strength, like SNR or  $C/N_0$ , have attracted much attention in multipath related studies although most of the approaches are found in post-processing applications (Rost and Wanninger, 2009). Compared to code or carrier-phase observations, the  $C/N_0$  values are usable without sophisticated pre-processing steps and attributed to one satellite-receiver propagation channel, i.e. no double differences are formed. First results of this type of investigation were presented in Axelrad *et al.* (2009) while newer ones can be found in Bilich *et al.* (2008), Rost and Wanninger (2009), Rost (2011). The basic idea is that the  $C/N_0$  values follow a nominal curve with respect to the satellite elevation that is mainly determined by the antenna gain pattern. Thus, deviations from this pattern can be easily identified and attributed to reflected and/or diffracted signals. Major restrictions

are (i) proprietary algorithms and definitions of the  $C/N_0$  values given by the commercial receivers. Different manufactures use different algorithms for the calculation of this type of observations. (ii) Different receivers (especially older ones) use different quantization levels (e.g. 1 dB-Hz instead of 0.1 dB-Hz) which can be very coarse for certain type of applications. (iii), the gain pattern of the receiving antenna is often unknown. Recently and very encouraging, some antenna manufacturers have published receiver antenna gain patterns for right-hand and left-hand circular polarization, like Leica (2014). It would be very useful if in future more manufacturers could follow this example. Finally,  $C/N_0$ -based observation weighting is very often used to reduce the impact of reflection and/or diffraction effects on the observation level (Lau and Cross (2006), Hartinger and Brunner (1999), Wieser (2001)).

Receiver-internal multipath mitigation/detection techniques incorporate different signal processing strategies for the reduction of this type of errors. The cornerstone approach for this category of approaches is the narrow-correlator technology (Van-Dierendonck *et al.*, 1992). It was demonstrated that by reducing the spacing of the early and late correlators from 1 chip to 0.1 chips, a significant reduction of multipath error could be achieved. In this way, MPCs with large extra path delay could be filtered out. Since then, several other approaches were developed, most of them for the mitigation of code multipath and much fewer for phase multipath. The majority of the internal approaches incorporate the use of several early and late correlators with different spacing between them. The correlator outputs are then used for the formation of different multipath mitigation discriminators or the detection of the deformed slopes of the correlation peak. One of the most characteristic approaches is the High Resolution Correlator (McGraw and Braasch, 1999), where the code discriminator is formed by two pairs of early-late correlators. Strobe Correlator (Garin and Rousseau (1996), Garin and Rousseau (1996)) and Vision Correlator (Fenton and Jones, 2005) are other receiver internal techniques. A breakthrough in the receiver internal approaches happened in 1995, when Novatel introduced the Multipath Estimating Delay-Lock Loop (MEDLL) (Townsend *et al.* (1995b), Townsend *et al.* (1995a)). According to Lawrence (2003), the MEDLL is a maximum likelihood estimation technique pioneered by Van Nee (Van-Nee, 1995) at Delft University of Technology and it improves the C/A-code narrow correlator performance by configuring the residual pseudorange error to a smaller region of secondary path relative delay. Since then, different approaches have been developed incorporating multiple correlators and estimation theory. In Haker and Raquet (2012) a new signal decomposition and parametrization Algorithm (SDPA) is presented for the tracking of the direct path and multipath ray waveform parameters. Montloin *et al.* (2012) develop a model that allows the mitigation of multipath effects during taxi and parking operations in an airport area while requiring a basic and simple 3D model of the airport. Different tracking strategies are utilized in Ziedan (2012) for multipath mitigation purposes. Both closed loop tracking and open loop tracking are utilized to accommodate various multipath patterns. In Giger (2011) a comparison of three different signal tracking approaches in a simulated realistic multipath environment is performed. The approaches under investigation are the scalar tracking loops, vector delay locked loops and joint tracking loops. A Multipath Estimating Delay Locked Loop is implemented in Langer *et al.* (2011) based on Fast Iterative Maximum Likelihood Algorithm. High sensitivity receivers have also been used for multipath related studies as in Xie *et al.* (2011) and He and Petovello (2013). Finally, an analysis of early-late phase for the L1 and L2C signals for detecting multipath is presented in Mubarak and Dempster (2010). The multipath detection performance of this approach has been validated using probabilities of false alarm and detection. Despite the evolve of the receiver internal mitigation approaches, MPCs of relative short extra paths (less than 30 m) still cause errors in all types of GNSS observables. An overview work on receiver internal approaches with very interesting references can be found in Iriglier (2008) and Van-Dierendonck (1997). Also, aspects of multipath propagation and the impact on the signal processing modules of the receiver can be found in text books about software-defined GNSS receivers, like Borre *et al.* (2007), Tsui (2005) or Pany (2010).

A lot of effort was given to the antenna design. In Moernaut and Orban (2009), basic aspects of GNSS antennas are presented while more details can be found in recently published textbooks on GNSS antennas (e.g. Rao *et al.* (2013)). A first approach consists in using antenna elements with

a large ground-plane which increases the directivity of the antenna for the upper hemisphere and reduces reflections from below the antenna horizon. However, diffraction at the edges occurs and cause severe problems (Tranquilla *et al.*, 1994). Subsequently, choke ring antennas were developed (Blakney *et al.*, 1986) and are widely used now, especially for reference station applications. Even though they attenuate MPCs coming from negative elevation angles relative to the antenna horizon, their design cannot mitigate MPCs coming from positive elevation angles. Modern designs use variable choke-ring depths (Filippov *et al.*, 1999). Assuming a change of polarization of the RHCP GNSS signals upon reflection, a basic principle applied in all GNSS antennas is to increase the sensitivity for RHCP and to simultaneously decrease the sensitivity of LHCP signals. It should be stated that different attempts to reduce the multipath reflection by applying micro-wave absorbing material are reported in literature, e.g. Ning *et al.* (2011). Newer antenna related approaches for multipath mitigation have been developed in the last years. In Kerkhoff *et al.* (2010) two different approaches to modifying the basic choke ring antenna design for multipath reduction are presented. One approach consists of placing a large metallic ground plane directly beneath the antenna and therefore shape the antenna radiation patterns near and below the horizon so as to reduce reception of multipath signals from those directions. The second approach examined, is to place a specific arrangement of radio frequency absorbing foam around and beneath the base of the antenna in order to attenuate incoming multipath signals before they reach the antenna. Another approach is developed for characterizing and compensating GNSS multipath by considering signal amplitude and phase variations in response to antenna motion (Ertan *et al.*, 2013).

Closely-spaced antennas (Ray (2000), Ray *et al.* (1998)) are also developed for the reduction of multipath errors. They form a type of small antenna arrays. Based on a least-squares adjustment, the multipath relative amplitude  $\alpha$ , the multipath relative phase ( $\Delta\Phi$ ) as well as azimuth and elevation of the assumed reflector can be estimated (Irsigler, 2008). Further developments lead to beam steering and adaptive beam forming antennas or antenna-receiver combination, like e.g. DLR GALANT receiver (Cuntz *et al.*, 2008). However, this interesting technology seems to be not mature enough to be installed at GNSS reference stations. Finally, dual polarized antennas have also been used for multipath related investigations (e.g. Groves *et al.* (2010)).

In Park *et al.* (2004) the concept of station calibration for multipath mitigation by a parabolic antenna was presented. However, the concept is not in operational use, today. Further approaches of station calibration try to randomize the multipath effect by shifting the antenna in a controlled manner using a robot (Böder (2002), Böder *et al.* (2001), Wübbena *et al.* (2006)). This method is very successful for in-situ calibration; however the efforts due to the operation of the robot are very large. The validity of the corrections is again restricted by the individual repeat times of the satellite orbits. In Dilssner *et al.* (2008) a separation of the so-called near- and far-field multipath is proposed by calibrating the antenna with and without the mounts like e.g. tripods or special metal adaptations. The difference in the determined phase center variations is attributed to the near-field multipath (Dilssner *et al.*, 2008).

New GNSS signals with different signal structures (e.g. AltBOC) have a better performance against multipath (e.g. Shetty *et al.* (2010), Schönemann *et al.* (2010), Montenbruck *et al.* (2011)). Nevertheless, short delay MPCs will still cause problems in all types of GNSS signal.

In order to get a better understanding of the physical processes involved in the multipath phenomenon, models from wave propagation are very useful and the development of different simulation tools that use 3D environment models to identify and/or quantify multipath effects is also a very active area of multipath related research. First results were given in Elósegui *et al.* (1995). More elaborated models are based on ray-tracing tools that use as a fundamental input the physical environment in which the antenna is placed, the receiving antenna position and the transmitting antenna position. Based on these input parameters, all possible signal paths are estimated and the geometric and electromagnetic properties of them are calculated. Ray-tracing simulation tools are widely used, for the simulation of wireless networks. In GNSS-related studies they were first presented in Lau (2005), while another ray-tracing approach, Weiss (2007), was used for the characterization and modelling of P-code multipath in different environments. Other recent approaches can be found in Liso *et al.* (2011), Liso *et al.* (2012),

Liso *et al.* (2013) or Liso and Kürner (2014). Based on digital terrain models, more complex scenarios like urban canyons are analysed, e.g. Bradbury *et al.* (2007). Besides deterministic channel models, stochastic modeling is applied in complex scenarios, like e.g. DLR's land mobile and aeronautic channel model (Steingass and Lehner, 2004) and subsequent work. Wang *et al.* (2013) are improving urban positioning accuracy using a 3D city model with optimized visibility prediction scoring. Suzuki and Kubo (2012) propose a technique based on multipath simulation using a 3D digital surface model for obtaining GNSS positioning in urban canyons and in Obst *et al.* (2012) a general and lightweight probabilistic positioning algorithm with integrated multipath detection through 3D environmental building models is presented. Finally, a purely statistical wideband land mobile channel model suitable for Global Navigation Satellite Systems (GNSS) software and hardware simulations is proposed in Prieto-Cerdeira *et al.* (2011).

In recent years, the concept of GNSS reflectometry (Martin-Neira, 1993) and scatterometry has strongly evolved (e.g. Jin *et al.* (2014), Cardellach (2001), Helm (2008), Garrison *et al.* (1997), Larson *et al.* (2008), Zavorotny *et al.* (2010), Rius *et al.* (2002)). Here multipath propagation is not considered as bias but as basic information. In the context of GNSS-R, much progress has been made, especially in the mathematical and physical modelling of the wave propagation. Hence, these publications can be a valuable source for mitigating multipath in positioning.

In indoor environments, multipath and refraction effects result in deep fading of GNSS signal power. Since there is no clear sky above the antenna, the received signals are transmitted through different construction material while effects of signal reflection and diffraction are also present. As a result, incoming signals are attenuated and in many cases reflected components are acquired and tracked by the receiver. Furthermore, due to the motion of the satellite the propagation path between the transmitting and the receiving antennas changes constantly. This results in changing multipath effects. The two major reasons for signal degradation in indoor scenarios are signal attenuation and multipath and they, both, result in a fading behaviour of the incoming signal power. In many GNSS indoor studies the primary concern is to counter attack this fading behaviour since analytical modelling of the electromagnetic interaction in such complex scenarios is very challenging. The fading behaviour results in signal processing problems. Weak signals are not so easily detectable (signal acquisition) and their parameters (delay, phase, and Doppler shift) cannot be easily tracked. The quality of GNSS observables from signals with low  $C/N_0$  is degraded and, furthermore, the satellite geometry is less suitable. As a consequence, the estimated positioning solution accuracy is very low. To improve the signal quality, the use of extended integration time is a typical solution (e.g. Julien (2005)). Longer integration periods increase the processing gain though, the 20 msec duration of the navigation bit restrict the integration time. Non coherent integration and squaring of the signal is one solution, although the squaring loss is affecting the processing gain and, furthermore, is getting bigger when the signals are getting weaker (Kaplan and Hegarty (2006)). Another drawback of very long integration periods is that the assumption that the Doppler shift stays constant within the signal snapshot used for the integration is not valid any more. The Doppler error caused by antenna motion and receiver clock instability may limit the duration of the integration time (Julien (2005)). On the other hand, the widening of the loop filter in indoor scenarios, to couple better with the Doppler errors will further degrade the signal quality because the noise level will rise. Lately, the concept of antenna diversity (e.g. Vaughan and Andersen (2003)) is applied to the GNSS case (Sadrieh, 2012). Signals captured from different antennas result in different and uncorrelated fading channels which can be combined. In this way, the fading behaviour can be reduced and this can increase signal detectability (e.g. Sadrieh (2012)).

### 3.2. GNSS Multipath Aspects

In a typical receiver architecture, MPCs with relative extra path delay larger than 1.5 chips or 450 meters will be automatically filtered out by the correlation process and will not bias the tracked signal. In a similar sense, for the P(Y) code, MPCs with extra path delays larger than 45 meters will not bias

the P(Y) code observations. Nevertheless, MPCs with shorter delays than the previously mentioned will contaminate the ranging observations. As already mentioned, different signal processing strategies can be utilized to filter out MPCs with relative large delays as, for example, to narrow the spacing between the early and late correlators or to form combinations/differences between the different correlators and mitigate multipath on the discriminator level. Such approaches, on the other hand, are not applicable for very short delay MPCs (e.g. extra path length of the order of a few meters) which is very often the case in real life scenarios (e.g. reference station applications).

Considering only the C/A code and neglecting the navigation data and the Doppler shift of the MPCs, the transmitted signal model introduced in previous the section (eq. 2.72) can be expanded for the case of a compound signal (i.e. LOS and MPC) and written as (Van-Nee, 1991):

$$s_{L1}(t) = \sqrt{2P_{C/A}}x_{C/A}(t)\cos(2\pi f_{L1}t + \vartheta_{L1}) + \sqrt{2P_{C/A}} \sum_{i=1}^n \alpha_i x_{C/A}(t - \tau_i) \cos(2\pi f_{L1}t + \vartheta_{L1} + \Delta\Phi_i). \quad (3.1)$$

This formula represents the general case of a GNSS signal in the presence of  $n$  MPCs with  $\alpha_i$  the relative amplitude of the  $i^{th}$  MPC which is mainly determined by the reflection process and the receiving antenna gain pattern as shown in Smyrnaiois *et al.* (2013), Smyrnaiois and Schön (2015) and Granger and Simpson (2008). In the following chapters of the thesis, GNSS signal amplitude/power modelling will be treated in detail together with the development of generalized expressions for the simulation of multipath effects on the GNSS observables.  $\Delta\Phi_i$  is the relative phase between the  $i^{th}$  MPC and the LOS component and  $\tau_i$  the relative delay between the  $i^{th}$  MPC and the LOS signal. These three multipath parameters together with other tracking parameters (e.g. correlator spacing), when known, can determine the impact of multipath propagation on the GNSS observables.

### 3.2.1. Types of Multipath Interactions

Different types (and combinations) of multipath interaction result in compound signal tracking by the receiver and in variety and diversity of multipath propagation effects. Such interactions can be specular or diffused reflections and edge diffraction or shadowing effects. Receiver hardware induced multipath effects are reported in (Kelly, 2000).

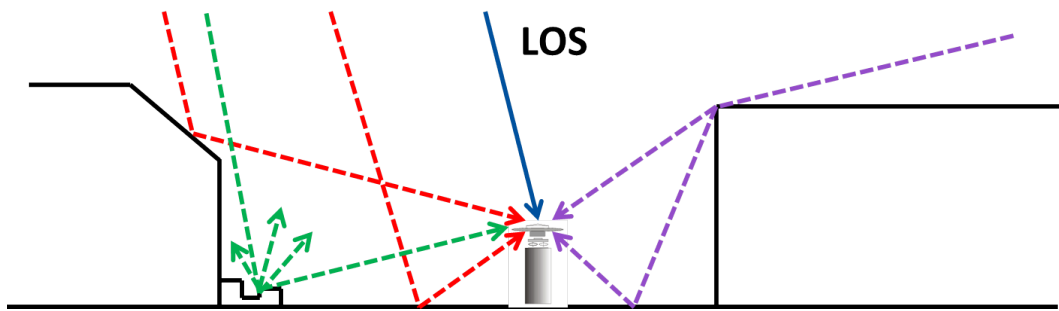


Figure 3.1.: Different types of multipath interactions.

### 3.2.2. Diffraction Induced Multipath Effects

The diffraction mechanism is described in many textbooks on electromagnetic theory and antennas and by many theories like physical optics or geometrical theory of diffraction. The uniform theory of diffraction (UTD) is often used by simulation tools and it is a uniform version of the geometrical theory of diffraction that was first published in Kouyoumjian and Pathak (1974). It approximates near

electromagnetic fields as quasi-optical and uses ray diffraction to determine diffraction coefficients for each diffracting object-source combination which are then used to calculate the field strength and the phase for each direction away from the diffracting point (Kouyoumjian and Pathak, 1974).

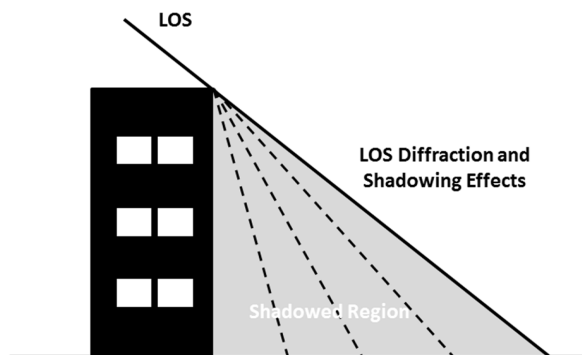


Figure 3.2.: LOS diffraction and shadowing effects.

In GNSS literature, diffraction effects are investigated for different scenarios like e.g. urban canyons (Groves, 2011). Shadowing effects are investigated in Wanninger *et al.* (2000). Stochastic modelling and weighted schemes of the GNSS observables in the presence of diffraction is examined in Wieser (2001). LOS diffraction and shadowing effects result in deep fading of signal amplitude (e.g. Wanninger *et al.* (2000), Wieser (2001)) and, therefore, in the degradation of the ranging observations quality and/or losses of lock.

### 3.2.3. Diffused Reflection

In the general case, reflected signals are composed both of the specular and from the diffused parts. It is therefore possible to split the scattering process into two contributions (Cardellach, 2001); the specular or coherent term and the diffused or non-coherent term where the specular term is characterized by its high directivity, while the diffused spreads the signal into a wide range of low power scattered directions (Cardellach, 2001). The specular part will always travel the shorter path between the reflecting surface and the receiving antenna.

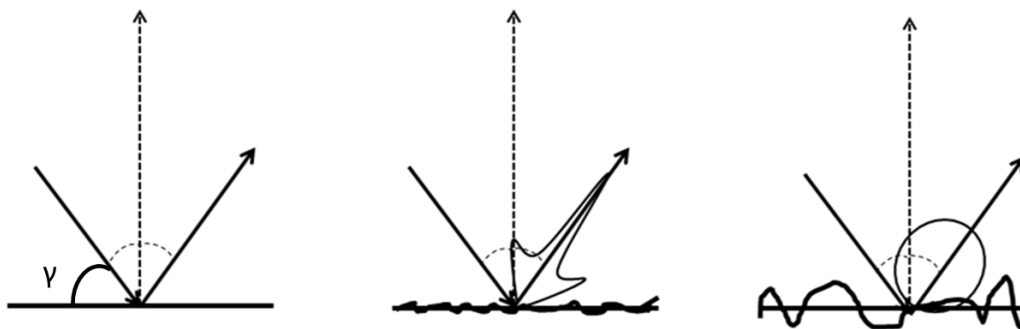


Figure 3.3.: Scattering with both the specular part and the diffused part. When the surface is smooth (relative to the wavelength) the specular contribution is dominant, while when the roughness increase the diffused component is more dominant and signal power is spread over various direction. Similar figure can be found in Cardellach (2001).



The surface roughness or smoothness is defined with respect to the wavelength ( $\lambda$ ), the grazing/reflection angle ( $\gamma$ ) and the surface irregularities ( $\Delta h$ ). Thus, the same surface can be seen as rough for small wavelengths and smooth for larger ones. Since the different GNSS frequencies are in L-band, the roughness of a reflector and its impact in the reflection process is assumed very similar between the different GNSS frequencies and for the same incident/grazing angle. The path difference between two rays reflected from a rough surface with height irregularities  $\Delta h$  is equal to (Beckmann and Spizzichino, 1963):

$$\Delta r = 2\Delta h \sin(\gamma). \quad (3.2)$$

and the phase difference is the equal to:

$$\Delta\phi = \frac{4\pi\Delta h}{\lambda} \sin(\gamma). \quad (3.3)$$

By arbitrarily choosing  $\Delta\phi = \frac{\pi}{2}$  and substituting in eq. 3.3, the criterion whether a reflection is specular or diffused (Rayleigh criterion) can be approximated by (Beckmann and Spizzichino, 1963):

$$\Delta h < \frac{\lambda}{8\sin(\gamma)}. \quad (3.4)$$

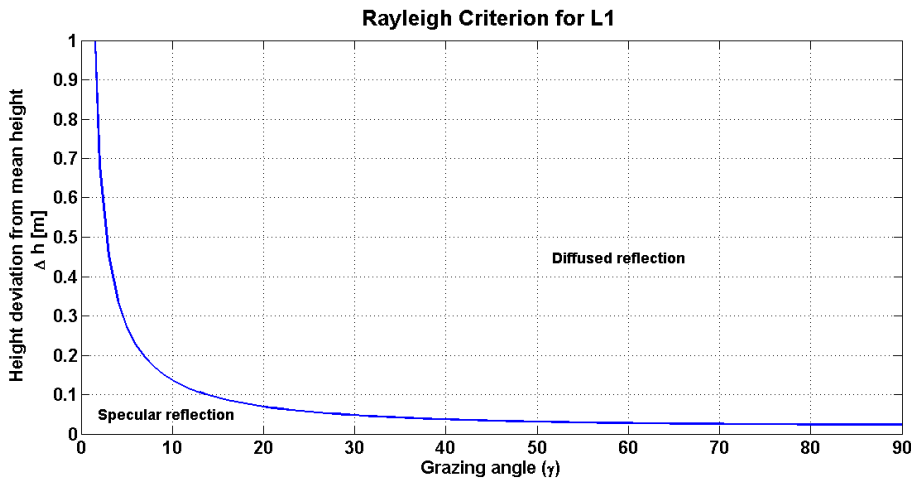


Figure 3.4.: Rayleigh criterion for L1.

In fig. 3.4, the visualization of the Rayleigh criterion is plotted, similar plots can be found in Hannah (2001) and in Irsigler (2008) where the Rayleigh criterion is plotted for different GNSS frequencies also. The y axis is the standard deviation of the reflector height from a mean reflector height, and the x axis is the grazing/reflection angle. This plot shows, as a rule of thumb, under which combination of  $\Delta h$  and  $\gamma$  (Rayleigh criterion) will the reflection be specular or diffused. Thus, for example, if we consider a ground reflector with height deviations of the order of 0,15 meters, the reflection can be considered specular for satellite elevations smaller than  $10^\circ$  while for higher satellite elevations a diffused component will also exist.

Diffused reflection can be treated as a further attenuation of the specular component by multiplying the reflection coefficients by a scaling factor Flock (1987):

$$\rho_s = e^{-\frac{\Delta h^2}{2}} I_0 \frac{\Delta h^2}{2}, \quad (3.5)$$

where  $I_0 \frac{\Delta h^2}{2}$  is the modified Bessel function of  $\frac{\Delta h^2}{2}$  (Flock, 1987). According to Hannah (2001), the non-specular part of the reflection process is statistically random with a Rayleigh distribution with probability density function (PDF) and as such is treated in Masters (2004). The PDF for a Rayleigh distribution reads:

$$p_r = \frac{r}{\sigma^2} e^{-\frac{r^2}{2\sigma^2}}, \quad (3.6)$$

with  $r$  the envelop of the distribution and  $\sigma$  the standard deviation (Vaughan and Andersen, 2003). The Rayleigh distribution is also used for the characterization of the fading behaviour in indoor scenarios. As mentioned in Zaheri *et al.* (2009), Rayleigh indoor scenarios occur when the LOS component does not exist or is attenuated significantly and no dominant signal component is seen by the receiver.

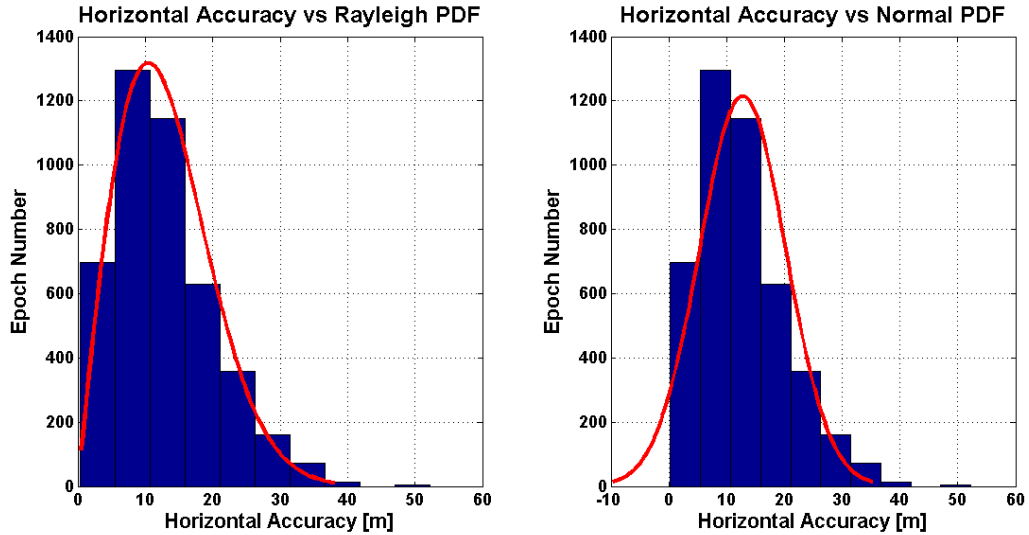


Figure 3.5.: Rayleigh versus normal distributions of estimated horizontal accuracy in an indoor scenario.

In fig. 3.5, a histogram plot of the estimated horizontal accuracy is plotted together with the Rayleigh (left side) and the normal (right side) fitted PDFs. With the normal-Gaussian distribution having a PDF:

$$f(x) = \frac{1}{\sigma\sqrt{2\pi}} e^{-\frac{1}{2}\left(\frac{x-\mu}{\sigma}\right)^2}, \quad (3.7)$$

with  $\mu$  the mean and  $\sigma$  the standard deviation. The data were captured and analysed by the author in the framework of an indoor experiment during the course of BERTA project.

### 3.2.4. Specular Reflection

In the case of specular reflection, the signal power reaches the receiving antenna from only one direction. The reflection process and the resulting impact on the reflected field (i.e. attenuation and depolarization) can be described by Fresnel reflection coefficients. The reflection coefficients for the linear, horizontal and vertical, components can be expressed as (Hannah, 2001):

$$R_H = \frac{\sin\vartheta - \sqrt{\epsilon - \cos^2\vartheta}}{\sin\vartheta + \sqrt{\epsilon - \cos^2\vartheta}}, \quad (3.8)$$

and

$$R_V = \frac{\epsilon \sin\vartheta - \sqrt{\epsilon - \cos^2\vartheta}}{\epsilon \sin\vartheta + \sqrt{\epsilon - \cos^2\vartheta}}, \quad (3.9)$$

with

$$\epsilon = \epsilon_r - j60\lambda\sigma. \quad (3.10)$$

$\epsilon$  is complex dielectric constant,  $\epsilon_r$  is the relative permittivity,  $\lambda$  is the wavelength of the carrier and  $\sigma$  the conductivity of the reflector. The reflection coefficient are complex numbers that describe the impact of the reflection process on the magnitude and phase of the incident field (depolarization). They are directly related with the transmitter-reflector-receiver geometry and with the material properties of the reflector. Exemplary material properties can be found in literature (e.g. ITU-R (1992), Hannah (2001)) for the GNSS frequencies. The ones that are used in this thesis can be seen in table 3.1.

Reflector Material	Relative Permittivity ( $\epsilon_r$ )	Conductivity ( $\sigma$ ) [S/m]
Wet Ground	30	$2 \cdot 10^{-1}$
Metal	$1 \cdot 10^4$	0
Concrete	3	$2 \cdot 10^{-5}$
Sea Water	20	4

Table 3.1.: Exemplary reflector material properties.

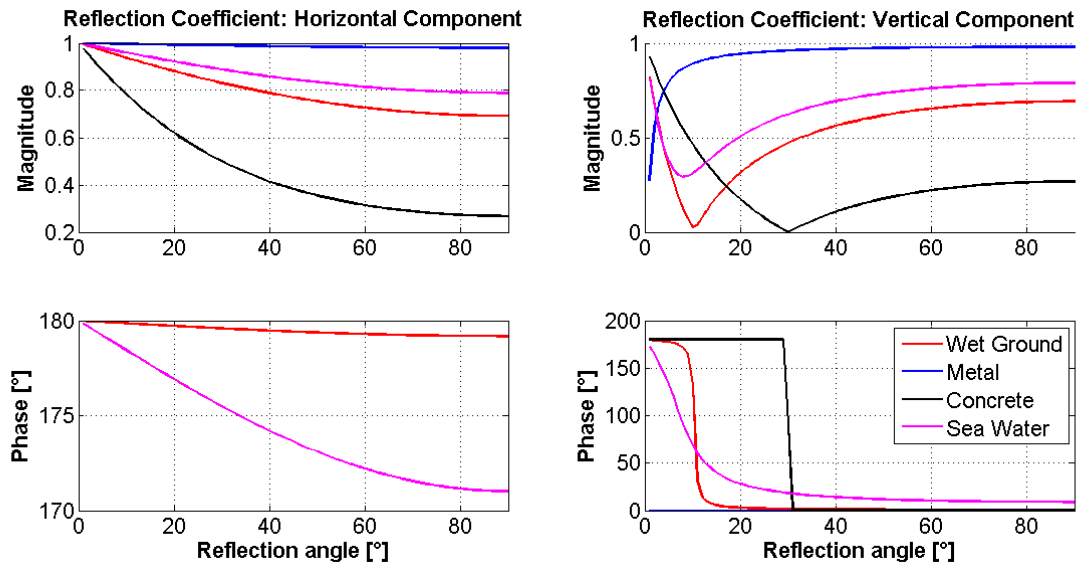


Figure 3.6.: Reflection coefficients for L1 carrier for different reflectors and for a satellite arc from  $0^\circ$  up to  $90^\circ$ .

In fig. 3.6, the reflection coefficients for the linear components are plotted for the L1 carrier and the exemplary material properties of table. 3.1. They indicate how the electrical field components of the incident field will be changed upon reflection, regarding magnitude and phase.

Looking at reflection coefficients for the different reflection angles in fig. 3.6 and for concrete reflector, it can be seen that when the reflection angle approaches  $0^\circ$ , both components have equal magnitude. For reflection angles between  $0^\circ$  and  $30^\circ$ , the magnitude of the linear components is different and thus, the polarization becomes elliptical with the eccentricity of the polarization ellipse getting higher. The sense of rotation of the electric field vector does not change. At around  $30^\circ$ , the vertical component is zero (Brewster angle), and the reflected field is linearly (horizontally) polarized. For reflection angles larger than  $30^\circ$  the reflected field change sense of rotation, the phase of the vertical components flips  $180^\circ$  and the eccentricity of the polarization ellipse get smaller as the reflection angle increases. For a reflection angle of about  $90^\circ$ , the reflected signal has an orthogonal, to the initial, polarization since the magnitude of the linear components is equal.

When the material properties change, losses and depolarization effects on the reflected field are different. For example, the angle for which the magnitude of the vertical component is zero or minimum (pseudo-Brewster angle) varies significantly between the different reflectors. Furthermore, small magnitude changes between the different frequencies (e.g. L1 and L5) may occur as it can be noticed in fig. 3.7 were the Fresnel coefficient are plotted for L5 frequency.

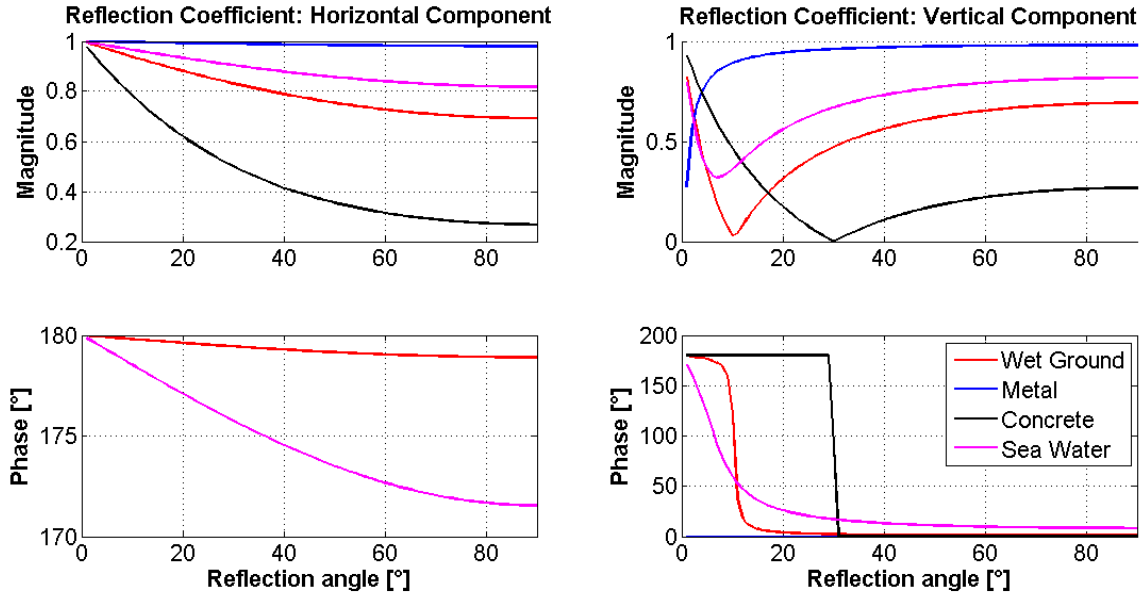


Figure 3.7.: Reflection coefficients for L5 carrier for different reflectors and a satellite arc from 0° up to 90°.

The reflection coefficients can also be expressed for the circular components (see fig. 3.8) of the two orthogonal polarizations ( $R_{co}$ ,  $R_{cross}$ ). For the RHCP GNSS signals,  $R_{co}$  can be associated with the RHCP component while  $R_{cross}$  represents the orthogonal LHCP component.

$$R_{co} = \frac{R_H + R_V}{2}, \quad (3.11)$$

$$R_{cross} = \frac{R_H - R_V}{2}. \quad (3.12)$$

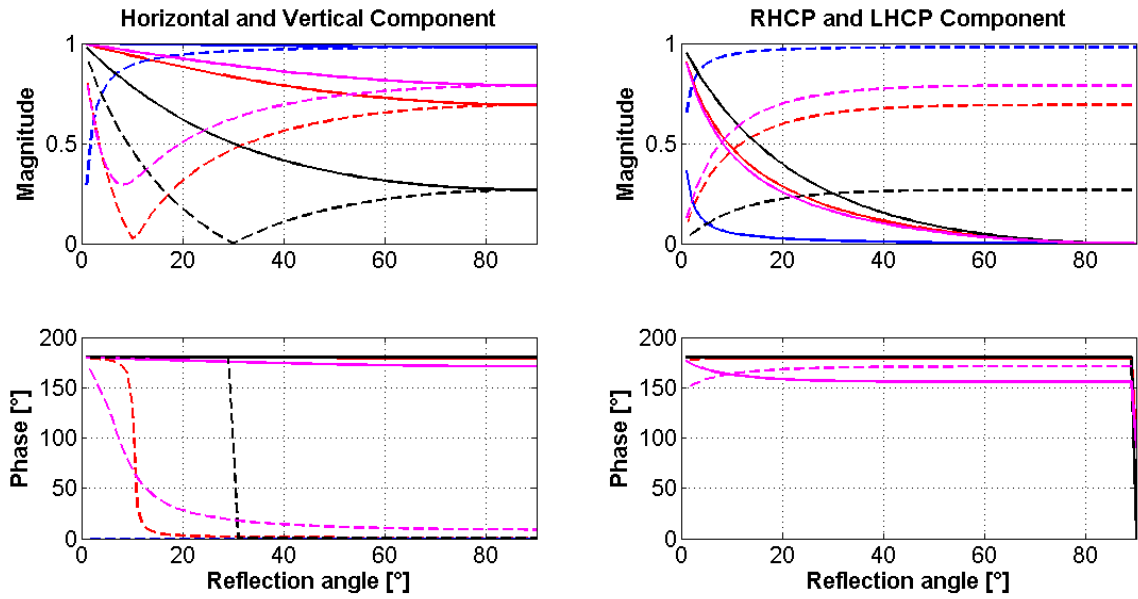


Figure 3.8.: Linear versus circular reflection coefficients (magnitude and phase) for L1.

### Fresnel Zones

Specular reflection can be approximated as a single point reflection, nevertheless the Fresnel zone/ellipsoid criterion can be utilized to identify reflecting surfaces or other obstructions of the LOS path between the transmitting and the receiving antennas. The Fresnel ellipsoid is defined as the locus of points for which the sum of distances from two antennas is an integral number of half wavelengths greater than the length of the direct ray between the antennas (IEEE, 1997). Transmitting and receiving antennas are the focal points of the ellipse. Fresnel zones/ellipse for a ground reflection is defined, according to IEEE (1997), as the locus of points in the ground plane for which the sum of the distances from the two antennas is an integral number of half wavelengths greater than the length of the specular reflected ray.

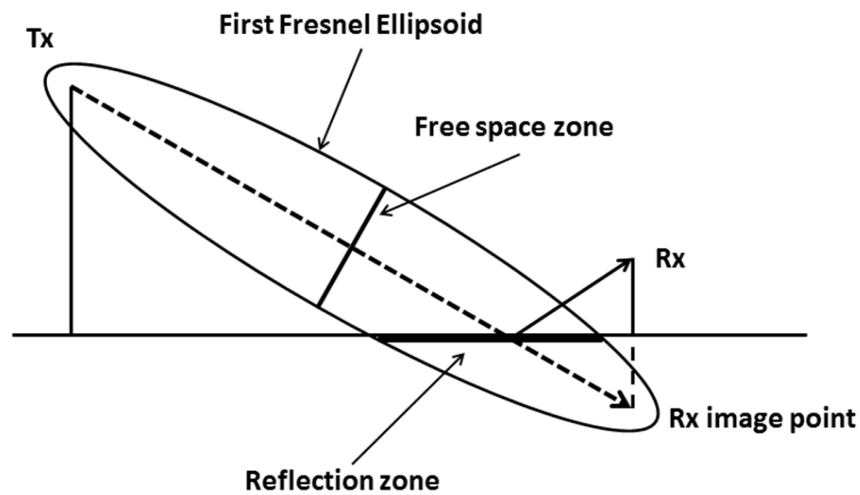


Figure 3.9.: First Fresnel ellipsoid and reflection zone.

The reflection zone size is dependent on the height of the antenna above the ground reflector. The size of the reflection zone gets bigger when the antenna height increases. The eccentricity of the reflection zone approaches 1 when the satellite is at the very zenith. When the satellite elevation is at around  $0^\circ$ , the eccentricity approaches 0. Fresnel ellipse and related aspects can be found in several GNSS multipath related publications (e.g. Irsigler (2008), Larson and Nievinski (2012))

### 3.3. Multipath Characterization

The extra path between the direct and one delayed MPC can be directly derived from the geometrical characteristics of the scenario. In fig. 3.10 the geometry of a single reflection from a tilted reflector is visualized, a similar figure can be found in Bilich and Larson (2007).

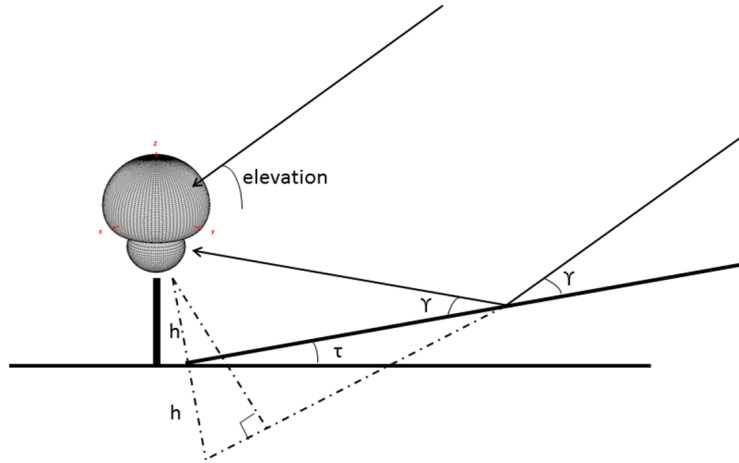


Figure 3.10.: Reflection geometry where the reflector is tilted by an angle  $\tau$  about the horizontal plane. The reflection angle is  $\gamma$  and the height above the reflector is  $h$ .

Directly from the before mentioned figure and as shown in Georgiadou and Kleusberg (1988) the extra path difference ( $\delta$ ) between the direct and indirect signal reads:

$$\delta = 2h \sin(\gamma), \quad (3.13)$$

with  $h$  the height of the antenna above the reflector and  $\gamma$  the reflection angle. If the reflector is assumed a horizontal one, then the reflection angle is equal to the elevation of the satellite. The relative phase ( $\Delta\Phi$ ) of the reflected signal with respect to the direct one reads:

$$\Delta\Phi = \frac{2\pi\delta}{\lambda}, \quad (3.14)$$

where  $\delta$  is expressed in meters and  $\lambda$  is the wavelength. It should be noticed at this point that the expression for the relative phase,  $\Delta\Phi$ , does not include phase shifts that may occur due to the reflection process itself.

#### Multipath Phase Rates

Multipath effects in the GNSS observables exhibit a sinusoidal-like behaviour. Multipath fading behaviour is directly visible in the  $C/N_0$  observables. In the range observables differences should be formed, or residuals should be analysed to isolate these periodic signal variations.

Irsigler (2010) characterized multipath phase rates in different multipath environments and derived distributions of them for a multitude of different antenna locations. In Bilich *et al.* (2008) multipath fading rates were used in the framework of a multipath mitigation approach for GNSS carrier phase observations.

Assuming a ground reflection scenario and the reflection angle  $\gamma$  of eq. 3.13 equal with the satellite elevation, multipath frequency variations [Hz] can be computed as (Bilich *et al.* (2008), Irsigler (2010)):

$$f_{mpc} = \frac{1}{2\pi} \cdot \frac{d\Delta\Phi}{dt} = \frac{4\pi h}{2\pi\lambda} \cos(El) \cdot \frac{dEl}{dt}. \quad (3.15)$$

In fig. 3.11, the computed multipath phase rates (in blue) are plotted for two exemplary observed PRN arcs with two different antenna heights above the ground reflector. For the two plots in the left column, the antenna height was set to 1.36 m and for the two plots in the right column to 2.05 m. The satellite elevation is plotted in green colour. It can be noticed in these plots that multipath phase rates increase when the distance between the reflector and the antenna increases. Similar plots can be found in Irsigler (2010).

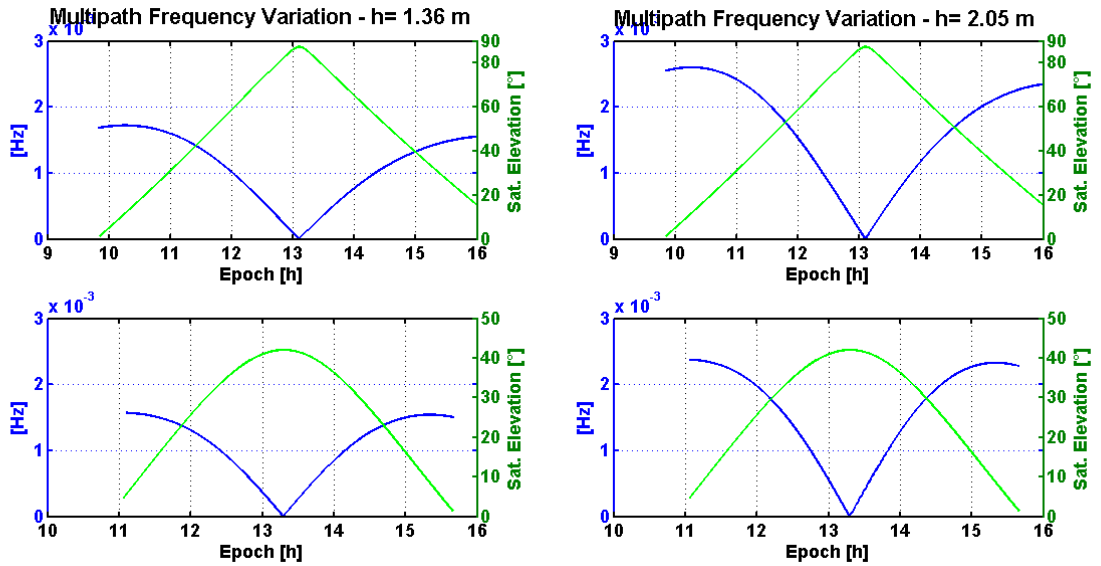


Figure 3.11.: Multipath phase rates for two exemplary PRN arcs and two different antenna heights above the ground reflector.

### 3.3.1. Signal Tracking in the Presence of Multipath

In the presence of multipath, a compound signal is tracked by the receiver. The GNSS signal in the presence of multipath can be represented by eq. 3.1. In fig. 3.12 the visualization of the correlation function for the C/A code is plotted. In the left side, the correlation function of the LOS signal components is illustrated. Assuming no noise and an infinite frond-end bandwidth, the correlation function has the shape of a triangle. In the right side of the same figure, the correlation function of the C/A code in the presence of multipath is plotted. As it can be noticed in this figure the shape of the correlation function is deformed due to additional delayed and attenuated signal components. As a result, biases are introduced in the tracking output results and therefore, in the measured, by the receiver, range observations.



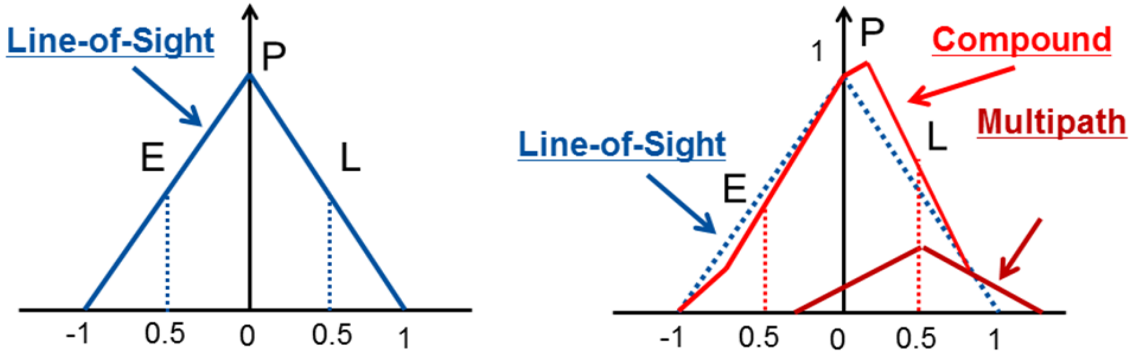


Figure 3.12.: The correlation function of the C/A code for the LOS signal (left side) and a compound signal (right side).

The correlation output between the received, compound, signal and the locally generated replicas by the receiver for the early, late and prompt correlators can be written as:

$$I_E = AR(\delta\tau - \frac{d}{2})\cos(\phi_\epsilon) + A \sum_{i=1}^n \alpha_i R(\delta\tau - \tau_i - \frac{d}{2})\cos(\phi_\epsilon + \Delta\Phi_i), \quad (3.16)$$

$$I_L = AR(\delta\tau + \frac{d}{2})\cos(\phi_\epsilon) + A \sum_{i=1}^n \alpha_i R(\delta\tau - \tau_i + \frac{d}{2})\cos(\phi_\epsilon + \Delta\Phi_i), \quad (3.17)$$

$$I_P = AR(\delta\tau)\cos(\phi_\epsilon) + A \sum_{i=1}^n \alpha_i R(\delta\tau - \tau_i)\cos(\phi_\epsilon + \Delta\Phi_i), \quad (3.18)$$

$$Q_E = AR(\delta\tau - \frac{d}{2})\sin(\phi_\epsilon) + A \sum_{i=1}^n \alpha_i R(\delta\tau - \tau_i - \frac{d}{2})\sin(\phi_\epsilon + \Delta\Phi_i), \quad (3.19)$$

$$Q_L = AR(\delta\tau + \frac{d}{2})\sin(\phi_\epsilon) + A \sum_{i=1}^n \alpha_i R(\delta\tau - \tau_i + \frac{d}{2})\sin(\phi_\epsilon + \Delta\Phi_i), \quad (3.20)$$

$$Q_P = AR(\delta\tau)\sin(\phi_\epsilon) + A \sum_{i=1}^n \alpha_i R(\delta\tau - \tau_i)\sin(\phi_\epsilon + \Delta\Phi_i). \quad (3.21)$$

In the above equations for the representation of the correlator output of the I and Q branches in the presence of multipath, the navigation data and noise are omitted.  $\Delta\Phi_i$  stands for the relative phase of the  $i^{th}$  multipath component,  $\tau_i$  for the relative delay,  $\alpha_i$  for the relative amplitude,  $\delta\tau$  is the time delay error,  $\phi_\epsilon$  is the phase error, R is the correlation function, d the correlator spacing and A the signal amplitude.

The discriminators that were presented in the previous chapter and are calculated as a function of the correlator outputs are biased by multipath propagation. The arctan discriminator in the presence of multipath can be written as (Braasch, 1996):

$$D_{phase} = \frac{Q_{prompt}}{I_{prompt}} = \frac{AR(\delta\tau)\cos(\phi_\epsilon) + A \sum_{i=1}^n \alpha_i R(\delta\tau - \tau_i)\sin(\phi_\epsilon + \Delta\Phi_i)}{AR(\delta\tau)\cos(\phi_\epsilon) + A \sum_{i=1}^n \alpha_i R(\delta\tau - \tau_i)\cos(\phi_\epsilon + \Delta\Phi_i)}, \quad (3.22)$$

The expression for the carrier phase error due to multipath can be derived by zeroing the discriminator (Irsigler, 2008) (i.e. setting the  $Q_{prompt}$  equal to zero):

$$AR(\delta\tau)\cos(\phi_\epsilon) + A \sum_{i=1}^n \alpha_i R(\delta\tau - \tau_i) \sin(\phi_\epsilon + \Delta\Phi_i) = 0. \quad (3.23)$$

By rearranging the above equation, assuming one MPC and solving for the phase error  $\phi_\epsilon$ , the phase error due one multipath component reads:

$$\phi_\epsilon = \arctan \left( \frac{\alpha R(\delta\tau - \tau) \sin(\Delta\Phi)}{R(\delta\tau) + \alpha R(\delta\tau - \tau) \cos(\Delta\Phi)} \right). \quad (3.24)$$

Looking at the previous equation, it can be remarked that the resulting error of the phase observations due to multipath is a function of the relative delay, relative amplitude and relative phase shift between the indirect and the direct signal components.

Eq. 3.24 is plotted for the evaluation of multipath error envelopes in fig. 3.13 given a certain relative delay in chips. The envelop in the left plot is computed for a relative amplitude  $\alpha = 0.8$  and in the right side plot for an  $\alpha = 0.3$ .

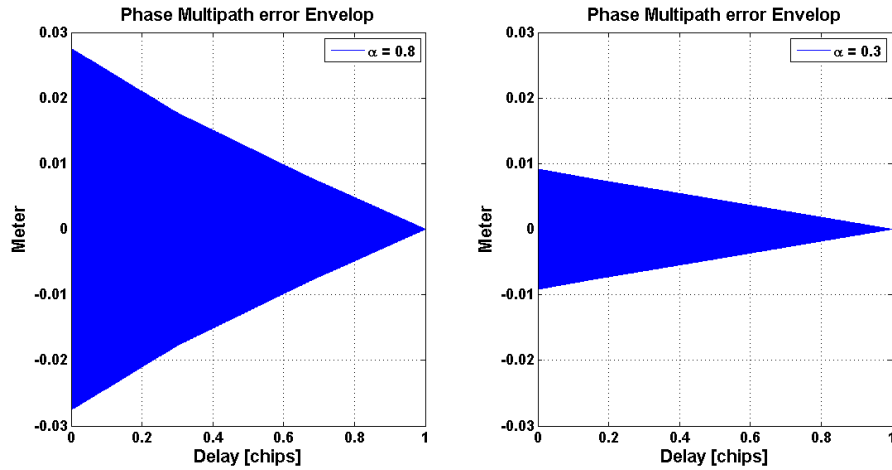


Figure 3.13.: Multipath phase error envelopes for a relative amplitude  $\alpha = 0.8$  (left side) and for a relative amplitude  $\alpha = 0.3$  (right side).

Assuming only very short delay multipath, of the order of 1 to 10 meters, and  $R(\delta\tau) \approx R(\delta\tau - \tau)$  the before mentioned equation, for one indirect signal component, can be further simplified as:

$$\phi_\epsilon = \arctan \left( \frac{\alpha \sin(\Delta\Phi)}{1 + \alpha \cos(\Delta\Phi)} \right). \quad (3.25)$$

The expression of the phase error due to multipath propagation of eq. 3.25 is used in different GNSS multipath related studies. One contribution of this work is to further generalize this expression by modelling the signal amplitude/power of both LOS and MP signal components. In this way multipath effects could be characterized in an epoch wise sense and for complete satellite arcs via realistic, simulated multipath signatures.

### 3.3.2. Two Ray Analysis

The expression of eq. 3.25 can also be derived from the vectorial representation of fig. 3.12. The correlation output of the prompt correlator in the presence of multipath can be visualized with the vectorial representation in fig. 3.14.

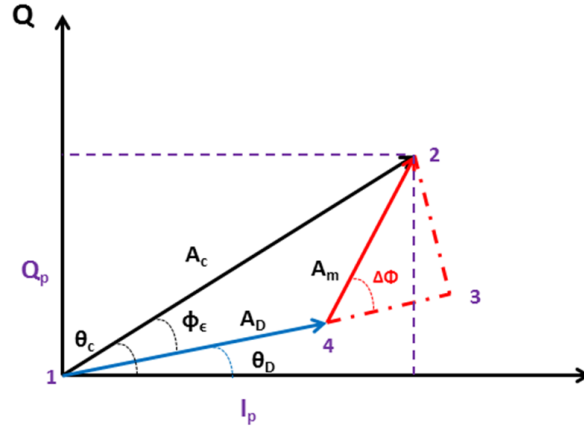


Figure 3.14.: Phase error of the PLL due to one multipath component in a vectorial representation.

Based on the correlation output of the prompt correlator, the receiver is tracking a compound signal which has a certain amplitude,  $A_c$ , and a certain phase  $\vartheta_c$ . The compound signal can be decomposed into the direct and indirect components. The direct (LOS) component is characterized by a certain amplitude,  $A_D$ , and phase,  $\vartheta_D$ . The multipath component has an amplitude  $A_m$  or relative to the direct, a relative amplitude which is equal to  $\alpha = \frac{A_m}{A_D}$  and a certain phase, relative to the phase of the direct signal,  $\Delta\Phi$ . Directly from this vector diagram, expressions for the amplitude of the compound signal  $A_c$  and the resulting phase error  $\phi_\epsilon$  can be derived as follows.

Assuming no noise and an infinite front-end bandwidth, the phase error,  $\phi_\epsilon$  is derived by the sides of the orthogonal triangle 123 as:

$$\tan(\phi_\epsilon) = \frac{\overline{23}}{\overline{14} + \overline{43}}. \quad (3.26)$$

Where  $\overline{14}$  is equal to the amplitude of the LOS phasor.  $\overline{23}$  is the opposite side of the triangle and  $\overline{14} + \overline{43}$  the adjacent side. By using a simple trigonometric function it can be shown that the  $\overline{23}$  side is equal to:

$$\overline{23} = A_m \sin(\Delta\Phi) = \alpha A_D \sin(\Delta\Phi), \quad (3.27)$$

and the  $\overline{43}$  side is equal to:

$$\overline{43} = A_m \cos(\Delta\Phi) = \alpha A_D \cos(\Delta\Phi). \quad (3.28)$$

Integrating eq. 3.27 and 3.28 into eq. 3.26, the expression for the phase error due to multipath can be derived as:

$$\tan\phi_\epsilon = \frac{\alpha A_D \sin(\Delta\Phi)}{A_D + \alpha A_D \cos(\Delta\Phi)}. \quad (3.29)$$

By rearranging eq. 3.29 and solving for the phase error  $\phi_\epsilon$  the expression for the phase error reads:

$$\phi_\epsilon = \arctan\left(\frac{\alpha \sin(\Delta\Phi)}{1 + \alpha \cos(\Delta\Phi)}\right). \quad (3.30)$$

An expression for the compound signal amplitude can also be derived from the vector diagram of fig. 3.14 as:

$$A_c^2 = (A_D + \overline{43})^2 + \overline{23}^2, \quad (3.31)$$

with  $\overline{43}$  and  $\overline{23}$  the sides of the 423 orthogonal triangle. Integrating eq. 3.27 and 3.28 into eq. 3.31 we have:

$$A_c^2 = (A_D + A_m \cos(\Delta\Phi))^2 + A_m^2 \sin^2(\Delta\Phi), \quad (3.32)$$

with  $A_m = \alpha A_D$  we have:

$$A_c^2 = (A_D + \alpha A_D \cos(\Delta\Phi))^2 + \alpha^2 A_D^2 \sin^2(\Delta\Phi), \quad (3.33)$$

$$A_c^2 = A_D^2 + 2\alpha A_D^2 \cos(\Delta\Phi) + (\alpha A_D \cos(\Delta\Phi) \cdot \alpha A_D \cos(\Delta\Phi)) + \alpha^2 A_D^2 \sin^2(\Delta\Phi), \quad (3.34)$$

the term in the parenthesis can be rearranged using trigonometric identities as:

$$(\alpha A_D \cos(\Delta\Phi) \cdot \alpha A_D \cos(\Delta\Phi)) = \alpha^2 A_D^2 \frac{1}{2} \cos(2\Delta\Phi) + 1. \quad (3.35)$$

by replacing  $\cos(2\Delta\Phi) = 2\cos^2(\Delta\Phi) - 1$  eq. 3.35 can be rewritten as:

$$\alpha^2 A_D^2 \frac{1}{2} 2\cos^2(\Delta\Phi) - 1 + 1 = \alpha^2 A_D^2 \cos^2(\Delta\Phi). \quad (3.36)$$

By replacing the term in the parenthesis of eq. 3.34 by eq. 3.36, eq. 3.34 can be rewritten as:

$$A_c^2 = A_D^2 + 2\alpha A_D^2 \cos(\Delta\Phi) + \alpha^2 A_D^2 \cos^2(\Delta\Phi) + \alpha^2 A_D^2 \sin^2(\Delta\Phi), \quad (3.37)$$

since  $\cos^2(\Delta\Phi) + \sin^2(\Delta\Phi) = 1$ , the well known equation for the compound signal amplitude for one multipath component reads:

$$A_c^2 = A_D^2 + 2\alpha A_D^2 \cos(\Delta\Phi) + \alpha^2 A_D^2, \quad (3.38)$$

or

$$A_c = A_D \sqrt{1 + 2\alpha \cos(\Delta\Phi) + \alpha^2}. \quad (3.39)$$

Looking at eq. 3.30 and 3.38 one may notice that when  $\Delta\Phi = 0^\circ/180^\circ$ ,  $A_c$  =maximum/minimum, while when  $\Delta\Phi = 90^\circ$  the phase error  $\phi_\epsilon$  is maximum. For a number of n multipath components, eq. 3.30 can be written as:

$$\phi_\epsilon = \arctan \left( \frac{\sum_{i=1}^n \alpha_i \sin(\Delta\Phi_i)}{1 + \sum_{i=1}^n \alpha_i \cos(\Delta\Phi_i)} \right), \quad (3.40)$$

The compound signal amplitude in the presence of  $k$  MPCs (see eq. 3.33) can be rewritten as:

$$A_c = A_D \sqrt{\left(1 + \sum_{i=1}^n \alpha_i \cos(\Delta\Phi_i)\right)^2 + \left(\sum_{i=1}^n \alpha_i \sin(\Delta\Phi_i)\right)^2}. \quad (3.41)$$

Some of the introduced equations can be approximated based on the geometry of the scenario, like e.g., the relative phase of a MPC,  $\Delta\Phi$ . Nevertheless, the reflection process itself and the receiving antenna will introduce additional phase shifts and, furthermore, they will have a direct impact on the resulting amplitude of both the direct and the indirect signal components. Thus, one contribution of this thesis is to further generalize the previously presented formulas by introducing compact expressions for the computation of the amplitude/power information.



## 4. Characterization of a Pseudo-satellite Multipath Scenario

In this chapter, the characterization of a multipath pseudolite scenario is presented. For the analysis of pseudolite data, dedicated navigation algorithms were developed. Data from the German maritime Galileo test bed, SEA GATE, were analysed in order to exploit the advantages as well as the drawbacks of such an infrastructure and characterize the overall multipath contamination at the PSL reference stations positions.

The analysis identified certain issues that should be further investigated in the future to exploit the full potentials of such an environment. One of the most crucial drawbacks of such an environment is the need of dedicated receivers that are able to track and demodulate the PSL signals. This need can cause a reduction of the potential users of such an infrastructure. On the other hand, PSL-based positioning in such localized environments can yield significant advantages for different navigation applications since the solution accuracy is higher when compared with the accuracy of a GNSS based solution. The main reason for this is the absence of ionospheric refraction.

Multipath effects in the PSL scenario under investigation are different when compared with the GNSS case. The transmitting and the receiving PSL antennas are static, and such biases are constant. Obstructions of the LOS caused by different moving objects in the region are identified in the residual analysis. Such effects are present in the PSL data sets due to the following reasons. The AoD of the PSL signals is near the horizon (i.e. near  $0^\circ$  elevation angle) and some of the moving objects (e.g. ships) are the largest objects in the area.

### 4.1. SEA GATE data processing

The German maritime Galileo test bed, SEA GATE, is located in Rostock harbour area. This marine Galileo test infrastructure consists of three segments. The transmitting segment (Sende-Segment), consists of nine PSLs that are transmitting Galileo like navigation signals. The control segment (Monitor- und Kontroll-Segment) consists of two reference stations (RS1 and RS2) that are continuously monitoring the system. Furthermore, they generate differential correction terms which are transmitted to the users and, therefore, acts also as a local area PSL-augmentation system. Finally, the user segment (Nutzer-Segment) consists of two receivers that are tracking the PSL signals on board of a ship. The ship Mecklenburg Vorpommern Fährschiff is using the PSL signals and the differential correction terms during the docking manoeuvres inside the harbour area. A critical analysis of PSL data that were captured on-board of Mecklenburg Vorpommern Fährschiff can be found in Schön *et al.* (2014).

In this chapter, the data analysis of the PSL and GPS data from the two reference stations is presented. The analysis is performed via dedicated matlab algorithms that were developed for this purpose. One goal of this analysis is the development of dedicated PSL data processing algorithms that can be expanded in the future and used for PSL investigation in different Gate environments.



Figure 4.1.: Rostock harbour area and Sea Gate infrastructure consisting of nine pseudolites (PSLs) and the two monitoring stations (RS1 and RS2). Adopted from Dietz *et al.* (2010)

## 4.2. Parameter Estimation and Least-squares theory

The method of least squares for estimating unknown parameters is based on minimizing the sum of the squares of the residuals (i.e. the deviations of the observations from their expected values). The PSL observation equation (like the GPS observation equation) that will be explained in the next section is not linear. Following the standard procedure for a least squares solution, a linearisation of the observation equations is performed in this case. More details for the Gauss Markov model and the linearisation process can be found in Koch (1999).

Let a system of linearised observation equations:

$$l + v = Ax, \tag{4.1}$$

where  $l$  is a vector containing the observables, often called the observed minus computed (OMC) vector with:

$$l = \hat{l} - f(x_0), \tag{4.2}$$

The inconsistencies between the model and the observations are expressed by means of the residual vector  $v$ .  $A$  is the design matrix containing the partial derivatives of the observation equations w.r.t. the unknowns and describes the relationship between the observations and the unknowns.  $x$  is the vector containing the unknowns.

The least squares criterion, states that the optimum estimate of the unknowns,  $\hat{x}$ , for  $x$  is the one that will minimize the sum of the squared residuals:



$$v^T v = (A\hat{x} - l)^T (A\hat{x} - l) = \text{minimum}. \quad (4.3)$$

When weights are associated with the observations, then the weight matrix  $P$  should also be included and the previous can be written as:

$$v^T P v = (A\hat{x} - l)^T P (A\hat{x} - l) = \text{minimum}. \quad (4.4)$$

In this case, the least squares criterion states that the optimal estimator for the unknowns  $x$  is the estimator that is minimizing the sum of the squares of the weighted residuals. The best estimate of  $x$  is found through the normal equations system (Koch, 1999) as:

$$\hat{x} = (A^T P A)^{-1} (A^T P l), \quad (4.5)$$

with the normal equation matrix  $N = A^T P A$  and the inverse of this matrix is the cofactor matrix  $Q_{xx} = (A^T P A)^{-1}$  which is used for the computation of the variance-covariance matrix ( $C_{xx}$ ) of the unknowns as:

$$C_{xx} = m_0^2 Q_{xx}, \quad (4.6)$$

with  $m_0$  the empirical variance of the unit weight being equal to:

$$m_0 = \sqrt{\frac{v^T P v}{n - u}}, \quad (4.7)$$

where  $n$  denotes the number of observations and  $u$  the number of unknowns. The number  $n - u$  is the redundancy or the number of degrees of freedom.

### 4.3. PSL Observational Model

The mathematical model for the PSL code observables is defined in a similar sense as GPS code observation equation:

$$P^{psl} = \rho_r^{psl} + c\delta t_r - c\delta t^{psl} + T + M + \epsilon_{P_{psl}}, \quad (4.8)$$

with

- $P^{psl}$  Pseudorange observation from a certain PSL at L1 frequency
- $\rho_r^{psl}$  Geometrical distance between the transmitting and receiving antennas
- $\delta t_r$  Receiver clock error
- $\delta t^{psl}$  Satellite clock error
- T Refraction caused by neutral atmosphere
- M Multipath effects
- $\epsilon_{P_{psl}}$  Code observation noise and remaining errors

The observation equation is not linear and a linearisation is needed in order to set up the design matrix  $A$ . For the modelling of the tropospheric refraction an empirical model from electronic distance measurements was adopted (Rüeger, 1996):

$$N = \frac{77.624}{273.15 + T} (P - e) + \frac{64.70}{273.15 + T} \left( 1 + \frac{5748}{273.15 + T} \right) e, \quad (4.9)$$

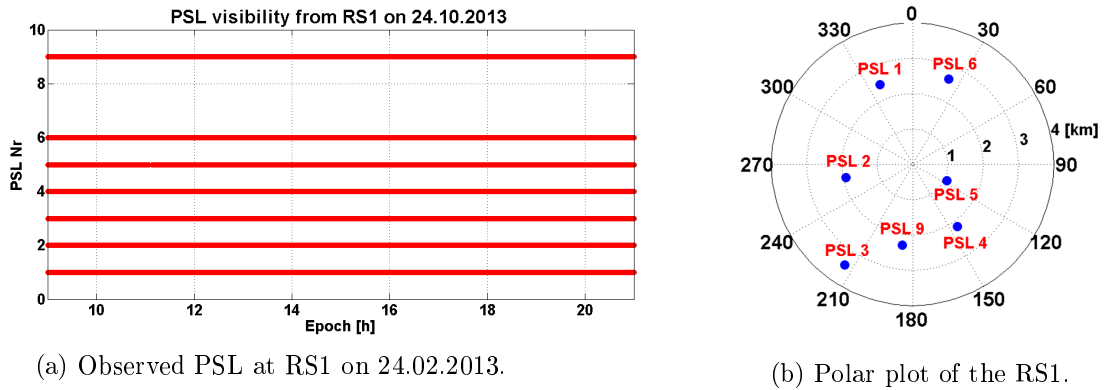
with the partial damp water vapour factor  $e$  equal to:

$$e = H0.0611 * 10^{\frac{7.5T}{237.3 + T}}, \quad (4.10)$$

with  $T$  the temperature in [ $^{\circ}\text{C}$ ],  $P$  the pressure in [mbar] and  $H$  the humidity. The parameter need for the empirical model were acquired from the meteorological file (.met file) of the Warnemünde IGS reference station located in the Rostock harbour area.

#### 4.4. Data Analysis from RS1 and RS2

The processed data were captured at RS1 and RS2 on 24.10.2013. PSL and GPS data were captured for an observation period of 12 hours. In fig. 4.2a and 4.3a the visibility plots of the observed PSLs are presented. Loss of tracking was observed only for PSL2 for 311 epochs during the whole observational period at RS1. PSL 7 was not active during the observational period while no data from PSL 8 were available at RS1. Data from PSL 8 were captured at RS2 for the same observational period. Loss of lock at RS2 was observed for PSL2 (111 epochs) and for PSL5 (213 epochs). The data rate of the processed data is 1 sec. Fig. 4.2b and 4.3b are the polar plots of the PSLs as observed from RS1 and RS2.



(a) Observed PSL at RS1 on 24.02.2013.

(b) Polar plot of the RS1.

Figure 4.2.: Visibility and polar plots of the observed PSLs on 24.02.2013 from RS1.

RS1	Elevation [ $^{\circ}$ ]	Azimuth [ $^{\circ}$ ]	Distance [m]
PSL1	0.861	337.826	2442.570
PSL2	-0.215	258.862	1925.176
PSL3	-0.135	213.930	3436.087
PSL4	1.894	144.342	2180.106
PSL5	1.500	115.307	1068.831
PSL6	1.081	22.907	2628.126
PSL9	0.777	187.119	2305.544

Table 4.1.: Elevation, azimuth and distance of the observed PSLs relative to RS1.

In table 4.1 and 4.2 an overview of the spherical coordinates and the distance of the PSLs relative RS1 and RS2 are presented. One may notice that the transmitting antennas are placed almost on the

same plane (i.e. the elevation all observed PSLs is about  $1^\circ$ ). This difficult geometry results in very high GDOP values and thus, the precision of the 3D positioning is very low (i.e. estimated coordinate differences are of the order of 100 m). Nevertheless, a 2D solution is possible and such information is sufficient for marine navigation applications since nautical charts are 2D charts.

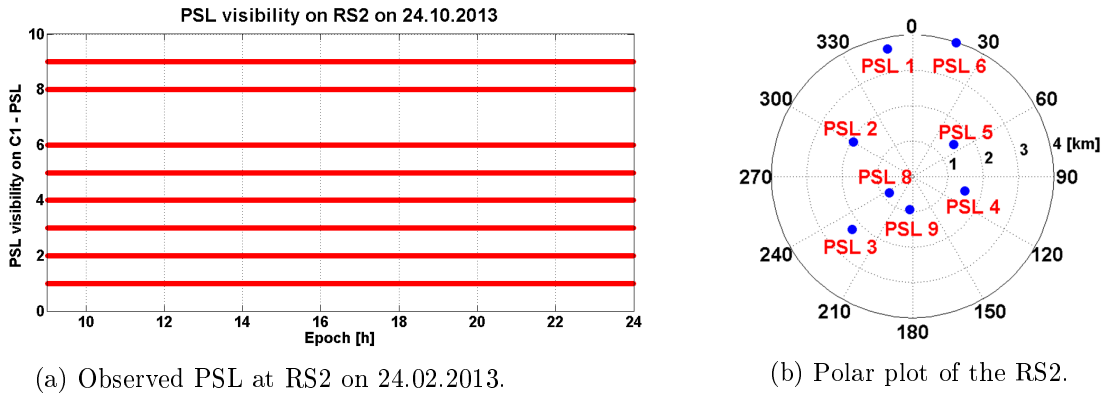


Figure 4.3.: Visibility and polar plots of the observed PSLs on 24.02.2013 from RS2.

RS2	Elevation [°]	Azimuth [°]	Distance [m]
PSL1	0.640	348.819	3683.089
PSL2	-0.064	300.223	1945.614
PSL3	-0.065	228.750	2274.566
PSL4	2.880	105.827	1538.194
PSL5	1.278	52.684	1476.136
PSL6	0.779	18.067	3967.798
PSL8	0.970	234.676	797.406
PSL9	2.233	184.753	940.190

Table 4.2.: Elevation, azimuth and distance of the observed PSLs relative to RS2.

In parallel to the PSL data recording, GPS data were also captured at both reference stations. In the visibility plots (fig. 4.4) for C/A code (C1) observables it can be seen that loss of lock or data gaps (red cycles) had occurred for almost all observed PRNs during the observational period and this is an indication of poor signal quality.

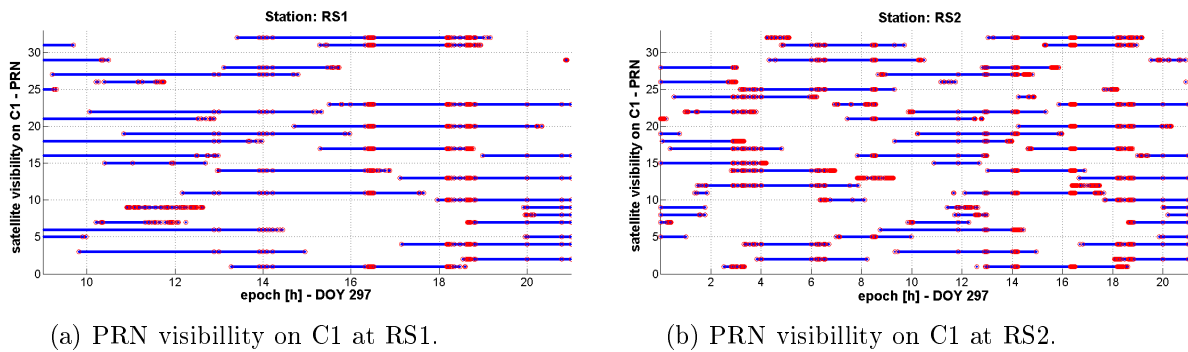
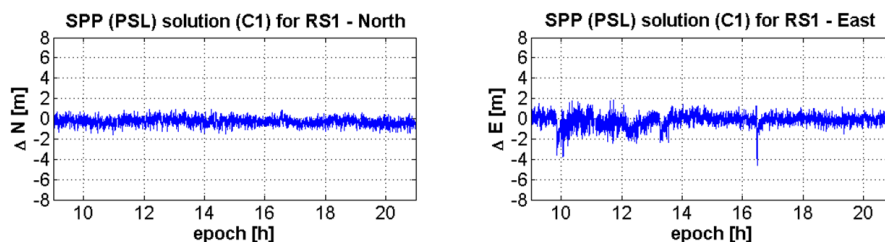


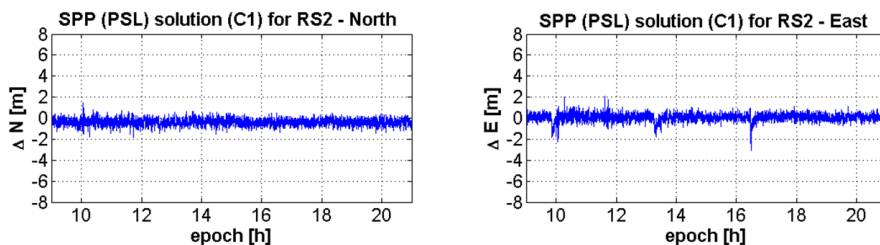
Figure 4.4.: Observed GPS satellites at RS1 and RS2 on 24.02.2013.

#### 4.4.1. SPP Pseudolites versus GPS

For the processing of the PSL data, a dedicated SPP algorithm was developed. The resulting HDOP from the PSL data at RS1 and RS2 is of the order of 2.2. Fig. 4.5 shows the estimated coordinate differences for RS1 (fig. 4.5a) and RS2 (fig. 4.5b). The coordinate differences between the nominal coordinates of RS1 and the estimated ones are of the order of 0.5 meters for the North component and slightly worse for the East component. The estimated precision for the coordinate differences at RS2 is of the same order of magnitude. The resulting and averaged for the whole observational period standard deviation for the north component is 0.35 m and for the east component is 0.45 m for both reference stations.

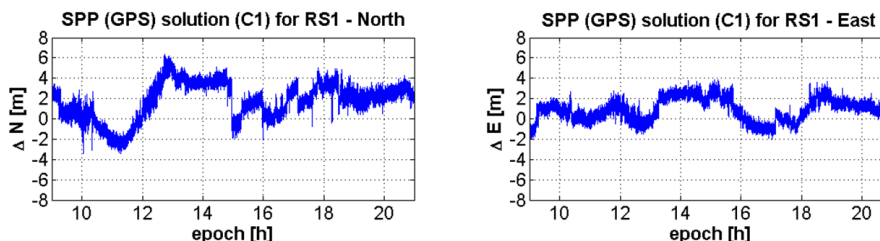


(a) SPP from pseudolite (C1) for RS1.

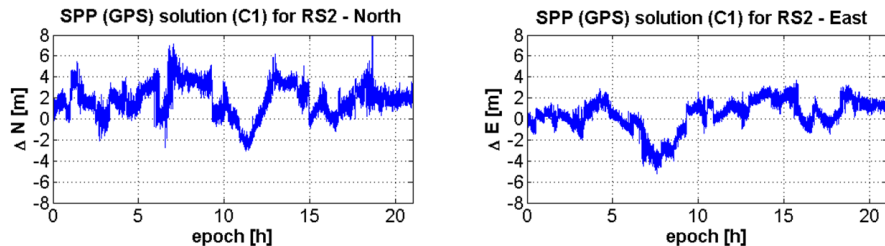


(b) SPP from pseudolite (C1) for RS2.

Figure 4.5.: PSL C1 2D solution. Estimated coordinate differences for RS1 and RS2 on 24.02.2013.



(a) SPP from GPS (C1) for RS1.



(b) SPP from GPS (C1) for RS2.

Figure 4.6.: GPS C1 2D solution. Estimated coordinate differences for RS1 and RS2 on 24.02.2013.

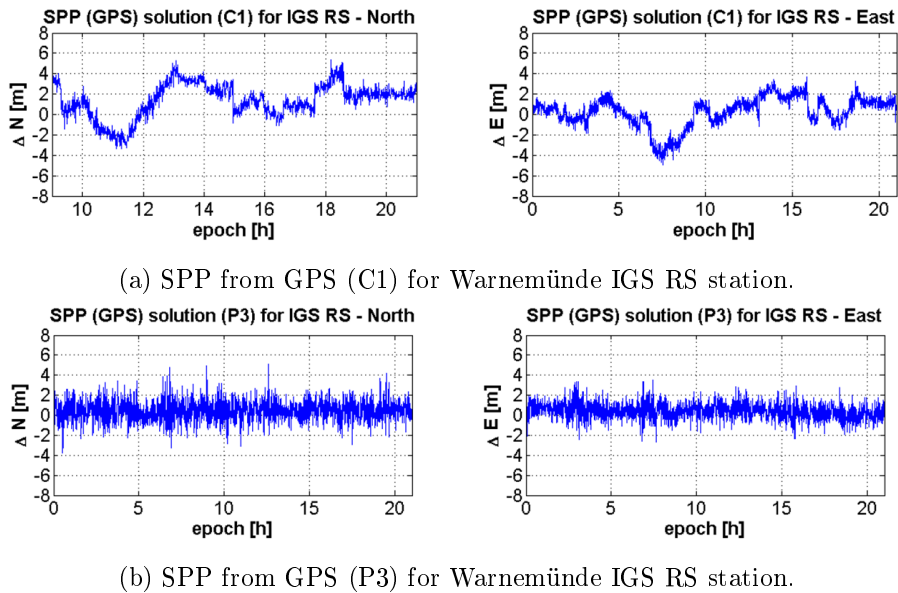


Figure 4.7.: GPS C1 and P3 2D solutions. Estimated coordinate differences for Warnemünde IGS RS station on 24.02.2013.

In fig. 4.6 the GPS C1 code-based solution is plotted for RS1 (fig. 4.6a) and for RS2 (fig. 4.6b). The solution is estimated in an epoch wise sense. The strong signature which can be seen in the plotted time series are attributed to strong ionospheric activities. To cross-check this hypothesis, the SPP solution of the nearby IGS reference station (Warnemünde in Rostock harbour area) was also estimated. In fig. 4.7a it can be noticed that a similar signature is present in the estimated coordinate time series. The ionosphere-free linear combination of code observables (P3) was formed and the P3 SPP solution for the IGS reference station was estimated. In fig. 4.7b the P3 solution is plotted where the impact of the ionosphere is eliminated and this confirmed our hypothesis of ionospheric refraction. Unfortunately, such a solution cannot be estimated for RS1 (or RS2), since only single frequency data are available. Mainly, due to the absence of ionospheric refraction, from the PSL data, a more precise 2D solution is possible when comparing with code-based single frequency GPS SPP. Furthermore, when the ionospheric free LC is formed, for the reduction of the impact of ionosphere, the resulted noise level is higher when compared to the PSL solution.

#### 4.4.2. Residuals of the PSL Code-phases

An-modelled error sources (e.g. multipath) are present in the residuals of the observations and can be identified. The overall goal of this investigation is to develop dedicated algorithms for PSL data analysis. The residual analysis can be used for characterizing the multipath contamination at RS1 and RS2. This characterization is useful since these two stations are used for monitoring purposes of the whole system. Moreover, they are used for the generation of differential correction terms that are then transmitted to the user in order to further augment PSL positioning when ships are docking in the harbour area.

In fig. 4.8 and fig. 4.10, the residuals of the observations are plotted for RS1 and RS2. In fig. 4.9 and fig. 4.11 the residuals of the observations from both reference stations are illustrated in boxplots. The central red line in the boxes of these figures marks the median of the time series and the blue boxes are the 25th and 75th percentiles. The black lines represent the entire data range. Thus, they represent the maximum and minimum distributions. Lastly, the red crosses represent individual outliers present in the data set. In fig. 4.9, the seventh both represent the residuals from PSL 9 and in fig. 4.11 the seventh and eighth boxes represent the residuals from PSL 8 and PSL 9 respectively.

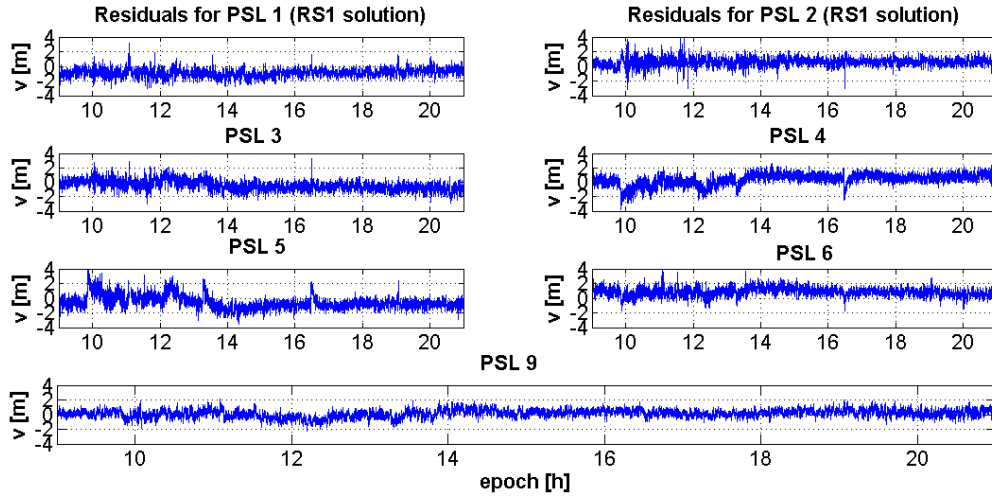


Figure 4.8.: Residuals of the PSL code-phases at RS1.

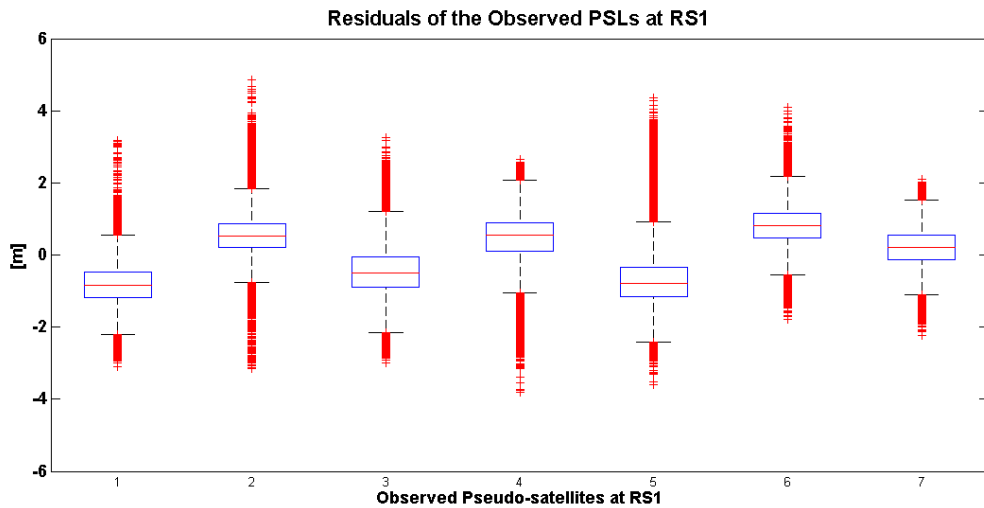


Figure 4.9.: Boxplot of the residuals of the PSL code-phases at RS1.

Looking at the boxplots for both reference stations it can be noticed that most of the outliers are present in the residuals of PSL2, PSL4 and PSL5. This can be noticed in the plotted time series of the residuals in fig. 4.8 and fig. 4.10 also. According to the observation equation (i.e. eq. 4.8) the only un-modelled error source present in the observations is multipath. Constant multipath components during the whole observational period would result in a constant shift of the residual time series (i.e. fixed offset bias) since both the receiving and transmitting antennas are located in fixed positions. Therefore, the different spikes present in fig. 4.8 and fig. 4.10 are attributed to strong reflections and/or obstructions of the LOS between the two RSs and the observed PSLs from moving objects (e.g. trains, ships, cranes) in the harbour area.

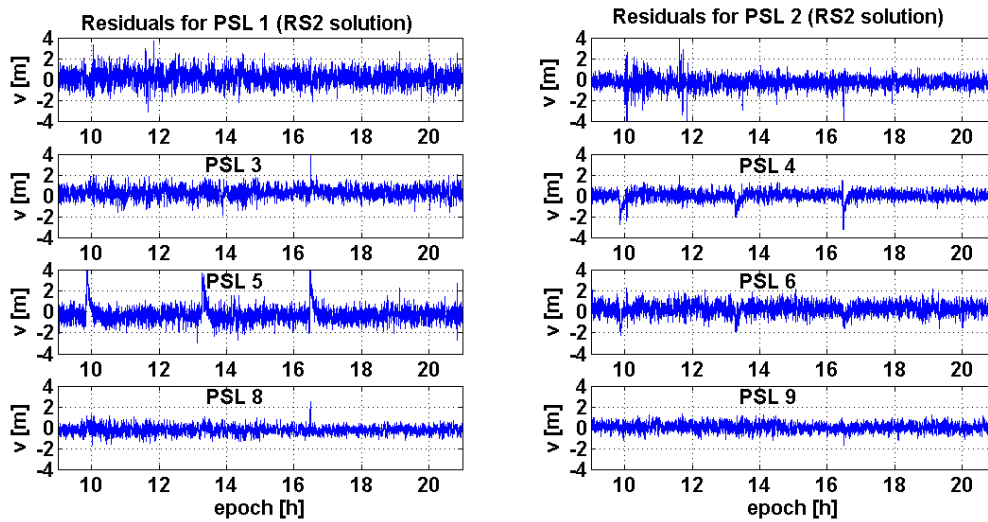


Figure 4.10.: Residuals of the PSL code-phases at RS2.

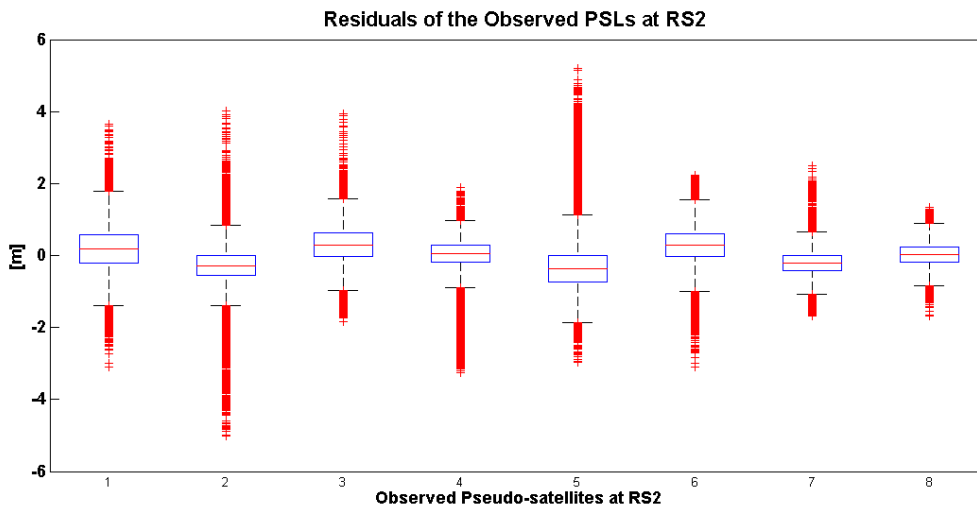


Figure 4.11.: Boxplot of the residuals of the PSL code-phases at RS2.

A comparison between the residuals of the observations at RS1 and RS2 indicates that the impact of multipath and/or shadowing is different at the two reference station locations. The different impact of multipath effects is something that is expected, since multipath effects are station specific biases and the over all multipath contamination is dependent on the physical environment in which the antenna is placed. Furthermore, from the residuals of RS1 and RS2 it is clearly visible that PSL 2, PSL 5 and PSL 4 are mostly biased since obstructions of the line-of-sight between these three PSLs and the two reference stations have repeatedly occurred during the observational period. Moreover looking at the time series of the computed residuals for both reference stations, it can be seen that after 17:00 GPS time (i.e. 18:00 local time) such effects are not so often present in the time series and the residuals for all observed PSL are rather smooth. Due to the previous we attribute the multipath effects to construction work that took place in the area enclosed by RS1, RS2, PSL 4 and PSL 5 as well as other activities that are taking place during the working hours (e.g. railway activities). In the case of PSL 2, obstruction effects are, most probably, caused by ships docking in the harbour area between the PSL

2 and the two reference stations.

## 4.5. Discussion

In this chapter, an analysis of PSL data from the German maritime Galileo test bed, SEA GATE, which is located in Rostock harbour area was presented. For the analysis of the PSL data, dedicated positioning algorithms were developed.

In summary, our analysis identified certain issues that should be further investigated in the future to exploit the full potentials of such an environment. Some of the issues are commonly occurring when PSL signals are utilized. On the other hand, PSL-based positioning in such localized environments yields significant advantages for different navigation application since the solution accuracy is higher than the navigation solution with GNSS signals. The main reason for this is the absence of ionospheric refraction which is the largest error source in (outdoor) navigation applications.

The overall multipath contamination of data captured by the two reference stations was examined. In the scenario under investigation, both the transmitting and the receiving antennas are static and such biases, when the reflector is also static, are constant. In contrast, such effects for satellite signals will not be constant. Nevertheless, obstructions of the LOS caused by different objects moving in the region are causing a further degradation of the positioning solution. Many of the large ferries that are moving within the harbour area are much larger than any other contraction in the area (e.g. buildings). Furthermore, the AoA of the PSL signals w.r.t. the receiving antennas are near to  $0^\circ$  and in some cases even negative elevation angles are identified.

Further expansion of the developed algorithms should include integrity monitoring since this is very critical for ship navigation and docking inside a harbour area. Last but not least, a combined PSL-GNSS solution can also be included in a future expansion.



## 5. On the Impact of Different $C/N_0$ Estimation Algorithms

In the following chapter of this thesis, the  $C/N_0$  observables are characterized and simulated without considering the impact of the receiver in the process. In this chapter, an investigation is described to characterize whether the receiver and the different  $C/N_0$  estimation algorithms utilized for the estimation of these GNSS observables have an impact on them. This investigation shows that this GNSS observable may slightly vary between different receivers. In the resulting estimated  $C/N_0$  time series from four different estimation algorithms, various linear trends were identified.

### 5.1. Introduction

In order to characterize the impact of the receiver on the resulting  $C/N_0$  observables, an experiment was conducted on the rooftop of the geodetic institute of the university of Hannover. The rooftop environment is illustrated in fig. 5.1 and the red circle indicate the pillar on which the receiving antenna was mounted. One hour data sets were captured on two different observational days. The experimental set up consist of a Leica AX1202GG antenna which was connected to a splitter where two geodetic receivers were connected (a Leica GX1230 GG and a Javad G3T Delta) for data recording. In parallel, IF raw GNSS signal was also recorded with a Nord Nav software receiver. The experimental set-up and the receiving antenna can be seen in fig. 5.2.

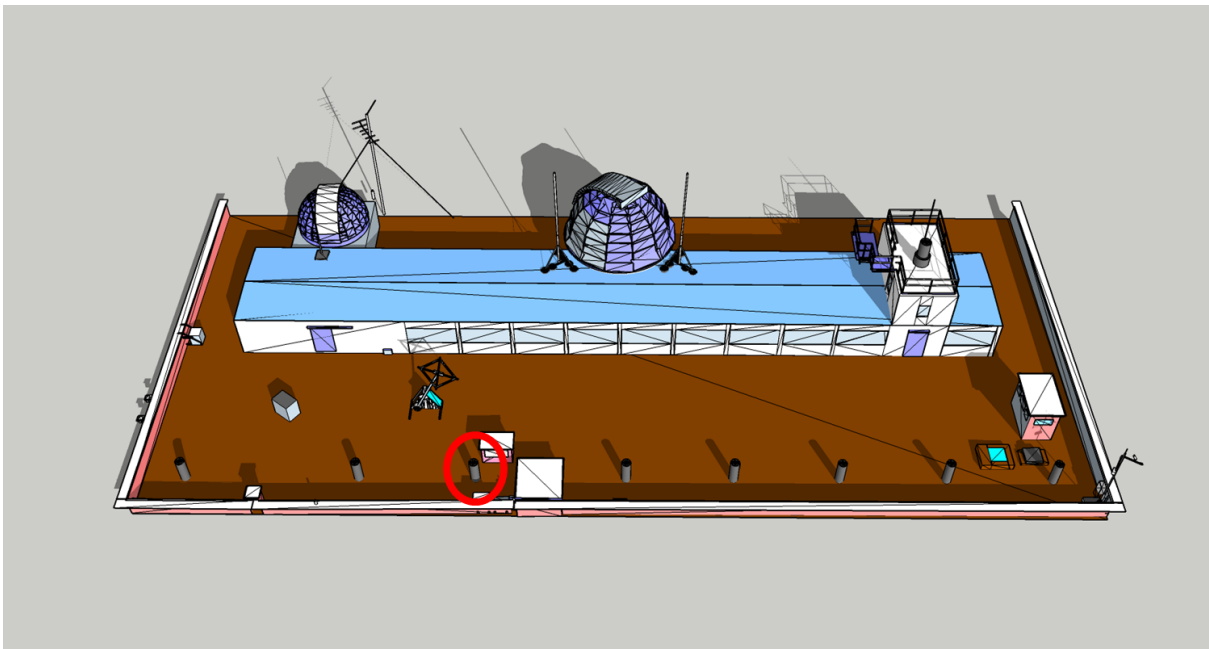


Figure 5.1.: The rooftop environment of the geodetic institute of the university of Hannover.

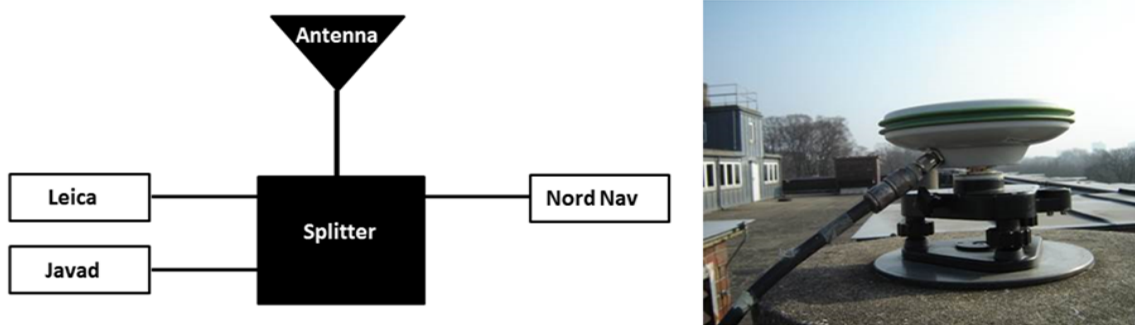


Figure 5.2.: Experimental set-up and receiving antenna of the GIH rooftop experiment.

## 5.2. Sidereal Repeatability of GNSS Ground Tracks

As mentioned in the introductory section, two geodetic receivers were mounted on the same antenna, and they recorded GNSS data in parallel on two different observational days. In a first step, the observed  $C/N_0$  values will be used for the computation of the repetition time of the GPS satellites. In a second step, the time series of the different receivers and observational days will be plotted together to characterize the impact of the different receivers in the signal strength observables.

It is known that the GPS satellites repeat their ground track after one sidereal day (i.e.  $23^h$  and  $56^{min}$ ) and will rise above the local horizon about 4 min earlier each day. Strictly speaking, each GPS satellite has its own repetition time that deviates, slightly, from this nominal repetition period. In Agnew and Larson (2007) two different approaches are presented for the calculation of the repeat time of the GPS satellite orbits. The one is using the orbital period and the other the topocentric positions of the satellites (Agnew and Larson, 2007). In our case, we will use the repetition of the multipath signatures present in the captured  $C/N_0$  data on the different observational days for the computation of the repeat time of the satellite tracks.

In a very straightforward way, the repeat time is computed by firstly de-trending the time series and, in a second step, by cross-correlating the time series from the different observational days. Thus, we can identify the epoch, in each observational day, where the correlation value is maximum. In fig. 5.3 the observed  $C/N_0$  time series on two different observational days and by two different geodetic receivers are illustrated. Eight exemplary PRNs are visualized in this plot. In table 5.1 an overview of the repeat time of all observed PRNs is presented. The plots are generated after the exact repeat time of each PRN is computed and, thus, one can notice how the multipath signatures in the data also repeat after three sidereal days. The different quantization levels of the two receivers can also be noticed. For the Leica GX1230 GG receiver the quantization levels is 0.1 dB and for the Javad G3T Delta is 0.25 dB. Moreover, it can be seen in these plots that the time series from the different receivers deviate from each other. Apart from the different signal strength levels (the signal strength with Javad receive is, in general, higher), different trends can be noticed. These trends, for each receiver, are repeating on the different observational days.

To validate if these differences are occurring due to the different algorithms used by the different receivers for the estimation of the  $C/N_0$  observables, the raw IF GNSS signal that was recorder in parallel will be used. Thus, in a next step, different  $C/N_0$  estimation algorithms will be implemented in software to characterize their impact on the GNSS signal strength observables.

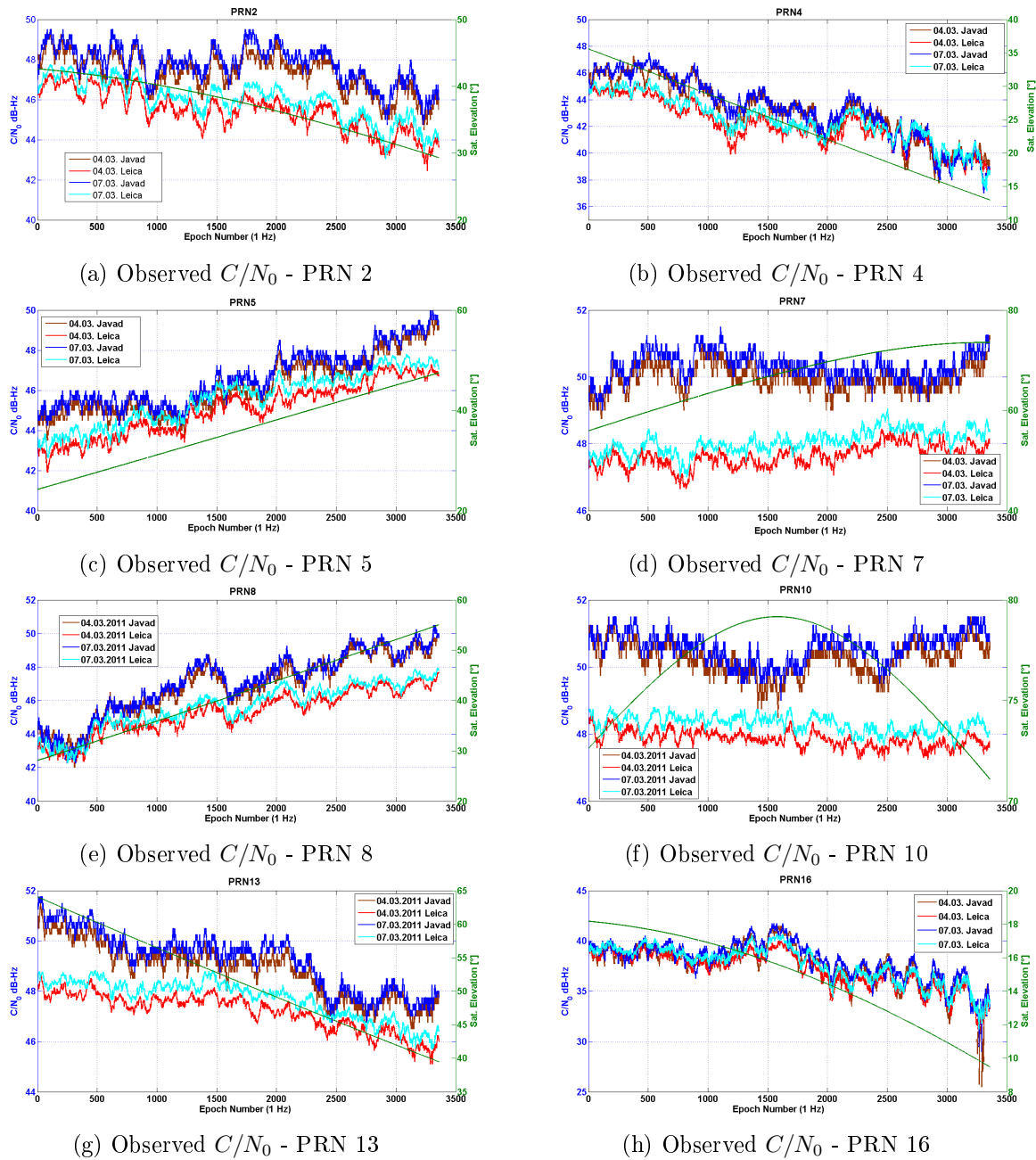


Figure 5.3.: Sidereal repeatability of multipath fading as observed by two geodetic receivers (04.03.2011 and 07.03.2011).

### 5.3. I and Q Data Analysis

IF raw GNSS signal was recorded in parallel to data capture with the Nord Nav software receiver. The major advantage of such receivers is that the raw signal can be replayed and reprocessed with different receiver configurations. This is a major advantage of software receivers that can give users additional flexibility. On the other hand, the size of the raw signal records/files can be rather big (e.g. several gigabytes for 1 hour of raw signal record) and this increases the storage needs and the processing capacity for such data files.

In this case, the free-ware software receiver by Borre *et al.* (2007) was used and modified for the reprocessing of the recorded raw GNSS signal captured by the Nord Nav receiver. The algorithm was modified in order to track GNSS signal with longer, than 1 msec, integration intervals. Furthermore,

PRN	Day 1	Start Time	End Time	Day 2	Start Time	End Time
PRN2	04.03.2011	14:21:51	15:17:48	07.03.2011	14:09:15	15:05:12
PRN4	04.03.2011	14:21:51	15:17:48	07.03.2011	14:09:23	15:05:20
PRN5	04.03.2011	14:21:51	15:17:48	07.03.2011	14:09:22	15:05:19
PRN7	04.03.2011	14:21:51	15:17:48	07.03.2011	14:09:32	15:05:29
PRN8	04.03.2011	14:21:51	15:17:48	07.03.2011	14:09:18	15:05:15
PRN10	04.03.2011	14:21:51	15:17:48	07.03.2011	14:09:33	15:05:30
PRN13	04.03.2011	14:21:51	15:17:48	07.03.2011	14:09:44	15:05:41
PRN16	04.03.2011	14:21:51	15:17:48	07.03.2011	14:09:47	15:05:44
PRN23	04.03.2011	14:21:51	14:58:02	07.03.2011	14:09:18	14:48:29
PRN26	04.03.2011	14:45:54	15:14:14	07.03.2011	14:36:38	15:01:58
PRN29	04.03.2011	14:21:51	15:13:42	07.03.2011	14:36:38	15:01:58

Table 5.1.: Sidereal repeatability (GPS time) of the observed PRNs.

based on the post correlation outputs, different  $C/N_0$  estimation algorithms were implemented. Namely, the narrow-wide band power ratio (Sharawi *et al.*, 2007), the squared signal-to-noise variance estimator (Sharawi *et al.*, 2007), the differential estimator (Pany and Eissfeller, 2006) and squaring estimator (Pany and Eissfeller, 2006) were implemented in software.

### 5.3.1. Narrow-Wide Band Power Ratio Estimator

The power ratio method (Sharawi *et al.* (2007), Parkinson and Spilker (1996a)) is commonly used method in GNSS literature. This approach is used in different publications like e.g. Sharawi *et al.* (2007), Pini *et al.* (2008) for different type of applications. The power ratio or wide to narrow ratio estimator involves the comparison of the power of two different bandwidths in order to estimate the  $C/N_0$  of the captured signal. Based on the I and Q correlation outputs, the wide band power (WBP) is formed as:

$$WBP_k = \sum_{i=1}^M (I^2 + Q^2), \quad (5.1)$$

with  $i$ , the correlation output.  $M$  is having a maximum value of 20 when the integration time is 1 msec. The narrow band power (NBP) can be computed as:

$$NBP_k = \left( \sum_{i=1}^M I \right)^2 + \left( \sum_{i=1}^M Q \right)^2. \quad (5.2)$$

The ratio of eq. 5.2 to eq. 5.1 yields an estimate of the noise power at each epoch as:

$$NP_k = \frac{NBP}{WBP}. \quad (5.3)$$

Estimate of the expected noise power value is the average of eq. 5.4 with the output rate  $M$ :

$$\mu_{NP} = \frac{1}{h} \left( \sum_{k=1}^h NP \right). \quad (5.4)$$

Finally, the  $C/N_0$  observable is given as (Parkinson and Spilker, 1996a):

$$C/N_0 = 10 \log_{10} \left( \frac{1}{T} \frac{\mu_{NP} - 1}{M - \mu_{NP}} \right), \quad (5.5)$$

where  $T$  is the integration interval. In fig. 5.4 the estimated  $C/N_0$  time series with the power ratio estimator is illustrated for four exemplary observed PRNs. For the estimation, an integration time of 1 msec was utilized.  $M$  was set to 20, and  $h$  was set to 50. Thus the algorithm's output rate of the  $C/N_0$  observables is 1 Hz. A 30 min IF signal record was processed for the generation of fig. 5.4.

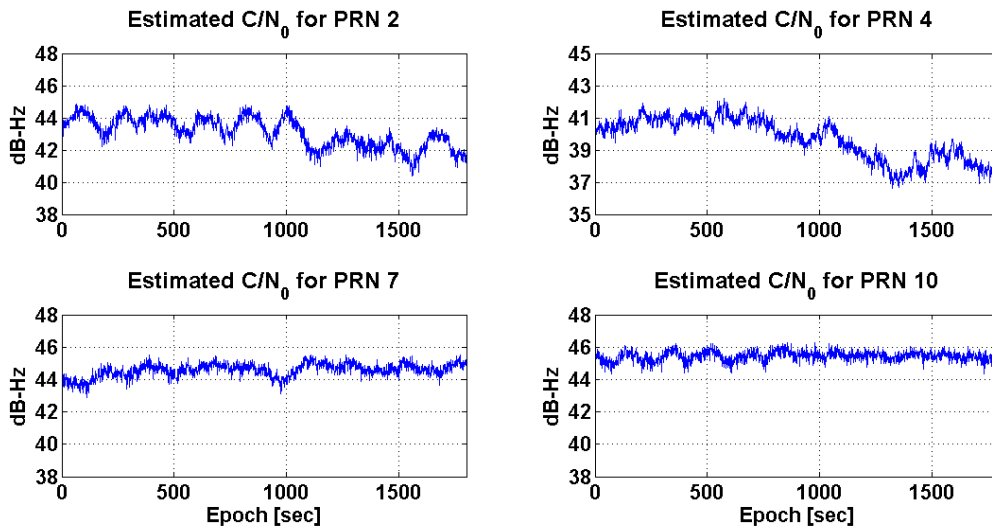


Figure 5.4.: Estimated  $C/N_0$  time series by the power ratio estimator for four exemplary PRNs and 30 min IF signal record. The observables are estimated with 1 sec interval.

### 5.3.2. Variance Summing Estimator

The variance summing method for the estimation of the  $C/N_0$  observable is, as the power ratio method, a low complexity and easy to implement method. This approach is described in several paper like e.g. Sharawi *et al.* (2007), Pini *et al.* (2008) and Falletti and Presti (2011). The  $Z$  samples of the times series used for the signal strength computation is found as (Sharawi *et al.*, 2007):

$$Z = (I^2 + Q^2), \quad (5.6)$$

with the mean of the sample time series equal to:

$$\bar{Z} = \frac{1}{k} \sum_{1}^k Z, \quad (5.7)$$

with  $k$ , the number of samples used for the estimation rate of the  $C/N_0$  observables. The variance is equal to:

$$\sigma_Z^2 = \frac{1}{k-1} \sum_1^k Z - \bar{Z}. \quad (5.8)$$

The average carrier power (ACP) is given by:

$$ACP = \sqrt{\bar{Z}^2 - \sigma_Z^2}, \quad (5.9)$$

and the variance of the noise accumulation term for the I and Q noise components is computed as (Sharawi *et al.*, 2007):

$$\sigma_{IQ}^2 = \frac{1}{2} \left( \bar{Z} - \sqrt{\bar{Z}^2 - \sigma_Z^2} \right). \quad (5.10)$$

Finally the  $C/N_0$  observables are given by:

$$C/N_0 = 10 \log_{10} \left( \frac{\sqrt{\bar{Z}^2 - \sigma_Z^2}}{2T\sigma_{IQ}^2} \right), \quad (5.11)$$

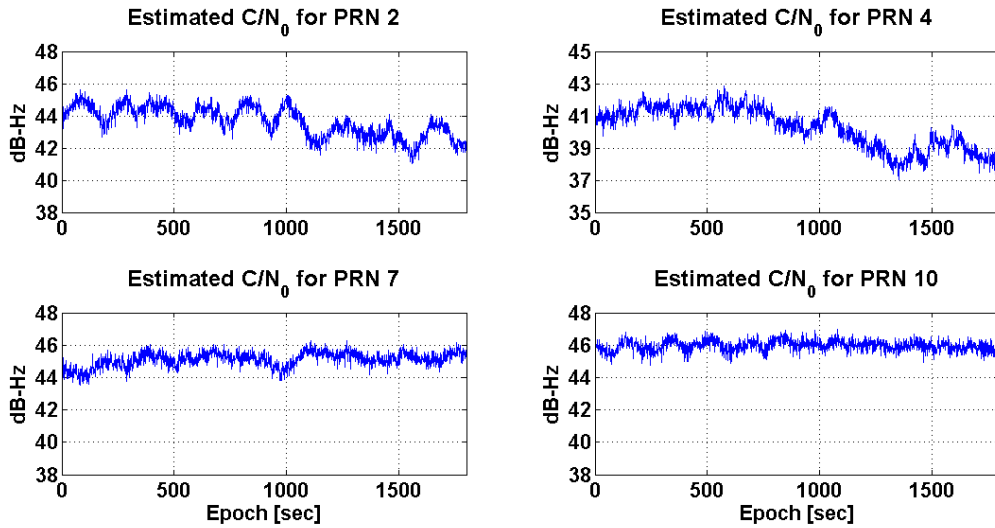


Figure 5.5.: Estimated  $C/N_0$  time series by the variance summing estimator for four exemplary PRNs and for 30 min IF signal record

with  $T$  the integration period. In fig. 5.5 the estimated  $C/N_0$  time series with the power ratio estimator is illustrated for four exemplary observed PRNs. For the estimation, an integration time ( $T$ ) of 1 msec was utilized. The number of samples ( $k$ ) that were used for the generation of the plot is 1000, which corresponds to 1 Hz data rate. A 30 min IF signal record was processed for the generation of fig. 5.5.

### 5.3.3. Squaring and Differential Estimators

The squaring and the differential estimators are described in Pany and Eissfeller (2006). These  $C/N_0$  estimators can be used in low signal power levels (Pany and Eissfeller, 2006) and their implementation is more complex when compared to the previously presented algorithms. The increase in the implementation complexity is mainly due to a scaling factor that is involved in these methods. For the

calibration of the scaling factor  $\alpha$  the evaluation of the prompt correlator of a channel where no signal is present is utilized.

For squaring estimator method, the  $C/N_0$  observables are estimated as the expected values of (Pany and Eissfeller, 2006):

$$\langle \Xi_{square} \rangle = \frac{1}{2\alpha^2 TM} \left( \sum_{j=1}^M |P_j^2| - 2M\alpha^2 \right), \quad (5.12)$$

with T is the accumulation interval, M is the rate time and thus the average total time is  $T_{total}=TM$ . P is the prompt correlator and  $\alpha$  is the noise calibration factor:

$$\alpha^2 = \frac{1}{2K} \left\langle \sum_{j=1}^K |P_j^2| \right\rangle, \quad (5.13)$$

with K is the number of prompt correlators used for the computation. The variance is calculated as (Pany and Eissfeller, 2006):

$$\langle (\Xi_{square} - \langle \Xi_{square} \rangle)^2 \rangle = \frac{1}{T^2 M} (1 + 2C/N_0 T). \quad (5.14)$$

The  $C/N_0$  observables are given by:

$$C/N_0 = 10 \log_{10}(\Xi_{square}). \quad (5.15)$$

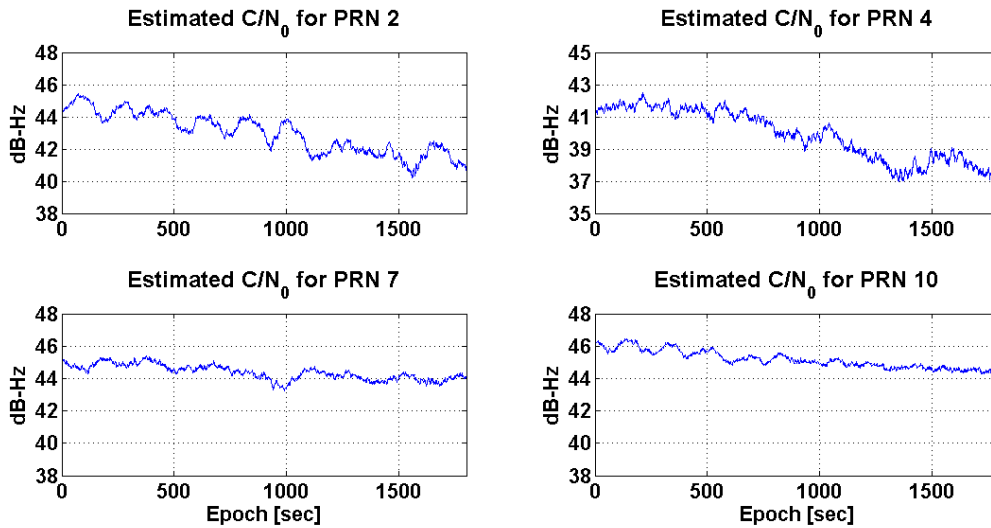


Figure 5.6.: Estimated  $C/N_0$  time series by the squaring estimator for four exemplary PRNs and for 30 min IF signal record.

In fig. 5.6 the estimated  $C/N_0$  time series with the power ratio estimator is illustrated for four exemplary observed PRNs. For the estimation, an integration time of 1 msec was utilized and M is set to 1000 so that the output rate of the observables is 1 Hz. A 30 min IF signal record was processed for the generation of fig. 5.6.

The differential estimation is computed by multiplying two consequent prompt correlators belonging to the same navigation data bit and averaging the real part of the product (Pany and Eissfeller, 2006) as:

$$\langle \Xi_{diff} \rangle = \frac{1}{2\alpha^2 TM} \sum_{j=1}^M \text{Re}\{P_j \bar{P}_{j+1}\}, \quad (5.16)$$

where  $\alpha$  is the scaling factor. The variance as (Pany and Eissfeller, 2006):

$$\langle (\Xi_{diff} - \langle \Xi_{diff} \rangle)^2 \rangle = \frac{1}{2T^2 M} (1 + 2C/N_0 T). \quad (5.17)$$

The  $C/N_0$  observables are given by:

$$C/N_0 = 10 \log_{10}(\Xi_{diff}). \quad (5.18)$$

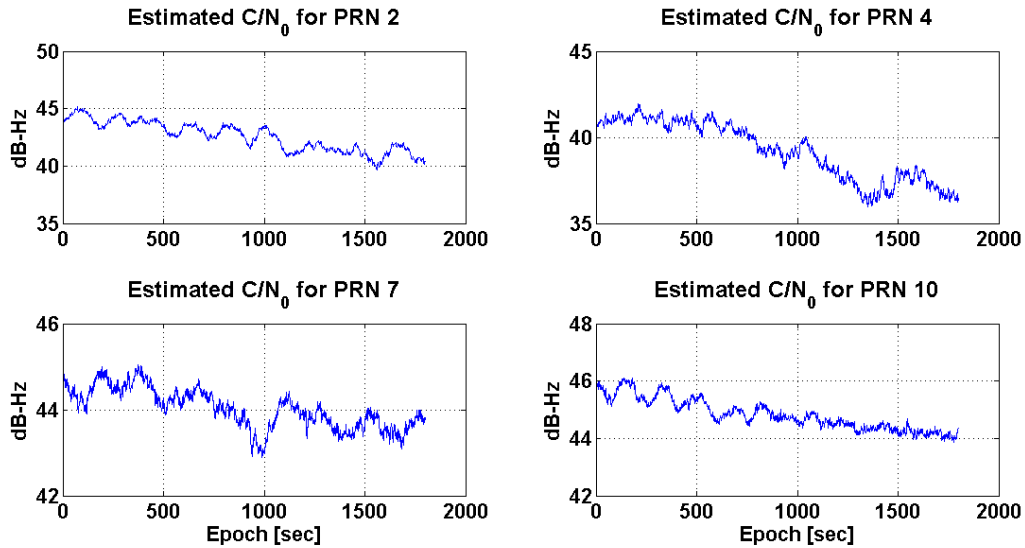


Figure 5.7.: Estimated  $C/N_0$  time series by the differential estimator for four exemplary PRNs and for 30 min IF signal record.

In fig. 5.8 the estimated  $C/N_0$  time series with the power ratio estimator are illustrated for four exemplary observed PRNs. For the estimation, an integration time of 1 msec was utilized and  $M$  was set to 1000 which correspond to 1 Hz rate. A 30 min IF signal record was processed for the generation of fig. 5.8.

## 5.4. Comparison of Different Algorithms

In fig. 5.8, the estimated  $C/N_0$  time series for the four different estimation algorithms are plotted together for four observed PRNs. The duration of the IF signal record is 30 min. In blue color is the resulting  $C/N_0$  values estimated with the narrow-wide band power ratio estimator, in red with the variance summing estimator, in black with the differential estimator and in green color with the squaring estimator.



Multipath fading behaviour is identical between the different algorithms for all PRNs. The noise level of the NWPR and VSE algorithms is higher than for the differential and the squaring estimators. One reason for this is the scale factor and the calibration process that is required for the implementation of the differential and squaring estimators. An overview of the minimum and maximum power levels of the different estimators and PRNs can be seen in tables 5.2 and 5.3. For the estimation of the  $C/N_0$  time series of fig. 5.8 the correlation outputs of the prompt correlator with 1 msec integration time were used. The  $C/N_0$  observables are estimated with 1 Hz rate.

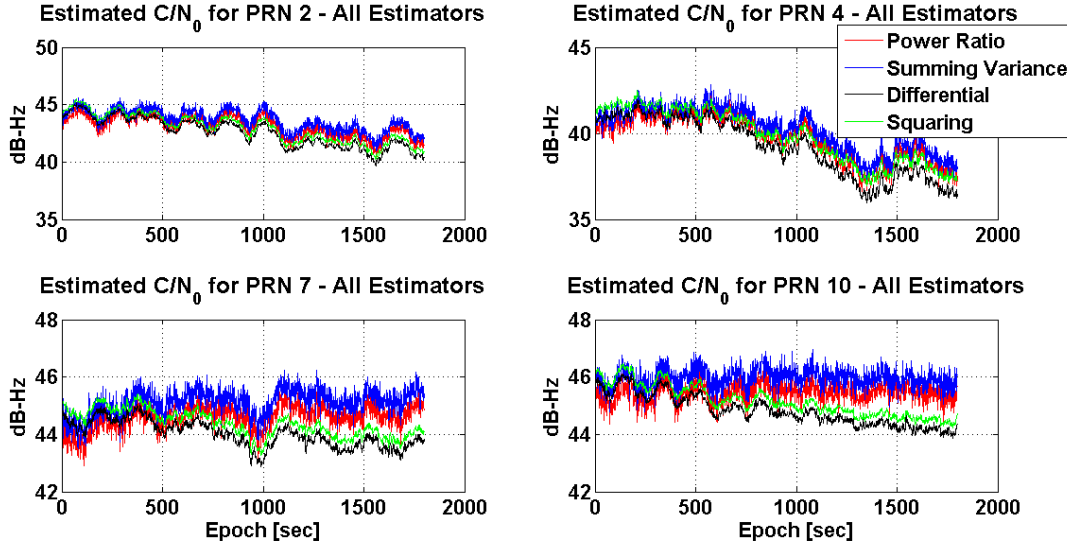


Figure 5.8.: Estimated  $C/N_0$  time series by the different estimators for four exemplary PRNs and for 30 min IF signal record.

PRN	NWPR	min	max	VSE	min	max
PRN2		40.37	44.83		41.01	45.62
PRN4		36.60	42.21		37.03	42.85
PRN7		42.89	45.50		43.38	46.25
PRN10		44.34	46.30		44.78	46.97

Table 5.2.: Narrow-Wide Power Ratio and Variance Summing estimators minimum/maximum estimated values for the observed PRNs.

In a next step, an 1 hour raw signal record was reprocessed using integration intervals of 1 and 5 msec. In this case, only PRN2 is evaluated. The post correlation output values were used for the estimation of the  $C/N_0$  observables with the four different estimation algorithms. In fig. 5.9 the resulting time series are plotted. For the plots of the first column of this figure, post correlation values with 1 msec integration time were used as an input for the estimation algorithms. In the second, post correlation values with 5 msec integration time were used. In the first row, the plotted time series are generated with a data rate of 1 Hz, in the second with 2 Hz and in the third with 10 Hz. In table 5.4 an overview of the minimum and maximum estimated values between the different algorithms is presented. The algorithms are evaluated for correlation values with 1 and 5 msec integration intervals. Longer integration intervals result in an increase of the estimated signal power. On the other hand

PRN	DE	min	max	SE	min	max
PRN2		39.66	45.15		40.23	45.47
PRN4		35.94	41.97		36.98	42.50
PRN7		42.88	45.04		43.25	45.40
PRN10		43.88	46.11		44.24	46.46

Table 5.3.: Differential and Squaring estimators minimum/maximum estimated values for the observed PRNs.

no impact on multipath signatures as well as the different linear trends present in the time series is noticed.

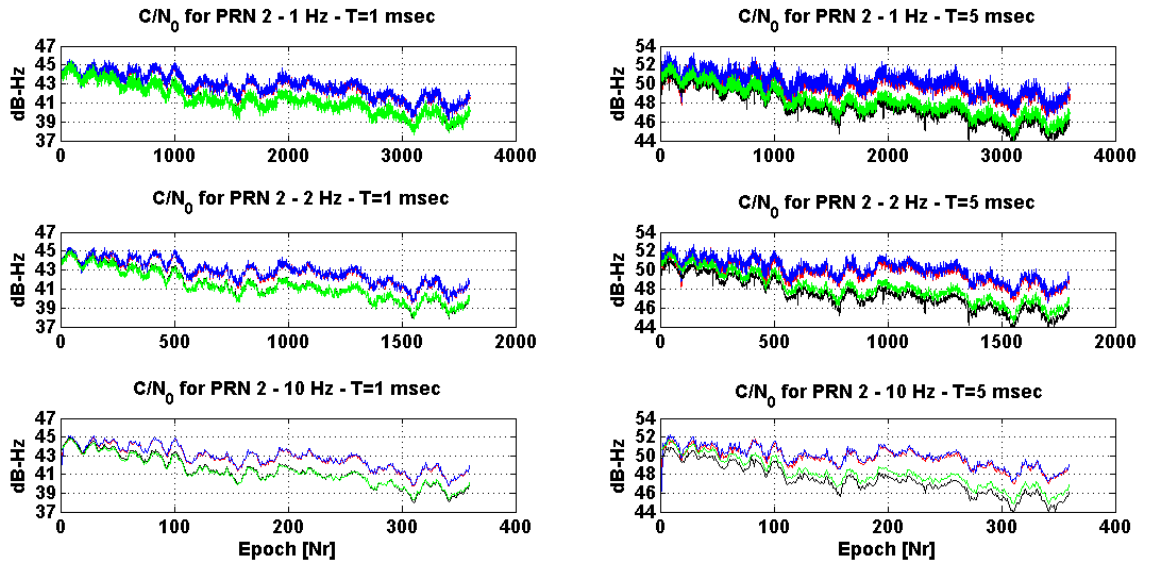


Figure 5.9.: Estimated  $C/N_0$  time series by the different estimators for PRN2 for 1 hour IF signal record. The signal was reprocess with 1 and 5 msec integration time and with different data output rates.

PRN2	T=1 msec	min	max	T=5 msec	min	max
NWPR		39.13	44.83		46.74	53.80
VSE		37.22	45.62		46.28	53.38
DE		37.79	45.15		44.96	52.60
SE		37.64	45.47		44.10	52.30

Table 5.4.:  $C/N_0$  time series versus integration time for PRN2 and for 1 hour IF raw signal record.

In the last step, regression lines were fitted to the estimated  $C/N_0$  time series. The functional model

for a straight line read:

$$y = ax + b. \quad (5.19)$$

with  $a$  and  $b$  the unknown parameters and  $y$  the  $C/N_0$  (observations) measurements. For the estimation of the unknown parameters of the linear problem of 5.19 a linear Gauss-Markov adjustment model (Koch, 1999) was implemented and the solution was estimated via a normal equation system as:

$$A\hat{x} = l + v. \quad (5.20)$$

with  $A$  the design matrix:

$$A = \begin{pmatrix} x_1 & 1 \\ x_2 & 1 \\ x_3 & 1 \\ \cdot & \cdot \\ x_n & 1 \end{pmatrix}, l = \begin{pmatrix} y_1 \\ y_2 \\ y_3 \\ \cdot \\ y_n \end{pmatrix}, \quad (5.21)$$

$\hat{x}$  the vector containing the adjusted unknowns coefficient of the straight line,  $l$  the observation vector and  $v$  the residual vector.  $\hat{x}$  is obtained by solving the normal equation system as:

$$\hat{x} = (A^T A)^{-1} (A^T l) \quad (5.22)$$

In fig. 5.10, the  $C/N_0$  time series of the different estimation algorithms of PRN 10 for 30 min signal record is plotted together with the fitted regression lines. The fitted lines between the NWPR and the SV estimators and the differential and squaring estimators show different linear trends. The slope/tilting of the regression lines is not identical for the different estimated time series. Therefore, we can conclude that the choice of  $C/N_0$  estimation algorithm will have an impact on the resulting signal power observables measured by different receivers.

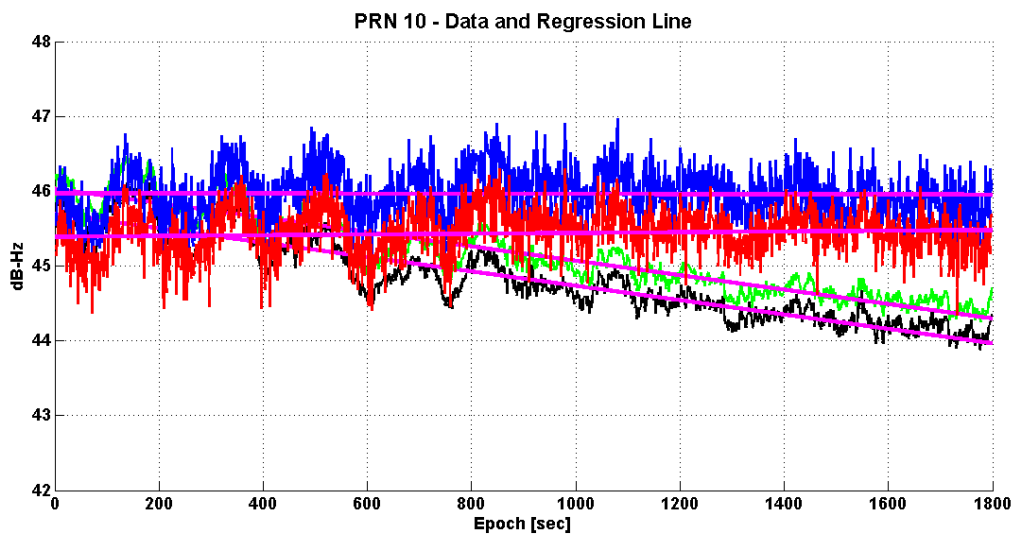


Figure 5.10.: Estimated  $C/N_0$  time series by the different estimators for PRN10 for 30 min IF signal record and the fitted regression lines.

## 5.5. Discussion

The focus of this thesis is the analytical modelling of and simulation of the impact of multipath propagation on the GNSS observables. In the next chapter, the received signal power will be simulated as a function of the satellite to receiver distance, the (complex) gain patterns of the satellite and the receiving antennas, the power at the input of the satellite antenna and reflection process (for the indirect signals). The impact of the receiver will be neglected.

Thus, in this section, an investigation was presented for the characterization of the impact of the different estimation algorithms that are used for computing the  $C/N_0$  observables. The investigation showed that this type of observable slight vary between different receivers. The different  $C/N_0$  estimation algorithms that are implemented in software showed differences on the resulting power and noise level as well as the presence of different linear trends in the estimated time series.

## 6. Development of a Generalized Multipath Model

In this chapter, analytical expressions for the computation of the received GNSS signal power, both of direct and indirect signal components, will be presented in details. They are integrated into the formulas for the phase error due to multipath and the compound signal amplitude that were explained in the third chapter (i.e. eq. 3.30 and 3.39). Thus, by further generalize the previously mentioned equations multipath effects on the GNSS observables can be simulated and characterized for complete satellite arcs. The major advantage of the presented approach is, its low implementation complexity.

The theoretical description of the developed expressions is presented first. Then, a detailed simulation analysis is taking place for the characterization of the impact multipath propagation on the GNSS observables. Crucial parameters involved in the process are simulated w.r.t. their influence on the resulting phase error and signal power. Finally, the analysis of two controlled experiments is presented for the validation of the findings. The experimental set-up of the two measurement campaigns is controlled in such a way, that the combined impact of multipath propagation on the carrier-phase observations at two antenna locations is isolated and compared with the simulations.

### 6.1. GNSS Signal Power Modelling

For the computation of the LOS signal power the Friis transmission equation (see eq. 2.64) is evaluated in its simplest form. Or, to state it differently, the absolute value of the evaluated expression is equivalent with eq. 2.64. Thus, apart from the gain information, the free space path loss and the power input at the transmitting antenna are also considered. The antennas gain patterns are modelled by the appropriate Jones vector (i.e. see eq. 2.39). For the multipath component, a similar type of link budget computation is performed where the reflection process is taken into account.

The expressions were first presented in Smyrnaioi *et al.* (2012) and with more details in Smyrnaioi *et al.* (2013). A simulation analysis is performed in Smyrnaioi and Schön (2015). Due to algorithm implementation issues, the expressions were not evaluated as a whole in the previously mentioned investigations. Only the receiving antenna gain pattern, and the (RHCP) polarization of the transmitted signal were considered. For the MP component, the reflection process was also considered. Under these assumptions, the resulting signal amplitude/power, in dB, of the LOS component is determined by the antenna (RHCP) gain (i.e. by the antenna response to a RHCP signal). For the reflected signals the resulting amplitude/power, in dB, is computed as a function of the reflection process and the receiving antenna gain pattern for both orthogonal polarizations (i.e. by the antenna response to an elliptical polarized signal). A similar multipath characterization can be found in Granger and Simpson (2008) in the framework of an investigation for multipath mitigation techniques suitable for geodetic antennas.

In this case, the algorithm is complete and the expressions are evaluated as a whole. Thus, the satellite antenna (complex) gain pattern, the receiving antenna (complex) gain pattern, free space path loss and the transmitted signal power are the input parameters for the computation of the power of the satellite-receiver link, both for the direct and for multipath signals. The only assumption, in this case, is the azimuthal symmetry of the receiving antenna gain patterns.

The received signal power at the receiving antenna can be computed as absolute value of:

$$S_{los} = P_t \mathbf{E}_{\mathbf{rx}}^H \mathbf{E}_{\mathbf{tx}} A_{los} e^{-j\alpha}. \quad (6.1)$$

Where  $\mathbf{E}_{\mathbf{rx}}^H$  is the Jones vector of the receiving antenna containing the gain information, and  $\mathbf{E}_{\mathbf{tx}}$  is the Jones vector of the incident signal which contains the gain information of the transmitting antenna. The superscript, H, denotes the Hermitian conjugate.  $P_t$  is the power at the satellite antenna input, which is equal to 27 Watt (14.3 dBW) according to the system specifications (NavstarGPS, 2011) and  $A_{los}$  is the free space path loss/attenuation, which is equal to:

$$A_{los} = \left( \frac{\lambda}{4\pi R_{txrx}} \right)^2, \quad (6.2)$$

with  $R_{txrx}$  the transmitter/receiver distance and  $\lambda$  the corresponding wave length (i.e. 0.19 m for L1). Finally,  $e^{-j\alpha}$  is the carrier of the LOS signal with  $\alpha$  the phase in  $[\circ]$ . The phase of the LOS component is set to  $0^\circ$ . The absolute value of equation eq. 6.1 is equivalent with the one of eq. 2.64. The phase information is also present in eq. 6.1 (i.e. complex signal). Atmospheric and other losses (e.g. cable losses) are not considered.

The Jones vector of the receiving antenna, which represents the receiving antenna gain pattern, reads:

$$\mathbf{E}_{\mathbf{rx}} = \frac{1}{\sqrt{2}} \begin{bmatrix} G_{rhcp_{AoA}}^{rx} + G_{lhcp_{AoA}}^{rx} \\ -jG_{rhcp_{AoA}}^{rx} - G_{lhcp_{AoA}}^{rx} \end{bmatrix}, \quad (6.3)$$

where  $G_{rhcp_{AoA}}^{rx}$  and  $G_{lhcp_{AoA}}^{rx}$  are the gain information of the receiving antenna for the corresponding AoA of the incident wave. In a similar sense the Jones vector of the transmitting antenna as a function of the satellite antenna gain for both orthogonal polarizations reads:

$$\mathbf{E}_{\mathbf{tx}} = \frac{1}{\sqrt{2}} \begin{bmatrix} G_{rhcp_{AoD}}^{tx} + G_{lhcp_{AoD}}^{tx} \\ -jG_{rhcp_{AoD}}^{tx} - G_{lhcp_{AoD}}^{tx} \end{bmatrix}. \quad (6.4)$$

The received signal power for one exemplary PRN arc is plotted in fig. 6.1. In the left side of this figure the received signal power is computed using eq. 2.64 and in the right side as the absolute value of eq. 6.1.

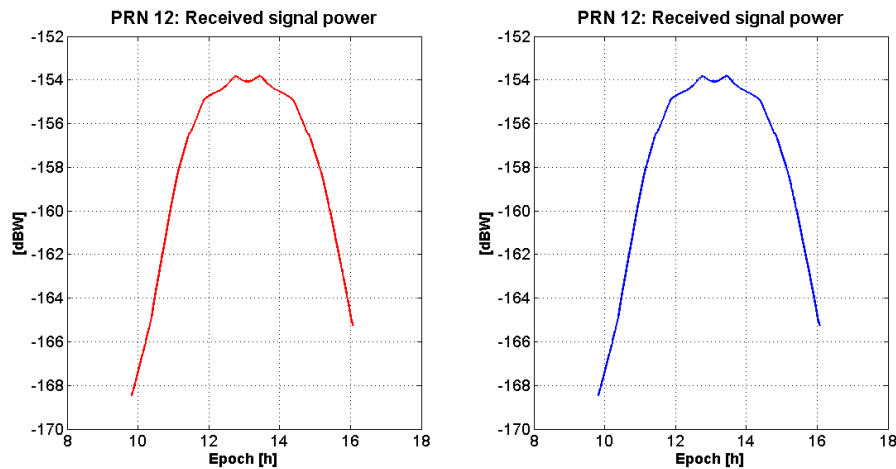


Figure 6.1.: Received signal power for the LOS component computed with eq. 2.64 (left side in red) and with eq. 6.1 (right side in blue) for an exemplary, observed, PRN arc.

For the general case of a multipath component, eq. 6.1 can be rewritten as:

$$S_{mpc} = P_t \mathbf{E}_{rx}^H H \mathbf{E}_{tx} A_{mpc} e^{-j\beta}. \quad (6.5)$$

The polarization matrix,  $H$ , is defined as (Maltsev *et al.* (2011)):

$$H = \begin{bmatrix} \cos(\Psi_{rx}) & \sin(\Psi_{rx}) \\ -\sin(\Psi_{rx}) & \cos(\Psi_{rx}) \end{bmatrix} \begin{bmatrix} R_H & 0 \\ 0 & R_V \end{bmatrix} \begin{bmatrix} \cos(\Psi_{tx}) & \sin(\Psi_{tx}) \\ -\sin(\Psi_{tx}) & \cos(\Psi_{tx}) \end{bmatrix}. \quad (6.6)$$

With  $e^{-j\beta}$ , the carrier of the MPC and  $\beta$  the phase in [°] which is set equal to  $\Delta\Phi$ .  $A_{mpc}$  is the free space loss for the MPC component. Matrix  $H$  is composed of the Jones matrix to account for the impact of the specular reflection and the rotation matrices. They account for the transformation of the initial coordinate system to the coordinate system after the reflection since the polarization characteristic of the reflected signal are associated with a different, from the initial one, coordinate system. The rotation matrices are rotating the coordinate system around the axis pointing into the direction of propagation. Terrestrial measurements took place during different experimental measurement campaigns to obtain the knowledge of the exact geometry (i.e. orientation of the reflector in space) and to allow the implementation of this transformation. The angles  $\Psi_{tx}$  and  $\Psi_{rx}$  are computed in the following way:

$$\Psi_{tx} = \tan^{-1} \left( \frac{\|\hat{n} \times \hat{txp}\|}{\hat{n} \cdot \hat{txp}} \right), \quad (6.7)$$

$$\Psi_{rx} = \tan^{-1} \left( \frac{\|\hat{n} \times r\hat{x}p\|}{\hat{n} \cdot r\hat{x}p} \right), \quad (6.8)$$

with  $\hat{n}$  the normal to the incident plane, which is defined by the transmitter, receiver and reflection point positions.  $\hat{txp}$  is the unit vector between the transmitting antenna and the reflection point and  $r\hat{x}p$  is the unit vector between the reflection point and the receiving antenna.

Integrating eq. 6.1 and 6.5 into the expressions for the phase error (eq. 3.30) and the compound signal amplitude (eq. 3.39) yields the generalized formulas for the impact of multipath propagation on the phase and SNR observations for single reflection as:

$$\phi_\epsilon = \arctan \left( \frac{\left( \frac{|S_{mpc}|}{|S_{los}|} \right) \sin(\Delta\Phi_{cor})}{1 + \left( \frac{|S_{mpc}|}{|S_{los}|} \right) \cos(\Delta\Phi_{cor})} \right), \quad (6.9)$$

and

$$A_c = |S_{los}| \sqrt{1 + 2 \left( \frac{|S_{mpc}|}{|S_{los}|} \right) \cos(\Delta\Phi_{cor}) + \left( \frac{|S_{mpc}|}{|S_{los}|} \right)^2}. \quad (6.10)$$

The relative phase  $\Delta\Phi_{cor}$  in the above equations also accounts for additional phase shifts due to the reflection process and the receiving antenna. It is computed as:

$$\Delta\Phi_{cor} = \tan^{-1} \left( \frac{\text{Im}(S_{mpc})}{\text{Re}(S_{mpc})} \right). \quad (6.11)$$

The equations for multiple-MPCs (i.e. eq. 3.40 and eq. 3.41) can be expanded in a similar sense.

On the left side of fig. 6.2 the received signal power of a compound signal (i.e. LOS and one MPC) is plotted versus the relative amplitude  $\alpha$ . On the right side of the same figure, the corresponding phase

error is plotted together with the relative amplitude for the exemplary, observed, PRN arc. As it can be noticed from these figures, multipath interference becomes stronger when the reflected signal power is higher (i.e. when the relative amplitude approaches 1). The simulations were performed using eq. 6.9 and eq. 6.10.

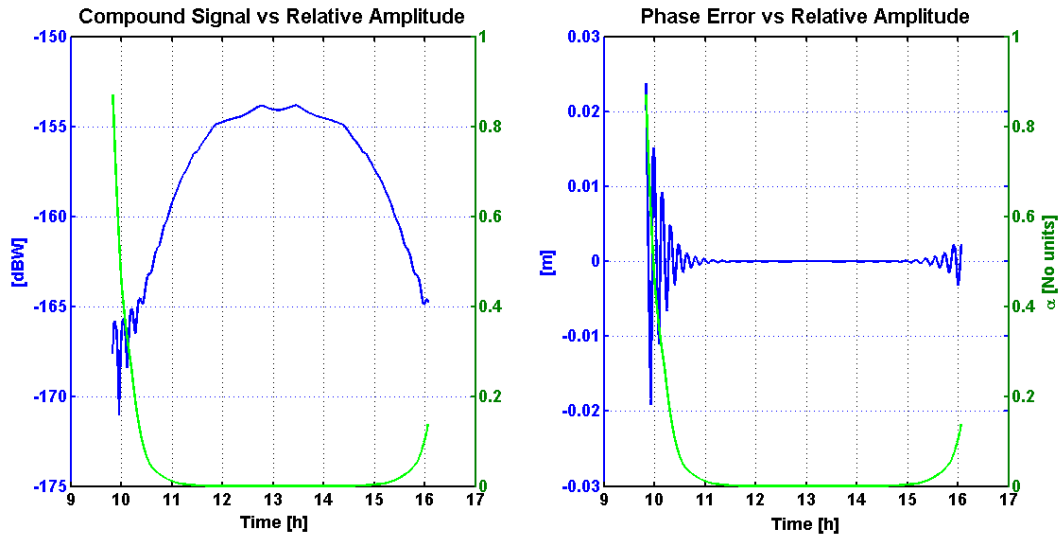


Figure 6.2.: Simulated compound signal power versus phase error and relative amplitude for an exemplary, observed, PRN arc.

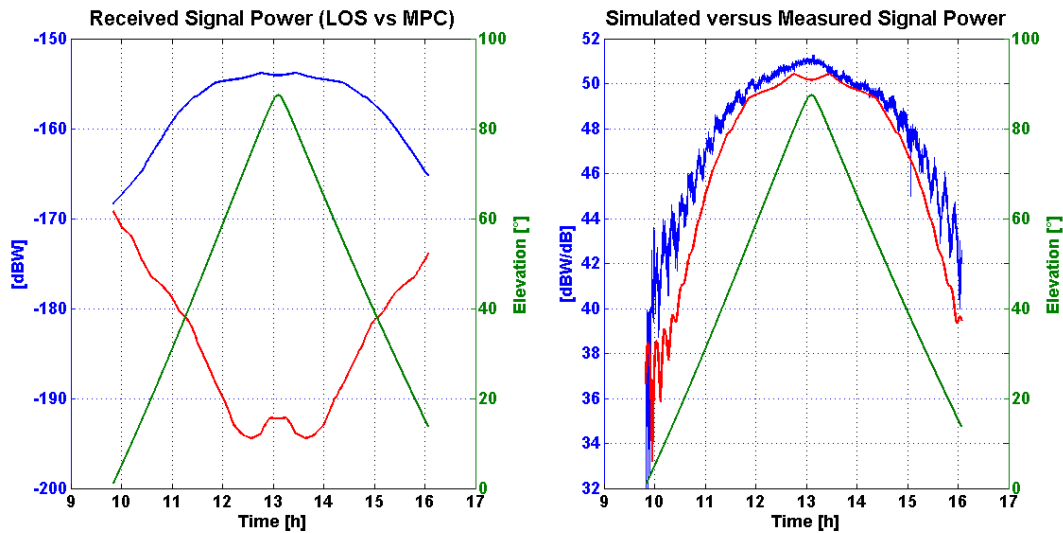


Figure 6.3.: Received signal power of LOS/MP signal components (left side) and compound signal power versus observed  $C/N_0$  for an exemplary, observed, PRN arc.

In fig. 6.3 the received signal power for both the direct (in blue) and the indirect (in red) signal components are plotted in the left sub-figure for an exemplary observed PRN arc. In the right sub-figure, the compound signal power is plotted together with the observed  $C/N_0$  time series of the exemplary PRN. The simulated compound signal power is shifted w.r.t. the maximum observed signal power for visualization purposes. For the simulations, the reflector was modelled as a concrete



one and the receiving antenna gain patterns of fig. 6.14a were used together with the satellite gain of fig. 2.14. Signal power at the input of the transmitting antenna was set to 14.3 dBW. For  $A_{los}$ , the L1 wavelength was considered while the transmitted-receiver range was calculated from the known satellite and receiver positions. The simulations are performed in an epoch-wise sense. The geometric situation is depicted in fig. 6.4.

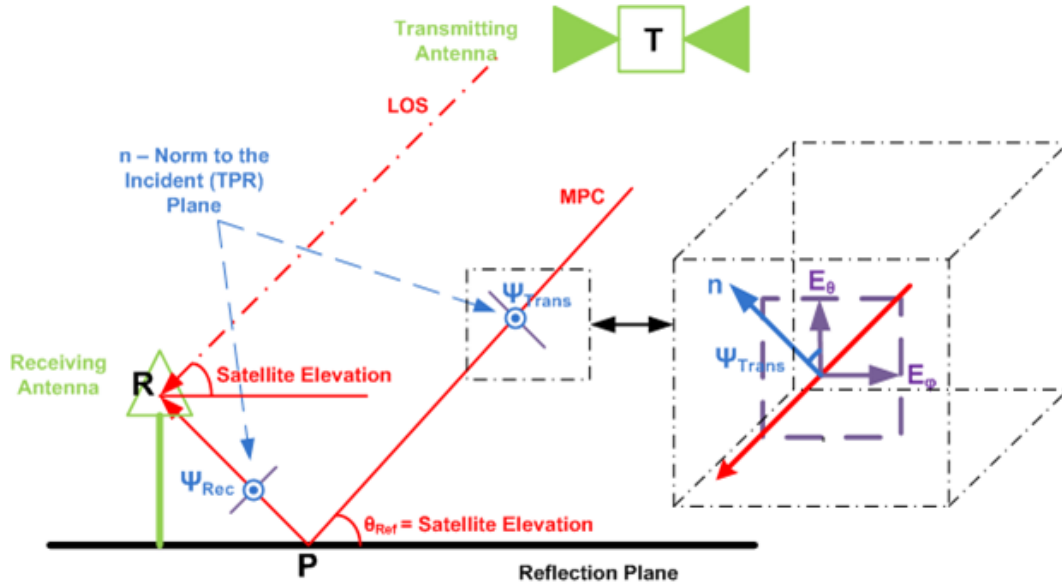


Figure 6.4.: Reflection geometry of a ground reflection scenario. Adopted from Smyrnaio and Schön (2015)

Since the relative information (i.e. relative amplitude) is present in the expression for the phase error (see eq. 6.9), the most crucial parameters for the resulting multipath error magnitude are the gain of the receiving antenna and the reflection process. All other parameters present in the expressions 6.1 and 6.5 are equal for the direct and indirect signal components and will cancel when the ratio is formed. The only deviation can come from the geometrical distance  $R_{txrx}$  of the direct and indirect signals that for the case of short delay MPC can be considered negligible. Nevertheless, for MPCs with a relatively large extra path w.r.t. the LOS component this assumption is not any more valid. Thus, and as mentioned in Granger and Simpson (2008), in order to minimize the impact of multipath on the observables the relative amplitude,  $\alpha$ , should be kept as low as possible. This can be achieved, for the ground MPC case, if the side and the back lobes of the receiving antenna are much weaker relative to the main lobe of the gain pattern.

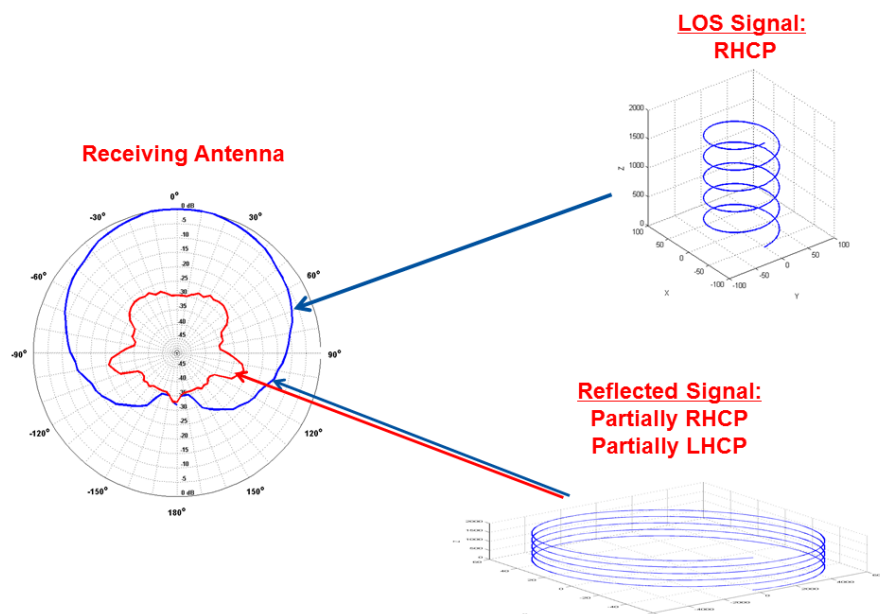


Figure 6.5.: Key factors for the resulting magnitude of the relative amplitude of short delay multipath signals are the impact of the reflection process together with the gain characteristics of the receiving antenna.

Fig. 6.5 shows the key parameters that will dictate the magnitude of the relative amplitude and, therefore, the magnitude of the resulting error due to multipath propagation. They are the gain patterns for both orthogonal polarizations together with the polarization state of the direct and reflected signals.

## 6.2. Simulation Analysis

In the following, a simulation study is described where the most crucial parameters involved in the process and their impact on the resulting multipath errors are going to be characterized.

Key parameters and their impact on the resulting multipath effects that will be investigated in this simulation study are the station height, the reflector material properties, the receiving antenna gain, the antenna orientation and the antenna polarization. As a general remark to the reader it should be pointed out that for the scenario under investigation the elevation angle of the satellite is equal to the reflection angle (see fig. 6.4).

### 6.2.1. Received signal power of direct and indirect signal components

In a first step, the received signal power of the direct and indirect signal components will be simulated with respect to different reflectors and antenna orientations and polarization. For the simulations of the different reflectors, the relative permittivity and conductivity of the different exemplary materials of table 3.1, for L-band frequencies, are used together with the gain of fig. 6.6a. The gain patterns for both orthogonal polarizations are rotated  $180^\circ$  to simulate an antenna looking downwards and they are reversed to simulate a LHCP antenna. The used gain diagrams for this part of the simulation study can be seen in fig. 6.6. They are assumed symmetrical in azimuth.

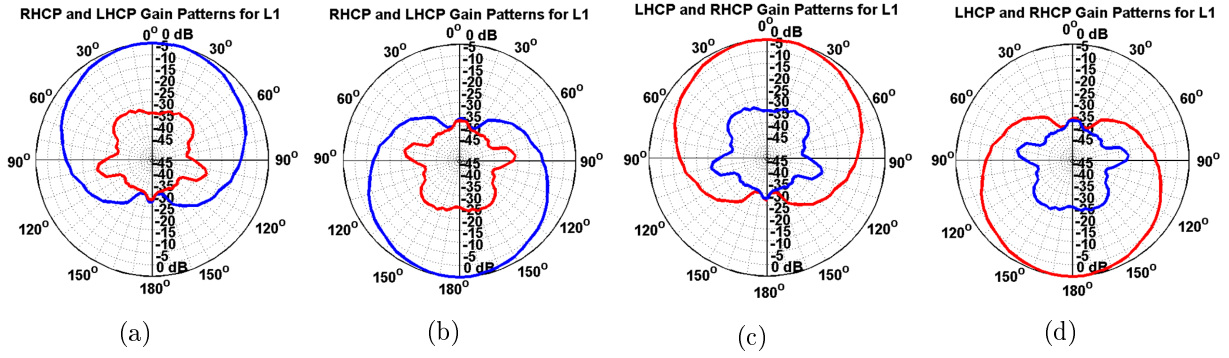


Figure 6.6.: Exemplary gain patterns (a-d) for both orthogonal components (RHCP component in blue and for LHCP component in red), for L1 frequency, that are used for the simulations.

The simulation are performed for one satellite arc and concrete, metal, wet ground and sea water reflectors. The reflector is assumed horizontal and the simulations are repeated for the different gains of fig. 6.6. The geometry of the scenario is illustrated in fig. 6.4.

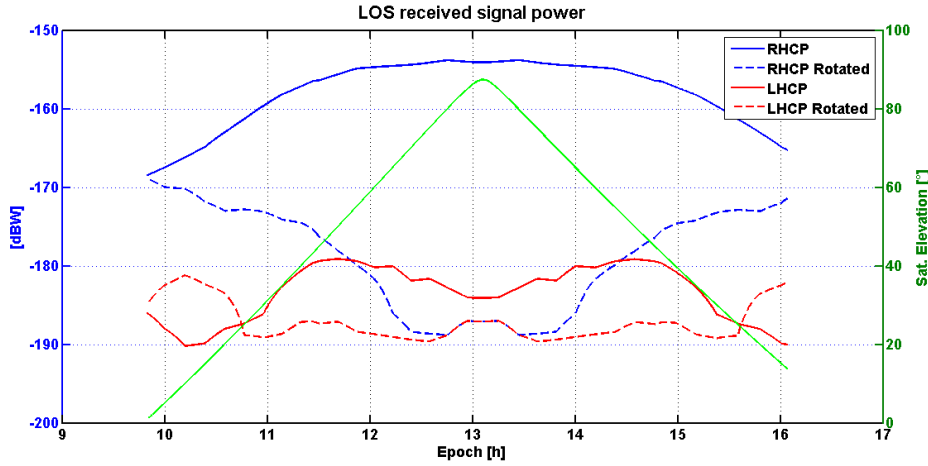


Figure 6.7.: Received signal power of the LOS component w.r.t. different antenna orientations and polarizations. The satellite gain adopted from Kronman (2000).

In fig. 6.7 the simulated received signal power is plotted for the LOS component and the different antennas of fig. 6.6. The observed satellite arc is from  $0^\circ$  up to about  $90^\circ$  and back down to about  $15^\circ$ . The satellite elevation is plotted in green color. At about 13:00 GPS time, the computed signal power at the output of the two rotated antennas is equal (see the dashed lines at about 13:00). For these epochs, the satellite is at the very zenith and the AoA is about  $0^\circ$ . The gain patterns for both orthogonal polarizations of fig. 6.6b and 6.6d are equal in magnitude for this AoA and the LOS component is assumed RHCP. For the same AoA (at about  $0^\circ$ ) the difference in the received signal power computed with the gain patterns of fig. 6.6a (solid blue line) and 6.6c (solid red line) is about 30 dBW. The difference of the co- and cross polarized components of these gains is about 30 dB at the very zenith (see fig. 6.6a and 6.6c).

Assuming an AR of -1.2 dB for all possible off-nadir angles (NavstarGPS, 2011), the cross-polar components (LHCP) of the satellite antenna gain can be computed as:

$$G_t^{lhcp} = G_t^{rhcp} \left( \frac{-AR + 1}{-AR - 1} \right). \quad (6.12)$$

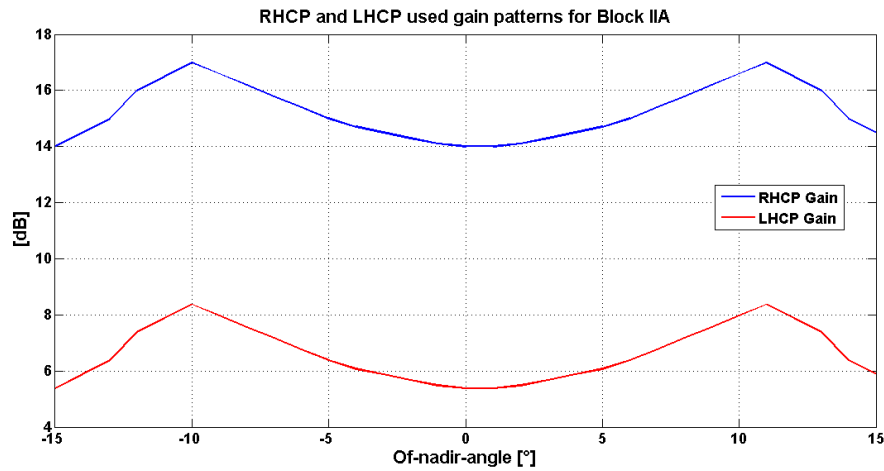


Figure 6.8.: Satellite antenna gain for co- (in blue) and cross (in red) polarized components. The RHCP component was adopted from Kronman (2000) and the LHCP is computed from eq. 6.12.

Using the satellite partial gains of fig. 6.8, the received signal power of the LOS component for the scenario of fig. 6.7 is illustrated in fig. 6.9.

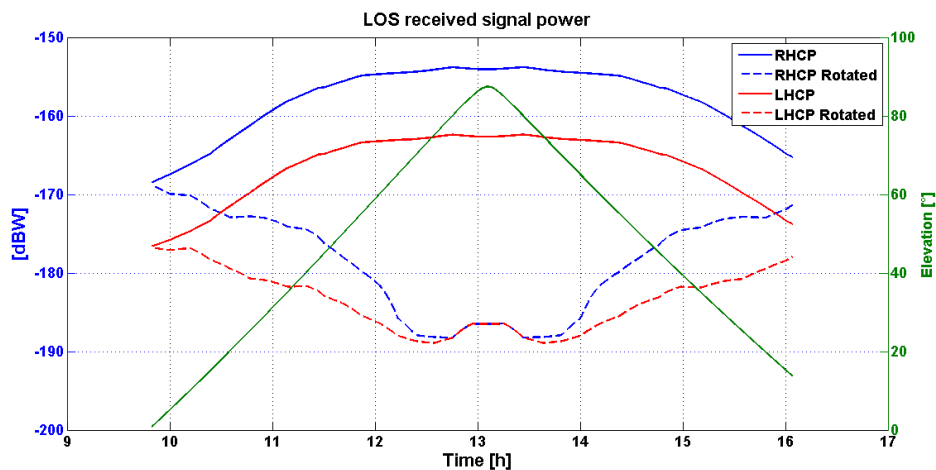


Figure 6.9.: Received signal power of the LOS component w.r.t. different antenna orientations and polarizations. The partial satellite gain patterns of fig. 6.8 are utilized the satellite antenna modelling.

In fig. 6.10 the received signal power of a MPC is plotted for the gain patterns of fig. 6.6 and for four different reflectors. The satellite elevation is plotted in green color. The intersection point, in each plot, of the dashed curves as well as of the solid ones indicate the situation where the reflection angle is equal to the Brewster angle. In other words, the reflected signal component is linear polarized since the vertical component of the field vector is zero (or minimum). In this figure one may notice that the received signal power of a signal component coming from below the horizon of the antenna will be higher when the antenna is looking at the nadir direction. Furthermore, the received signal power of a signal reflected by sea water and received by an LHCP antenna looking to the nadir is higher than from a signal reflected by a concrete reflector.

As a general remark, it can be stated that GNSS signals reflected with grazing angles smaller than the Brewster angle (i.e. with an RHE polarization state) will be stronger after an RHCP antenna. On the contrary, signals reflected with reflection angles larger than the Brewster angle (i.e. with an LHE polarization state) will be stronger after an LHCP antenna.

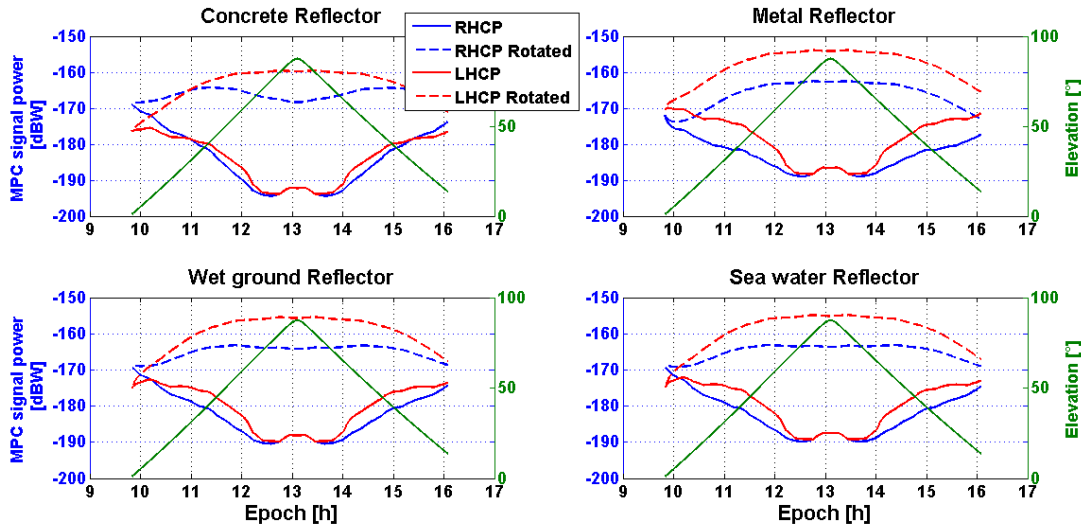


Figure 6.10.: Received signal power of a multipath component for different reflectors. The simulations are repeated for different antenna orientations and different polarization. The satellite elevation is plotted in green color.

### 6.2.2. Phase error w.r.t. antenna height and carrier frequency

The impact of the antenna height above the ground reflector is investigated in this section. The simulations were repeated for three different antenna heights. The gain patterns for both orthogonal polarizations of fig. 6.14a are used for the simulations. Antenna heights above the ground reflector of 4, 2 and 0.5 meters were arbitrarily chosen for the simulations.

The resulting phase error for the different antenna heights are plotted in right side fig. 6.11. The change of the antenna height results in different frequency modulation of the resulting phase error time series. The higher the antenna set-up, the higher the frequency of the oscillation. On the other hand, the resulting phase error envelope is the same. Similar multipath signatures are presented in Nievinski and Larson (2014). In the left side of the same figure, the power spectral density (PSD) of the before mentioned time series is plotted. PSD is computed by calculated the Fourier transform of the autocorrelation sequence using the Blackman-Tukey method (Blackman and Tukey, 1958). The computed power is plotted on a logarithmic scale [dB]. This graph shows one significant peak for each time series, which indicates the dominant frequency in each time series. The lower frequency is identified for the time series computed with an antenna height of 0.5 meter (i.e. 0.0036 Hz) and the higher for the one with antenna height of 4 meters (i.e. 0.0316 Hz).

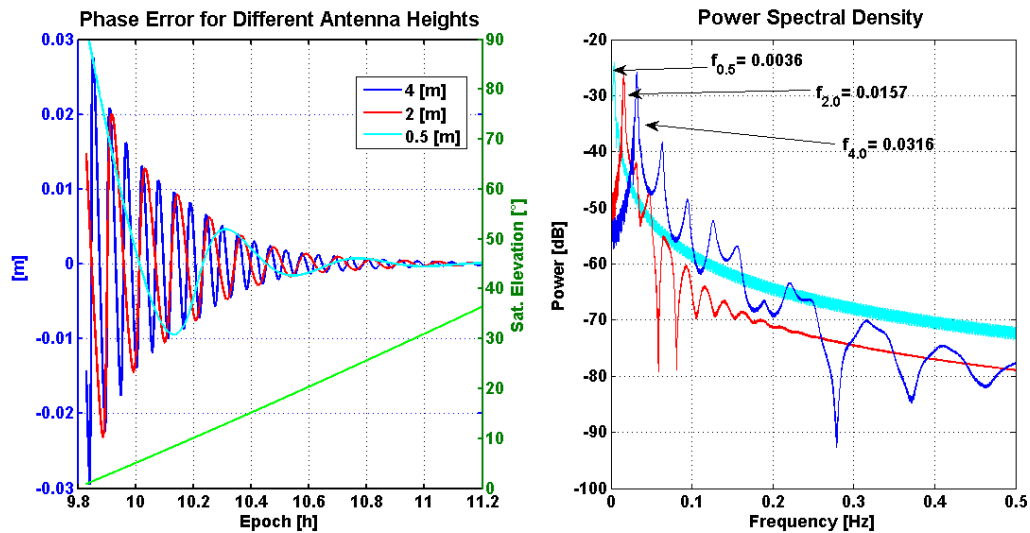


Figure 6.11.: Phase error for different antenna heights (right side) and power spectral density of the simulated time series (left side).

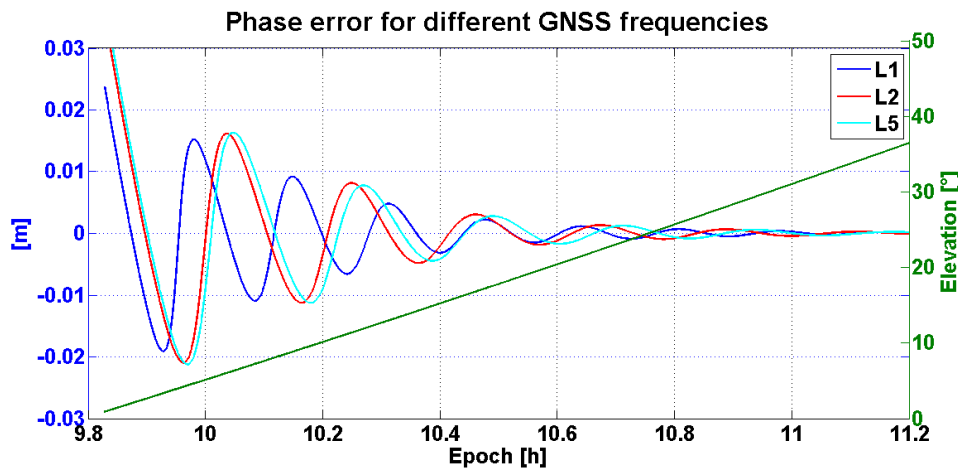


Figure 6.12.: Phase error for different GNSS carrier frequencies.

In fig. 6.12 the simulated phase error for the different GNSS carrier frequencies is illustrated. The simulations are performed for a concrete reflector and a satellite arc from  $0^\circ$  up to  $37^\circ$ . The gain of fig. 6.14a is used, and it is assumed identical for the different GNSS frequencies. Different frequency modulations between the different time series can be noticed as well as magnitude differences due to the different wavelengths.

### 6.2.3. Compound signal power and phase error w.r.t. different reflectors

The impact of different reflectors will be investigated next. We chose the exemplary material properties of concrete, sea water, wet ground and metal reflectors (see table 3.1). Since the impact will be much stronger for low elevation angles, only a part of the exemplary satellite arc is plotted. Fig. 6.13 illustrates the resulting multipath signatures for the compound signal [dBW] on the left side and the phase error [m] on the right side.

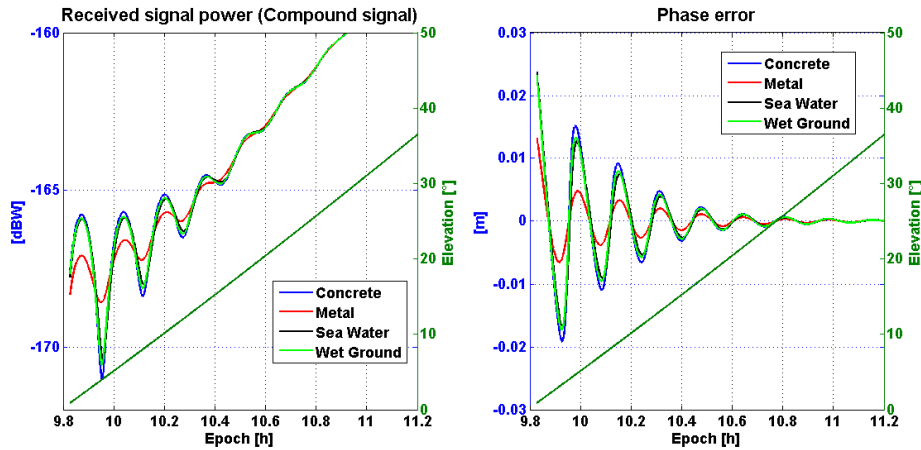


Figure 6.13.: Compound signal power and phase error for different reflectors.

The change of the material properties creates mainly a change in the amplitude of the variations. Frequency shifts between the different time series also occur. MPCs reflected from concrete terrain result in multipath signatures with larger magnitude, both for the phase observables as well as for the compound signal amplitude. On the other hand, MPCs reflected from a metal surface result in smaller, in magnitude, multipath signatures. This outcome, is attributed to the fact that the material properties of concrete cause a smoother change of the signal polarizations (from RH to LH), in contrast to the reflections coefficients of metal that create a more abrupt change (see fig. 3.6).

#### 6.2.4. Multipath Effects w.r.t. Different Receiving Antenna Gain Patterns

In this section, the impact of the receiving antenna on the resulting phase error and compound signal power is examined. In a first step, the phase error and the compound signal power is simulated. The partial gains of fig. 6.14a, fig. 6.14b and 6.17 are used for the simulations. These gain patterns have the same gain characteristics for positive elevation angles. For negative elevation angles the gain patterns of fig. 6.14b are set to a constant value of -45 dB for all possible angles of arrival (AoA) under the horizon of the antenna. On the other hand, the cross-polar gain pattern characteristics of fig. 6.17 are increased by about 25 dB.

In fig. 6.15 the resulting phase error for the three exemplary antennas is plotted. The phase error is computed via the evaluation of eq. 6.9. The exemplary satellite arc starts from about  $2^\circ$  up to  $90^\circ$  and back down to  $15^\circ$ . The reflector is modelled as concrete terrain. The plot in the middle of this figure shows no phase error. Due to the gain characteristics of the antenna of fig. 6.14b, MPC are suppressed and are very weak relative to the LOS components. On the other hand, the resulting phase error with the gain of fig. 6.17 (see the lower plot of fig. 6.15) is relatively higher when compared with the one computed with the antenna of fig. 6.14a (see the upper plot of fig. 6.15) especially for satellites elevation above  $25^\circ$ .

The same behaviour can be noticed in fig. 6.16 where the compound signal power is simulated for the same three exemplary antenna gain patterns. The blue curve is computed with the gain of fig. 6.14a, the red with the one of fig. 6.14b and the black with the one of fig. 6.17. In the no multipath interference is present with in the black curve, multipath interference is stronger for mid and high elevation angles when compared with the blue curve.

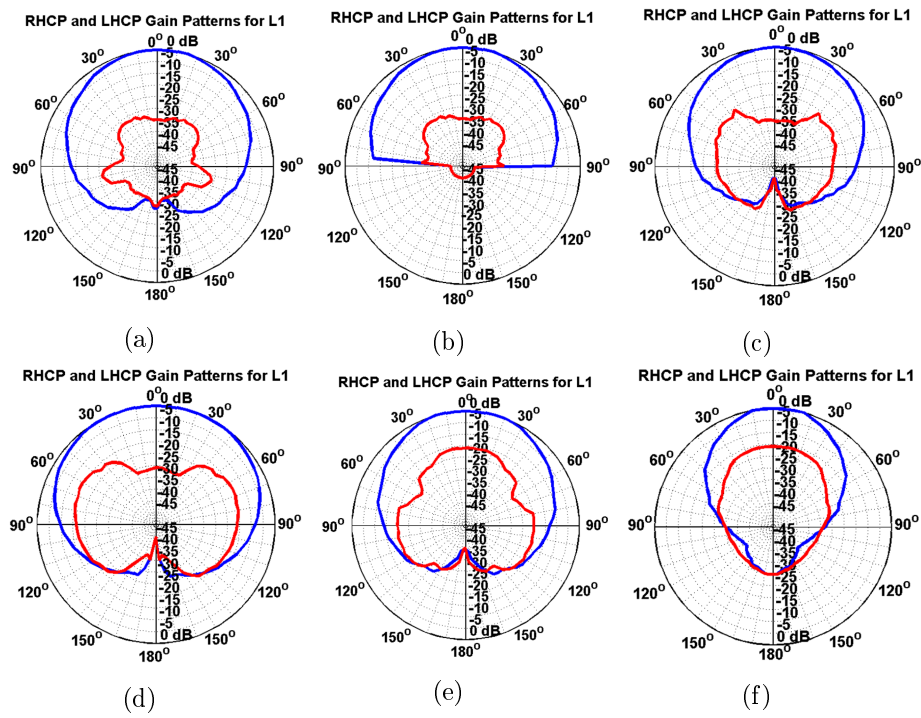


Figure 6.14.: Exemplary gain patterns (a-f) for both orthogonal components (RHCP in blue and for LHCP in red) for L1 that are used for the simulations.

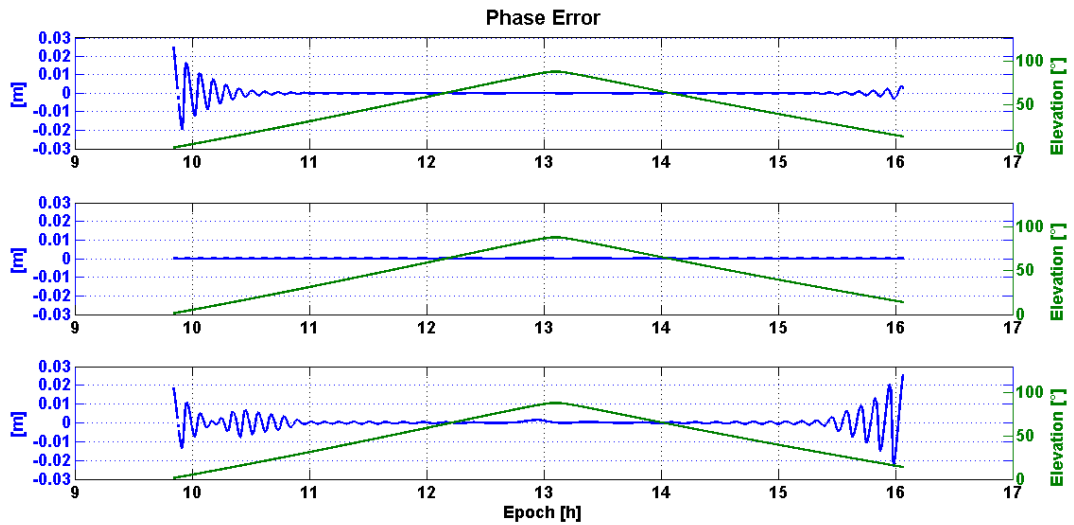


Figure 6.15.: Resulting phase error (m) for different antenna gain patterns. The gain patterns of fig. 6.14a were used for the simulations of the upper plot, of fig. 6.14b for the ones in the middle and for the lower plot the ones of fig. 6.17.



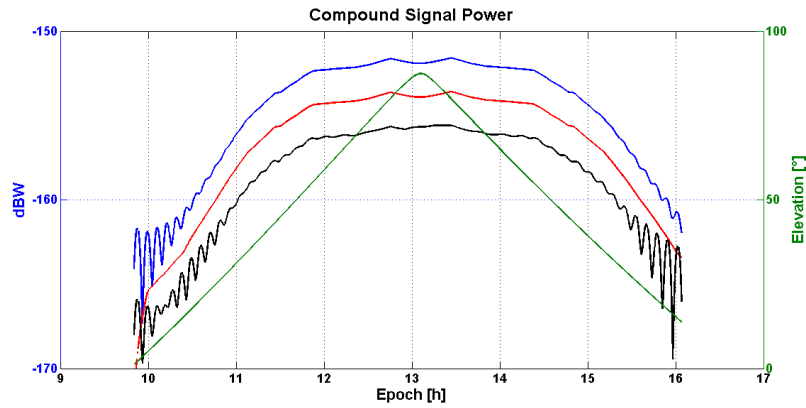


Figure 6.16.: Resulting compound signal power (dBW) for different antenna gain patterns. The gain patterns of fig. 6.14a are used for the simulations in blue color, of fig. 6.14b for the ones in red and the ones in black of fig. 6.17. A 2 dB shift between the different time series was introduced for visualization purposes.

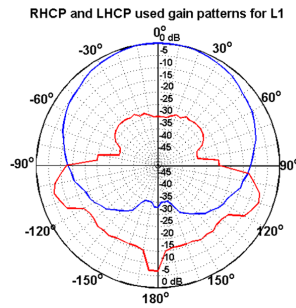


Figure 6.17.: Exemplary gain pattern with the same gain characteristics of the gain of fig. 6.14a for positive elevation angles. For negative angles, the cross-polar gain characteristics (in red) are increased by about 25 dB.

In a next step, we will investigate the resulting phase error and relative amplitude for the exemplary reflectors of table 3.1 and how they vary between the different receiving antennas of fig. 6.14. The exemplary satellite arc is from  $0^\circ$  up to  $30^\circ$  and the height of the antenna above the ground reflector is 1.36 m.

In fig. 6.18 the resulting phase error and the relative amplitude are plotted for the exemplary gain patterns and a concrete reflector. In fig. 6.19 the reflector is modelled as a metal one, in fig. 6.20 as wet soil and in fig. 6.21 as sea water.

For most of the exemplary gains of fig. 6.14 the resulting phase error and relative amplitude is of similar order of magnitude. In the phase domain, maximum differences in the order of 4 mm can be noticed. The resulting phase error and relative amplitude for the gain pattern of fig. 6.14f shows bigger deviations between the different reflectors when compared with the other antennas. For example, the resulting phase error signatures with this antenna are the smallest in magnitude when the exemplary material properties of concrete, wet soil and sea water are used. On the contrary, when the material properties of metal are used the resulting phase error magnitude, as well as the resulting relative amplitude, are much larger in magnitude when compared to the other antennas (e.g. of the order of 1 cm in the phase domain).

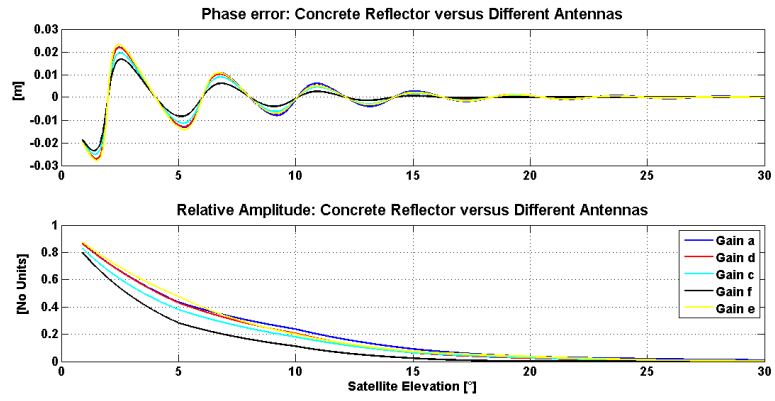


Figure 6.18.: Phase error and relative amplitude for concrete reflector and the exemplary gain patterns.

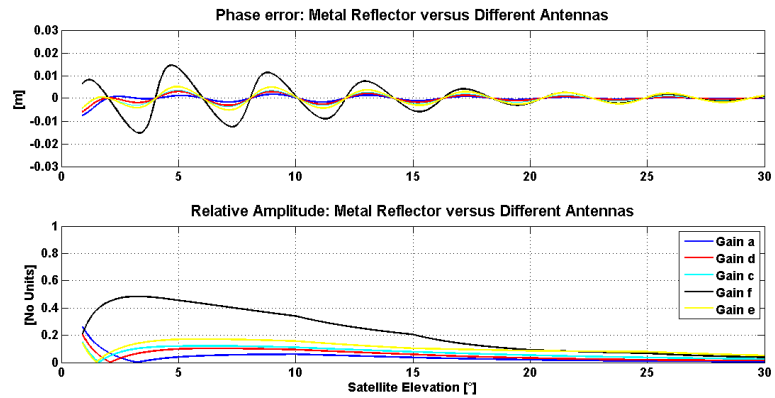


Figure 6.19.: Phase error and relative amplitude for a metal reflector and the exemplary gain patterns.

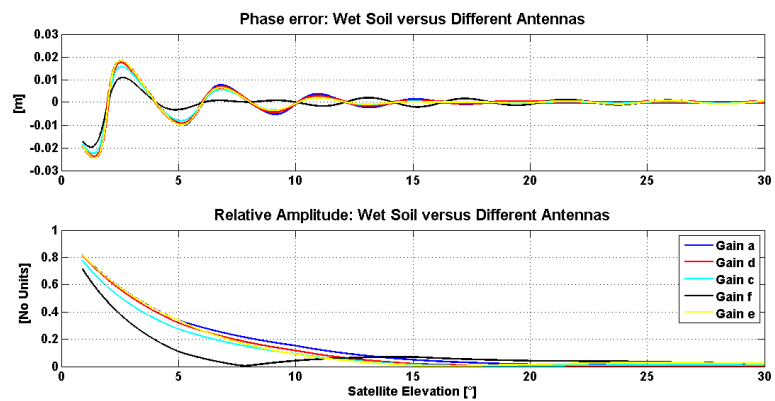


Figure 6.20.: Phase error and relative amplitude for a wet soil reflector and the exemplary gain patterns.

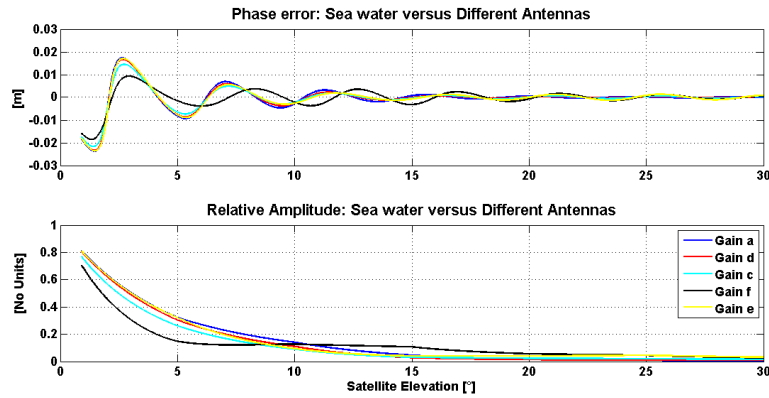


Figure 6.21.: Phase error and relative amplitude for sea water reflector and the exemplary gain patterns.

### 6.2.5. Discussion

In this section, a simulation analysis was presented for the characterization of multipath effects on the GNSS observables. The simulation analysis was performed by evaluating equations presented in the first section of this chapter and by changing the input parameters of the expression.

The analysis shows that the overall multipath contamination of the GNSS observables mainly depends on a combination of the depolarization effects (and losses) that occur due to the reflection process and the gain characteristics of the receiving antenna for co- and cross-polar components. Both, the impact of the reflection process and the gain characteristics of the receiving antenna vary since the geometry of a typical GNSS scenario is constantly changing due to the motion of the satellite (and maybe of the receiving antenna).

## 6.3. Experimental Validation

To validate the used expression for the received GNSS signal power of both the direct and indirect signal components, data sets were collected at the antenna reference open area test site at PTB Braunschweig during two different experimental measurement campaigns. This particular area was chosen due to the flat terrain characteristics and the lack of any, nearby the receiving antennas, constructions. In this way, we were sure that (specular) reflections could only occur from the ground reflector. The antennas of the observed baselines were mounted on tripods with different heights above the ground reflector in order to introduce asymmetry of the resulting multipath signatures at the different antenna locations. The antenna heights refer to the vertical distance between the mean phase center of the antenna and the ground reflector plane. Observation data from satellites above  $0^\circ$  elevation was used because complete satellite arcs are to be investigated and, furthermore, because multipath effects caused by ground reflections are much stronger at low satellite elevation angles.

### 6.3.1. First Experiment at PTB

The first experiment was conducted on 4.7.2012 and lasted about 7 hours. Data sets were collected in parallel by two Leica AX1202GG antennas which were spaced by about 20 m apart. The antennas were connected to two Leica GRX1200+GNSS receivers and their heights are 1.358 m, for the S1 station and 2.053 m for the S2 station. On the right side of fig. 6.23 all observed satellites during the 7 hours observational period are plotted w.r.t. to GPS time (h) for S1 (visibility plot). PRN 12 is indicated with red color because it is chosen as the reference PRN for the computation of the carrier-phase double differences (DD) that will be presented in the next section. They will be compared with the simulated phase DDs computed by the developed expressions of the previous section (see eq. 6.9). The skyplot

of all the observed PRNs at S1 station is illustrated in the right side of fig. 6.23. The experimental set-up of the short baseline with a high-low antenna configuration can be seen in fig. 6.22.



Figure 6.22.: Experimental set-up of the short baseline of the first experiment at PTB. S1 and S2 are the two antenna positions in a high-low set-up configuration.

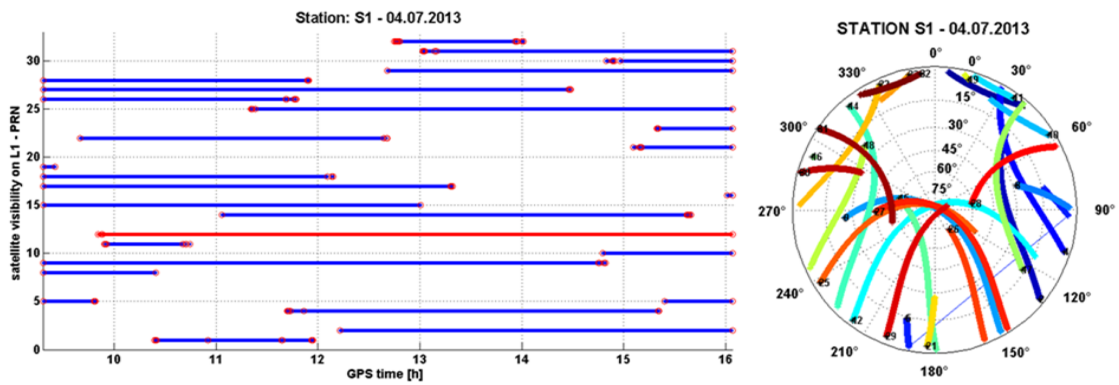


Figure 6.23.: Satellite visibility and skyplot at S1 station of the first experiment at the PTB antenna reference open area test site.

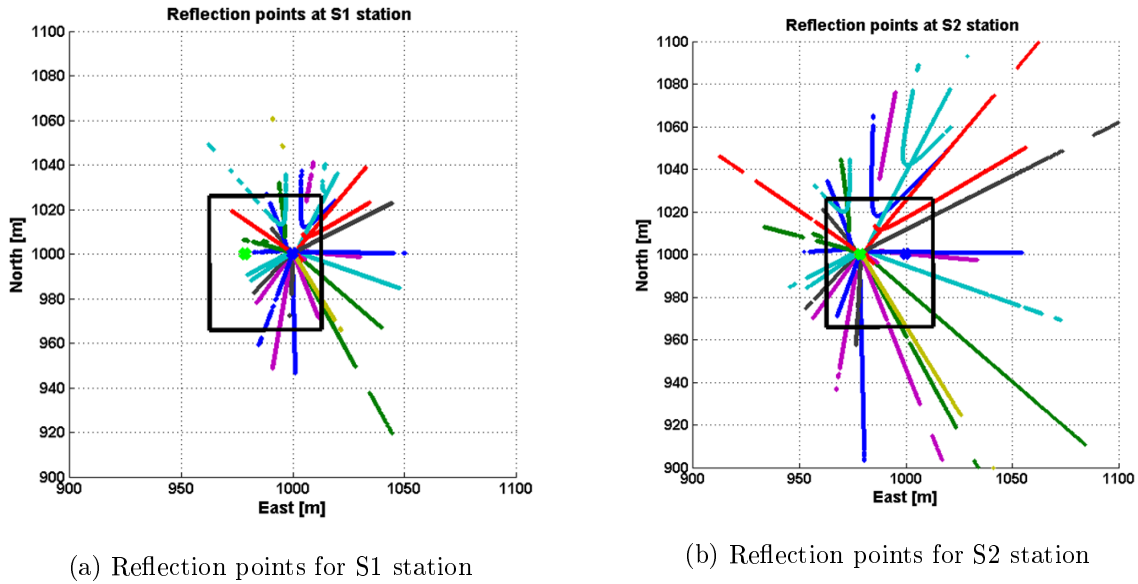


Figure 6.24.: Reflection points at S1 (a) and S2 (b) stations calculated using the captured data.

In fig. 6.24 the reflection points are presented for all observed PRNs. They are plotted together with the ground reflector and the two antenna positions in a local topocentric coordinate system. The origin of the system is at S1, and an offset of 1000 m for both the North and East components was added to avoid negative values. It can be seen in this figure that the reflection points at S2 are further away from the antenna when compared to the S1 station, due to the higher antenna set up.

### 6.3.2. Simulations versus Observations

In this section, the simulated phase error is going to be compared with the observed one for the validation of our findings. In order to isolate multipath effects in the carrier phase data, DDs were formed. By forming the DDs of a short baseline most of the distance dependent systematics as well as the receiver clock error cancel. Thus, in the resulting carrier phase DD residuals the over all multipath contamination of the phase observables from one pair of satellites at each of the two antenna positions is isolated.

In fig. 6.25 the simulated  $C/N_0$  (in blue) for one pair of satellites at both antenna locations is plotted together with the observed  $C/N_0$  (in red). In these plots, a shift between the observations and the simulation of 5 dB is introduced for visualization purposes since the power level of the simulations is below -150 dBW. The simulations are computed using eq. 6.10. The reflector is modelled as a concrete one and the gain patterns for both orthogonal polarizations of the Novatel GPS 701 antenna were used for modelling the receiving antennas. They were adopted from Novatel (2012) and were assumed similar with the gain pattern of Leica AX1202GG antennas that were used for data capture. The tilting of the reflector is also taken into account in the simulation (i.e. 3D geometry). The simulated versus observed  $C/N_0$  plots of all observed PRNs of the first experiment at PTB can be found in appendix A. The differences in the magnitude of the multipath interference, specially for medium and high satellite elevation angles that can be noticed in these figures are attributed to deviations of the actual from the used receiving antenna gain patterns.

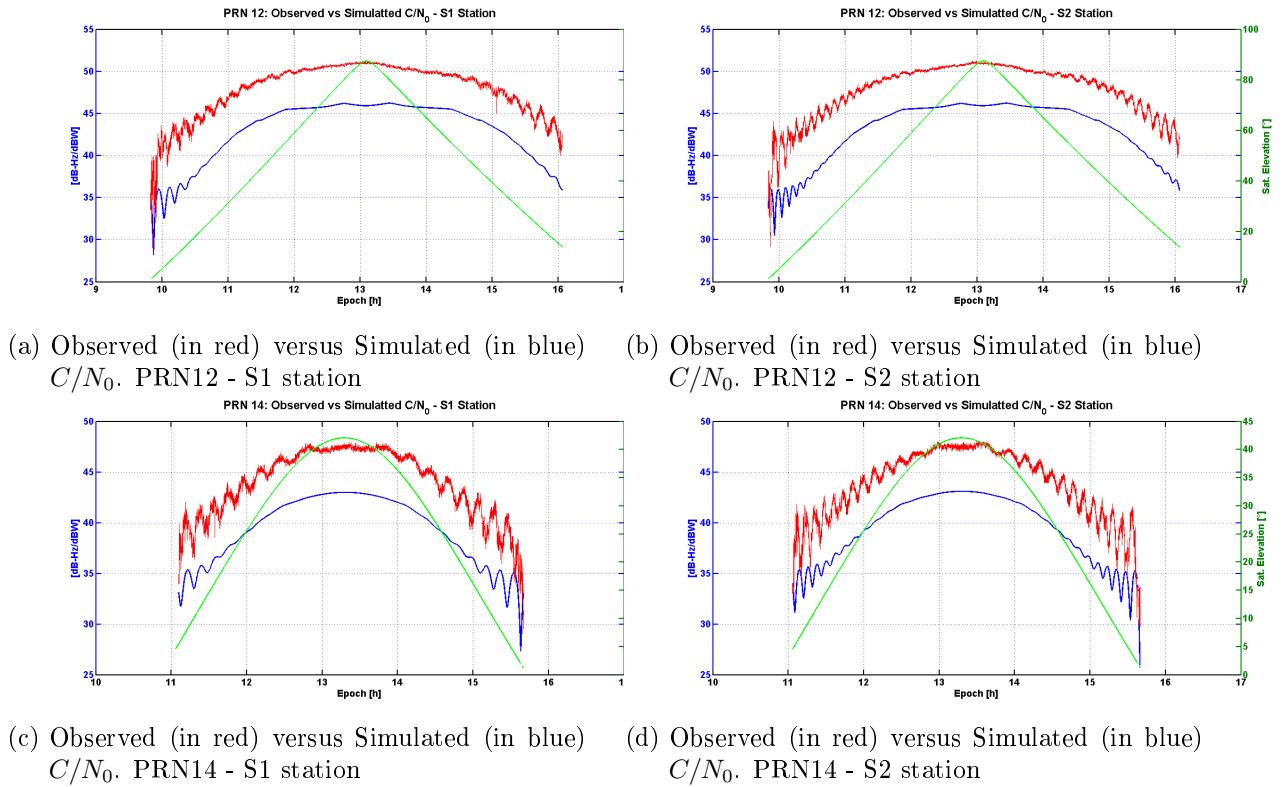


Figure 6.25.: Observed versus Simulated  $C/N_0$  for an exemplary pair of PRNs at both antenna locations of the first experiment at PTB. A shift of 5 dB between the observations and the simulation is introduced for visualization purposes

In fig. 6.26 the simulated phase error of the same exemplary pair of PRNs used in fig. 6.25 is illustrated. In the first row the resulting phase error for PRN 12 and PRN 14 is plotted for station S1. In the second row the phase error of the same PRNs is plotted for station S2. Different frequencies between of the resulting phase error time series at the two antenna locations can be noticed. They occur due to the different antenna heights above the ground reflector. The resulting phase error time series are, by satellite, single differenced (see the third row of fig. 6.26) and the simulated phase DDs residuals are formed by differencing the single difference (see the fourth row of fig. 6.26). For the generation of this figure, the reflector is modelled as a concrete one and the gain information for modelling the receiving antennas is adopted by Novatel (2012). The tilting of the reflector is also taken into account.

Looking closer at fig. 6.26 it can be noticed that the dominant multipath signature present in the simulated carrier phase DDs is very similar with the one present in the SD of PRN 14. This occurs because at about 11 o'clock and at about 15:30 o'clock the elevation of PRN 14 was below 10 deg. As already mentioned, multipath effects for low elevation satellites are stronger.

In fig. 6.27, the PSDs of the simulated time series of fig. 6.26 are illustrated. The phase error of PRN12 at S1 is plotted in red, of PRN12 at S1 in cyan, of PRN14 at S2 in black, of PRN12 at S1 in blue and PSD of the simulated DDs in green. In this plot it can be noticed that the dominant frequencies present in the time series for PRN14 at S1 and S2 stations are also identified in PSD of the DDs. On the other hand, the power of the dominant frequencies present in the time series of PRN12 for the two antenna locations are much weaker (about 25 dB) when compared with the power of the dominant frequencies present in the time series of PRN14 and they are not identified in the PSD of the simulated DDs time series.

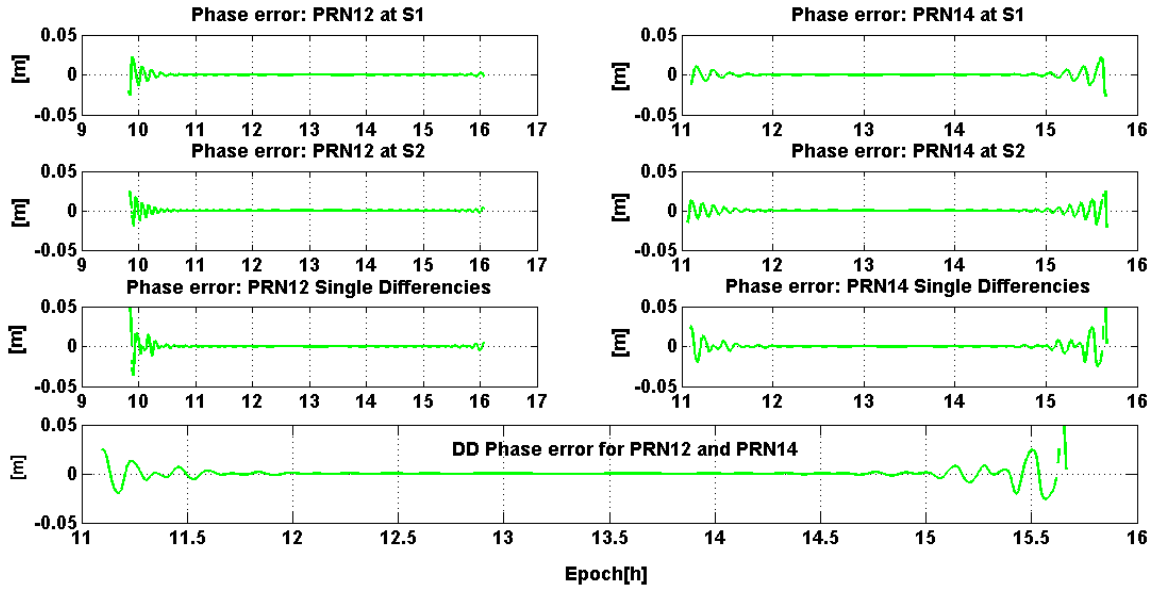


Figure 6.26.: Simulated phase error for an exemplary pair of PRNs at both antenna locations of the observed short baseline. The simulated phase error is by station single differenced in the third row. In the fourth row, the overall phase error present in the DD residuals is plotted by forming satellite differences of the single differences.

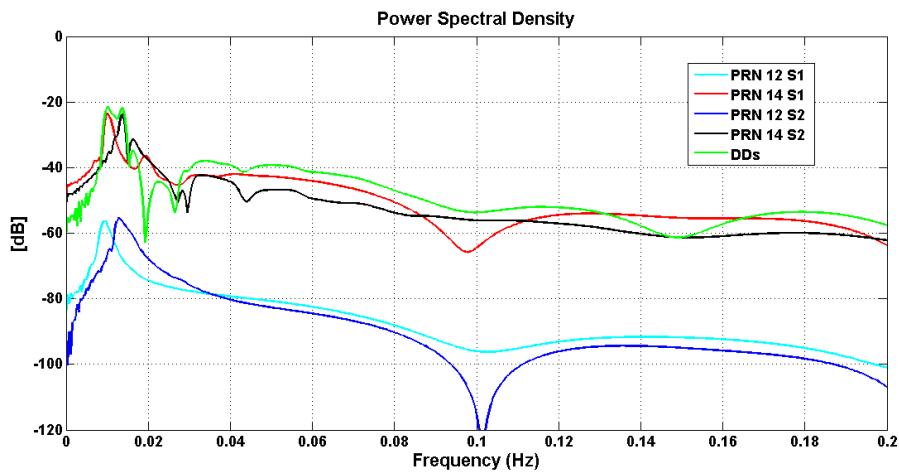


Figure 6.27.: PSD of the simulated phase error time series present in the DDs and of the simulated DDs.

In the left side of fig. 6.28 the observed versus simulated carrier phase DDs are plotted for one exemplary PRN pair. Observations are plotted in blue and simulations in green colors. In the right side of the same figure, the PSD of the observed (in red) and simulated (in blue) time series are plotted together with the cross-PSD (in black). Cross-PSD is computed by calculating the Fourier transform of the cross-correlation of between the observations and the simulations as in Blackman and Tukey (1958).

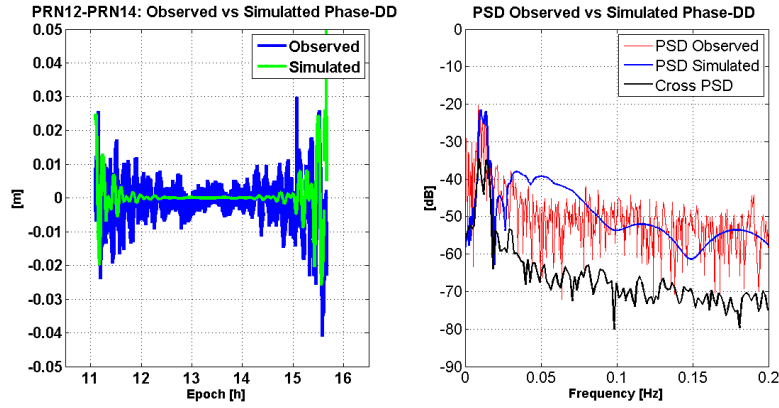


Figure 6.28.: PSD for the simulated and observed phase DDs versus cross-PSD between the observations and the simulations.

The spectral coherence/similarity between the all the observed and the simulated carrier phase DDs of the experiment is illustrated via the magnitude squared coherence ( $C_{xy}(f)$ ). The coherence is a number between 0 and 1 that indicates correlations between the frequency content of the observations and the simulations. It is computed as:

$$C_{xy}(f) = \frac{|PSD_{ObsSim}(f)|^2}{PSD_{Obs}(f)PSD_{Sim}(f)}. \quad (6.13)$$

Where,  $PSD_{ObsSim}(f)$  is the computed cross-PSD,  $PSD_{Obs}$  is the computed PSD from the time series of the observations and  $PSD_{Sim}$  is the computed PSD from the time series of the simulations. In table 6.1,  $C_{xy}(f)$  coefficients for all observations versus simulations are presented. The coefficients show an overall medium level of spectral coherence between the observations and the simulations.

DDs	$C_{xy}$	DDs	$C_{xy}$	DDs	$C_{xy}$
PRN12-PRN1	0.3	PRN12-PRN2	0.4	PRN12-PRN4	0.5
PRN12-PRN8	0.3	PRN12-PRN9	0.7	PRN12-PRN10	0.3
PRN12-PRN14	0.5	PRN12-PRN15	0.5	PRN12-PRN17	0.5
PRN12-PRN18	0.5	PRN12-PRN21	0.4	PRN12-PRN22	0.3
PRN12-PRN23	0.4	PRN12-PRN25	0.7	PRN12-PRN26	0.2
PRN12-PRN27	0.2	PRN12-PRN28	0.4	PRN12-PRN29	0.7
PRN12-PRN30	0.4	PRN12-PRN31	0.5		

Table 6.1.: Magnitude squared coherence between the observations and the simulations - First experiment at PTB.

In fig. 6.29 and 6.30 all computed, observed carrier phase DDs (in blue) during the 7 hours observational period are plotted together with the simulated ones (in green). For the simulations, the material properties of concrete were used together with the gain patterns of the Novatel 701 antenna that were assumed similar with the ones of Leica Ax1202GG. The tilting of the reflector was also taken into account. Despite the fact that for many epochs the reflection point was outside of the concrete reflector (see fig. 6.24) in the grass field surrounding the reflector, the tilting, and the material properties were assumed identical (i.e. the concrete reflector was extended infinitely). Last but not least, azimuthal symmetry of the receiving antenna gain was also assumed.



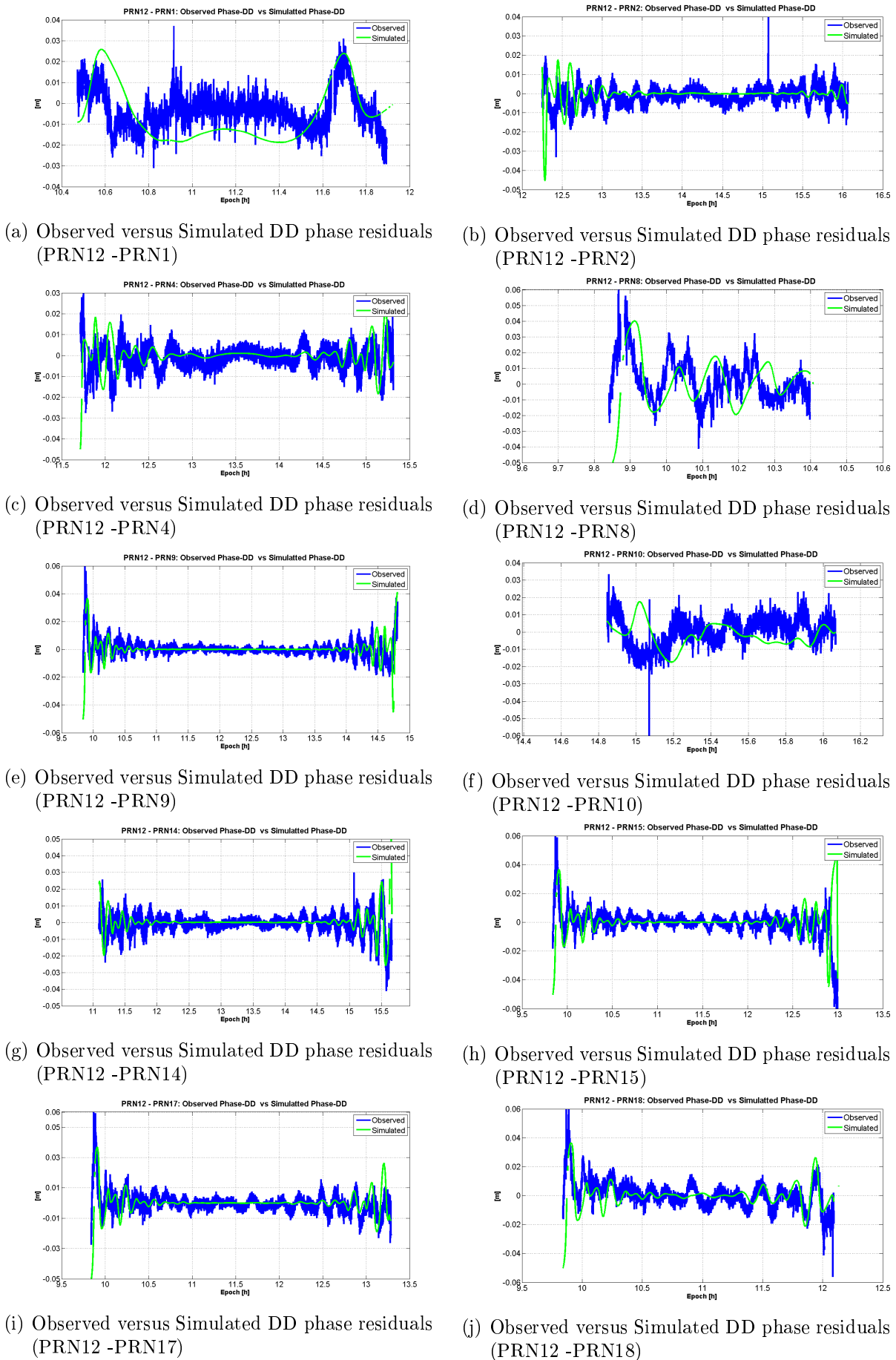
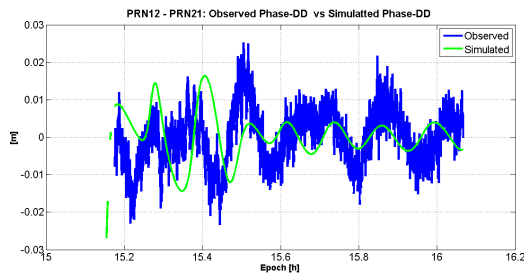
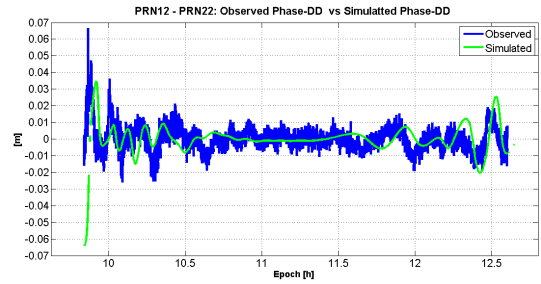


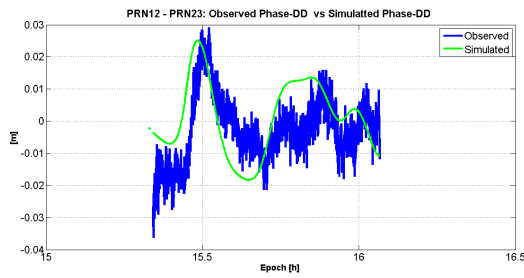
Figure 6.29.: Observed versus Simulated DD phase residuals of the observed, short baseline.



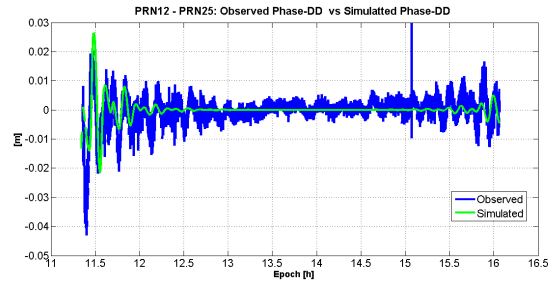
(a) Observed versus Simulated DD phase residuals (PRN12 -PRN21)



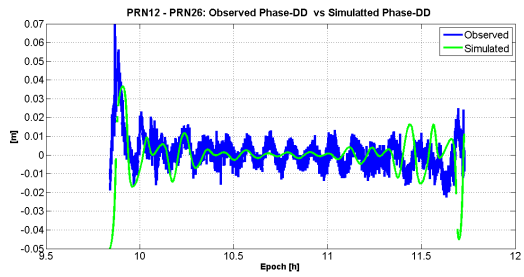
(b) Observed versus Simulated DD phase residuals (PRN12 -PRN22)



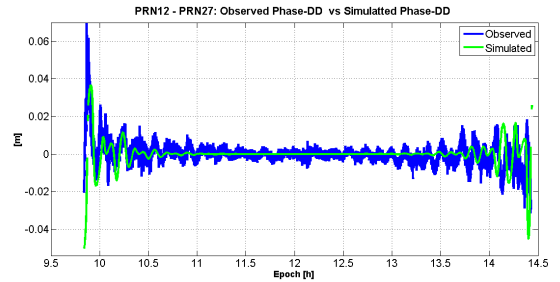
(c) Observed versus Simulated DD phase residuals (PRN12 -PRN23)



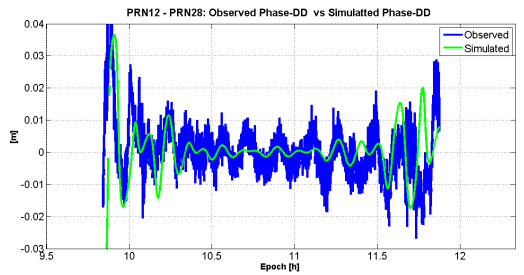
(d) Observed versus Simulated DD phase residuals (PRN12 -PRN25)



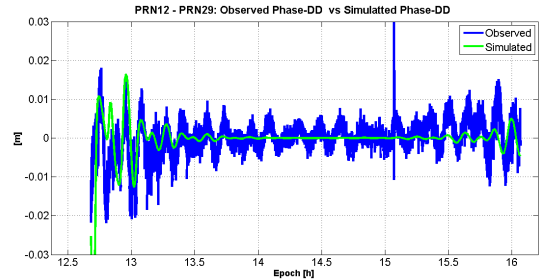
(e) Observed versus Simulated DD phase residuals (PRN12 -PRN26)



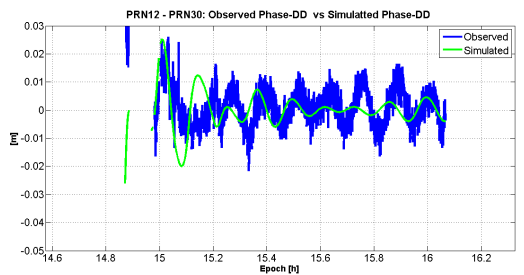
(f) Observed versus Simulated DD phase residuals (PRN12 -PRN27)



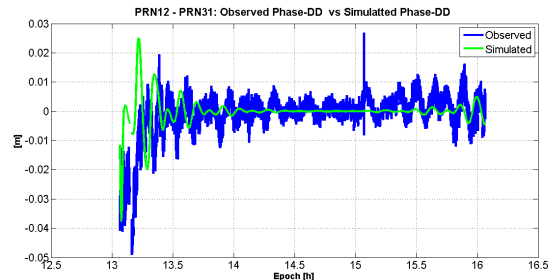
(g) Observed versus Simulated DD phase residuals (PRN12 -PRN28)



(h) Observed versus Simulated DD phase residuals (PRN12 -PRN29)



(i) Observed versus Simulated DD phase residuals (PRN12 -PRN30)



(j) Observed versus Simulated DD phase residuals (PRN12 -PRN31)

Figure 6.30.: Observed versus Simulated DD phase residuals of the observed, short baseline.

In the plotted simulated versus observed carrier phase DDs, it illustrated that the multipath signatures present in the data are also present in the simulations. Furthermore the magnitude of the oscillations, between observed and simulated time series is in good agreement for all computed phase DDs of the short baseline. Frequency shifts between the observations and the simulations can also be seen in these plots. The magnitude square coherence was computed as a quantitative measure of the similarity between the spectra of the observed and simulated time series. This coefficient corresponds the frequency which gives the maximum cross-PSD. In fig. 6.31, fig. 6.32 and fig. 6.33 the PSD for the simulated (in red) versus observed (in blue) phase DDs and cross-PSD between the observed and the simulated time series are plotted for three exemplary phase DDs time series. The first time series shows a high spectral coherence, the second a low and the third one a medium.

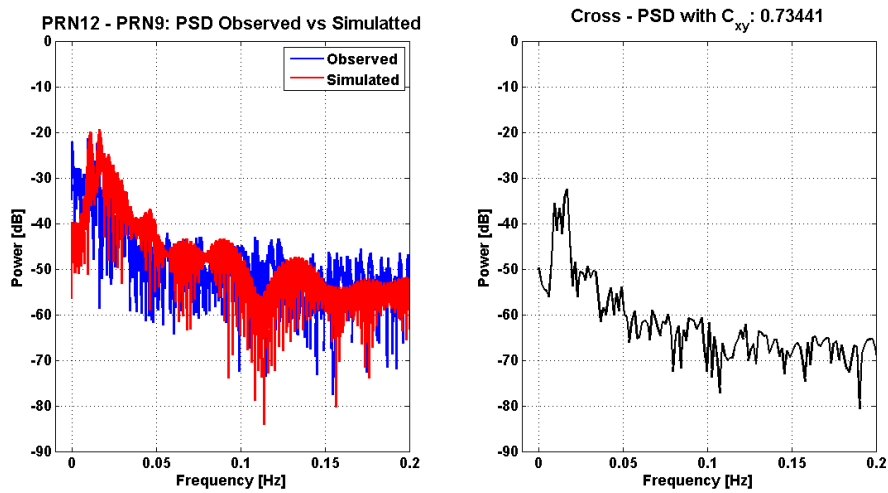


Figure 6.31.: PSD for the simulated and observed phase DDs versus cross-PSD between the observations and the simulations for the phase DDs formed with PRN12 and PRN9.

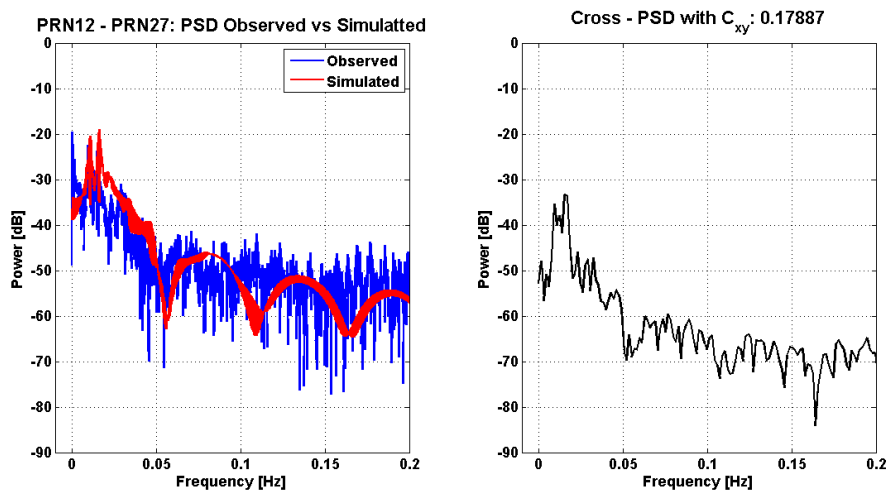


Figure 6.32.: PSD for the simulated and observed phase DDs versus cross-PSD between the observations and the simulations for the phase DDs formed with PRN12 and PRN27.

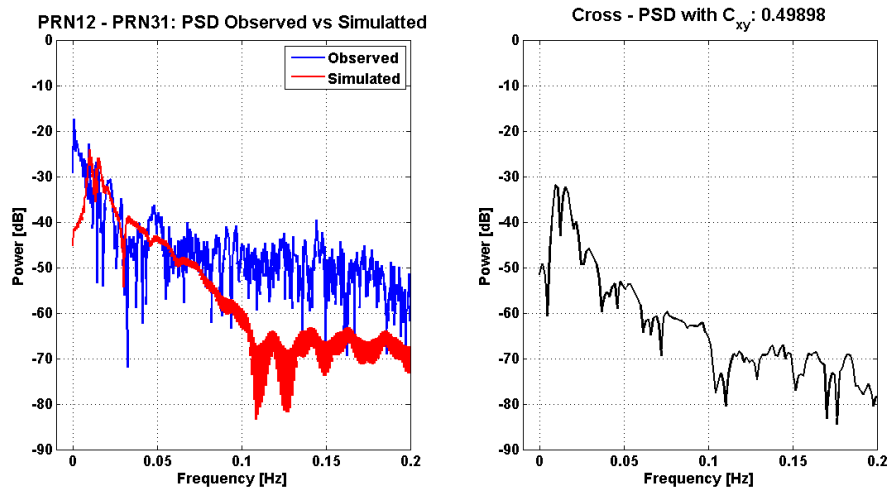


Figure 6.33.: PSD for the simulated and observed phase DDs versus cross-PSD between the observations and the simulations for the phase DDs formed with PRN12 and PRN31.

### 6.3.3. Discussion

In this part of the thesis, the results of a 7-hour controlled experiment, as well as a comparison between captured data and simulations, were presented. The time domain comparison between the simulations and the observations showed an overall good agreement of the resulting error magnitude due to multipath. Furthermore, the multipath signatures present in the data were also identified in the simulations. For the characterization of the frequency differences between the simulations and the observations a spectral analysis of the time series was performed. The analysis showed an overall medium level of spectral coherence.

Deviations between the observed and the simulated DD phase error as well as of the medium overall spectral coherence between them are attributed to the following factors. Deviations between the actual transmitting/receiving antenna gain patterns and the used ones. Geometry variations of the computed path of the reflected signals from the actual one since, for example, the tilting of the reflector is different in the area surrounding the concrete ground reflector. Moreover, for very low elevation angles diffraction and/or shadowing effects from the trees surrounding the grass field are occurring. Such effects that are not considered in the simulations are contributing to the spectral deviations between the simulation and the observations. Last but not least, the reception point of both the direct and indirect signal is considered the identical, though this may not be the case in reality. This effects can contribute to the geometry variations between the simulated path and the actual one of the reflected signals.

As a general remark for the presented analysis in can be stated that the simulated time series shown an overall slightly smaller phase error magnitude for medium and high elevation satellite when compared with the observations. For example, one may notice that multipath signatures from several epochs are larger in magnitude in the observed phase DDs while, for the same epochs, in the simulated time series no oscillations are visible.

### 6.3.4. Second Experiment at PTB

A second measurement campaign took place at the antenna reference open area test site at PTB Braunschweig. In this case, a baseline was measured for two following days and a different pair of antennas was used each day for data capture. The antennas were mounted on tripods on a high-low antenna set-up, again, to introduce asymmetry of the resulting multipath effects for the two antenna

locations. In a similar sense as with the first experiment, observation data from satellites above  $0^\circ$  were analysed because complete satellite arcs are to be investigated and, furthermore, because multipath signals from the ground are much stronger for low satellite elevation angles. The choice of this elevation mask, on the other hand, does not exclude diffraction and/or LOS obstruction effects caused by the trees in the surrounding area (see fig. 6.34). The data rate of the processed data is 1 Hz and absolute and individual phase center corrections from IfE Hannover were also taken into account during data processing. reflector into account.

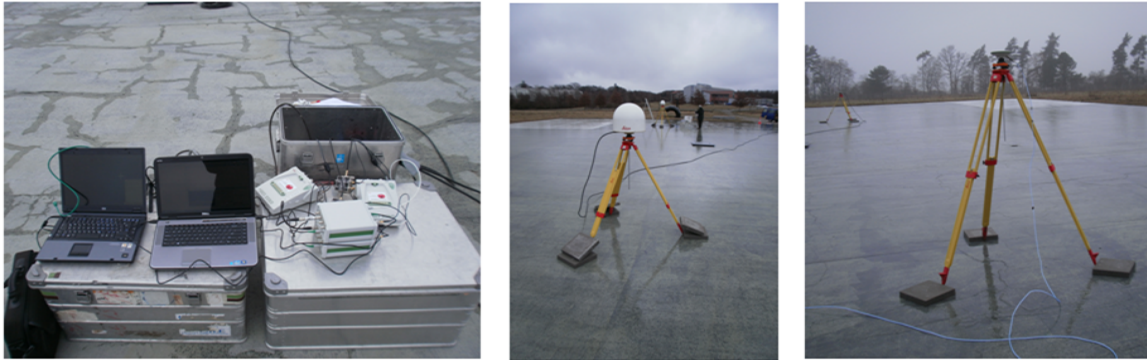


Figure 6.34.: Experimental set up at PTB Braunschweig antenna reference open area test site with one pair of pinwheel antennas and one pair of 3D choke ring antennas. Data were captured by two Leica GRX1200+GNSS receivers.

The experimental set up can be seen in fig. 6.34. The antenna heights are 1.244 m (S1 station) and 1.765 m (S2 station). In fig. 6.35 the corresponding visibility plot and skyplot for one of the two antenna locations of the experimental set-up are plotted. PRN 9 is plotted in red colour because it was chosen as the reference PRN for the formation of carrier-phase DD of the observed baselines that will be analysed in a next section of this chapter.

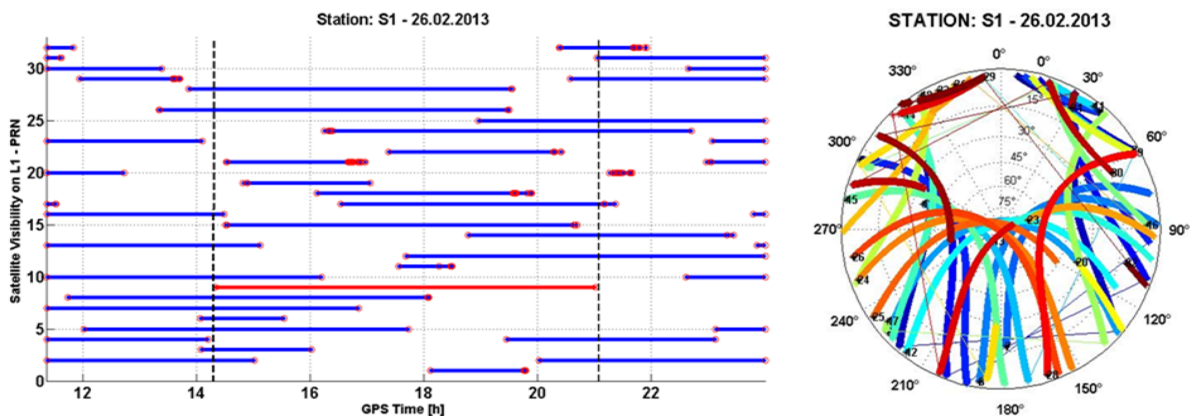


Figure 6.35.: Visibility plot on L1 and skyplot of the observed PRNs on 26.02.2013. In the visibility plot, PRN9 is plotted in red color because it is chosen as a reference PRN for the computation of the carrier-phase DDs.

### 6.3.5. Data Analysis

The baseline was measured in an environment where reflections could only occur by the ground. The data were captured on two consecutive days to investigate the sidereal repeatability of the multipath signatures. Due to the repeatability of the ground tracks of the GPS satellites, station dependent error sources (e.g. multipath) will exhibit the same behaviour after, approximately, one sidereal day when the environment in which the antenna is mounted as well as the used instrumentation do not change. Thus, multipath signatures in the GNSS observables will also repeat after one sidereal day. For the interested reader, in appendix B an investigation can be found for the computation of the repeat time of the satellite tracks. The repeat time is computed by taking into account the repetition of multipath signatures in present in the GNSS data of different observational days.

In this case, we chose to measure the baseline on the first day with a pair of pinwheel antennas (i.e. a Novatel GPS 703 GGG and a Leica AX1202GG antennas) and the second day with a pair of 3D choke ring antennas (i.e. two Leica AR25 antennas). Thus, since the only difference between the two different observational days are the receiving antennas, their impact on the resulting multipath contamination of the GNSS observables can be characterized. In a first step, the  $C/N_0$  observables are plotted for two exemplary PRNs, namely PRN 9 and PRN 26.

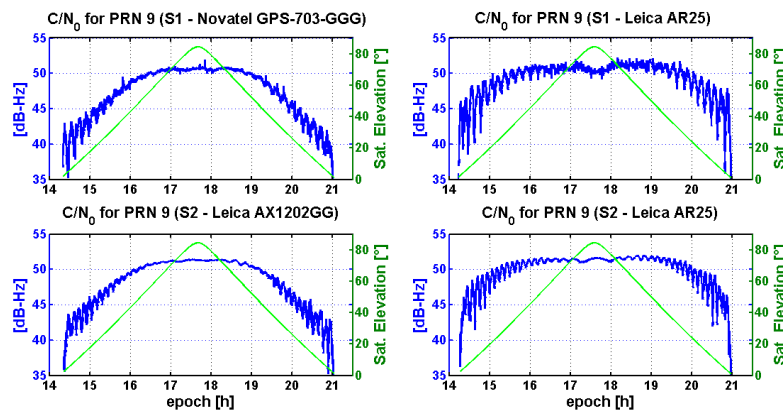


Figure 6.36.: Observed  $C/N_0$  of PRN 9 for both antenna positions. In the first column, the  $C/N_0$  values for both antennas positions of the first observational day are illustrated and in the second column of the second day.

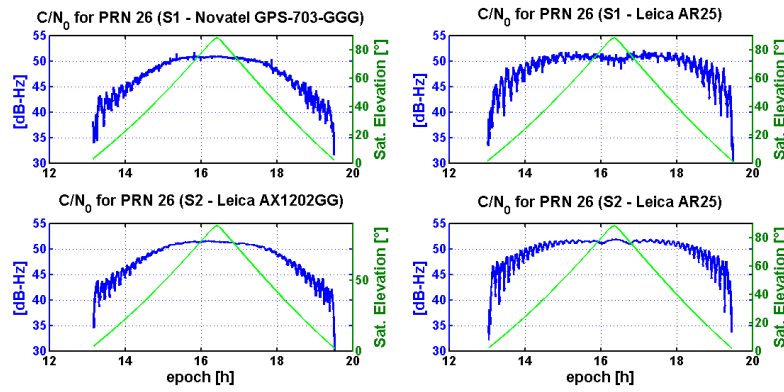


Figure 6.37.: Observed  $C/N_0$  of PRN 26 for both antenna positions. In the first column the  $C/N_0$  values for both antennas positions of the first observational day are illustrated and in the second column of the second day.

In fig. 6.36 and 6.37 the measured  $C/N_0$  is plotted for the two antenna locations on both observational days for two exemplary PRNs (PRN 9 and PRN 26). In the first column, the  $C/N_0$  time series for S1 and S2 stations and for the first observational day are illustrated. In the second column the time series of the second observational days can be seen. The differences of the resulting multipath signatures are attributed to the different antennas used for data capture during the two observational days. An inspection of the plots shows a stronger multipath interference (i.e. the fading behaviour is larger in magnitude) when the pair of 3D choke ring antennas is used.

In a next step, the multipath effects in the code domain are quantified for each station on the two observational days via the MP1 multipath free LC (see eq. 2.99).

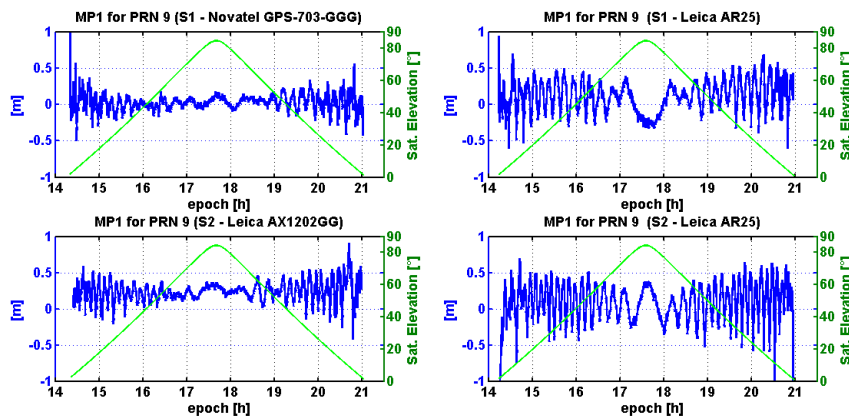


Figure 6.38.: MP1 LC time series of PRN 9 for both antenna locations. The MP1 LC time series for both antennas positions of the first observational day are illustrated in the first column and in the second column the ones of the second day.

In fig. 6.38 and 6.39 the computed multipath free LC are plotted for the two antenna position on both observational days and for the two exemplary RPNs. In the first column the  $MP1$  time series are plotted for S1 and S2 stations and for the first observational day. For day two, the corresponding plots can be seen in the second column. In table 6.2 the RMS error of the plotted time series is presented. Looking at the plots and the corresponding table it can be noticed that an overall slightly larger multipath contamination of the code-phase observations has occurred for the data sets captured

on the second observational day.

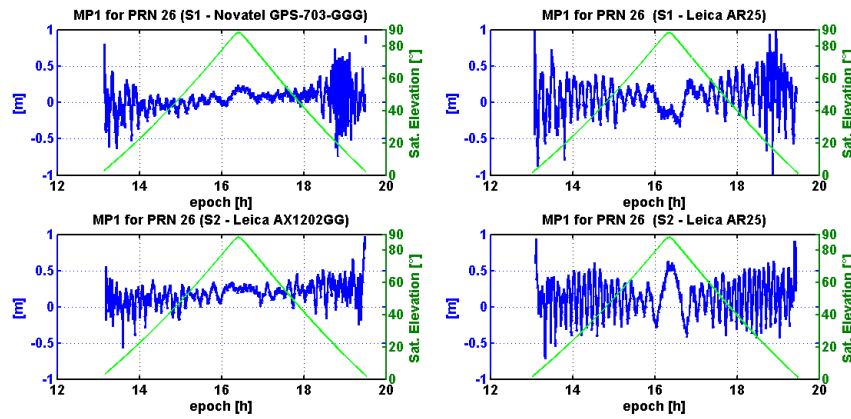
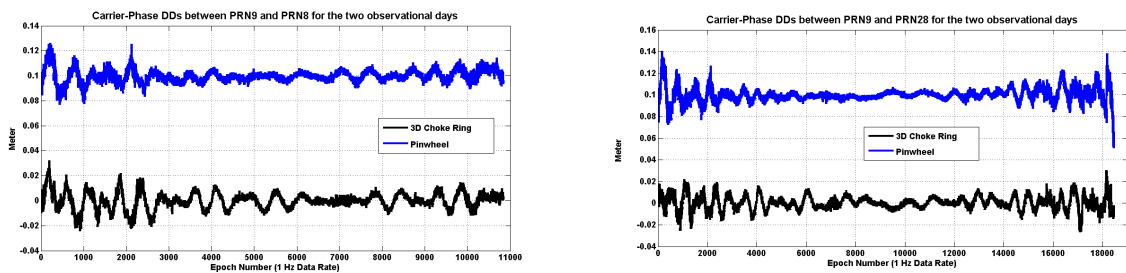


Figure 6.39.: MP1 LC time series of PRN 26 for both antenna locations. The MP1 LC time series for both antennas positions of the first observational day are illustrated in the first column and in the second column the ones of the second day.

PRN	Antenna	Station S1 [m]	Station S2 [m]
PRN9	Leica AX1202GG	0.214	-
PRN9	Novatel GPS-703-GGG	-	0.340
PRN9	Leica AR25	0.470	0.571
PRN26	Leica AX1202GG	0.356	-
PRN26	Novatel GPS-703-GGG	-	0.440
PRN26	Leica AR25	0.512	0.650

Table 6.2.: Average RMS of the multipath free linear combination (MP1) for the two stations and the different observational days for PRN9 and PRN26.



(a) Observed carrier-phase DDs between PRN 9 and PRN 8 for the two observational days.

(b) Observed carrier-phase DDs between PRN 9 and PRN 28 for the two observational days.

Figure 6.40.: Observed carrier-phase DDs on 26.02.2013 (in blue) on 27.02.2013 (in black) formed by two exemplary PRN pairs. A 0.1 (m) offset between the two time series is introduced for visualization purposes.

Finally, to this end, the carrier-phase DD residuals are computed to characterize multipath contamination of the carrier-phase observables. The DDs were computed by eq. 2.90. The DD ambiguity term present in the DD residuals was manually removed. In forming the DDs of a short



baseline, the combined impact of multipath propagation of two satellites at two antenna locations can be isolated and therefore characterized.

In fig. 6.40 the carrier-phase DDs are plotted for two exemplary pairs of satellites and for the two observational days. The time series in blue colour are the observed phase DDs with data captured by two pinwheel antennas (a Novatel GPS-703-GGG and a Leica AX1202GG antennas). The phase DDs from the data captured with a pair of Leica AR25 3D choke ring antennas are illustrated in black colour. The RMS of the exemplary time series of fig. 6.40 are presented in table 6.3.

Antennas	PRN 9 - PRN 8 [m]	PRN 9 - PRN 28 [m]
Pinwheel	0.006	0.006
3D Choke Ring	0.007	0.008

Table 6.3.: Average RMS of the double differenced phase observations on the two observational days.

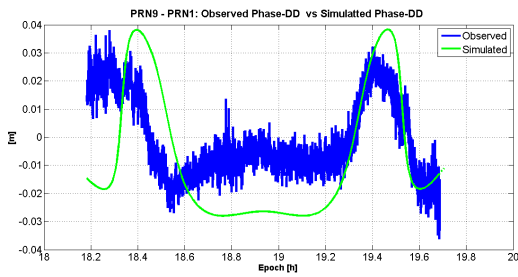
In this section, the data analysis of a controlled experiment was presented. The goal of the analysis was to characterize the overall multipath contamination of the captured GNSS data on two consecutive days using two different GNSS antennas types. Furthermore, the particular environment in which the antennas were placed was chosen due to the flat terrain characteristics and the lack of any nearby, the receiving antennas, constructions. In this way, we were assured that reflections would only occur by the ground and, therefore, arrive below the horizon of the antenna.

For the characterization of the overall multipath contamination of the GNSS observables, captured  $C/N_0$  data were analysed as well as code and phase observations. The multipath free linear combination was formed to access the overall multipath contaminating of the code-phases and the carrier-phase DDs of the observed baseline were formed for the characterization of multipath contamination of the carrier-phase observables. The data analysis shows an overall slightly better multipath mitigation performance of the pinwheel antennas compared to the 3D Choke ring antennas, for the scenario under investigation (i.e. ground reflection).

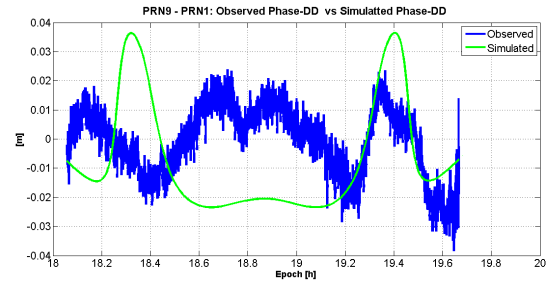
### 6.3.6. Simulation versus Observations

A comparison of the computed phase DDs with the simulated ones for the two days second experiment at PTB area will be presented in this section, as it was done in the previous section with the first experiment at PTB. The antenna gain patterns for both orthogonal polarizations of Novatel GPS 701 antenna were used for modelling the pair of antennas that were used during the first observational day. They were adopted from Novatel (2012). For the second observational day, the gain patterns for modelling the receiving antennas were adopted from Leica (2014). An azimuthal symmetry was assumed in both cases. The reflector was modelled as a concrete one and, furthermore, a survey took place in the area to take the tilting of the reflector

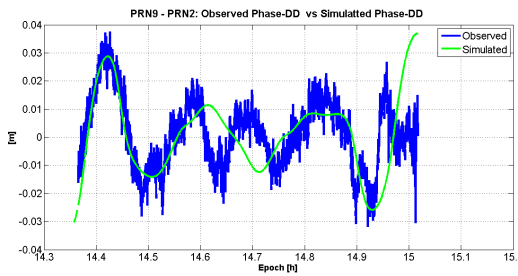
In tables 6.4 and 6.5 the magnitude squared coherence between the observations and the simulations is illustrated for all observed baselines of the first and second observational days. In fig. 6.41, 6.42, 6.43 and 6.44 the observed versus simulated phase DDs for the second experiment are plotted. In the left column one can see the data versus the simulations from the first day (26.02.2013) when two pinwheel antennas were used. In the right column the data versus the simulations of the second day (27.02.2013) are illustrated. Finally, in fig. 6.45, fig. 6.46 and fig. 6.47 the PSD for the simulated (in red) versus observed (in blue) and cross-PSD (in black) between the observations and the simulations of the DD residuals formed by exemplary PRN pairs for both observational days are plotted.



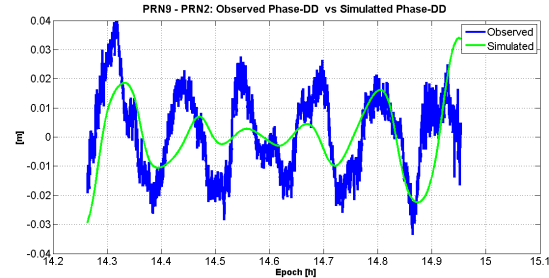
(a) Observed versus Simulated DD phase residuals (PRN9 - PRN1) - Day 1



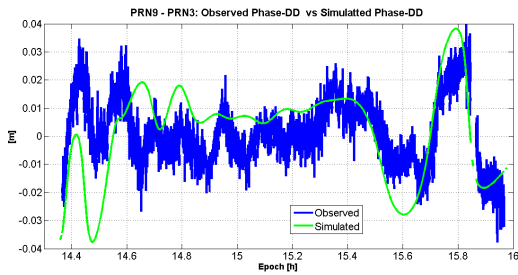
(b) Observed versus Simulated DD phase residuals (PRN9 - PRN1) - Day 2



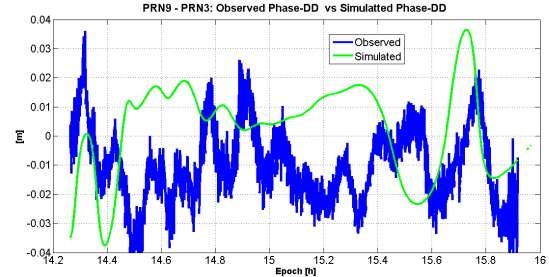
(c) Observed versus Simulated DD phase residuals (PRN9 - PRN2) - Day 1



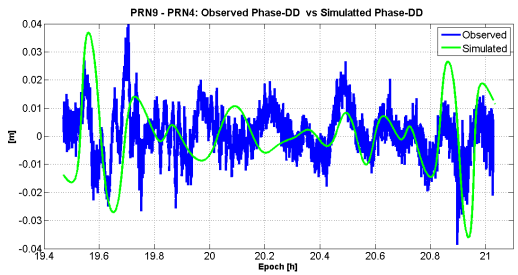
(d) Observed versus Simulated DD phase residuals (PRN9 - PRN2) - Day 2



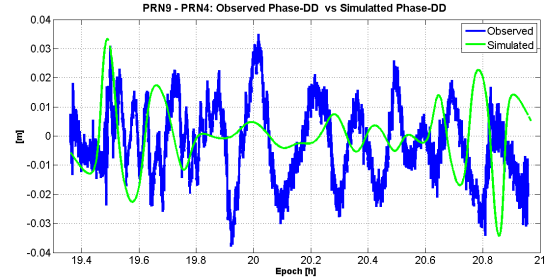
(e) Observed versus Simulated DD phase residuals (PRN9 - PRN3) - Day 1



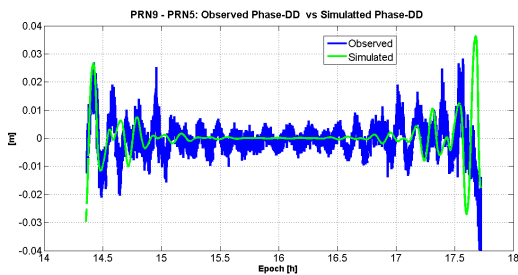
(f) Observed versus Simulated DD phase residuals (PRN9 - PRN3) - Day 2



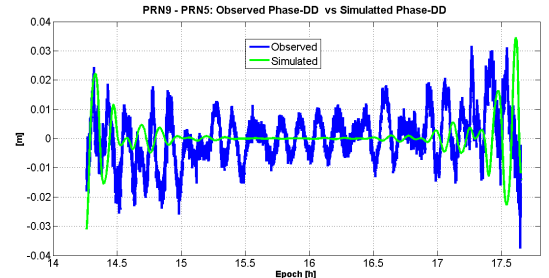
(g) Observed versus Simulated DD phase residuals (PRN9 - PRN4) - Day 1



(h) Observed versus Simulated DD phase residuals (PRN9 - PRN4) - Day 2



(i) Observed versus Simulated DD phase residuals (PRN9 - PRN5) - Day 1



(j) Observed versus Simulated DD phase residuals (PRN9 - PRN5) - Day 2

Figure 6.41.: Observed versus Simulated DD phase residuals of the observed, short baseline, of the second experiment at PTB on 26.02.2013 (left column) and on 27.02.2013 (right column)

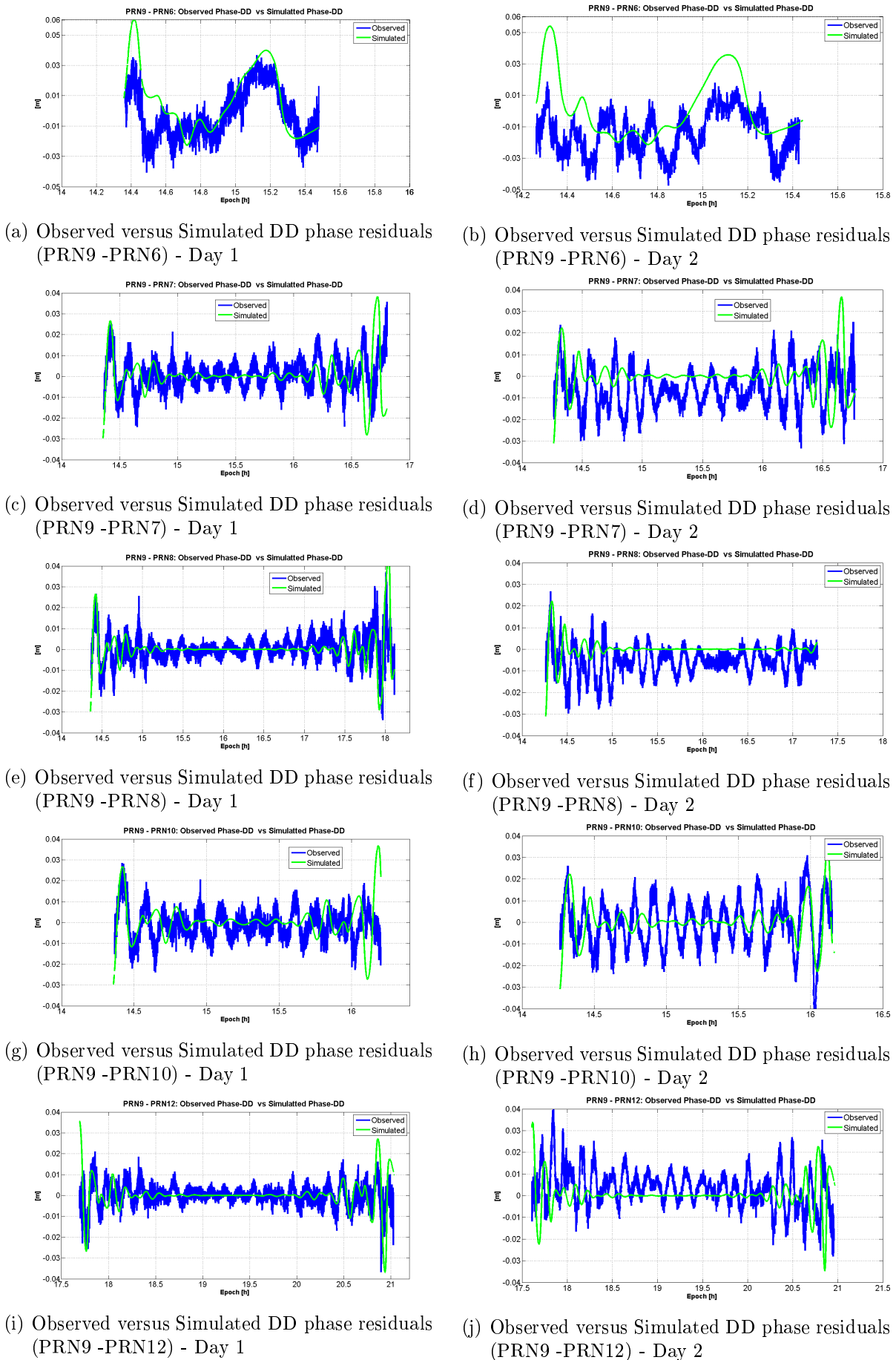
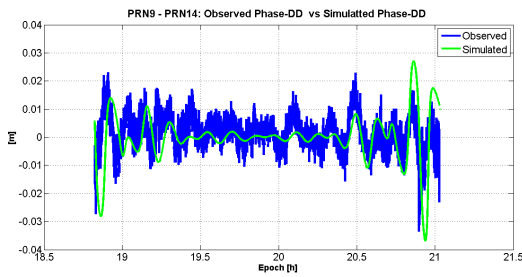
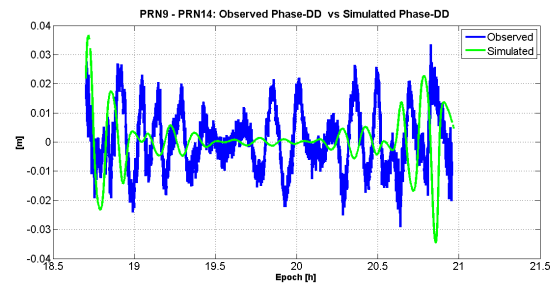


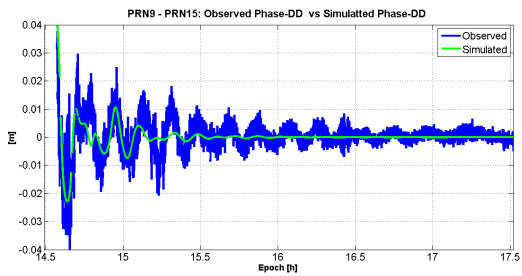
Figure 6.42.: Observed versus Simulated DD phase residuals of the observed, short baseline, of the second experiment at PTB on 26.02.2013 (left column) and on 27.02.2013 (right column)



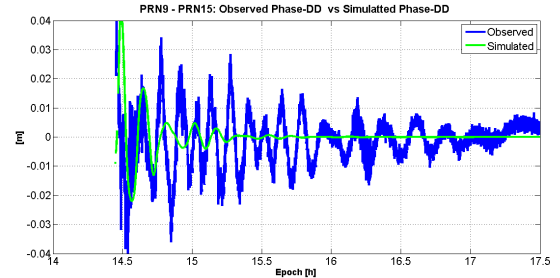
(a) Observed versus Simulated DD phase residuals (PRN9 - PRN14) - Day 1



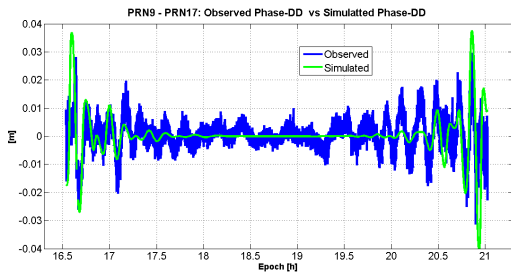
(b) Observed versus Simulated DD phase residuals (PRN9 - PRN14) - Day 2



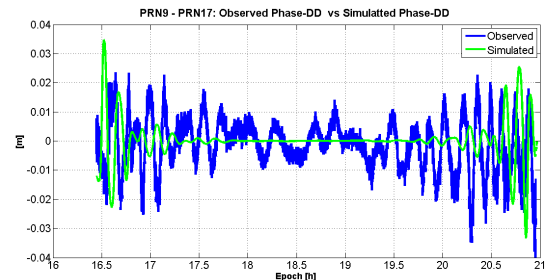
(c) Observed versus Simulated DD phase residuals (PRN9 - PRN15) - Day 1



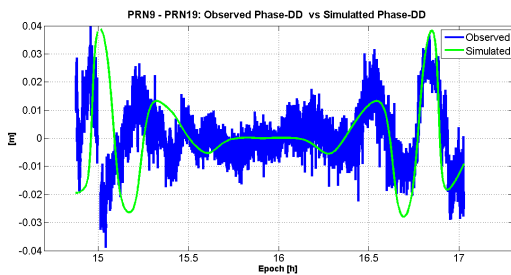
(d) Observed versus Simulated DD phase residuals (PRN9 - PRN15) - Day 2



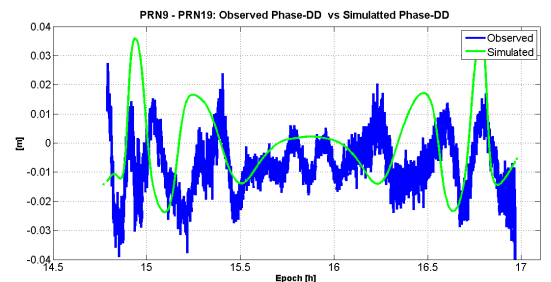
(e) Observed versus Simulated DD phase residuals (PRN9 - PRN17) - Day 1



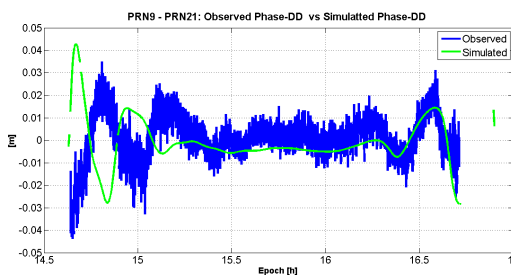
(f) Observed versus Simulated DD phase residuals (PRN9 - PRN17) - Day 2



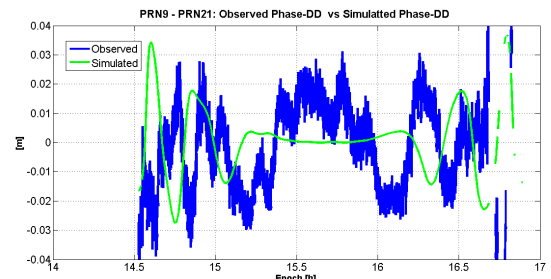
(g) Observed versus Simulated DD phase residuals (PRN9 - PRN19) - Day 1



(h) Observed versus Simulated DD phase residuals (PRN9 - PRN19) - Day 2



(i) Observed versus Simulated DD phase residuals (PRN9 - PRN21) - Day 1



(j) Observed versus Simulated DD phase residuals (PRN9 - PRN21) - Day 2

Figure 6.43.: Observed versus Simulated DD phase residuals of the observed, short baseline, of the second experiment at PTB on 26.02.2013 (left column) and on 27.02.2013 (right column)

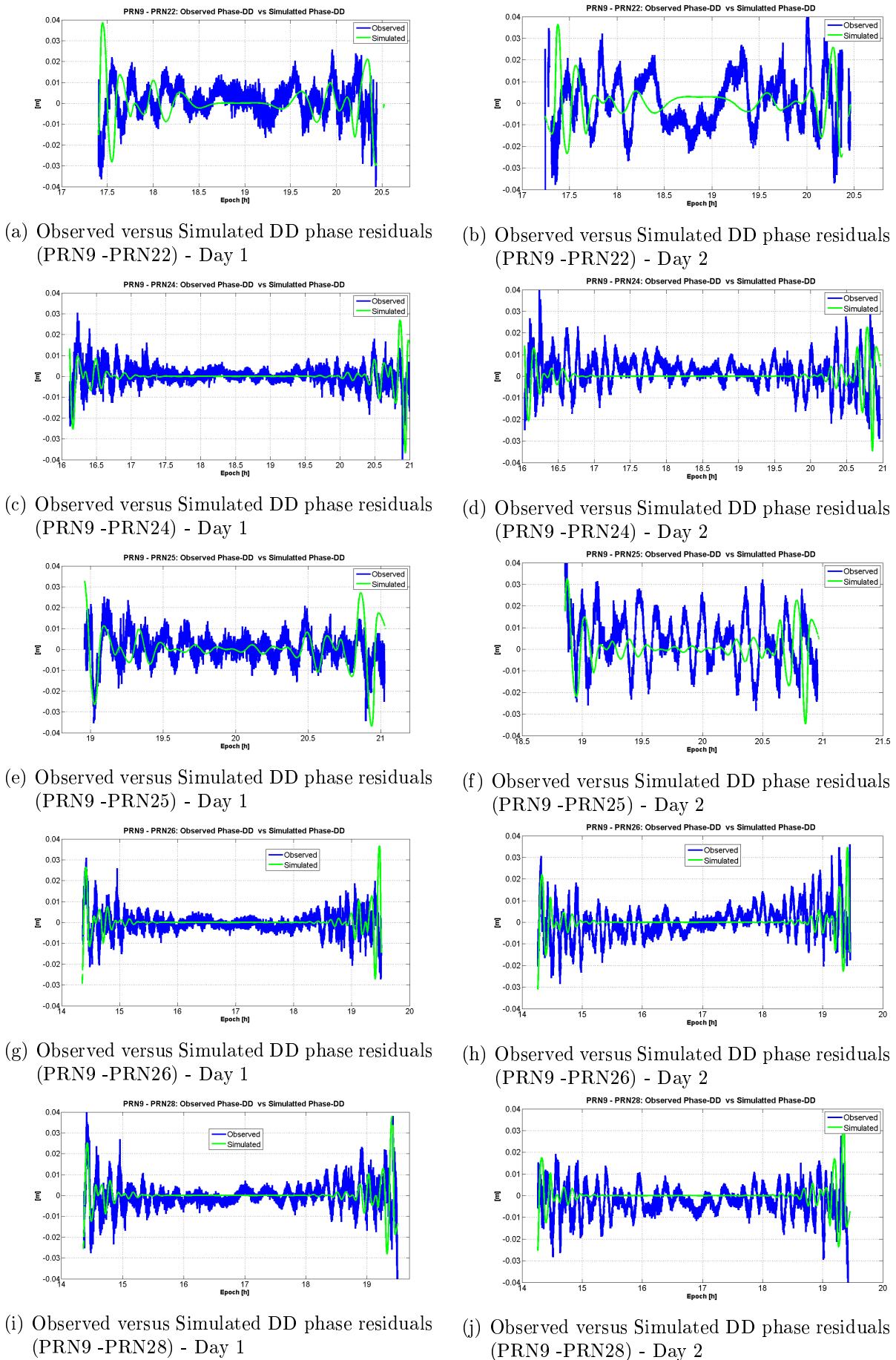
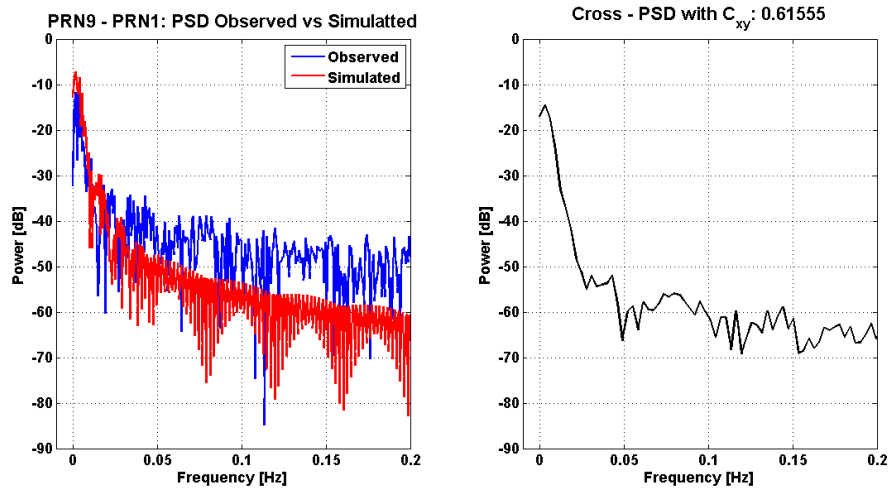
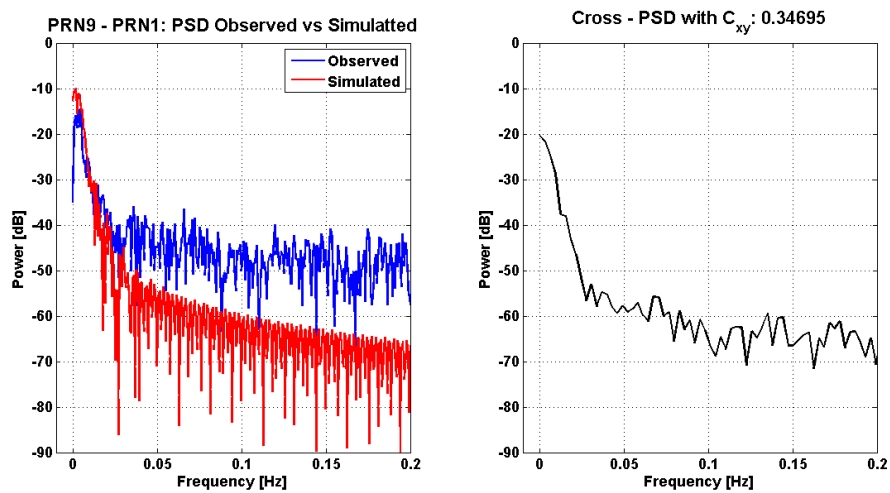


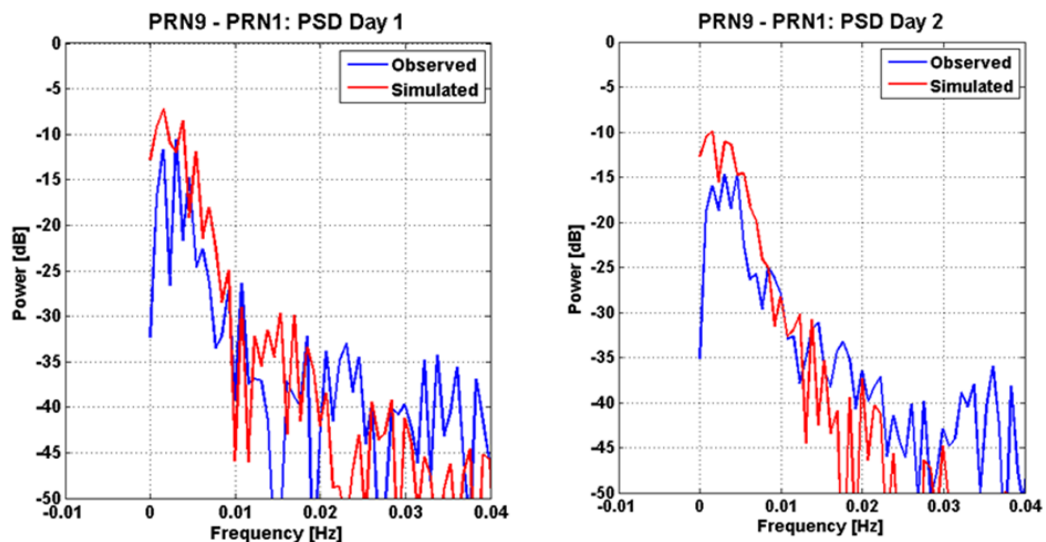
Figure 6.44.: Observed versus Simulated DD phase residuals of the observed, short baseline, of the second experiment at PTB on 26.02.2013 (left column) and on 27.02.2013 (right column)



(a) Left side: PSD for the simulated (in red) versus observed (in blue) phase DDs formed with PRN9 and PRN1. Right side: cross-PSD between the observations and the simulations. Day 1

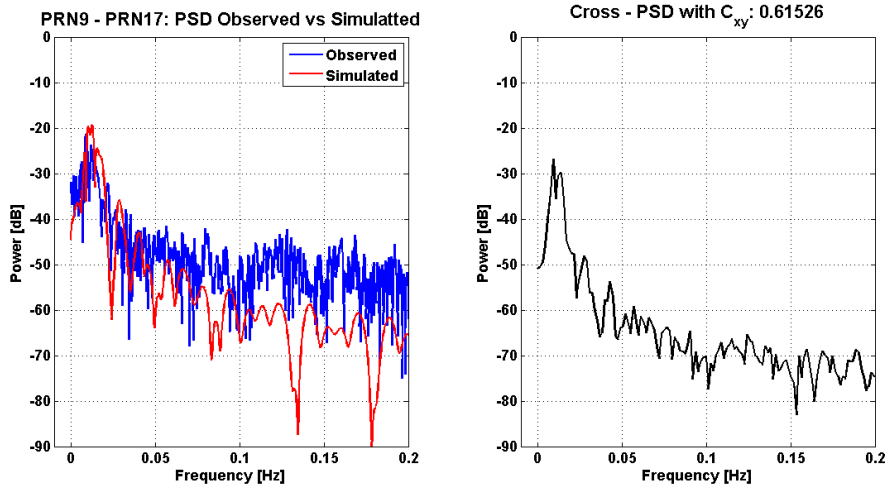


(b) Left side: PSD for the simulated (in red) versus observed (in blue) phase DDs formed with PRN9 and PRN1. Right side: cross-PSD between the observations and the simulations. Day 2

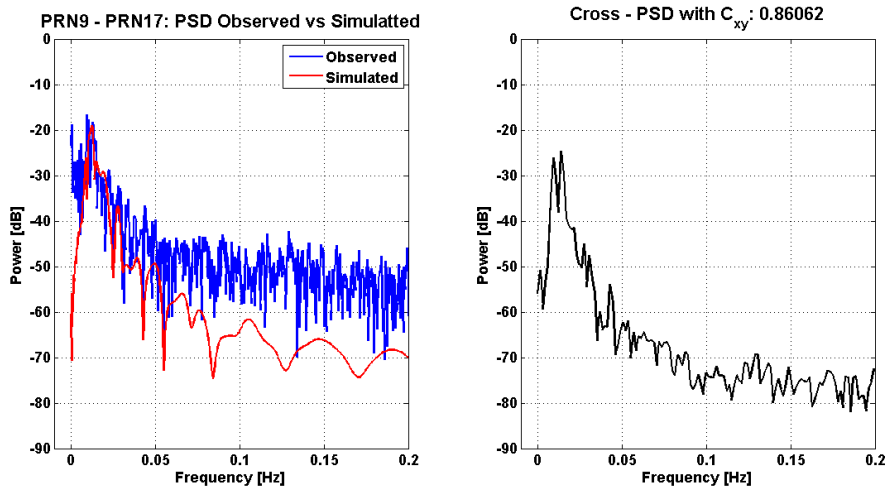


(c) Left side: PSD for the simulated (in red) versus observed (in blue) phase DDs formed with PRN9 and PRN1 for Day 1. Right side: PSD for the simulated (in red) versus observed (in blue) phase DDs formed with PRN9 and PRN1 for Day 2

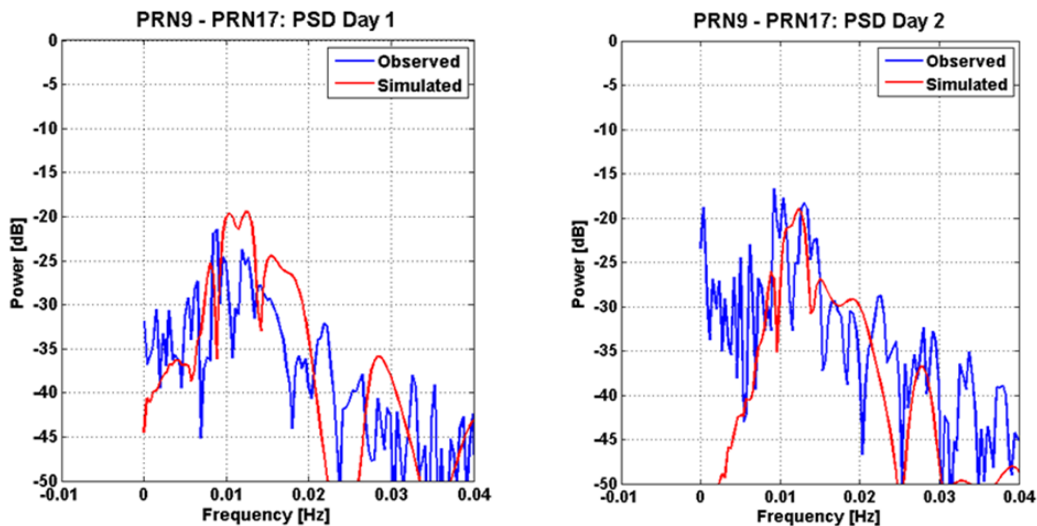
Figure 6.45.: PSD for the simulated (in red) versus observed (in blue) and cross-PSD between the observations and the simulations of the DD residuals formed by PRN9 and PRN1 for both observational days.



(a) Left side: PSD for the simulated (in red) versus observed (in blue) phase DDs formed with PRN9 and PRN17. Right side: cross-PSD between the observations and the simulations. Day 1

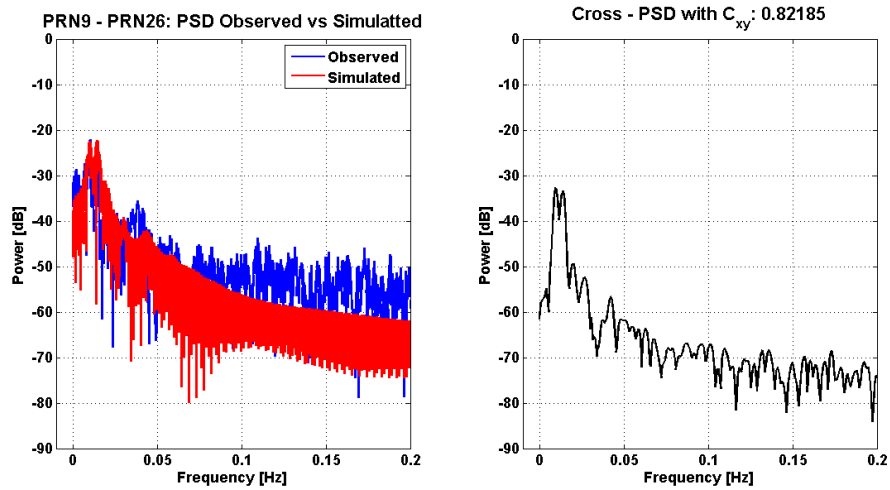


(b) Left side: PSD for the simulated (in red) versus observed (in blue) phase DDs formed with PRN9 and PRN17. Right side: cross-PSD between the observations and the simulations. Day 2

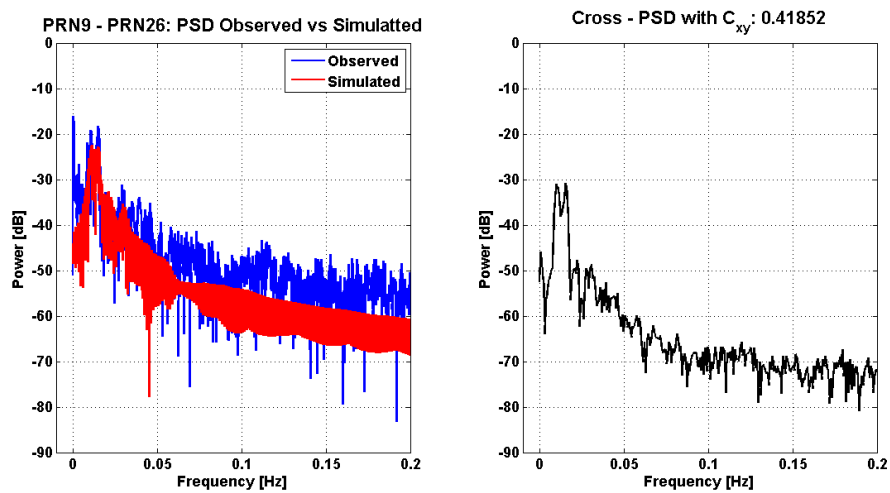


(c) Left side: PSD for the simulated (in red) versus observed (in blue) phase DDs formed with PRN9 and PRN17 for Day 1. Right side: PSD for the simulated (in red) versus observed (in blue) phase DDs formed with PRN9 and PRN17 for Day 2

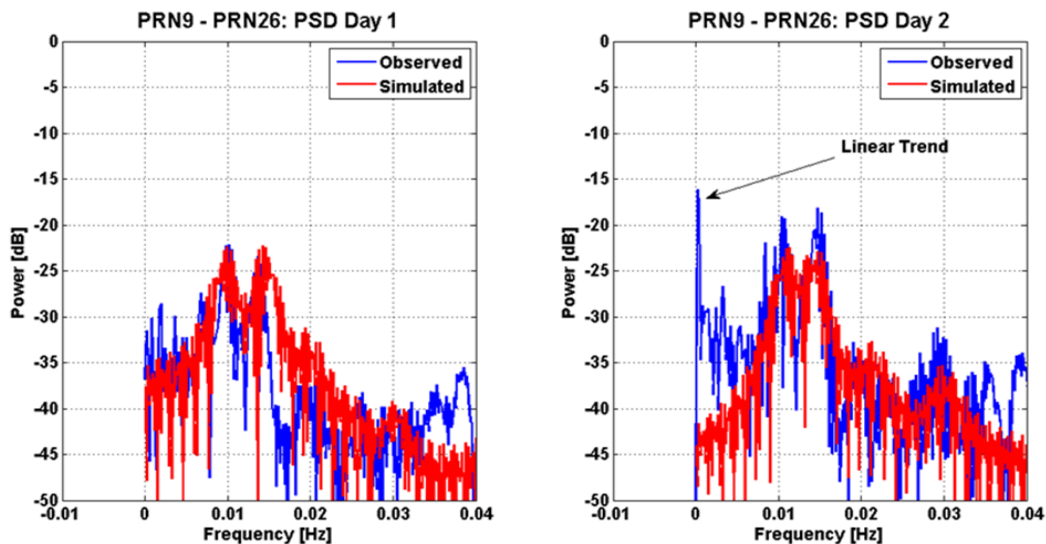
Figure 6.46.: PSD for the simulated (in red) versus observed (in blue) and cross-PSD between the observations and the simulations of the DD residuals formed by PRN9 and PRN17 for both observational days.



(a) Left side: PSD for the simulated (in red) versus observed (in blue) phase DDs formed with PRN9 and PRN26. Right side: cross-PSD between the observations and the simulations. Day 1



(b) Left side: PSD for the simulated (in red) versus observed (in blue) phase DDs formed with PRN9 and PRN26. Right side: cross-PSD between the observations and the simulations. Day 2



(c) Left side: PSD for the simulated (in red) versus observed (in blue) phase DDs formed with PRN9 and PRN26 for Day 1. Right side: PSD for the simulated (in red) versus observed (in blue) phase DDs formed with PRN9 and PRN26 for Day 2

Figure 6.47.: PSD for the simulated (in red) versus observed (in blue) and cross-PSD between the observations and the simulations of the DD residuals formed by PRN9 and PRN26 for both observational days.



DDs	$C_{xy}$	DDs	$C_{xy}$	DDs	$C_{xy}$
PRN9-PRN1	0.6	PRN9-PRN2	0.4	PRN9-PRN3	0.1
PRN9-PRN4	0.5	PRN9-PRN5	0.2	PRN9-PRN6	0.6
PRN9-PRN7	0.3	PRN9-PRN8	0.4	PRN9-PRN10	0.5
PRN9-PRN12	0.4	PRN9-PRN14	0.6	PRN9-PRN15	0.1
PRN9-PRN17	0.6	PRN9-PRN19	0.3	PRN9-PRN21	0.2
PRN9-PRN22	0.7	PRN9-PRN24	0.6	PRN9-PRN25	0.6
PRN9-PRN26	0.8	PRN9-PRN28	0.7		

Table 6.4.: Magnitude squared coherence between the observations and the simulations - Second experiment at PTB, day 1.

DDs	$C_{xy}$	DDs	$C_{xy}$	DDs	$C_{xy}$
PRN9-PRN1	0.3	PRN9-PRN2	0.3	PRN9-PRN3	0.3
PRN9-PRN4	0.2	PRN9-PRN5	0.4	PRN9-PRN6	0.2
PRN9-PRN7	0.4	PRN9-PRN8	0.6	PRN9-PRN10	0.4
PRN9-PRN12	0.7	PRN9-PRN14	0.5	PRN9-PRN15	0.5
PRN9-PRN17	0.9	PRN9-PRN19	0.5	PRN9-PRN21	0.5
PRN9-PRN22	0.7	PRN9-PRN24	0.4	PRN9-PRN25	0.4
PRN9-PRN26	0.4	PRN9-PRN28	0.4		

Table 6.5.: Magnitude squared coherence between the observations and the simulations - Second experiment at PTB, day 2.

### 6.3.7. Discussion

In this section, the analysis of a two days controlled experiment was presented in details. The only difference in the experimental set-up between the two consequent observational days is the different receiving antennas that are used for data capture. The data analysis showed slightly different overall multipath contamination for the two observational days. These small deviations are attributed to the different antennas that were used for data capture.

The time domain comparison of the real with the simulated time series shows an overall better similarity between the observations and the simulations for the first observational day. For the second day, in many cases, the simulations do not match with the observed data. Both phase shifts and differences in the resulting error magnitude can be noticed. The spectral analysis of the time series showed an overall medium level of spectral coherence between the observations and the simulations for both observational days.

Deviations between the observed and the simulated DD phase error as well as of the overall spectral coherence between them are attributed to the same factors as with the first experiment. Deviations between the actual transmitting/receiving antenna gain patterns and the used ones. The time domain plots of the first observational day show an overall closer match. Thus, it can be stated that the used gain patterns and the actual ones are rather similar. Moreover, as it was noticed in the first experiment, the simulated time series showed an overall slightly smaller phase error magnitude for medium and high elevation satellite when compared with the observations. For the second observation day, the deviations are slightly larger and furthermore, 180° phase shifts between the simulation and the observations are identified (e.g. see fig. 6.43j, 6.44b, 6.44f). The spectral coherence between the

simulation and the observations of the second observational day is of a medium level as with the first observational day.

In general, the deviations between observed and simulated data are attributed to geometry variations of the computed path of the reflected signals from the real one. The diffraction and/or shadowing effects from the trees surrounding the grass field that are occurring and are not considered in the simulations. Last but not least, geometry variations between the computed path and the actual one of the reflected signals due to the phase pattern deviations of the receiving antenna for the direct and indirect signals.

## 7. Summary and Conclusions

Multipath propagation is the dominant error source in high precision GNSS applications. Since the beginning of the 70<sup>s</sup> many researchers have been involved in the characterization and modelling of this systematic error source. Despite the large number of approaches developed during the course of these years a universal solution of this problem, in terms of a standard correction model, has not been achieved until the time of writing. The different approaches for the characterization and/or mitigation of multipath effects present in the scientific literature are very diverse. They can be categorized into signal processing approaches, observation domain approaches, antenna related approaches and propagation related approaches.

This work is seen from its author as a research work which attempts to explain the phenomenon and the impact that it has on the GNSS carrier-phase and  $C/N_0$  observables. This thesis is divided as follows. Chapters 2 and 3 present different aspects of the satellite based navigation systems as well as multipath related ones. In chapter 4, we present work which is relevant to pseudo-satellite positioning and the development of dedicated pseudolite navigation algorithms. Additionally, in the framework of this investigation, multipath effects for pseudolite systems are also characterized in terms of residual analysis. In chapter 5 different  $C/N_0$  estimation algorithms and their impact on the signal strength observables is investigated. Chapter 6 is the core of the work. In this chapter, we present the formulation of analytical expressions for the computation/simulation of the impact of multipath propagation on the GNSS observables. A dedicated simulation tool is developed and used in extensive simulation analysis. Two controlled experiments are also performed for the validation of the findings as well as for the algorithm implementation. The thesis is concluded in chapter 7. In appendix A  $C/N_0$  data versus simulations for all the data captured during the two different experiments are illustrated.

The major contribution of this work is the formulation of compact expressions for the computation of the received signal power of both direct and indirect GNSS signal components and the development of an algorithm that evaluates them. The power of the LOS component is computed via the Friis transmission equation. The gain pattern of the transmitting and receiving antennas are modelled by the corresponding Jones vectors. In modelling the antennas patterns in such a way, apart from the gain information, the phase information is also present. The formulation used for the computation of the power of the LOS component is extended for the general case of a MPC by taking into account the reflection process. The specular reflection process is modelled by the Fresnel coefficients that are introduced in the corresponding Jones matrix.

The algorithm input parameters are the satellite position, the receiving antenna position and the gain patterns of the satellite and the receiving antennas. The gain values for the corresponding AoD and AoA of the transmitting/receiving antennas are identified based on the geometry of the scenario and are used for the computation of the Jones vectors of the antennas for the corresponding epoch. Additionally, free space path loss is also computed from the known satellite and receiving antennas positions. In a last step a complex vector multiplication is performed, where the absolute value gives the power information of the received signal component and the imaginary part gives the phase information. The phase of the direct signal is set to a constant value of  $0^\circ$  and of the indirect signal is equal to the relative phase ( $\Delta\Phi$ ) between the direct and indirect signals. The computation of the relative phase includes the impact of the reflection process as well as the impact of the antenna. The corresponding phase error and compound signal power are computed in the last step.

The main goal of this work is to further strengthen the understanding of GNSS multipath. This is achieved by developing a new approach for modelling the impact of multipath propagation on the GNSS observables. This approach can be used as an alternative to pre-existing methods present

in the scientific GNSS literature for quantifying and characterizing multipath effects for positioning and/or remote sensing type of investigations. In this work, multipath characterization is performed in a simple and compact way by the evaluation of one expression for each GNSS observation type. The used expressions are explained in detail together with all involved input parameters. Those are the transmitting/receiving antenna gain patterns, the reflector material properties and the geometrical characteristics of the path of the reflected signals. For the simulation analysis the previously mentioned input parameters are modified in order to simulate and characterize different scenarios.

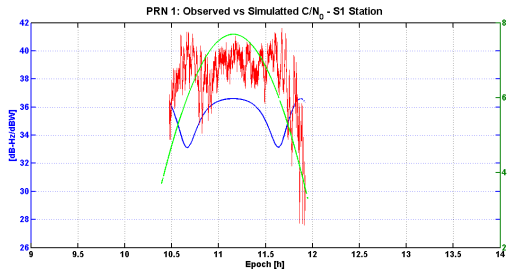
Two controlled experiments as well as the comparison between the captured data and the simulations are presented in detail for the validation of the findings as well as for the characterization of the deviations between the data and the simulations. Those two experiments took place in an area where reflections could occur only from the ground. The flat terrain characteristics of the selected environment allowed the knowledge of the geometrical characteristics of the path of the reflected signals. The experimental set-up of the baseline allowed the isolation of the overall multipath contamination of the phase observables at the two antenna locations. Thus, a comparison with the simulations was possible. The time domain comparison between the simulations and the observations showed consistency for two of the three observational days. For the characterization of the frequency differences between the simulations and the observations, a spectral analysis of the time series was performed. This analysis showed an overall medium level of a spectral coherence.

Deviations between the data and the simulations are attributed to the following factors. Geometry deviations, deviations from the actual antenna gain diagrams and deviations from the actual material properties. Finally, other effects that are present in the data and are not considered for the simulations, i.e. LOS obstruction effects for very low elevation satellites caused by trees, also contribute to the previously mentioned deviations.

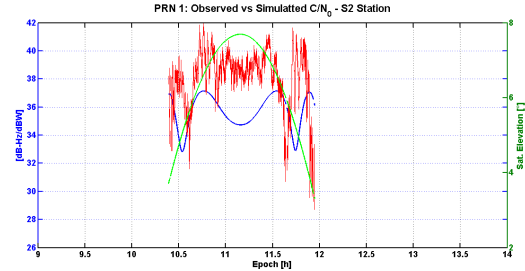
Such compact expressions for the simulation of multipath effects on the GNSS observables has never been presented in the GNSS literature. The commonly used expressions for the impact of multipath propagation on the carrier phase and  $C/N_0$  observables are further generalized by integrating compact expressions for the computation of the received signal power of direct and indirect signal components. Thus, in this work, it is demonstrated that multipath effects on GNSS observables (phase and  $C/N_0$ ) can be characterized in a simple and compact way, for complete satellite arcs.

# A. Data Analysis from PTB Experiments

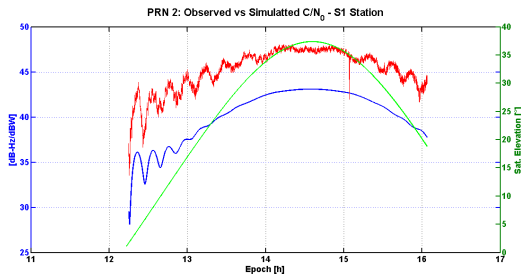
## A.1. First experiment at PTB - $C/N_0$ Observed versus Simulated



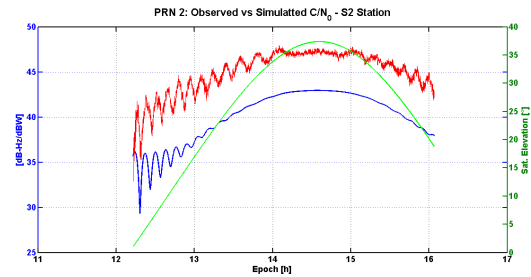
(a) Observed versus Simulated  $C/N_0$ . PRN1 - S1 station



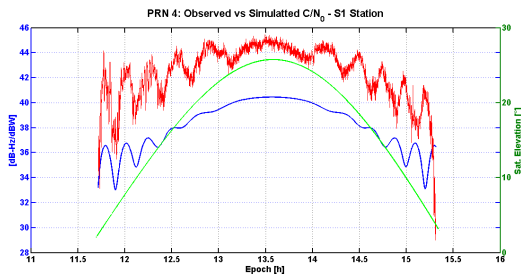
(b) Observed versus Simulated  $C/N_0$ . PRN1 - S2 station



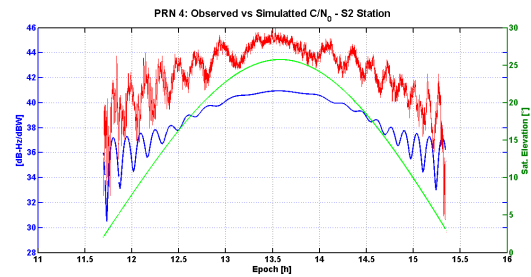
(c) Observed versus Simulated  $C/N_0$ . PRN2 - S1 station



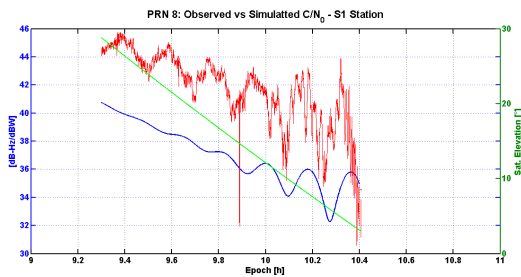
(d) Observed versus Simulated  $C/N_0$ . PRN2 - S2 station



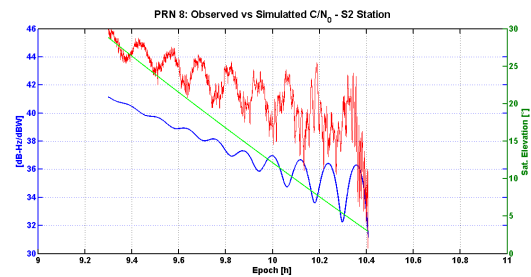
(e) Observed versus Simulated  $C/N_0$ . PRN4 - S1 station



(f) Observed versus Simulated  $C/N_0$ . PRN4 - S2 station

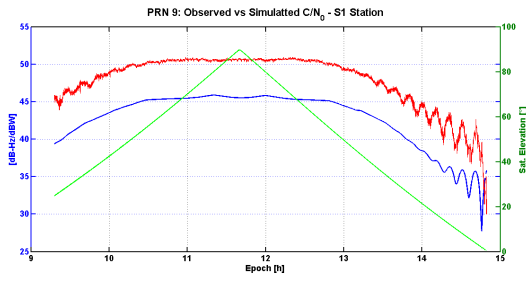
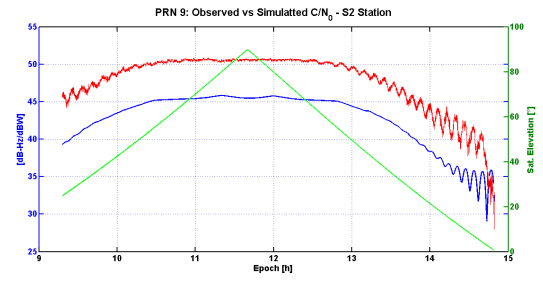
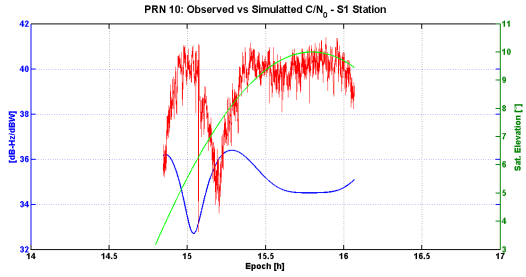
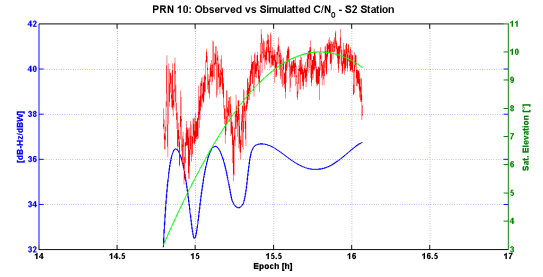
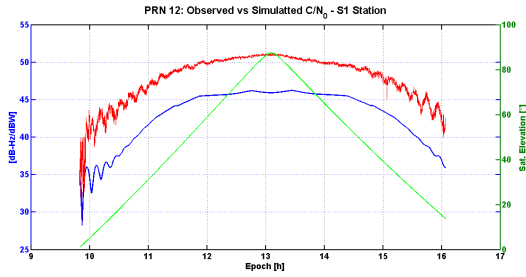
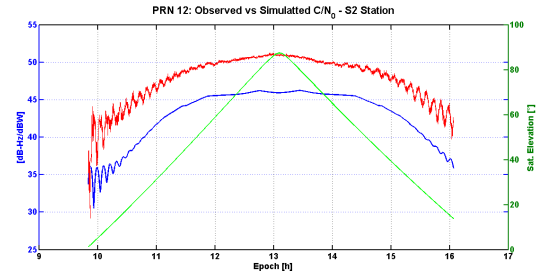
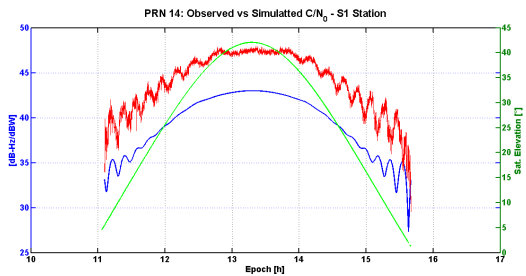
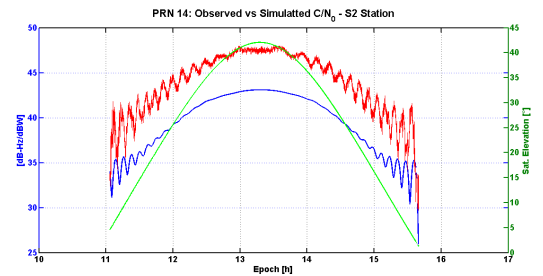
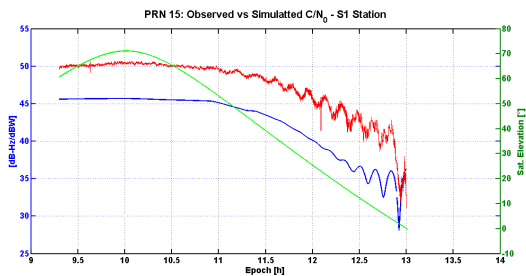
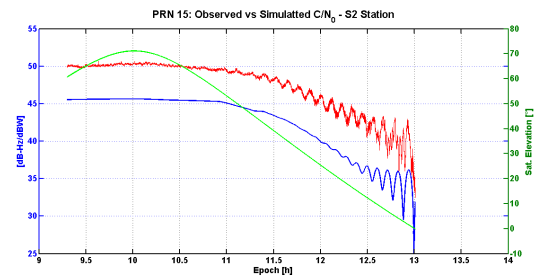


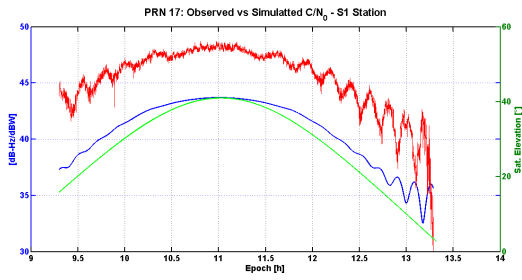
(g) Observed versus Simulated  $C/N_0$ . PRN8 - S1 station



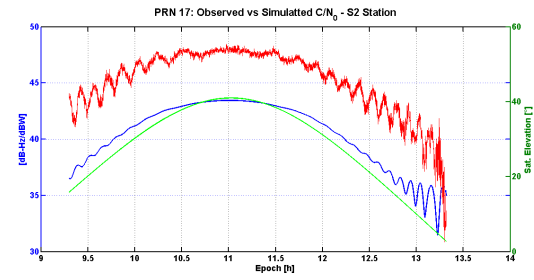
(h) Observed versus Simulated  $C/N_0$ . PRN8 - S2 station

Figure A.1.: Observed versus simulated  $C/N_0$  - First experiment at PTB.

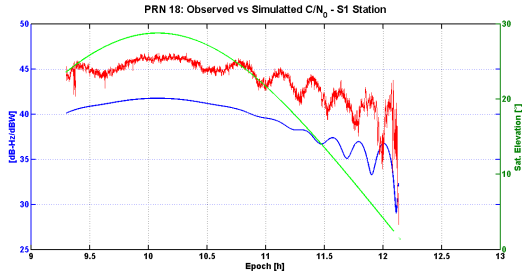
(a) Observed versus Simulated  $C/N_0$ . PRN9 - S1 station(b) Observed versus Simulated  $C/N_0$ . PRN9 - S2 station(c) Observed versus Simulated  $C/N_0$ . PRN10 - S1 station(d) Observed versus Simulated  $C/N_0$ . PRN10 - S2 station(e) Observed versus Simulated  $C/N_0$ . PRN12 - S1 station(f) Observed versus Simulated  $C/N_0$ . PRN12 - S2 station(g) Observed versus Simulated  $C/N_0$ . PRN14 - S1 station(h) Observed versus Simulated  $C/N_0$ . PRN14 - S2 station(i) Observed versus Simulated  $C/N_0$ . PRN15 - S1 station(j) Observed versus Simulated  $C/N_0$ . PRN15 - S2 stationFigure A.2.: Observed versus simulated  $C/N_0$  - First experiment at PTB.



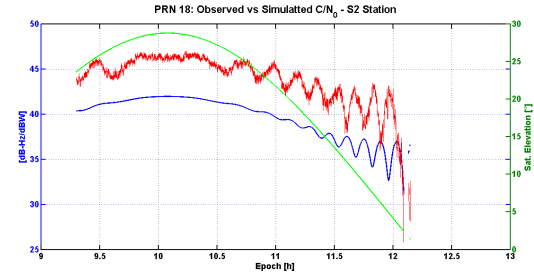
(a) Observed versus Simulated  $C/N_0$ . PRN17 - S1 station



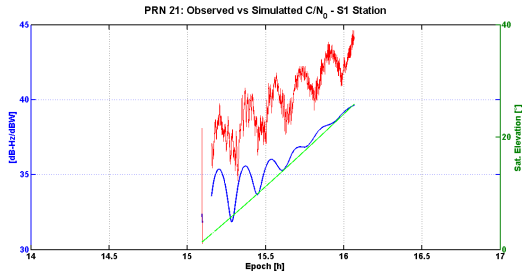
(b) Observed versus Simulated  $C/N_0$ . PRN17 - S2 station



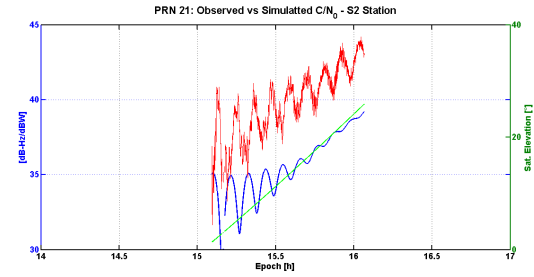
(c) Observed versus Simulated  $C/N_0$ . PRN18 - S1 station



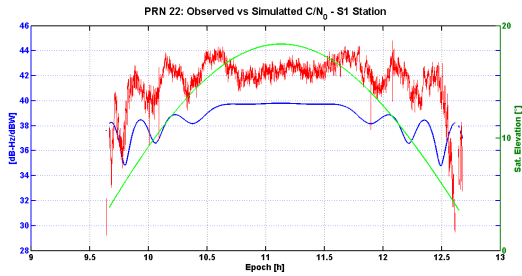
(d) Observed versus Simulated  $C/N_0$ . PRN18 - S2 station



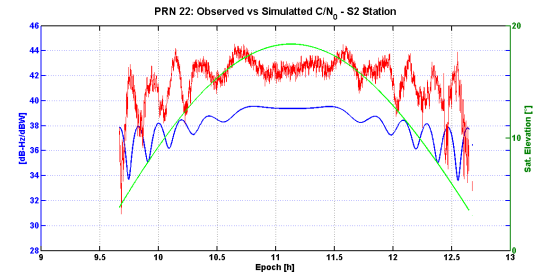
(e) Observed versus Simulated  $C/N_0$ . PRN21 - S1 station



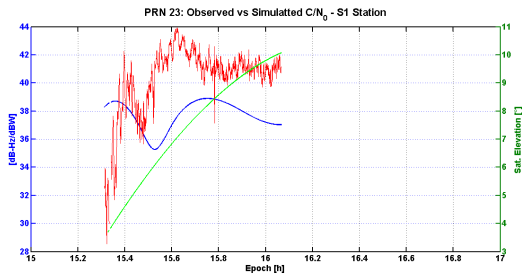
(f) Observed versus Simulated  $C/N_0$ . PRN21 - S2 station



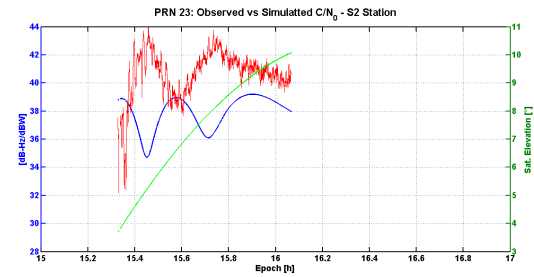
(g) Observed versus Simulated  $C/N_0$ . PRN22 - S1 station



(h) Observed versus Simulated  $C/N_0$ . PRN22 - S2 station

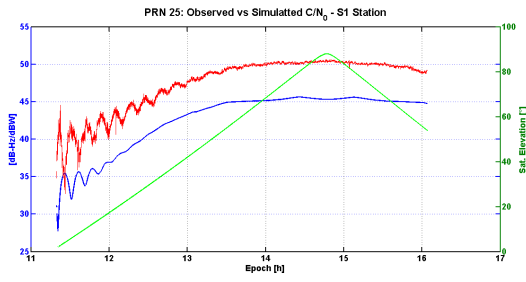
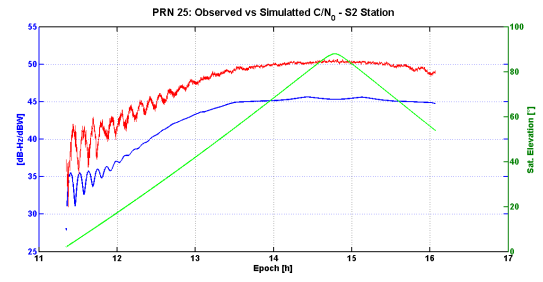
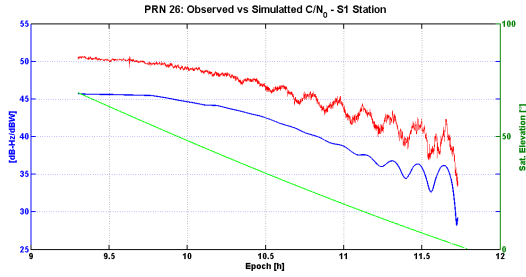
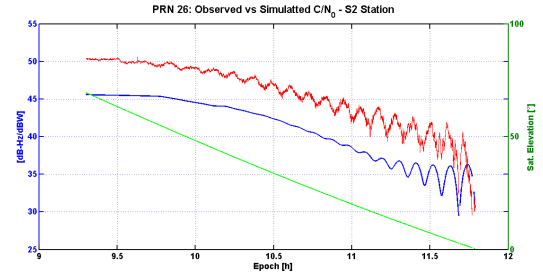
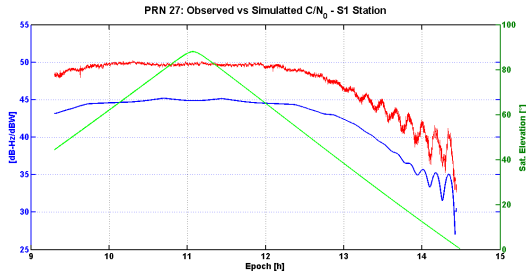
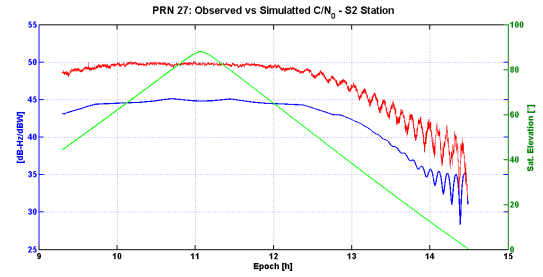
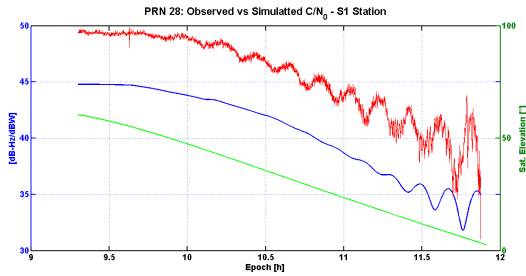
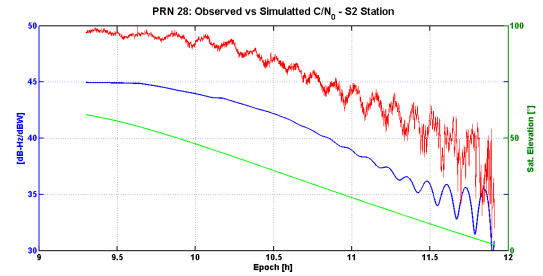
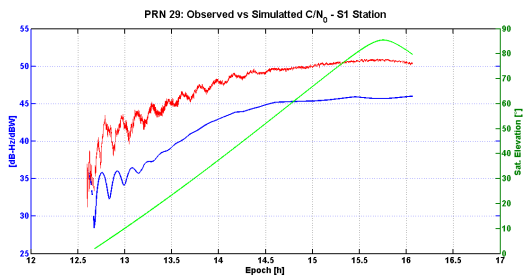
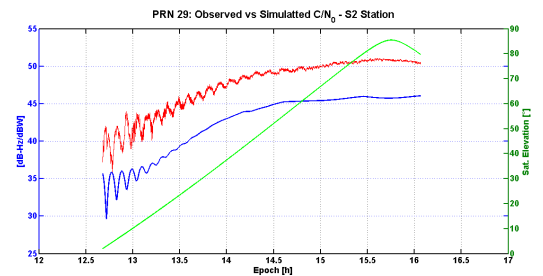


(i) Observed versus Simulated  $C/N_0$ . PRN23 - S1 station

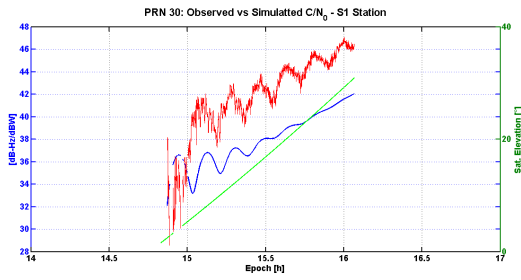


(j) Observed versus Simulated  $C/N_0$ . PRN23 - S2 station

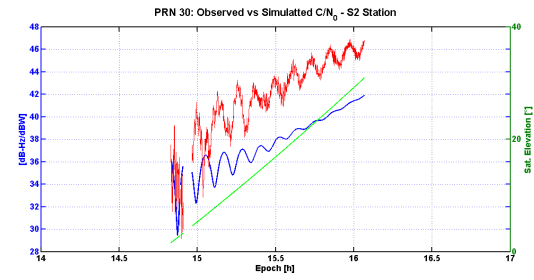
Figure A.3.: Observed versus simulated  $C/N_0$  - First experiment at PTB.

(a) Observed versus Simulated  $C/N_0$ . PRN25 - S1 station(b) Observed versus Simulated  $C/N_0$ . PRN25 - S2 station(c) Observed versus Simulated  $C/N_0$ . PRN26 - S1 station(d) Observed versus Simulated  $C/N_0$ . PRN26 - S2 station(e) Observed versus Simulated  $C/N_0$ . PRN27 - S1 station(f) Observed versus Simulated  $C/N_0$ . PRN27 - S2 station(g) Observed versus Simulated  $C/N_0$ . PRN28 - S1 station(h) Observed versus Simulated  $C/N_0$ . PRN28 - S2 station(i) Observed versus Simulated  $C/N_0$ . PRN29 - S1 station(j) Observed versus Simulated  $C/N_0$ . PRN29 - S2 stationFigure A.4.: Observed versus simulated  $C/N_0$  - First experiment at PTB.

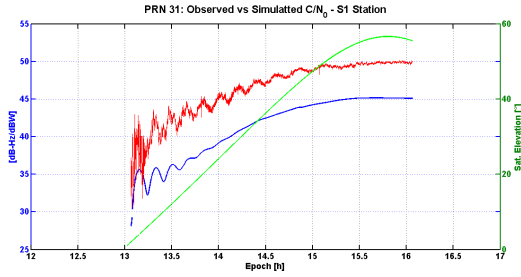




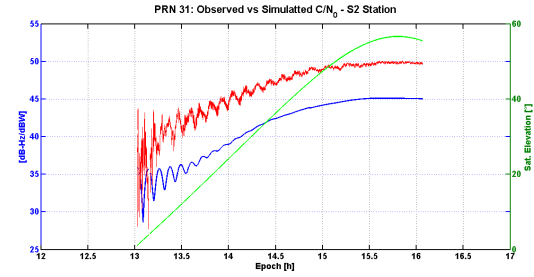
(a) Observed versus Simulated  $C/N_0$ . PRN30 - S1 station



(b) Observed versus Simulated  $C/N_0$ . PRN30 - S2 station



(c) Observed versus Simulated  $C/N_0$ . PRN31 - S1 station

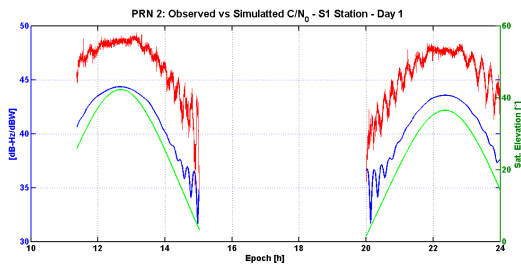


(d) Observed versus Simulated  $C/N_0$ . PRN31 - S2 station

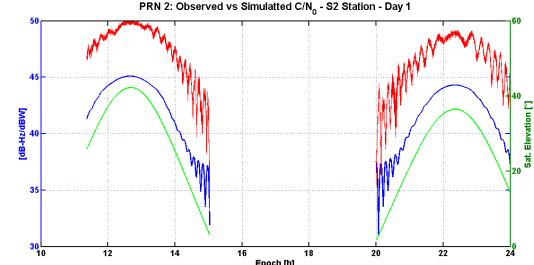
Figure A.5.: Observed versus simulated  $C/N_0$  - First experiment at PTB.

## A.2. Second experiment at PTB

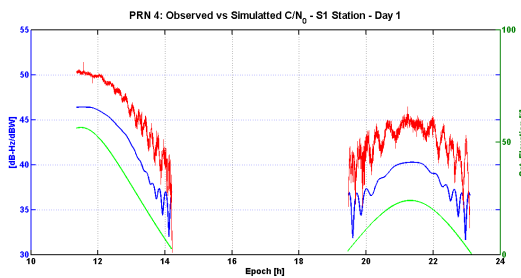
### A.2.1. $C/N_0$ Observed versus Simulated - Day 1



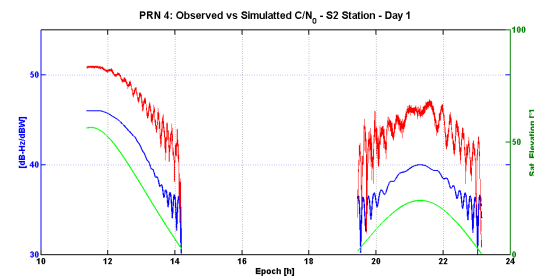
(a) Observed versus Simulated  $C/N_0$ . PRN2 - S1 station



(b) Observed versus Simulated  $C/N_0$ . PRN2 - S2 station

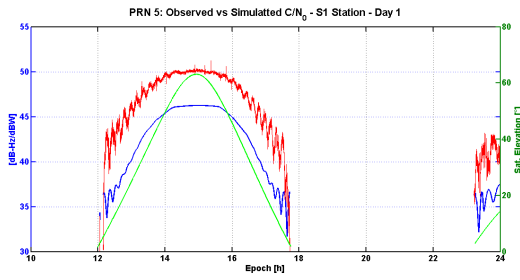
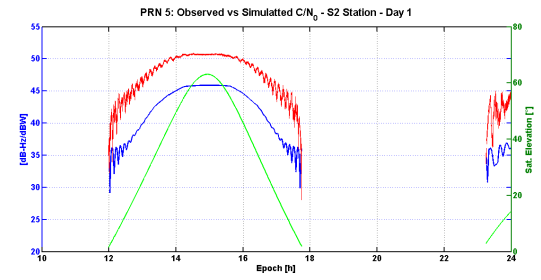
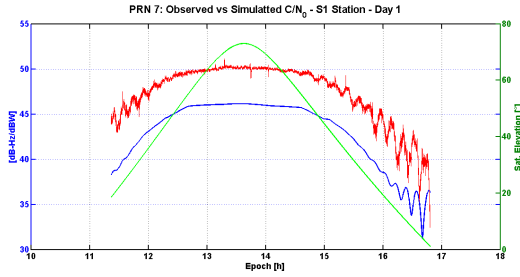
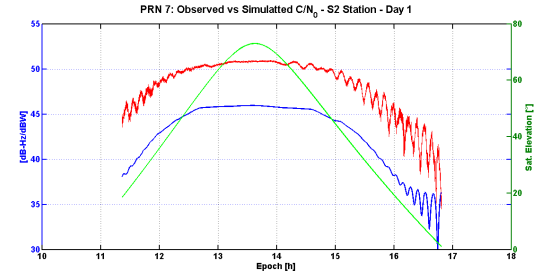
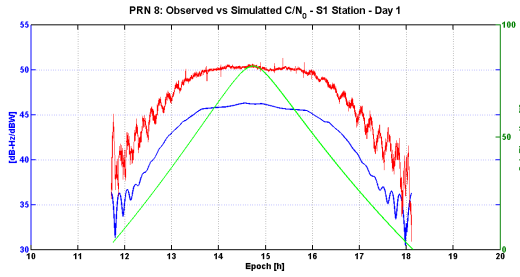
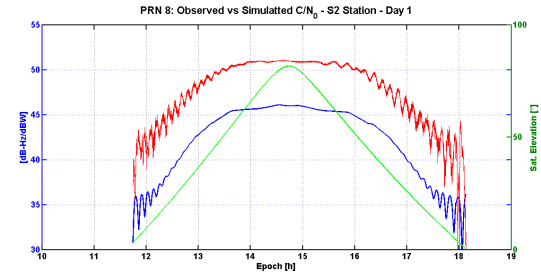
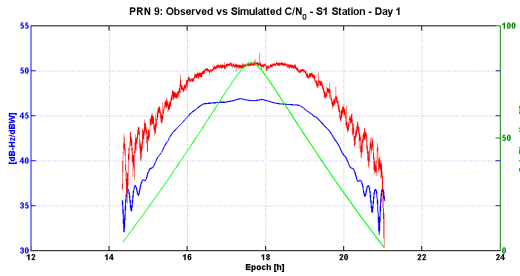
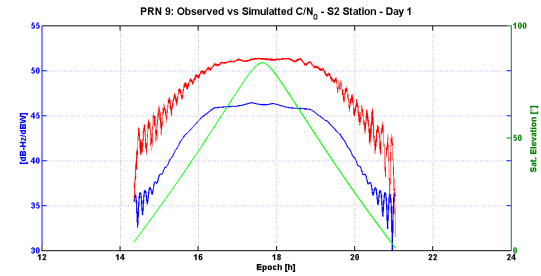
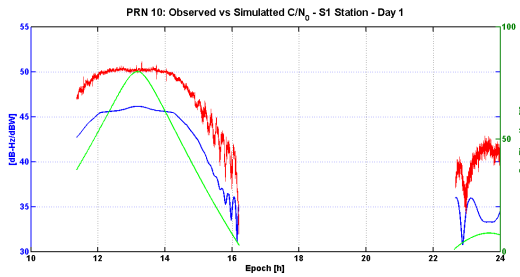
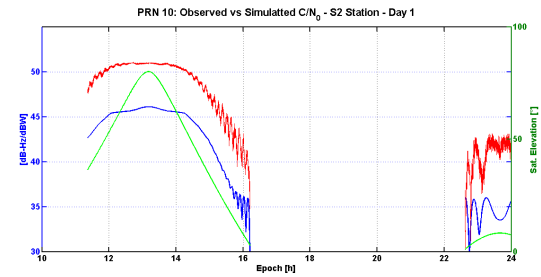


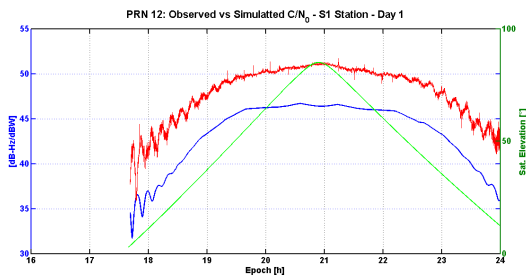
(c) Observed versus Simulated  $C/N_0$ . PRN4 - S1 station



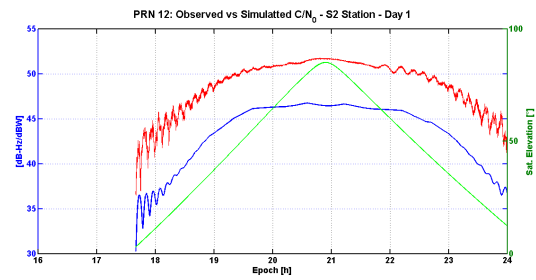
(d) Observed versus Simulated  $C/N_0$ . PRN4 - S2 station

Figure A.6.: Observed versus simulated  $C/N_0$  - Second experiment at PTB - on 26.02.2013.

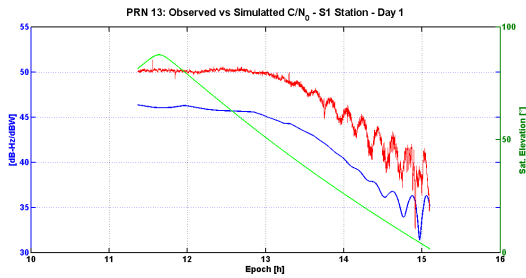
(a) Observed versus Simulated  $C/N_0$ . PRN5 - S1 station(b) Observed versus Simulated  $C/N_0$ . PRN5 - S2 station(c) Observed versus Simulated  $C/N_0$ . PRN7 - S1 station(d) Observed versus Simulated  $C/N_0$ . PRN7 - S2 station(e) Observed versus Simulated  $C/N_0$ . PRN8 - S1 station(f) Observed versus Simulated  $C/N_0$ . PRN8 - S2 station(g) Observed versus Simulated  $C/N_0$ . PRN9 - S1 station(h) Observed versus Simulated  $C/N_0$ . PRN9 - S2 station(i) Observed versus Simulated  $C/N_0$ . PRN10 - S1 station(j) Observed versus Simulated  $C/N_0$ . PRN10 - S2 stationFigure A.7.: Observed versus simulated  $C/N_0$  - Second experiment at PTB - on 26.02.2013.



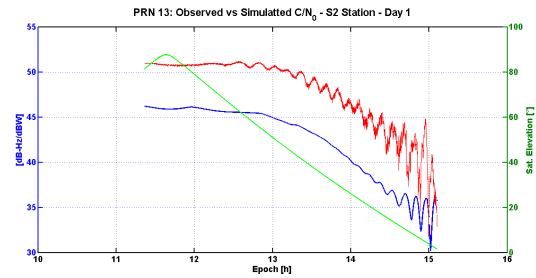
(a) Observed versus Simulated  $C/N_0$ . PRN12 - S1 station



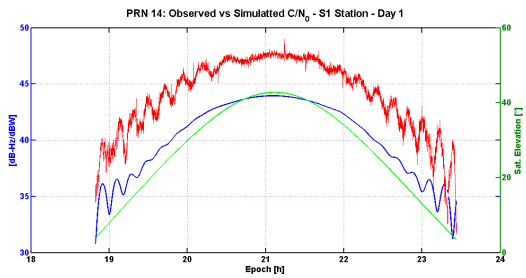
(b) Observed versus Simulated  $C/N_0$ . PRN12 - S2 station



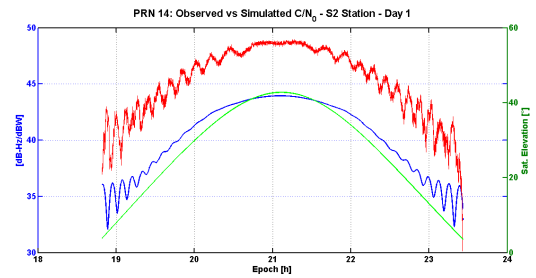
(c) Observed versus Simulated  $C/N_0$ . PRN13 - S1 station



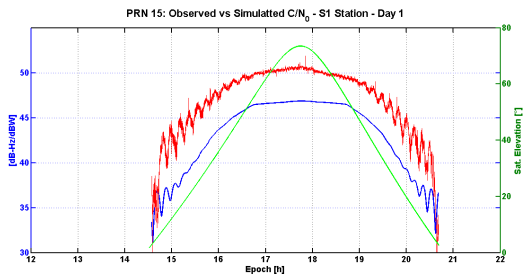
(d) Observed versus Simulated  $C/N_0$ . PRN13 - S2 station



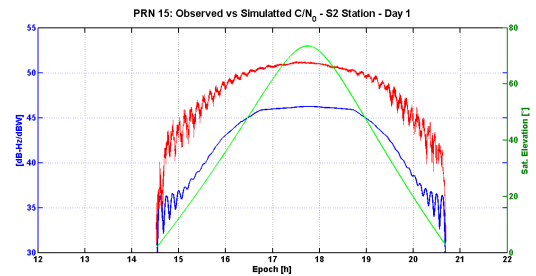
(e) Observed versus Simulated  $C/N_0$ . PRN14 - S1 station



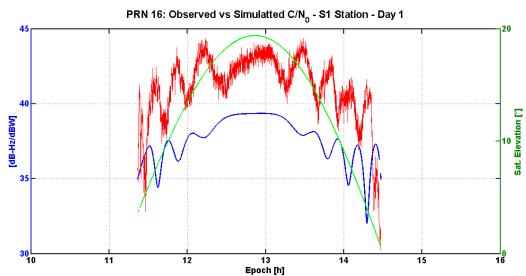
(f) Observed versus Simulated  $C/N_0$ . PRN14 - S2 station



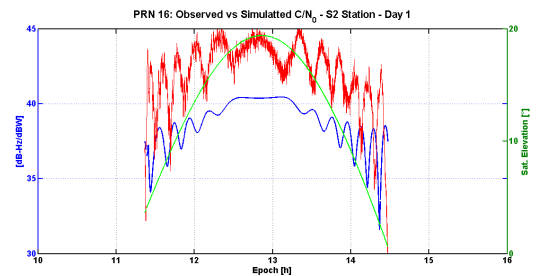
(g) Observed versus Simulated  $C/N_0$ . PRN15 - S1 station



(h) Observed versus Simulated  $C/N_0$ . PRN15 - S2 station

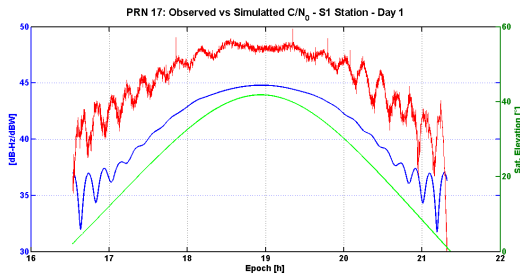
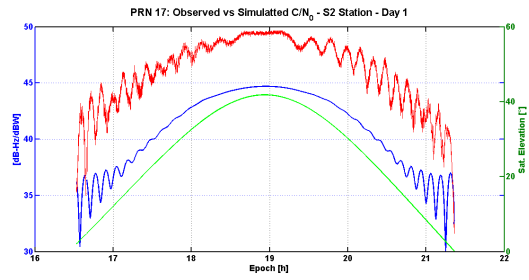
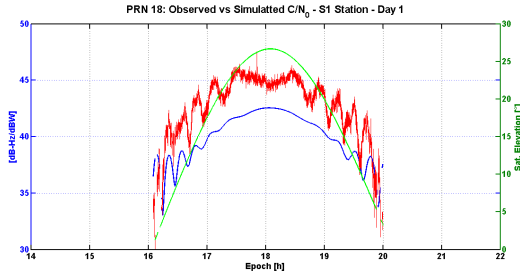
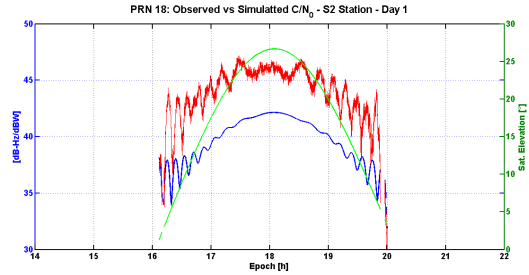
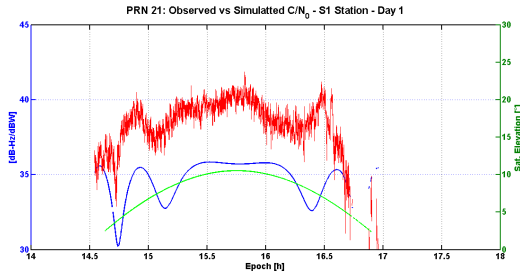
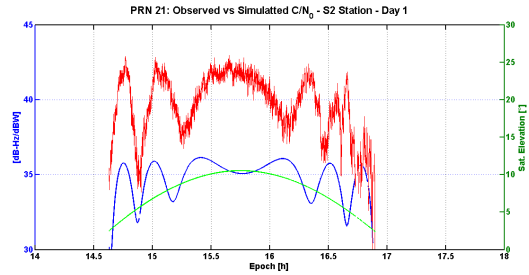
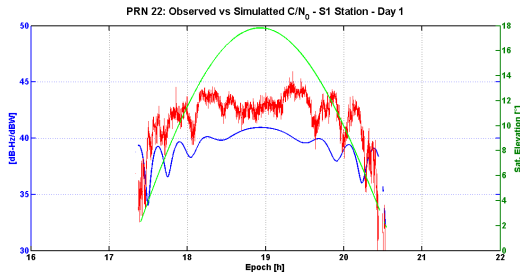
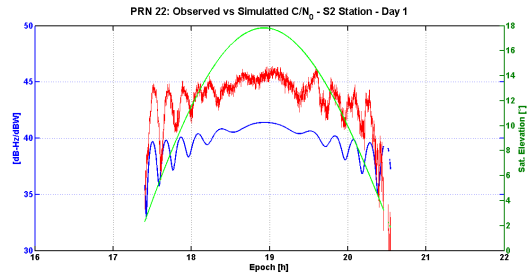
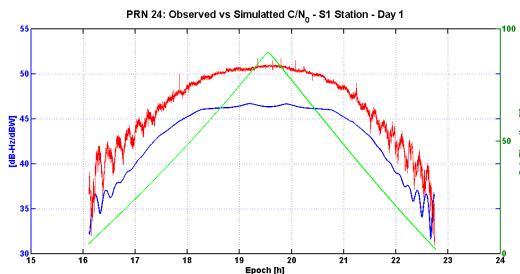
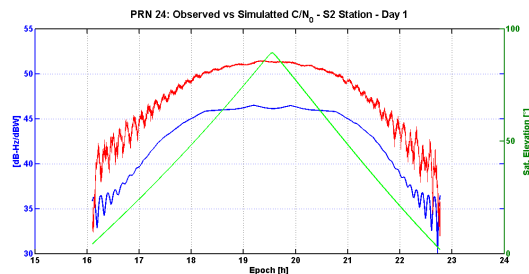


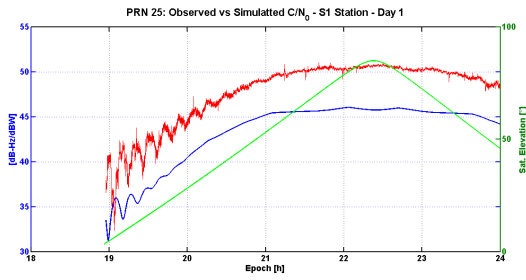
(i) Observed versus Simulated  $C/N_0$ . PRN16 - S1 station



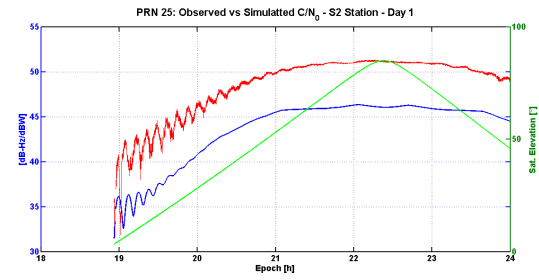
(j) Observed versus Simulated  $C/N_0$ . PRN16 - S2 station

Figure A.8.: Observed versus simulated  $C/N_0$  - Second experiment at PTB - on 26.02.2013.

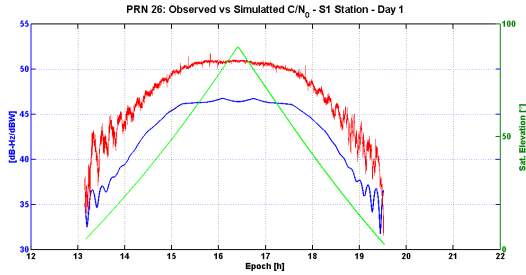
(a) Observed versus Simulated  $C/N_0$ . PRN17 - S1 station(b) Observed versus Simulated  $C/N_0$ . PRN17 - S2 station(c) Observed versus Simulated  $C/N_0$ . PRN18 - S1 station(d) Observed versus Simulated  $C/N_0$ . PRN18 - S2 station(e) Observed versus Simulated  $C/N_0$ . PRN21 - S1 station(f) Observed versus Simulated  $C/N_0$ . PRN21 - S2 station(g) Observed versus Simulated  $C/N_0$ . PRN22 - S1 station(h) Observed versus Simulated  $C/N_0$ . PRN22 - S2 station(i) Observed versus Simulated  $C/N_0$ . PRN24 - S1 station(j) Observed versus Simulated  $C/N_0$ . PRN24 - S2 stationFigure A.9.: Observed versus simulated  $C/N_0$  - Second experiment at PTB - on 26.02.2013.



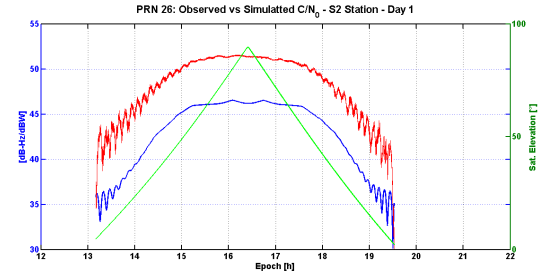
(a) Observed versus Simulated  $C/N_0$ . PRN25 - S1 station



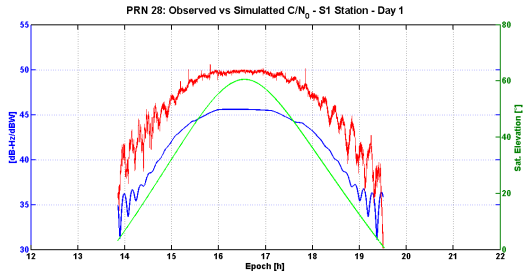
(b) Observed versus Simulated  $C/N_0$ . PRN25 - S2 station



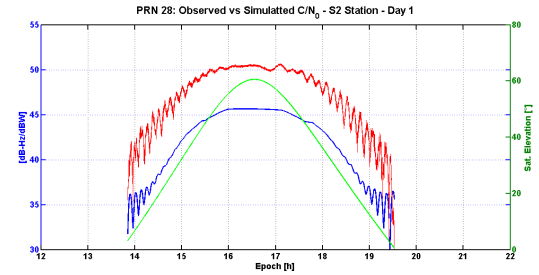
(c) Observed versus Simulated  $C/N_0$ . PRN26 - S1 station



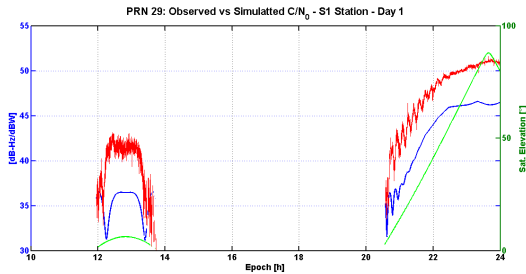
(d) Observed versus Simulated  $C/N_0$ . PRN26 - S2 station



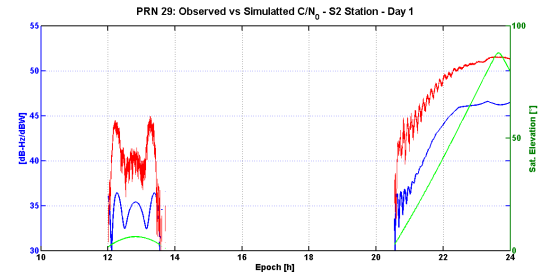
(e) Observed versus Simulated  $C/N_0$ . PRN28 - S1 station



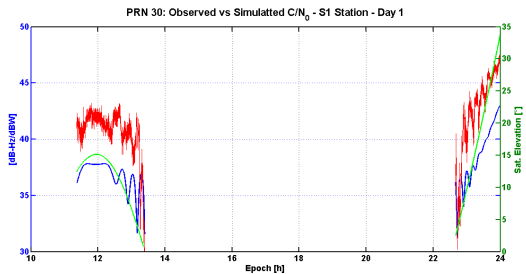
(f) Observed versus Simulated  $C/N_0$ . PRN28 - S2 station



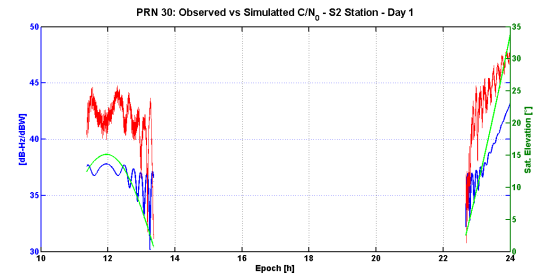
(g) Observed versus Simulated  $C/N_0$ . PRN29 - S1 station



(h) Observed versus Simulated  $C/N_0$ . PRN29 - S2 station

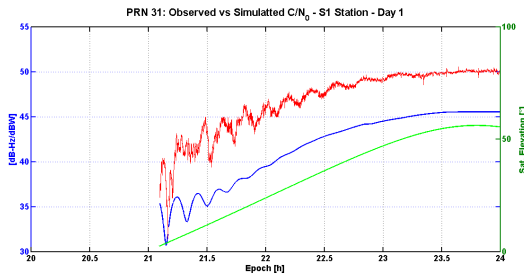
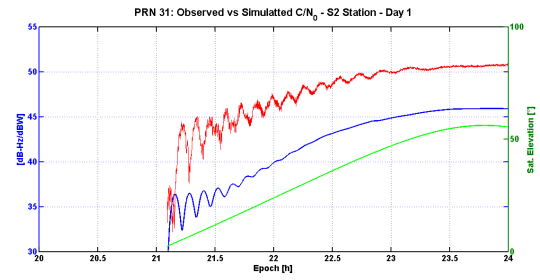


(i) Observed versus Simulated  $C/N_0$ . PRN30 - S1 station

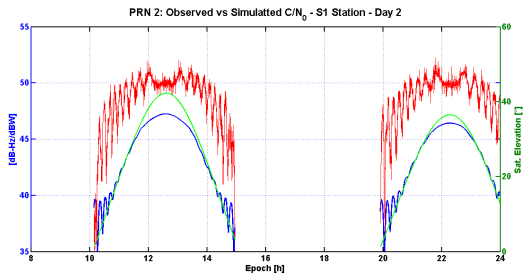
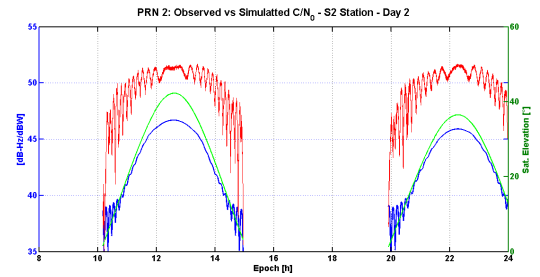
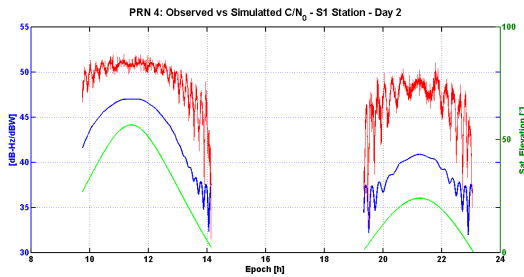
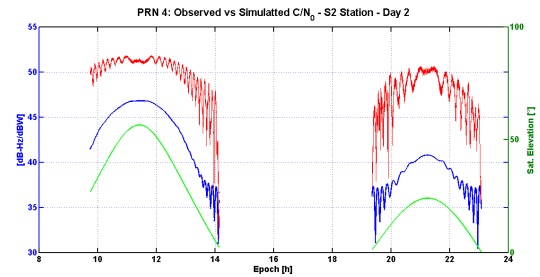
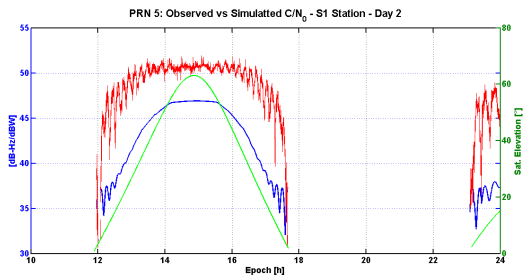
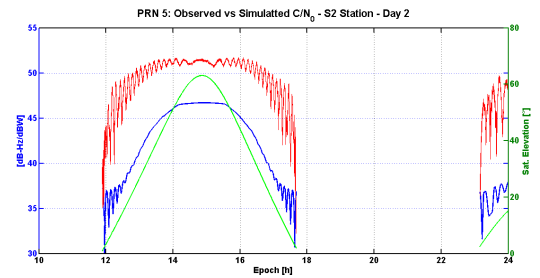


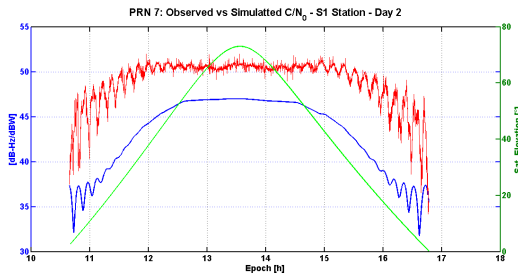
(j) Observed versus Simulated  $C/N_0$ . PRN30 - S2 station

Figure A.10.: Observed versus simulated  $C/N_0$  - Second experiment at PTB - on 26.02.2013.

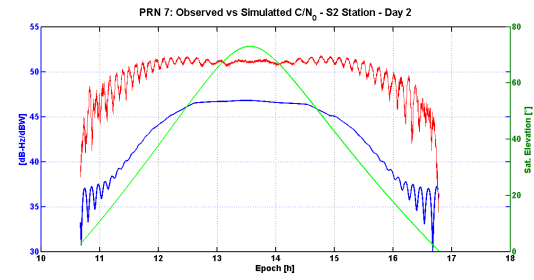
(a) Observed versus Simulated  $C/N_0$ . PRN31 - S1 station(b) Observed versus Simulated  $C/N_0$ . PRN31 - S2 stationFigure A.11.: Observed versus simulated  $C/N_0$  - Second experiment at PTB - on 26.02.2013.

### A.2.2. $C/N_0$ Observed versus Simulated - Day 2

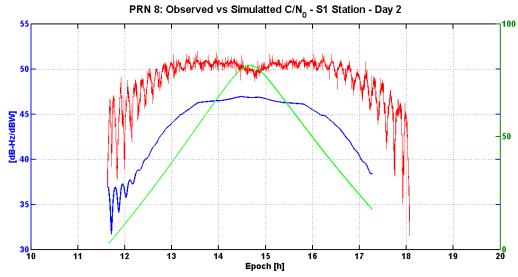
(a) Observed versus Simulated  $C/N_0$ . PRN2 - S1 station(b) Observed versus Simulated  $C/N_0$ . PRN2 - S2 station(c) Observed versus Simulated  $C/N_0$ . PRN4 - S1 station(d) Observed versus Simulated  $C/N_0$ . PRN4 - S2 station(e) Observed versus Simulated  $C/N_0$ . PRN5 - S1 station(f) Observed versus Simulated  $C/N_0$ . PRN5 - S2 stationFigure A.12.: Observed versus simulated  $C/N_0$  - Second experiment at PTB - on 27.02.2013.



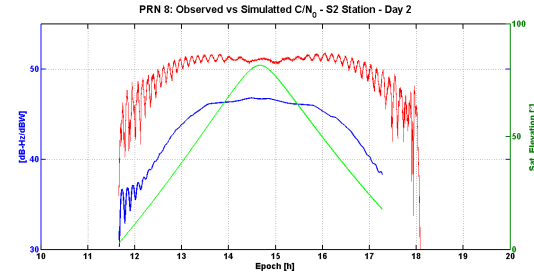
(a) Observed versus Simulated  $C/N_0$ . PRN7 - S1 station



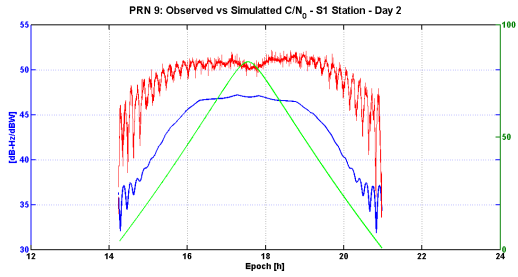
(b) Observed versus Simulated  $C/N_0$ . PRN7 - S2 station



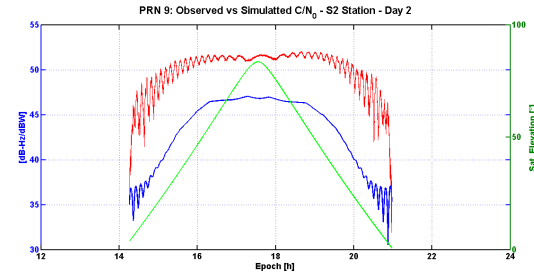
(c) Observed versus Simulated  $C/N_0$ . PRN8 - S1 station



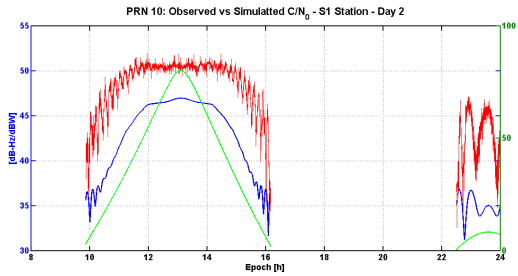
(d) Observed versus Simulated  $C/N_0$ . PRN8 - S2 station



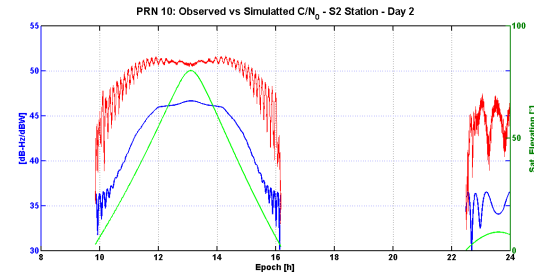
(e) Observed versus Simulated  $C/N_0$ . PRN9 - S1 station



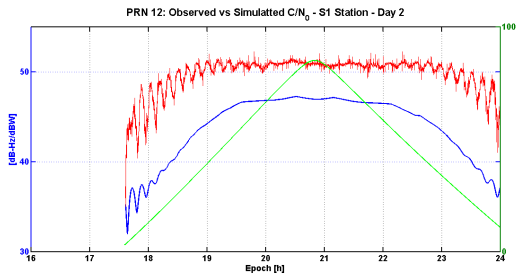
(f) Observed versus Simulated  $C/N_0$ . PRN9 - S2 station



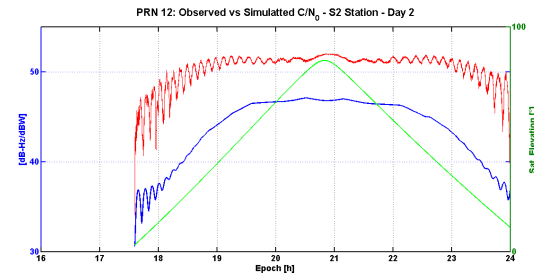
(g) Observed versus Simulated  $C/N_0$ . PRN10 - S1 station



(h) Observed versus Simulated  $C/N_0$ . PRN10 - S2 station

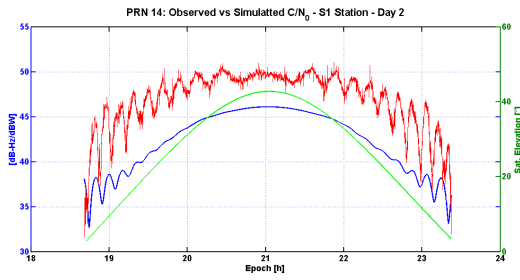
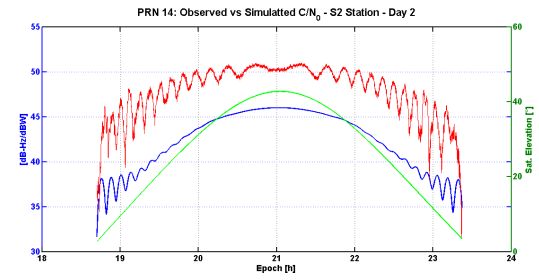
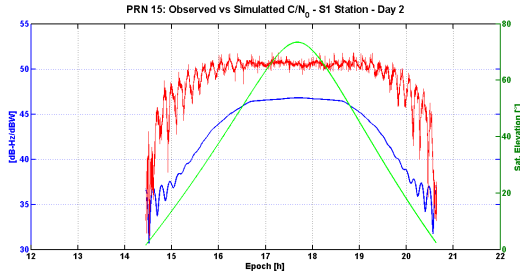
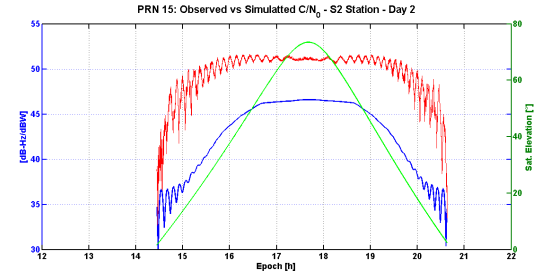
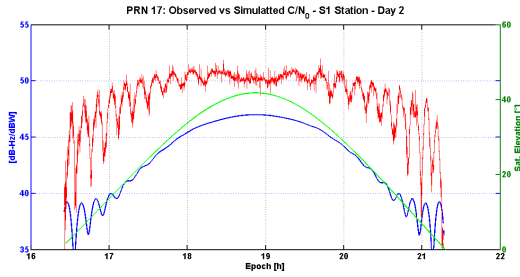
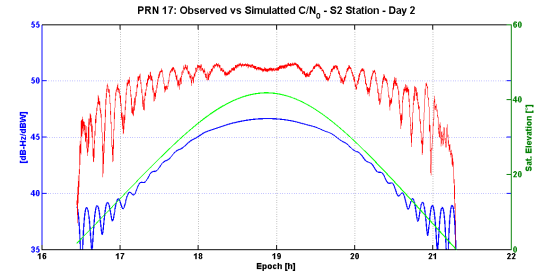
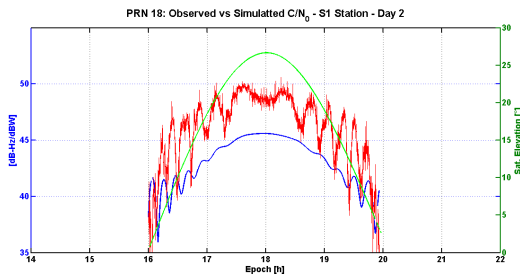
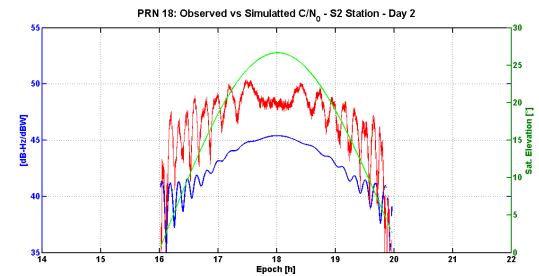
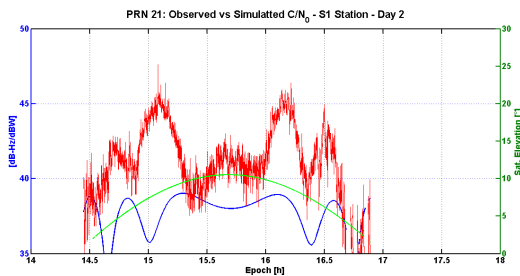
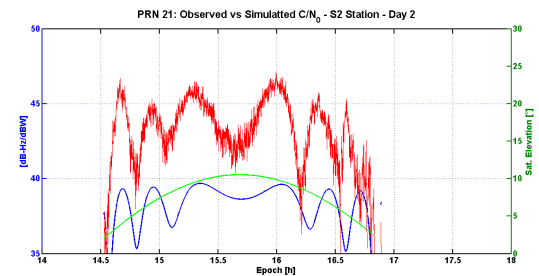


(i) Observed versus Simulated  $C/N_0$ . PRN12 - S1 station

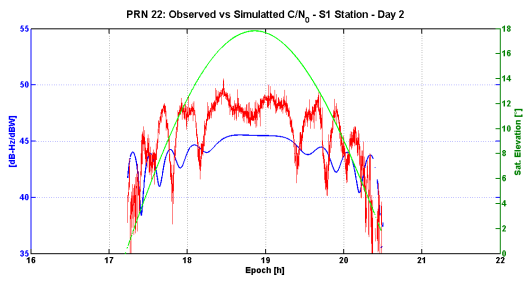
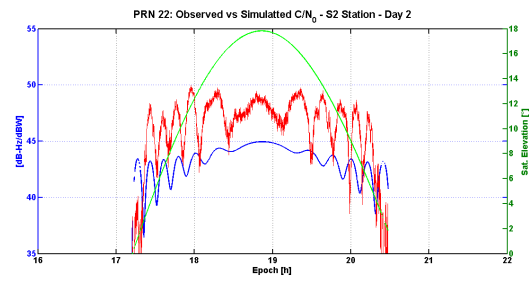
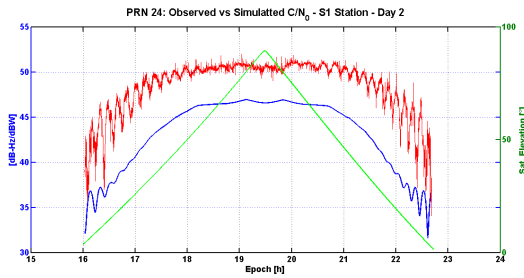
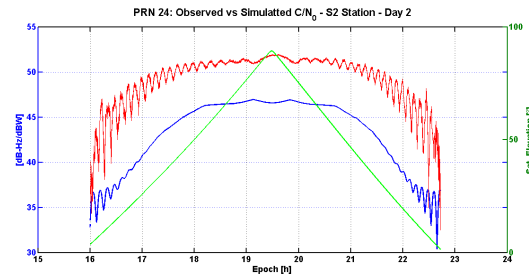
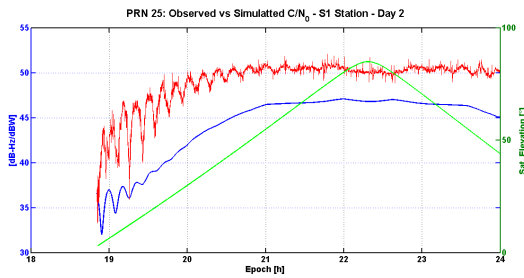
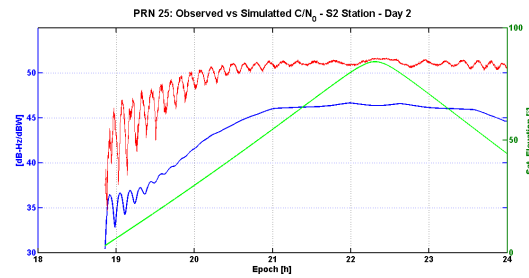
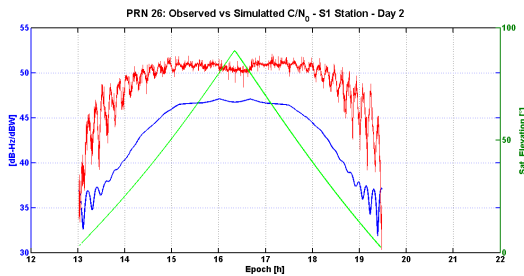
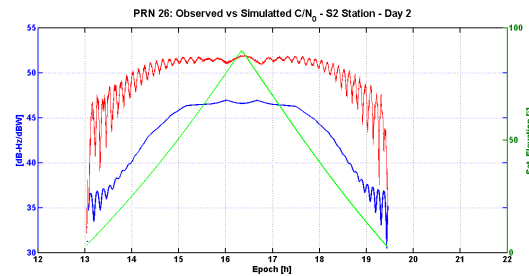
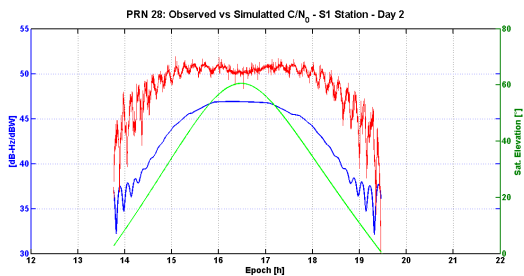
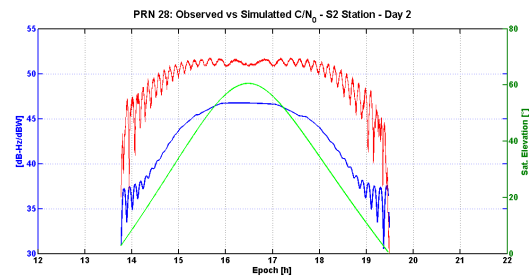


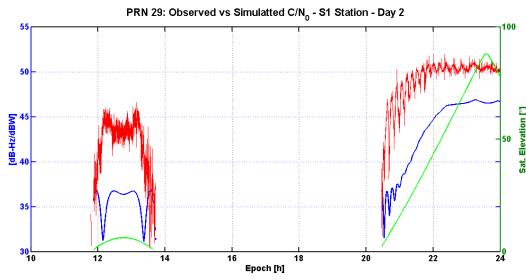
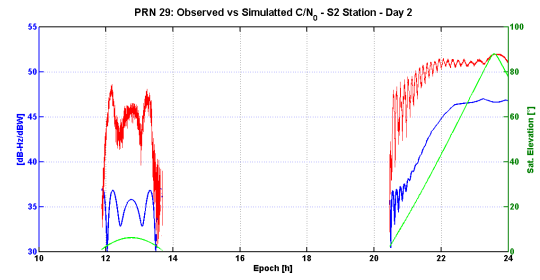
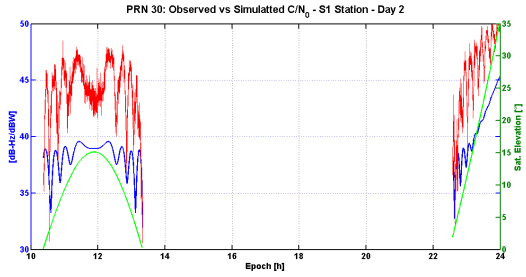
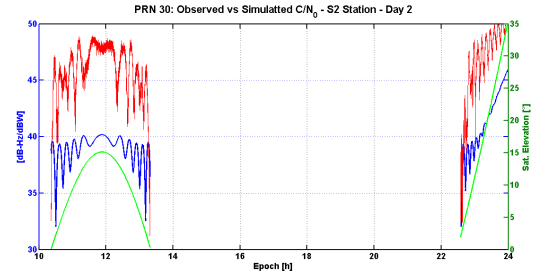
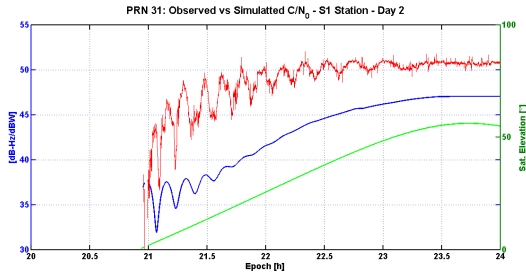
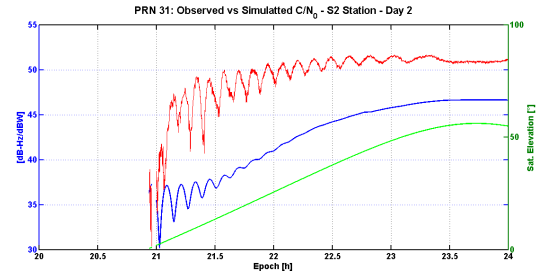
(j) Observed versus Simulated  $C/N_0$ . PRN12 - S2 station

Figure A.13.: Observed versus simulated  $C/N_0$  - Second experiment at PTB - on 27.02.2013.

(a) Observed versus Simulated  $C/N_0$ . PRN14 - S1 station(b) Observed versus Simulated  $C/N_0$ . PRN14 - S2 station(c) Observed versus Simulated  $C/N_0$ . PRN15 - S1 station(d) Observed versus Simulated  $C/N_0$ . PRN15 - S2 station(e) Observed versus Simulated  $C/N_0$ . PRN17 - S1 station(f) Observed versus Simulated  $C/N_0$ . PRN17 - S2 station(g) Observed versus Simulated  $C/N_0$ . PRN18 - S1 station(h) Observed versus Simulated  $C/N_0$ . PRN18 - S2 station(i) Observed versus Simulated  $C/N_0$ . PRN21 - S1 station(j) Observed versus Simulated  $C/N_0$ . PRN21 - S2 stationFigure A.14.: Observed versus simulated  $C/N_0$  - Second experiment at PTB - on 27.02.2013.



(a) Observed versus Simulated  $C/N_0$ . PRN22 - S1 station(b) Observed versus Simulated  $C/N_0$ . PRN22 - S2 station(c) Observed versus Simulated  $C/N_0$ . PRN24 - S1 station(d) Observed versus Simulated  $C/N_0$ . PRN24 - S2 station(e) Observed versus Simulated  $C/N_0$ . PRN25 - S1 station(f) Observed versus Simulated  $C/N_0$ . PRN25 - S2 station(g) Observed versus Simulated  $C/N_0$ . PRN26 - S1 station(h) Observed versus Simulated  $C/N_0$ . PRN26 - S2 station(i) Observed versus Simulated  $C/N_0$ . PRN28 - S1 station(j) Observed versus Simulated  $C/N_0$ . PRN28 - S2 stationFigure A.15.: Observed versus simulated  $C/N_0$  - Second experiment at PTB - on 27.02.2013.

(a) Observed versus Simulated  $C/N_0$ . PRN29 - S1 station(b) Observed versus Simulated  $C/N_0$ . PRN29 - S2 station(c) Observed versus Simulated  $C/N_0$ . PRN30 - S1 station(d) Observed versus Simulated  $C/N_0$ . PRN30 - S2 station(e) Observed versus Simulated  $C/N_0$ . PRN31 - S1 station(f) Observed versus Simulated  $C/N_0$ . PRN31 - S2 stationFigure A.16.: Observed versus simulated  $C/N_0$  - Second experiment at PTB - on 27.02.2013.

## Bibliography

- Agnew, D. and Larson, K. (2007). Finding the repeat times of the GPS constellation. *GPS Solutions*, 11, Pages 71–76.
- AntennaTheory (accessed 16.12.2014). Antenna Theory. <http://www.antenna-theory.com/>.
- Axelrad, P., Comp, C., and Macdoran, P. (2009). SNR-based multipath error corection for GPS differential phase. *IEEE Transaction on Aerospace and Electronic Systems*, 3, Pages 81–87.
- Azzam, R. M. and Bashara, N. M. (1987). *Ellisometry and polarized light*. Elsevier Science Ltd.
- Balanis, C. A. (2005). *Antenna theory, analysis and design*. John Wiley and Sons, Inc. Third edition.
- Bartrop, K., Stafford, J., and Elrod, B. (1996). Local DGPS with pseudoliteaugmentation and implementation considerations for LAAS. Pages 449–459. Proceedings of the 9th International Technical Meeting of the Satellite Division of the Institute of Navigation (GPS ION-96). 17-20 September 1996, Kansas City, Missouri, USA.
- Beckmann, P. (1968). *The depolarization of electromagnetic waves*. THE GOLEM PRESS.
- Beckmann, P. and Spizzichino, A. (1963). *The scattering of electromagnetic waves from rough surfaces*. Pergamon press.
- Bilich, A. (2006). *Improving the Precision and Accuracy of Geodetic GPS: Application to Multipath and Seismology*. PhD thesis, University of Colorado.
- Bilich, A. and Larson, K. M. (2007). Mapping the GPS multipath enviroments using the signal-to-noise ratio (SNR). *Radio Science*, 43.
- Bilich, A., Larson, K., and Axelrad, P. (2008). Modeling GPS phase multipath with SNR: Case study from the Salar de Uyuni, Boliva. *Journal of Geophysical Research*, 113.
- Blackman, R. B. and Tukey, J. W. (1958). *The measurement of power spectra from the point of view of communication engineering*. Dover Publications.
- Blakney, T., Connell, D., Lamberty, B., and Lee, J. (1986). Broad-band antenna sructure having frequency-independent, low loss ground plane . Patent.
- Böder, V. (2002). *Zur hochpräzisen GPS-Positions- und Lagebestimmung unter besonderer Berücksichtigung mariner Anwendungen*. PhD thesis, Leibniz Universität Hannover.
- Böder, V., Menge, F., Seeber, G., Wübbena, G., and Schmitz, M. (2001). How to Deal With Station Dependent Errors - New Developments of Absolute Field Calibration of PCV and Phase-Multipath With a Precise Robot. In *Proceedings of the 14th t International Technical Meeting of the Satellite Division of the Institute of Navigation , Salt Lake City, Utah*.
- Borre, K., Ahoos, D. M., Bertelsen, N., Rinder, P., and Jensen, S. H. (2007). *A Software-Defined GPS and Galileo Receiver*. Birkhäuser Basel.
- Braasch, M. (1996). *Multipath effects, in GPS Positioning System Theory and Applications Vol. 1. Editited by B. W. Parker and J. J. Spiker*, Volume Progress in Astronautics and Aeronautics Vol. 163.

- Bradbury, J., Ziebart, M., Cross, P., Boulton, P., and Read, A. (2007). Code multipath modelling in the urban environment using large virtual reality city models: Determining the local environment. *Journal of Navigation*, 60, Pages 95–105.
- Cardellach, E. (2001). *Sea surphase determination using GNSS reflected signals*. PhD thesis, Universitat Politècnica de Catalunya.
- Chen, X., Parini, C. G., Collins, B., Yao, Y., and Rehman, M. U. (2012). *Antennas for Global Navigation Satellite Systems*. John Wiley and Sons, Ltd Publication, United Kingdom.
- Cobb, H. S. (1997). *GPS Pseudolites: Theory, Design, and Applications*. PhD thesis, Stanford University.
- Cuntz, M., Denks, H., Konovaltsev, A., Hornbostel, A., Dreher, A., and Meurer, M. (2008). GALANT Architecture design and first results of a novel galileo navigation receiver demonstrator with array antennas. In *Proceedings of the 21st International Technical Meeting of the Satellite Division of the Institute of Navigation , Savannah*.
- Dietz, H., Sasum, R., and Kleemann, F. (2010). SEA GATE Standorte Informationsdokument. Technical Report, RST.
- Dilssner, F., Seeber, G., Wübenna, G., and Schmitz, M. (2008). Impact on Near-Field Effects on the GNSS Position Solution. In *Proceedings of the 21st International Technical Meeting of the Satellite Division of The Institute of Navigation (ION GNSS 2008), Savannah, GA, September 16 - 19*.
- DLR (accessed 04.11.2014). DLR - aviationGATE. [http://www.dlr.de/rd/en/desktopdefault.aspx/tabid-5962/9711\\_read-21310/](http://www.dlr.de/rd/en/desktopdefault.aspx/tabid-5962/9711_read-21310/).
- Elósegui, O., Davis, J., Jaldehag, R., Johansson, J., Niell, A., and Shapiro, I. (1995). Geodesy using the Global Positioning System: The effects of signal scattering on estimates of site position. *Journal of Geophysical Research*, 15, Pages 9921–9934.
- Ertan, T., Psiaki, M. L., O’Hanlon, B. W., Merluzzi, R. A., and Powell, S. P. (2013). GNSS Multipath Mitigation using High-Frequency Antenna Motion. In *Proceedings of the 26th International Technical Meeting of the Satellite Division of The Institute of Navigation, Nashville, Tennessee, September 16-20*, Pages 154–175.
- ESA (2015). European GNSS (Galileo) Open Service Signal in Space Interface Control Document. Technical Report, European Space Agency.
- Falletti, E. and Presti, L. L. (2011). Low complexity carrier-to-noise ratio estimators for GNSS digital receivers. *IEEE transaction on aerospace and electronic systems*.
- Fenton, P. and Jones, J. (2005). Theory and Performance of Novatel Inc.’s Vision Correlator. In *Proceedings of the 18th International Technical Meeting of the Satellite Division of The Institute of Navigation , Long Beach, California, September 13 - 16*, Pages 2178–2186.
- Filippov, V., Sutiadin, I., and Ashjaee, J. (1999). Measured Characteristics of Dual Depth Dual Frequency Choke Ring for Multipath Rejection in GPS Receivers. In *Proceedings of the 12th International Technical Meeting of the Satellite Division of the Institute of Navigation (ION GPS 1999), Nashville*, Pages 793–796.
- Flock, W. L. (1987). *Propagation effects on satellite systems at frequencies below 10 GHz*. Nasa reference publication 1108(02).
- Garin, L. and Rousseau, J. (1996). Enhanced Storbe Correlator Multipath Rejection for Code and Carrier. In *Proceedings of the 10th International Technical Meeting of the Satellite Division of The Institute of Navigation (ION GPS 1996), Kansas City, Missouri, September 16 - 19*, Pages 559–568.

- Garrison, J., Katzberg, S., and Howell, C. (1997). Detection of Ocean Reflected GPS Signals: Theory and Experiment. In *Proceedings of the IEEE Engineering new New Century , Southeastcon, Blacksburg, VA*, Pages 290–294.
- Genrich, J. and Bock, Y. (1992). Rapid resolution of crustal motion at short ranges with the global positioning system. *Geophysical Research Letters*, 97, Pages 3261–3269.
- Georgiadou, Y. and Kleusberg, A. (1988). On carrier signal multipath effects in relative GPS positioning. *Manuscripta Geodaetica*, 13, Pages 172–179.
- Giger, K. (2011). Multisatellite Tracking GNSS Receivers in Multipath Environments. In *Proceedings of the 24th International Technical Meeting of the Satellite Division of The Institute of Navigation, Portland OR, September 19-23*, Pages 1140–1151.
- Godsoe, D. A. (2010). *A real-time software GNSS receiver development framework*. PhD thesis, University of New Brunswick.
- Goebell, S. and King, M. A. (2011). Effects of azimuthal multipath asymmetry on long GPS coordinate time series. *GPS Solutions*, 15, Pages 287–297.
- Gold, R. (1967). Optimal binary sequences for spread spectrum multiplexing. *Information Theory, IEEE Transactions on IEEE Transactions on Information Theory*, 13, Pages 619–621.
- Granger, R. and Simpson, S. (2008). An analysis of multipath mitigation techniques suitable for geodetic antennas. In *Proceedings of the 21st International Technical Meeting of the Satellite Division of The Institute of Navigation , Savannah, GA, September 16 - 19*, Pages 2755–2765.
- Granström, C. (2006). *Site-Dependent Effects in High-Accuracy Applications of GNSS*. PhD thesis, Chalmers University of Technology.
- Groves, P. D. (2011). Shadow matching: a new GNSS positioning technique for urban canyons. *Journal of navigation*, , Pages 417–430.
- Groves, P. D., Jiang, Z., Skelton, B., Cross, P. A., Lau, L., Adane, Y., and Kale, I. (2010). Novel Multipath Mitigation Methods using a Dual-polarization Antenna. In *Proceedings of the 23rd International Technical Meeting of the Satellite Division of The Institute of Navigation, Portland, OR, September 21-24*, Pages 140–151.
- Hagerman, L. (1973). Effects on multipath of coherent and non coherent PRN ranging receiver. Technical Report, The Aerospace Corporation.
- Haker, M. E. and Raquet, J. F. (2012). Tracking Multipath in Received GNSS Signals through use of a Signal Decomposition and Parameterization Algorithm. In *Proceedings of the 25th International Technical Meeting of the Satellite Division of The Institute of Navigation, Nashville TN, September 17-21*, Pages 151–156.
- Hannah, B. (2001). *Modeling and Simulation of GPS Multipath Propagation*. PhD thesis, Queensland University of Technology.
- Hartinger, H. and Brunner, F. (1999). Variances of GPS phase observations: the SIGMA- $\epsilon$  model. *GPS Solutions*, 2, Pages 35–43.
- Hatch, R. (1986). Dynamic advanced GPS at the centimeter level. In *Proceedings of the 4th international geodetic symposium on satellite positioning, Austin, Texas*.
- He, Z. and Petovello, M. (2013). Multipath Mitigation by Voting Channel Impulse Response in Navigation Domain with High-sensitivity GNSS Receivers. In *Proceedings of the 26th International Technical Meeting of the Satellite Division of The Institute of Navigation, Nashville, Tennessee, September 16-20*, Pages 2749–2758.

- Hegarty, C. J. and Chatre, E. (2008). Evolution of the Global Navigation Satellite System (GNSS). In *Proceedings of the IEEE*, Volume 96, Pages 1902–1917.
- Helm, A. (2008). *Ground-based GPS Altimetry with the L1 Open GPS receiver using carrier phase-delay observations of reflected GPS signals*. PhD thesis, GFZ Potsdam.
- Hirrlinger, A. and Engler, E. (2010). On Hilbert Huang Transform and its Application to GNSS Signal Multipath Characterization. In *Proceedings of the 23rd International Technical Meeting of the Satellite Division of The Institute of Navigation, Portland, OR, September 21-24*, Pages 217–223.
- Hofmann-Wellenhof, B., Lichtenegger, H., and Wasle, E. (2008). *GNSS Global Navigation Satellite Systems*. Springer Wien New York.
- IEEE (1997). IEEE standard definitions of terms for radio wave propagation. Technical Report, Wave propagation standards committee of the antennas and propagation society.
- IEEE (2003). IEEE standard test procedures for antennas. Technical Report, The institute of electrical and electronics engineers, Inc.
- IEEE (2004). IEEE standard definitions of terms for antennas. Technical Report, Antenna standards committee of the IEEE antennas and propagation society.
- IFEN (accessed 04.11.2014). IFEN - GATE. <http://www.gate-testbed.com/>.
- IGS (accessed 13.11.2014). IGS - Products. <http://www.igs.org>.
- Irsigler, M. (2008). *Multipath propagation, mitigation and monitoring in the light of Galileo and the modernized GPS*. PhD thesis, Bundeswehr University Munich.
- Irsigler, M. (2010). Characterization of multipath phase rates in different multipath environments. *GPS Solutions*, 14, Pages 305–317.
- ITU-R (1992). Electrical characteristics of the surface of the earth. Technical Report, ITU Radiocommunication Assembly.
- Iwabuchi, T., Shoji, Y., Shimada, S., and Nakamura, H. (2004). Tsukuba GPS Dense Net Campaign Observations: Comparison of the Stacking Maps of Post-fit Phase Residuals Estimated from Three Software Packages. *Journal of the Meteorological Society*, 82, Pages 315–330.
- Iwase, T., Suzuki, N., and Watanabe, Y. (2010). Estimation of Multipath Range Error for Detection of Erroneous Satellites. In *Proceedings of the 23rd International Technical Meeting of the Satellite Division of The Institute of Navigation, Portland, OR, September 21-24*, Pages 2228–2235.
- Jackson, M., Meertens, C., Andreatta, V., and Hove, T. V. (2000). GPS Receiver and Antenna Testing Report for SuomiNet. Technical Report, University NAVSTAR Consortium, Boulder CO.
- Jiang, Z., Groves, P. D., Ochieng, W. Y., Feng, S., Milner, C. D., and Mattos, P. G. (2011). Multi-Constellation GNSS Multipath Mitigation Using Consistency Checking. In *Proceedings of the 24th International Technical Meeting of the Satellite Division of The Institute of Navigation, Portland OR, September 19-23, 2011*.
- Jin, S., Cardellach, E., and Xie, F. (2014). *GNSS remote sensing. Theory Methods and Applications*. Springer Netherlands.
- Julien, O. (2005). *A real-time software GNSS receiver development framework*. PhD thesis, University of Calgary.
- Kaplan, E. and Hegarty, C. (2006). *Understanding GPS, Principles and Applications*. ARTECH HOUSE, Boston - London.

- Kelly, J. (2000). Multipath Errors Induced by Electronic Components in Receiver Hardware. In *Proceedings of the 2000 National Technical Meeting of The Institute of Navigation January 26 - 28, Anaheim, CA*, Pages 706–715.
- Kerkhoff, A., Harris, R. B., Petersen, C. P., and Pickard, A. (2010). Modifications to GPS Reference Station Antennas to Reduce Multipath. In *Proceedings of the 23rd International Technical Meeting of the Satellite Division of The Institute of Navigation, Portland, OR, September 21-24*, Pages 866–878.
- Kersten, T. (2014). *Bestimmung von Codephasen-Variationen bei GNSS-Empfangsantennen und deren Einfluss auf die Positionierung, Navigation und Zeitübertragung*. PhD thesis, Leibniz Universität Hannover.
- King, M. A. and Watson, C. S. (2010). Long GPS coordinate time series: Multipath and geometry effects. *Journal of Geophysical Research*, 115.
- Koch, K. R. (1999). *Parameter estimation and hypothesis testing in linear models*. Springer-Verlag Berlin Heidelberg New York.
- Kouyoumjian, R. G. and Pathak, P. H. (1974). A uniform geometrical theory of diffraction for an edge in a perfectly conducting surface. *Proceedings of the IEEE*, 62, Pages 1448–1461.
- Kraus, J. D. (1998). *Antennas*. McGraw-Hill, New York, second edition.
- Kronman, J. D. (2000). Experience using GPS for orbit determination of a geosynchronous satellite. In *Proceedings of the 13th International Technical Meeting of the Satellite Division of The Institute of Navigation, Salt Lake City, UT, September 19-22*, Pages 1622–1626.
- Kuusniemi, H., Bhuiyan, M., Ström, M., Söderholm, S., Jokitalo, T., Cheng, L., and Chen, R. (2012). Utilizing pulsed pseudolites and high-sensitivity GNSS for ubiquitous outdoor/indoor satellite navigation. Indoor Positioning and Indoor Navigation (IPIN). 13-15 Nov. 2012, Sydney, Australia.
- Langer, M., Kiesel, S., Kief, K.-F., and Trommer, G. F. (2011). Simulation and efficient Implementation of a Multipath Estimating Delay Locked Loop using FIMLA Algorithm. In *Proceedings of the 24th International Technical Meeting of the Satellite Division of The Institute of Navigation, Portland OR, September 19-23*, Pages 1152–1161.
- Larson, K. and Nievinski, F. G. (2012). GPS snow sensing: results from the EarthScope Plate Boundary Observatory. *GPS Solutions*, 17, Pages 41–52.
- Larson, K., Small, E., Gutmann, E., Bilich, A., Axelrad, P., and Braun, J. (2008). Using GPS multipath to measure soil moisture fluctuations: initial results. *GPS Solutions*, 12, Pages 173–177.
- Lau, L. (2005). *Phase Multipath Modeling and Mitigation in Multiple Frequency GPS and Galileo Positioning*. PhD thesis, University College London.
- Lau, L. and Cross, P. (2006). A new signal-to-noise-ratio based stochastic model for GNSS highprecision carrier phase data processing algorithms in the presence of multipath errors. In *Proceedings of the 19th International Technical Meeting of the Satellite Division of The Institute of Navigation (ION GNSS 2006), Fort Worth, Texas, September 26 - 29*, Pages 276–285.
- Lawrence, R. (2003). How Good Can It Get with New Signals? Multipath Mitigation. *GPS World*.
- Le, A. Q. and Tiberius, C. (2006). Single-frequency precise point positioning with optimal filtering. *GPS Solutions*, 11, Pages 61–69.
- Leica (accessed in 17 September 2014). AR25 Choke Ring Antenna - White Paper. [http://www.leica-geosystems.de/downloads123/zz/nrs/AR25/white-tech-paper/AR25\\_WhitePaper.pdf](http://www.leica-geosystems.de/downloads123/zz/nrs/AR25/white-tech-paper/AR25_WhitePaper.pdf).

- Leick, A. (2004). *GPS Satellite Surveying*. John Wiley and Sons, Inc., Hoboken, New Jersey.
- Liso, M. N. and Kürner, T. (2014). Investigation on the influence of diffraction by wedges in satellite navigation systems. In *8th European Conference on Antennas and Propagation*, Pages 1598–1602.
- Liso, M. N., Jacob, M., Smyrnaio, M., Schön, S., and Kürner, T. (2011). Basic concepts for the modeling and correction of GNSS multipath effects using ray tracing and software receivers. In *IEEE-APS Topical Conference on Antennas and Propagation in Wireless Communications*, Pages 890–893.
- Liso, M. N., Smyrnaio, M., Schön, S., and Kürner, T. (2012). Investigation of diffraction effects in GNSS using ray tracing channel modelling. Preliminary results. In *6th European Conference on Antennas and Propagation*, Pages 3154–3158.
- Liso, M. N., Kürner, T., Smyrnaio, M., and Schön, S. (2013). Ray tracing multipath modelling in GNSS with a single reflector. In *7th European Conference on Antennas and Propagation*, Pages 3154–3158.
- Maltsev, A., Maslennikov, R., Lomayev, A., Sevastyanov, A., and Khoryaev, A. (2011). Statistical Channel Model for 60 GHz WLAN Systems in Conference Room Environment. *Radioengineering*, 20, Pages 409–422.
- Maqsood, M., Gao, S., Brown, T. W. C., Unwin, M., de vos Van Steenwijk, R., and Xu, J. D. (2013). A compact multipath mitigation ground plane for multiband antennas. *IEEE transactions on antennas and propagation*, 61, Pages 2775–2782.
- Martin, S., Kuhlen, H., and Abt, T. (2007). Interference and regulatory aspects of GNSS pseudolites. *Journal of Global Positioning Systems*, 6, Pages 98–107.
- Martin-Neira, M. (1993). A Passive Reflectometry and Interferometry System (PARIS): Application to Ocean Altimetry. *ESA Journal*, 17, Pages 331–355.
- Masters, D. S. (2004). *Surface remote sensing applications of GNSS bistatic radar: soil moisture and aircraft altimetry*. PhD thesis, University of Colorado.
- McGraw, G. A. and Braasch, M. S. (1999). GNSS multipath mitigation using gated and high resolution correlation concepts. In *Proceedings of the 1999 National Technical Meeting of The Institute of Navigation, San Diego, CA, January 25 - 27*, Pages 333–342.
- Miceli, R. J., Psiaki, M. L., ÓHanlon, B. W., and Chiang, K. Q. (2011). Real-Time Multipath Estimation for Dual Frequency GPS Ionospheric Delay Measurements. In *Proceedings of the 24th International Technical Meeting of the Satellite Division of The Institute of Navigation, Portland OR, September 19-23*, Pages 1173–1178.
- Misra, P. and Enge, P. (2006). *Global Positioning System. Signals, Measurements, and Performance*. Ganga-Jamuna Press.
- Moernaut, G. and Orban, D. (2009). GNSS antennas an introduction to bandwidth, gain pattern, polarization, and all that. *GPS World*, 20, Pages 42–48.
- Montenbruck, O., Hauschild, A., and Hessels, U. (2011). Characterization of GPS/GIOVE Sensor Stations in CONGO Network. *GPS Solutions*, 15, Pages 193–205.
- Montloin, L., Azoulai, L., Chen, A., Martineau, A., Milner, C., Chabory, A., and Macabiau, C. (2012). A GNSS Multipath Error Model for Airport Surface Operations. In *Proceedings of the 25th International Technical Meeting of the Satellite Division of The Institute of Navigation, Nashville TN, September 17-21*, Pages 210–228.



- Moore, M., Watson, C., King, M., McClusky, S., and Tregoning, P. (2014). Empirical modelling of site-specific errors in continuous GPS data. *Journal of Geodesy*, 88, Pages 887–900.
- Moradi, R., Schuster, W., Feng, S., Jokinen, A., and Ochieng, W. (2014). The carrier-multipath observable: a new carrier-phase multipath mitigation technique. *GPS Solutions*, 19, Pages 73–82.
- Mubarak, O. M. and Dempster, A. G. (2010). Analysis of early late phase in single-and dual-frequency GPS receivers for multipath detection. *GPS Solutions*, 14, Pages 381–388.
- NavstarGPS (1995). Global Positioning System Standard Positioning Service Signals Specification. Technical Report, NavstarGPS.
- NavstarGPS (2011). Global Positioning System Directorate Systems Engineering and Integration Interface Specification IS-GPS-200. Technical Report, NavstarGPS.
- Nievinski, F. G. and Larson, K. M. (2014). An open source GPS multipath simulator in Matlab/Octave. *GPS Solutions*, 18, Pages 473–481.
- Ning, T., Elgered, G., and Johansson, J. (2011). The impact of microwave absorber and radome geometries on GNSS measurements of station coordinates and atmospheric water vapour. *Advances in Space Research*, 47, Pages 186–196.
- Novatel (accessed in Nov 2012). GPS701 702GG. [http://webone.novatel.ca/assets/Documents/Papers/GPS701\\_702GG.pdf](http://webone.novatel.ca/assets/Documents/Papers/GPS701_702GG.pdf).
- Obst, M., Bauer, S., and Wanielik, G. (2012). Urban Multipath Detection and Mitigation with Dynamic 3D Maps for Reliable Land Vehicle Localization. In *Position Location and Navigation Symposium (PLANS), 2012 IEEE/ION, Myrtle Beach, South Carolina*, Pages 685–691.
- Pany, T. (2010). *Navigation Signal Processing for GNSS Software Receivers*. Artech House, Boston London.
- Pany, T. and Eissfeller, B. (2006). Use of a Vector Delay Lock Loop Receiver for GNSS Signal Power Analysis in Bad Signal Conditions. In *Position, Location, And Navigation Symposium, 2006 IEEE/ION*, Pages 893–903.
- Park, K., Elosegui, P., Davis, J., Jarlemark, P., Corey, B., Niell, A., Normandeau, J., Meertens, C., and Andreatta, V. (2004). Development of an Antenna and Multipath Calibration System for Global Positioning System Sites. *Radio Science*, 39.
- Parkinson, B. and Spilker, J. (1996a). *Global Positioning System: Theory and Applications. Volume I*. Americal Institute of Aeronautics and Astronautics, Inc.
- Parkinson, B. and Spilker, J. (1996b). *Global Positioning System: Theory and Applications. Volume II*. Americal Institute of Aeronautics and Astronautics, Inc.
- Pini, M., Falletti, E., and Fantino, M. (2008). Performance evaluation of  $C/N_0$  estimators using a real time GNSS software receiver. In *Spread spectrum techniques and applications. ISSSTA 2008. IEEE 10<sup>th</sup> symposium*, Pages 28–31.
- Prieto-Cerdeira, R., Schubert, F., Orus-Perez, R., Garcia-Molina, J., and Zanier, F. (2011). Flexible statistical multipath and shadowing model for software and hardware simulations. In *Proceedings of the 24th International Technical Meeting of the Satellite Division of The Institute of Navigation, Portland OR, September 19-23*, Pages 1804–1810.
- Rao, B. R., Kunysz, W., Fante, R., and McDonald, K. (2013). *GPS/GNSS Antennas*. Artech House, Boston London.

- Ray, J. (2000). *Mitigation of GPS Code and Carrier Phase Multipath Effects Using a Multi-Antenna System*. PhD thesis, University of Calgary.
- Ray, J., Cannon, M., and Fenton, P. (1998). Mitigation of Static Carrier Phase Multipath Effects Using Multiple Closely-Spaced Antennas. In *Proceedings of the 1th International Technical Meeting of the Satellite Division of the Institute of Navigation, ION GPS98, Nashville, Tennessee*, Pages 1025–1034.
- Rius, A., Aparicio, J., Cardellach, E., and Martin-Neira, M. (2002). Sea Surface State Measured Using GPS Reflected Signals. *Geophysical Research Letters*, 29, Pages 37–1–37–4.
- Rocken, C., Meertens, C., Stephens, B., Braun, J., Hove, T. V., Perry, S., Ruud, O., McCallum, M., and Richardson, J. (1996). UNAVCO Academic Research Infrastructure (ARI) Receiver and Antenna Test Report. Technical Report, UNAVCO.
- Rost, C. (2011). *Phasenmehrwegereduzierung basierend auf Signalqualitätsmessungen geodätischer GNSS-Empfänger*. PhD thesis, Bayerische Akademie der Wissenschaften.
- Rost, C. and Wanninger, L. (2009). Carrier phase multipath mitigation based on GNSS signal quality measurements. *Journal of Applied Geodesy*, 3, Pages 81–87.
- Rost, C. and Wanninger, L. (2010). Carrier Phase Multipath Corrections Based on GNSS Signal Quality Measurements to Improve CORS Observations. In *Position Location and Navigation Symposium (PLANS), 2010 IEEE/ION, Indian Wells/Palm Springs, California*.
- RST (accessed 04.11.2014). EADS RST - SEAGATE. <http://www.sea-gate.de/>.
- Rüeger, J. M. (1996). *Electronic distance measurements. An introduction*. Springer-Verlag Berlin Heidelberg.
- RWTH (accessed 04.11.2014). railGATE and automotiveGATE. <http://www.galileoabove.de/index.php?id=11&L=1&cHash=c9e187a97cab3478e0bbcedb94f69d89>.
- Sadrieh, S. N. (2012). *Improved navigation solution utilizing antenna diversity systems in multipath fading environments*. PhD thesis, University of Calgary.
- Schön, S., Alpers, P., and Smyrnaio, M. (2014). Troposphärische Modelle und adäquate Beobachtungsgewichtung für die Positionierung mit Pseudolites: Beispiel SEA GATE. In *Positionierung und Navigation für Intelligente Transportsysteme, Berlin, Germany*.
- Schönemann, E., Hauschild, A., Steigenberger, P., Springer, T., Dow, J., Montenbruck, O., Hugentobler, U., and Becker, M. (2010). New Results from GIOVE: The CONGO-Network and the Potential of Tracking Networks with Multiple Receiver and Antenna Types. In *EGU General Assembly, Vienna, Austria*.
- Seeber, G. (2003). *Satellite Geodesy, second edition*. Walter der Gruyter Berlin - New York 2003.
- Sharawi, M. S., Akos, D. M., and Aloj, D. N. (2007). GPS  $C/N_0$  estimation in the presence of interference and limited quantization levels. *IEEE Transactions on Aerospace and Electronic Systems*, 43, Pages 227–238.
- Shetty, P., Kakkar, A., Weinbach, U., and Schön, S. (2010). Experimental Analysis of Multipath Linear Combination of GPS and Galileo Signals. In *in Geodätische Woche, Köln, Oktober 5-7*. Poster.
- Simon, M. K., Omura, J. K., Scholtz, R. A., and Levitt, B. K. (1994). *Spread spectrum communications handbook (revised edition)*. McGraw-Hill, Inc.
- Smyrnaio, M. and Schön, S. (2015). GNSS antenna impact on the resulting multipath effects in carrier-phase and signal amplitude. In *International Association of Geodesy Symposia*.

- Smyrnaio, M., Schön, S., Liso, M., and Kürner, T. (2012). Ray-Tracing Approach versus Double Difference, Multipath Characterization in a Multiple Ray Scenario. In *6th ESA Workshop on Satellite Navigation Technologies and European Workshop on GNSS Signals and Signal Processing, ESA ESTEC, Noordwijk, Netherlands*.
- Smyrnaio, M., Schön, S., and Nicolas, M. L. (2013). *Multipath propagation, characterization and modeling in GNSS*. In: Geodetic Sciences - Observations, Modeling and Applications, Prof. Shuanggen Jin (Ed.), InTech, DOI: 10.5772/54567.
- Steingass, A. and Lehner, A. (2004). Measuring the Navigation Multipath Channel. A Statistical Analysis. In *Proceedings of the 17th International Technical Meeting of the Satellite Division of The Institute of Navigation (ION GNSS 2004), September 21 - 24, Long Beach, CA*, Pages 1157–1164.
- Stutzman, W. (1993). *Polarization in Electromagnetic Systems*. Artech House, Boston - London.
- Stutzman, W. L. and Thiele, G. A. (2013). *Antenna theory and design*. John Wiley and sons, Inc.
- Suzuki, T. and Kubo, N. (2012). GNSS Positioning with Multipath Simulation using 3D Surface Model in Urban Canyon. In *Proceedings of the 25th International Technical Meeting of the Satellite Division of The Institute of Navigation, Nashville TN, September 17-21*, Pages 438–447.
- Townsend, B., Fenton, P., Dierendonck, K. V., and Nee, R. V. (1995a). L1 Carrier Phase Multipath Error Reduction Using MEDLL Technology. In *Proceedings of the 8th International Technical Meeting of the Satellite Division of the Institute of Navigation, ION - GPS 1995, Palm Springs, California*.
- Townsend, B., Nee, R. V., Fenton, P., and Dierendonck, K. V. (1995b). Performance Evaluation of the Multipath Estimating Delay Lock Loop. *Journal of Navigation*, 42, Pages 503–514.
- Tranquilla, J., Carr, J., and Al-Rizzo, H. (1994). Analysis of a choke ring groundplane for multipath control in Global Positioning Systems (GPS) applications. *IEEE Transactions on Antennas and Propagation*, 42, Pages 905–911.
- Tsui, J. (2005). *Fundamentals of Global Positioning System Receivers. A Software Approach. Second ed.* John Wiley and Sons, Inc.
- Urlichich, Y., Subbotin, V., Stupak, G., Dvorkin, V., Povalyaev, A., Karutin, S., and Bakitko, R. (2011). GLONASS Modernization. *GPS World*.
- Van-Dierendonck, A. (1997). Evaluation of GNSS Receiver Correlation Processing Techniques for Multipath and Noise Mitigation. In *Proceedings of the 1997 National Technical Meeting of The Institute of Navigation, Santa Monica, CA*, Pages 207–215.
- Van-Dierendonck, A., Fenton, P., and Ford, T. (1992). Theory and performance of narrow correlator spacing in a GPS receiver. *Navigation*, 39, Pages 265–284.
- Van-Nee, R. (1991). Multipath effects on GPS code phase measurements. In *Proceedings of the 4th International Technical Meeting of the Satellite Division of The Institute of Navigation (ION GPS 1991), Washington, DC, September 11 - 13*, Pages 915–924.
- Van-Nee, R. (1995). *Multipath and Multi-Transmitter Interference in Spread-Spectrum Communication and Navigation Systems*. PhD thesis, Delf University of Technology.
- Vaughan, R. and Andersen, J. B. (2003). *Channels, propagation and antennas for mobile communication*. IET Electromagnetic waves series 50.
- Viterbi, A. J. (1979). Spread spectrum communications - myths and realities. *Communications Magazine, IEEE*, 17, Pages 11–18.

- Wang, L., Groves, P. D., and Ziebart, M. K. (2013). GNSS Shadow Matching: Improving Urban Positioning Accuracy Using a 3D City Model with Optimized Visibility Prediction Scoring Scheme. *Navigation*, 60, Pages 195–207.
- Wanninger, L., Frevert, V., and Wildt, S. (2000). Der Einfluss der Signalbeugung auf die präzise Positionierung mit GPS. *Zeitschrift für Vermessungswesen*, 125.
- Weinbach, U. (2013). *Feasibility and impact of receiver clock modeling in precise GPS data analysis*. PhD thesis, Leibniz Universität Hannover.
- Weiss, J. (2007). *Modeling and Characterization of Multipath in Global Navigation Satellite System Ranging Signals*. PhD thesis, University of Colorado.
- Wieser, A. (2001). *Robust and fuzzy techniques for parameter estimation and quality assessment in GPS*. PhD thesis, Technische Universität Graz.
- Wübbena, G., Menge, F., Schmitz, M., Seeber, G., and Völksen, C. (1996). A new approach for field calibration of absolute antenna phase center variations. In *Proceedings of the 9th International Technical Meeting of the Satellite Division of The Institute of Navigation, Kansas city, MO, September 17-20*, Pages 1205–1214.
- Wübbena, G., Schmitz, M., and Boettcher, G. (2006). Near-field Effects on GNSS Sites: Analysis using Absolute Robot Calibration and Procedures to Determine Corrections. In *IGS Workshop , Darmstadt, Germany*.
- Xie, P., Petovello, M. G., and Basnayake, C. (2011). Multipath Signal Assessment in the High Sensitivity Receivers for Vehicular Applications. In *Proceedings of the 24th International Technical Meeting of the Satellite Division of The Institute of Navigation, Portland OR, September 20-23*, Pages 1764–1776.
- Zaheri, M., Broumandan, A., O’Driscoll, C., and Lachapelle, G. (2009). Enhanced GNSS indoor signal detectability using polarization diversity. In *Proceedings of the 22th International Technical Meeting of the Satellite Division of The Institute of Navigation , Savannah, GA, September 22 - 25*, Pages 1756–1766.
- Zavorotny, V., Larson, K., Braun, J., Small, E., Gutmann, E., and Bilich, A. (2010). A physical model of GPS multipath caused by land reflections: toward bare soil moisture retrievals. *IEEE journal of Selected Topics in Applied Earth Observations and Remote Sensing*, 3, Pages 100–110.
- Zeimet, P. and Kuhlmann, H. (2008). On the accuracy of absolute GNSS antenna calibration and the conception of a new anechoic chamber. In *Proceedings of the FIG working week - Intergrating Generations, June 14-19, Stockholm, Sweden, 2008*.
- Ziedan, N. I. (2012). Multipath Channel Estimation and Pattern Recognition for Environment-Based Adaptive Tracking. In *Proceedings of the 25th International Technical Meeting of the Satellite Division of The Institute of Navigation, Nashville TN, September 17-21*, Pages 394–407.

# Acknowledgement

First of all, i would like to thank Steffen Schön for giving me the opportunity to work in the research field of GNSS multipath in the framework of BERTA project. I also appreciate his comments on this work and the freedom that he gave me to follow my research inters. I am also indebted to Christian Heipke and Lambert Wanninger for their willingness to review my thesis. Many thanks also go to Jürgen Müller and my colleagues at the Institute für Erdmessung for their help and collaboration during my 4.5 years in Hannover.

I would like to thank Thomas Kürner and Marcos Liso Nicolas for always being very warm hosts during my visits at the Institut für Nachrichtentechnik of the Technical University of Braunschweig. Our discussions and collaboration in the framework of BERTA project was of great importance for this work. Furthermore, i would like to thank Thorsten Schrader (PTB Braunschweig) for supporting the experiments at the antenna reference open area test site at PTB and Holm Dietz (RST Rostock System-Technik GmbH) for providing us the PSL data that were used in this thesis as well as for guiding us around the SEA GATE infrastructure in Rostock harbour area. Moreover, I truthfully thank Michael Heyl (DLR) for his supervision of BERTA related activities during the coarse of the project. I am also indebted to the space geodetic techniques section of GFZ Potsdam for hosting me in Potsdam and to IFEN GmbH for their continues support with the SX3 GNSS software receiver. Finally, i acknowledge GFZ Potsdam and DLR-GSOC for lending us their NordNav software receivers.

Above all i would like to thank my parents, my partner and my brother for their support during the ups and downs of this work. Finally, special thanks goes to all my friends for coping with me all difficulties during the course of this work with humour.



# Curriculum Vitae

- Since April 2015: PhD student, Institut für Erdmessung, University of Hannover, Hannover, Germany
- October 2010-March 2015: Scientific staff, Institut für Erdmessung, University of Hannover, Hannover, Germany
- October 2007-May 2010: Master of Science in geodesy and geoinformation science, TU Berlin, Berlin, Germany
- January 2001-May 2007: Bachelor of Science in surveying engineering, TEI of Athens, Athens, Greece
- September 1994-May 2000: High school, PSPA high school, Athens, Greece
- September 1988-May 1994: Primary school, PSPA primary school Athens, Greece
- August 1982: Born in Athens, Greece





# Declaration

I, Marios Smyrnaioi, hereby certify that I have completed the thesis independently and the used material by other is listed in the references. I did not pay any monetary benefits for regards to content. The dissertation has not been used as a M.Sc. or similar thesis before, and the thesis or parts of it have not been published before.

Berlin, 27 April 2016

